Battery-Powered RF Pre-Ionization System for the Caltech Magnetohydrodynamically-Driven Jet Experiment: RF Discharge Properties and MHD-Driven Jet Dynamics

Thesis by

Vernon H. Chaplin

In Partial Fulfillment of the Requirements

for the Degree of

Doctor of Philosophy

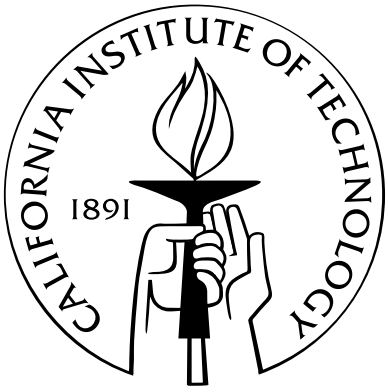

California Institute of Technology

Pasadena, California

2015

(Defended April 29, 2015)

Acknowledgments

My parents, David and Jane Chaplin, encouraged my interest in math from an early age and laid the foundations for my love of science by providing me with a childhood in which fun and learning were always intertwined. I am grateful for their unwavering commitment to my education, and for their continued love and support as I move forward toward a new chapter in life.

I was fortunate to attend several excellent schools prior to Caltech. Among the many terrific teachers from whose tutelage I benefited, my career trajectory was shaped most profoundly by Alice Snodgrass, my geometry teacher at John Burroughs School in St. Louis; Dr. Mac LaCasse, my physics and calculus teacher at Indian Springs School in Birmingham; and Professors David Cohen and Michael Brown, my undergraduate thesis advisors at Swarthmore College in Philadelphia.

Upon arriving at Caltech, I could not have chosen a better research advisor than Professor Paul Bellan. He is an innovative and brilliant plasma physicist, adept at everything from analytical theory to electrical circuit design, and he is also a superb writer, speaker, and teacher. However, these qualities are perhaps commonplace among Caltech professors, who are by definition among the very best in their fields. What truly makes Paul special is his kindness and good humor, and the supportive environment that he cultivates in his group. On more than one occasion, I stopped by Paul's office to apologize for burning out an expensive circuit component, and he immediately launched into a story about a mishap from his own research career, putting me at ease. I might have suspected that these stories were fabricated or embellished simply to make me feel better, were it not for the time I walked in on Paul during one of his rare sojourns in the lab and found that he had exploded a quartz tube in our test vacuum chamber, filling it with thousands of glass shards.

I know how hard it is to be interrupted while in the middle of a difficult problem and then have to pick it up again later, yet Paul is always willing to take a break from what he

is doing and engage in an in-depth discussion whenever a student knocks on his door. If he ever feels stressed because of an upcoming grant deadline or due to his students' floundering research progress, he hides it extremely well. I have tried to learn as much as possible from the examples he sets, noting his strategies for tackling physics problems and the way he balances his interests with practical considerations when deciding how to spend his time.

I have also benefited greatly from my interactions with other members of the Bellan group. Deepak Kumar, Rory Perkins, Auna Moser, and Eve Stenson were the most senior students when I arrived; they were instrumental in helping me learn the research ropes, and in more recent years, all four of them have given me valuable career advice. I was particularly inspired by the rigor of Rory's scientific approach, which I have tried to emulate.

KilByoung "KB" Chai, our postdoc since 2012, has broadened the group's horizons with his fascinating ice dusty plasma experiments, and I have learned much from his efficient approach to research and his relentless dedication to making things work in the lab. Recently when I have found myself going off on an unproductive tangent, I have often reminded myself to try to be more like KB. I also benefited from observing the care with which Professor Taiichi Shikama carried out his experiments and analysis during his one-year visit to Caltech, and I appreciated his help in understanding my spectroscopic data.

Bao Ha and Xiang Zhai will join me in graduating this summer—our years working together have been filled with good times and many fruitful scientific discussions. I am grateful to Bao for keeping the group's server and other computing infrastructure up and running, and to Xiang for playing a major role in setting up and testing the capacitor banks and other equipment for the new chamber on which Bao and I would ultimately carry out our thesis research.

Zach Tobin spent several weeks struggling to get IDL to communicate with the VME digitizer for the new experiments—I am extremely thankful for his persistence in this unenviable task. I also appreciated the many hours Mark Kendall spent studying for candidacy with me, even though he secretly had no intention of scheduling his exam that year.

Magnus Haw has quickly become a productive group member, and he is well equipped to take on the mantle of senior graduate student once Bao, Xiang, and I are gone. I am thankful to Magnus and KB for finding the stamina to read through my entire thesis draft and offer feedback. The group's new students, Ryan Marshall, Pakorn (Tung) Wongwaitayakornkul, and Young Yoon, have been admirably dedicated in finding time to learn about

the experiments in the midst of their busy four-class schedule, so the lab appears to be in good hands.

Dave Felt provided critical electrical engineering support during my time in the Bellan group, designing and building many of the circuits necessary for basic operation of the experiments. I also took advantage of a number of other excellent on-campus resources to accelerate my research progress, including Mike Gerfen in the Central Engineering machine shop, Joe Haggerty and company in the GALCIT machine shop, Mike Roy in the Chemistry Instrument Shop, Rick Gerhart in the glass shop, and Rick Germond in the facilities stockroom.

I have appreciated Connie Rodriguez's dedication to handling administrative tasks for the Bellan group, reconciling our unremitting stream of purchases, processing travel reimbursements, and keeping us informed about facilities work that might affect our lab. I have also received valuable assistance from Donna Driscoll in the physics department and Christy Jenstad in the applied physics and materials science department.

I would like to thank my candidacy committee, Professors Konstantinos Giapis, Christian Ott, and Dave Rutledge, and my thesis committee, Professors Konstantinos Giapis, Lynne Hillenbrand, and Joe Shepherd, for their helpful feedback and insightful questions.

Finally, I am grateful to my wife Cathy, who is the most wonderful teammate I could ever imagine. Thank you for your patience during these long graduate school years, and for bringing balance, joy, and laughter to my life every day. I am also indebted to our daughter June for learning to sleep through the night before my final push to finish this thesis. She has always been such a considerate girl.

Abstract

This thesis describes investigations of two classes of laboratory plasmas with rather different properties: partially ionized low pressure radiofrequency (RF) discharges, and fully ionized high density magnetohydrodynamically (MHD)-driven jets. An RF pre-ionization system was developed to enable neutral gas breakdown at lower pressures and create hotter, faster jets in the Caltech MHD-Driven Jet Experiment. The RF plasma source used a custom pulsed 3 kW 13.56 MHz RF power amplifier that was powered by AA batteries, allowing it to safely float at 4–6 kV with the cathode of the jet experiment. The argon RF discharge equilibrium and transport properties were analyzed, and novel jet dynamics were observed.

Although the RF plasma source was conceived as a wave-heated helicon source, scaling measurements and numerical modeling showed that inductive coupling was the dominant energy input mechanism. A one-dimensional time-dependent fluid model was developed to quantitatively explain the expansion of the pre-ionized plasma into the jet experiment chamber. The plasma transitioned from an ionizing phase with depressed neutral emission to a recombining phase with enhanced emission during the course of the experiment, causing fast camera images to be a poor indicator of the density distribution. Under certain conditions, the total visible and infrared brightness and the downstream ion density both increased after the RF power was turned off. The time-dependent emission patterns were used for an indirect measurement of the neutral gas pressure.

The low-mass jets formed with the aid of the pre-ionization system were extremely narrow and collimated near the electrodes, with peak density exceeding that of jets created without pre-ionization. The initial neutral gas distribution prior to plasma breakdown was found to be critical in determining the ultimate jet structure. The visible radius of the dense central jet column was several times narrower than the axial current channel radius, suggesting that the outer portion of the jet must have been force free, with the current parallel to the magnetic field. The studies of non-equilibrium flows and plasma

self-organization being carried out at Caltech are relevant to astrophysical jets and fusion energy research.

Contents

Chapter 1

Introduction

This thesis will describe experimental and theoretical investigations of radiofrequency (RF) plasma discharges and electromagnetically-driven plasma jets. An RF "pre-ionization system" was developed to enable the formation of hotter, faster laboratory plasma jets than was possible using DC high-voltage gas breakdown alone. The ultimate goal of this research was to improve our understanding of astrophysical accretion disk jets through scaled-down, reproducible laboratory experiments, and also to contribute to the development of practical nuclear fusion power through fundamental studies of plasma relaxation and non-equilibrium dynamics. Along the way, a number of interesting properties of RF discharges were discovered and analyzed. The richness of plasma physics was abundantly evident in the range of unexpected phenomena seen in these experiments—sorting out the physical explanations for the observed behaviors was an exciting and enjoyable pursuit that likely could have kept me busy for a lifetime. Alas, one should not remain in graduate school forever, so the remaining mysteries will have to be solved by a future student.

The remainder of this chapter will present some background on plasmas and describe applications of plasma physics to controlled fusion and astrophysical jets. An overview of the equipment and technologies used in the pulsed power plasma experiments in the Bellan lab at Caltech will be given, and the new pre-ionized jet experiments that are the subject of this thesis will be motivated. The following two chapters will cover the design of the RF plasma source, including the battery-powered RF power amplifier (Chapter 2), and experiments and modeling to characterize the equilibrium properties of the RF discharge and to determine the primary mechanism for coupling energy to the plasma (Chapter 3). Chapter 4 will describe the unexpectedly complex time-dependent expansion of the RF plasma into the jet experiment vacuum chamber, and the initially confusing observations will be explained with

the help of measurements from several complementary diagnostics and through comparisons with a detailed numerical model. The RF plasma evolution involved a fascinating afterglow phase in which the ion density and visible light emission both increased; these behaviors are the subject of Chapter 5.

Experiments on pre-ionized magnetohydrodynamically (MHD)-driven jets will be described in Chapter 6. The plasma parameters that were achieved differed by less than an order of magnitude from those obtained previously without pre-ionization, but the modified geometry of the experiment led to a notably different jet morphology, with possible implications for the radial structure of astrophysical jets. Appendices A–H contain detailed explanations of some of the circuit designs, diagnostic operating principles, and mathematical derivations referenced in the main text. Finally, Appendix I will describe the design of a new pre-ionized flux rope experiment that will build upon the lessons learned from the jet experiment, aiming to create significantly lighter, hotter current-carrying plasma loops using two RF plasma sources.

1.1 Plasmas

A plasma is an ionized gas, in which electromagnetic forces play an important role. The action of the Lorentz force on the charged particles in a plasma leads to a host of interesting and complex behaviors that are not seen in ordinary neutral fluids (liquids and gases), including non-intuitive single particle trajectories, fast-growing instabilities, and an impressive array of supported wave modes. Aside from the relatively exotic category of non-neutral plasmas (for example, pure electron [1] or positron [2] plasmas), plasmas are generally quasineutral, meaning that the ion and electron densities are equal over length scales much larger than a microscopic distance[1] called the Debye length:

$$\lambda_D \equiv \left(\sum_\sigma \frac{1}{\lambda_{D\sigma}^2} \right)^{-1/2} \quad ; \quad \lambda_{D\sigma} \equiv \sqrt{\frac{\epsilon_0 k T_\sigma}{n_\sigma q_\sigma^2}}. \tag{1.1}$$

The subscript σ refers to the charged particle species (either electrons or ions), n_σ is the particle density, q_σ is the species charge, and T_σ is the temperature, usually specified in

[1] The Debye length is < 1 mm for typical laboratory plasmas, but it can be a macroscopic length for low density astrophysical and space plasmas.

electron volts[2] (eV), so that Boltzmann's constant is $k = 1.6 \times 10^{-19}$ J/eV. The electrons and ions in a plasma often have different temperatures because collisional energy transfer between the species is very inefficient due to their large mass difference.

The vast majority of the ordinary matter in the universe is in the plasma state, so understanding plasma behavior is a central problem in astronomy and space physics. In this thesis we will focus particularly on accretion disks and the associated collimated jets; other topics of widespread interest include the solar core and atmosphere (and those of other stars), Earth's ionosphere and magnetosphere, and high energy cosmic rays. Plasmas appear naturally on Earth in the form of lightning and auroras, and man-made plasmas have many technological applications in fields ranging from integrated circuit fabrication to space propulsion. A particularly exciting application is controlled nuclear fusion, a tremendously promising but also immensely challenging pursuit that could eventually provide the world with a nearly limitless source of clean energy.

1.1.1 Kinetic Theory of Plasmas

The most straightforward way to analyze plasmas is to calculate the trajectories of individual charged particles while self-consistently updating the electric and magnetic fields that they create; unfortunately, such an approach is not practically feasible due to the sheer number of particles involved[3]. A statistical mechanical approach is therefore valuable. In one dimension, we define the distribution function $f_\sigma(x, v, t)$ to be the number of particles with position between x and $(x + dx)$ and velocity between v and $(v + dv)$ at time t. Extending this definition to three dimensions, we can calculate the temporal rate of change of $f_\sigma(\mathbf{x}, \mathbf{v}, t)$ at a given location $(\mathbf{x}, \mathbf{v})$ in six-dimensional phase space due to particles flowing into or out of the phase space volume of interest to derive the Boltzmann or Vlasov equation [4, Section 2.3]:

$$\frac{\partial f_\sigma}{\partial t} + \mathbf{v} \cdot \nabla f_\sigma + \nabla_v \cdot (\mathbf{a} f_\sigma) = \sum_\alpha C_{\sigma\alpha}(f_\sigma)\,, \tag{1.2}$$

[2] Although specifying temperatures in energy units is somewhat confusing, it is convenient for laboratory plasmas since typical electron temperatures range from a few eV for partially ionized gas discharges to ~ 10 keV for fusion plasmas. 1 eV = 11594 K, and room temperature is about 0.025 eV.

[3] "Particle-in-cell" simulations do apply this tactic but reduce the number of particles in the calculation by grouping many electrons or ions into a single macro-particle that moves as a unit. Densities of typical laboratory plasmas range from $\sim 10^{15}$ m^{-3} for a low-density gas discharge to $\sim 10^{32}$ m^{-3} for inertial confinement fusion plasmas [3].

where $\mathbf{a} = (q_\sigma/m_\sigma)(\mathbf{E} + \mathbf{v} \times \mathbf{B})$ is the acceleration of an individual particle due to the Lorentz force and $\nabla_v = \hat{x}\,(\partial/\partial v_x) + \hat{y}\,(\partial/\partial v_y) + \hat{z}\,(\partial/\partial v_z)$. $C_{\sigma\alpha}(f_\sigma)$ is the rate of change of the distribution function for species σ due to collisions with species α. An elastic collision causes a nearly instantaneous change in a particle's velocity and thus results in the effective destruction of a particle at the location $(\mathbf{x}, \mathbf{v}_{old})$ in phase space and the simultaneous creation of a particle at $(\mathbf{x}, \mathbf{v}_{new})$. Inelastic collisions, on the other hand, may cause ionization or recombination and thus actually change the total number of particles in the physical volume of interest.

1.1.2 Two-Fluid Model of Plasmas

The distribution function can be thought of as the probability for a randomly selected particle to be at position $\mathbf{x}$ with velocity $\mathbf{v}$ at time t. Integrating over all velocities gives the number density of species σ, i.e.,

$$n_\sigma(\mathbf{x}, t) = \int f_\sigma(\mathbf{x}, \mathbf{v}, t)\, d^3v. \tag{1.3}$$

The mean velocity is

$$\mathbf{u}_\sigma(\mathbf{x}, t) = \frac{\int \mathbf{v} f_\sigma(\mathbf{x}, \mathbf{v}, t)\, d^3v}{\int f_\sigma(\mathbf{x}, \mathbf{v}, t)\, d^3v} = \frac{\int \mathbf{v} f_\sigma(\mathbf{x}, \mathbf{v}, t)\, d^3v}{n_\sigma(\mathbf{x}, t)}. \tag{1.4}$$

These integrals are called "velocity moments" of the distribution function; in general, we calculate the "nth" moment by multiplying $f_\sigma(\mathbf{x}, \mathbf{v}, t)$ by $\mathbf{v}^n$ and integrating over velocity. We may also take moments of the entire Vlasov equation to derive a coarser "two-fluid" description of plasma dynamics in which the details of the velocity distribution are glossed over and only the mean fluid properties for each species are considered. For example, multiplying Eq. 1.2 by $\mathbf{v}^0 = 1$ and integrating over velocity gives the zeroth moment:

$$\int \left(\frac{\partial f_\sigma}{\partial t} + \mathbf{v} \cdot \nabla f_\sigma + \nabla_v \cdot (\mathbf{a} f_\sigma) \right) d^3v = \sum_\alpha \int C_{\sigma\alpha}(f_\sigma)\, d^3v, \tag{1.5}$$

which can be simplified to produce the two-fluid continuity equation for electrons and ions:

$$\frac{\partial n_\sigma}{\partial t} + \nabla \cdot (n_\sigma \mathbf{u}_\sigma) = G - L. \tag{1.6}$$

The terms on the right-hand side represent particle gains (G) due to ionization and losses (L) due to recombination. More specific expressions for the ionization and recombination rates will be given in later chapters.

The first moment of the Vlasov equation yields the two-fluid momentum equation:

$$n_\sigma m_\sigma \left(\frac{\partial}{\partial t} + \mathbf{u}_\sigma \cdot \nabla\right) \mathbf{u}_\sigma = n_\sigma q_\sigma \left(\mathbf{E} + \mathbf{u}_\sigma \times \mathbf{B}\right) - \nabla P_\sigma - \sum_\alpha \nu_{\sigma\alpha} m_\sigma n_\sigma \left(\mathbf{u}_\sigma - \mathbf{u}_\alpha\right), \quad (1.7)$$

where m_σ is the mass of an individual particle and $\nu_{\sigma\alpha}$ is the rate at which collisions transfer momentum from species σ to species α. $\left(\frac{\partial}{\partial t} + \mathbf{u}_\sigma \cdot \nabla\right)$ is a convective derivative, which captures the rate of change of a quantity in the reference frame moving at the mean fluid velocity $\mathbf{u}_\sigma$. If the velocity distribution is Maxwellian, i.e., if $f_\sigma(\mathbf{x}, \mathbf{v}, t) = n_\sigma \left(m_\sigma / 2\pi k_B T_\sigma\right)^{3/2} \exp\left(-m_\sigma \left(\mathbf{v} - \mathbf{u}_\sigma\right)^2 / 2k_B T_\sigma\right)$, then the pressure is given by the ideal gas law, $P_\sigma = n_\sigma k_B T_\sigma$. Collisions between particles tend to make the velocity distribution Maxwellian, but hot, low density plasmas are nearly collisionless, in which case a non-Maxwellian distribution can persist. In this case it is not possible to define a unique species temperature, and the Vlasov equation should be used to calculate the actual form of $f_\sigma(\mathbf{x}, \mathbf{v}, t)$.

Taking the second moment of the Vlasov equation leads to the two-fluid energy equation [5, Section 2.3], [4, Section 2.5]:

$$\frac{\partial}{\partial t}\left(\frac{3}{2} P_\sigma\right) + \nabla \cdot \left(\frac{3}{2} P_\sigma \mathbf{u}_\sigma\right) + P_\sigma \nabla \cdot \mathbf{u}_\sigma = -\nabla \cdot \mathbf{q}_\sigma + \mathbf{u}_\sigma \cdot \sum_\alpha m_\sigma n_\sigma \nu_{\sigma\alpha} \left(\mathbf{u}_\sigma - \mathbf{u}_\alpha\right) - \sum_\alpha \left(\frac{\partial W}{\partial t}\right)_{E\sigma\alpha}. \quad (1.8)$$

From left to right, the terms in this equation represent the rate of change of the thermal energy density, the divergence of the macroscopic thermal energy flux, the heating or cooling of the fluid due to changes in its volume, the divergence of the microscopic heat flux, the heating of species σ due to frictional drag on other species, and the net collisional energy transfer from species σ to other species. In order to close the system of two-fluid equations (which includes Eqs. 1.6, 1.7, and 1.8, plus Maxwell's equations), an approximation must be adopted for the heat flux $\mathbf{q}_\sigma$, since it only appears in the energy equation (in fact, each successive moment of the Vlasov equation introduces a new variable that did not appear in the previous moment equations—a clear limitation of the fluid approach). For processes with characteristic velocity $v_{char} \gg v_{T\sigma}$ (where the thermal velocity is defined as

$v_{T\sigma} \equiv \sqrt{2k_B T_\sigma / m_\sigma}$), we may set $\mathbf{q}_\sigma \approx 0$ (adiabatic regime). Another possibility is to set $\mathbf{q}_\sigma = -\kappa_{T\sigma} \nabla T_\sigma$, where $\kappa_{T\sigma}$ is the thermal conductivity; this approach will be utilized and explained in detail in Sec. 4.4.2.1.

1.1.3 Magnetohydrodynamics (MHD)

Another description of plasmas, known as magnetohydrodynamics (MHD), treats the electrons, ions, and neutrals together as a single fluid, with differences in the mean electron and ion velocities accounted for through the current density $\mathbf{J} = \sum_\sigma n_\sigma q_\sigma \mathbf{u}_\sigma$. Like the corresponding two-fluid equations, the MHD continuity and momentum equations can be derived from moments of the Vlasov equation, this time taking mass-weighted sums over the three species. The complete system of equations, in their most commonly used form, is

$$\frac{\partial \rho}{\partial t} + \nabla \cdot (\rho \mathbf{U}) = 0 \tag{1.9}$$

$$\rho \left(\frac{\partial}{\partial t} + \mathbf{U} \cdot \nabla \right) \mathbf{U} = \mathbf{J} \times \mathbf{B} - \nabla P + \rho \mathbf{g} \tag{1.10}$$

$$P \rho^{-5/3} = const. \tag{1.11}$$

$$\nabla \times \mathbf{E} = -\frac{\partial \mathbf{B}}{\partial t} \tag{1.12}$$

$$\nabla \times \mathbf{B} = \mu_0 \mathbf{J} \tag{1.13}$$

$$\mathbf{E} + \mathbf{U} \times \mathbf{B} = \eta \mathbf{J}. \tag{1.14}$$

Here $\rho = \sum_\sigma m_\sigma n_\sigma$ is the total mass density of the plasma, $\mathbf{U} = \sum_\sigma m_\sigma n_\sigma \mathbf{u}_\sigma / \rho$ is the center of mass velocity, η is the electrical resistivity, and $\mathbf{g}$ is the acceleration due to gravity, which has been included here because it is often important in astrophysics (it was neglected in the Vlasov and two-fluid models described previously).

Eq. 1.14 is the MHD Ohm's law—it is derived [4, Section 2.6] by making a number of approximations to the two-fluid electron momentum equation (Eq. 1.7). Its curl is often taken to yield the induction equation:

$$-\frac{\partial \mathbf{B}}{\partial t} + \nabla \times (\mathbf{U} \times \mathbf{B}) = \nabla \times \left(\frac{\eta}{\mu_0} \nabla \times \mathbf{B} \right). \tag{1.15}$$

Many plasmas are nearly perfectly conducting, so that $\eta \approx 0$ and the Ohm's law becomes

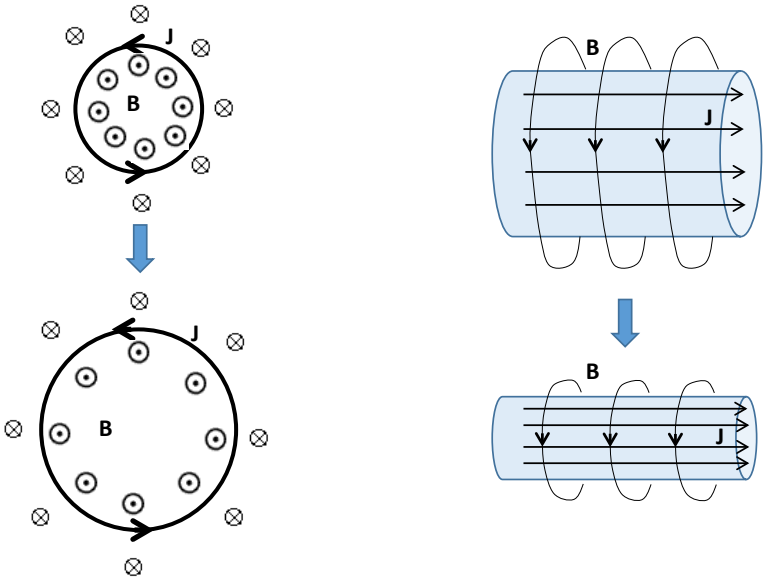

Figure 1.1: Illustration of the hoop force (left) and pinch force (right) for a current-carrying MHD plasma.

simply

$$\mathbf{E} + \mathbf{U} \times \mathbf{B} = 0, \tag{1.16}$$

which is known as the ideal MHD Ohm's law. From special relativity, the electric field $\mathbf{E}'$ in the plasma frame is related to the $\mathbf{E}$ and $\mathbf{B}$ fields in the lab frame by $\mathbf{E}' = \mathbf{E} + \mathbf{U} \times \mathbf{B}$, where $\gamma \approx 1$ has been used since non-relativistic MHD is only valid for $U \ll c$. Eq. 1.16 thus gives $\mathbf{E}' = 0$, so Faraday's law (the integral form of Eq. 1.12) implies that the magnetic flux Φ is constant in the frame of the plasma. This "frozen-in flux" property is a key characteristic of ideal MHD plasmas. A more rigorous derivation would use Eq. 1.15 to explicitly calculate the rate of change of the magnetic flux through a surface moving with the plasma [4, Section 2.6.4].

Many behaviors of MHD plasmas can be understood qualitatively by thinking of the plasma as a bundle of current-carrying wires. Since wires carrying parallel currents are attracted to one another, a current-carrying column of plasma will tend to contract radially—this is known as the "pinch force" (right panel of Fig. 1.1). On the other hand, a current-carrying loop has oppositely directed currents on either side, so the $\mathbf{J} \times \mathbf{B}$ force will cause it to expand—this is known as the "hoop force" (left panel of Fig. 1.1).

We can use vector identies to re-write the magnetic force term in Eq. 1.10 as [4, Section

9.5]

$$\mathbf{J} \times \mathbf{B} = \frac{1}{\mu_0} \left(-\nabla_\perp \left(\frac{B^2}{2} \right) + B^2 \hat{B} \cdot \nabla \hat{B} \right), \tag{1.17}$$

where $\hat{B} \cdot \nabla \hat{B}$ is a measure of the curvature of field lines. This equation shows that the magnetic force acts like a pressure in the directions perpendicular to the field and like a tension (which tries to straighten out field lines) in the direction parallel to the field. In this picture, the hoop force exists because there is greater magnetic pressure inside a current-carrying loop than outside it, while the pinch force is a manifestation of the tension of the azimuthal field lines surrounding a current-carrying plasma cylinder (see Fig. 1.1).

MHD is the simplest of the three models presented here and thus is well-suited for describing global plasma dynamics, particularly in situations with complicated geometry, for which using the more detailed models would be cumbersome. However, many important real-world plasma phenomena are not predicted by MHD, and we must frequently return to the two-fluid or Vlasov models to obtain a more complete physical picture. For example, a two-fluid model will be required to describe the expansion of an unmagnetized partially ionized plasma in Chapter 4, and the Vlasov equation is needed to understand the collisionless damping of electrostatic waves [4, Chapter 5].

1.1.4 Single Particle Motion: Guiding Center Drifts

While they have tremendous practical utility, the Vlasov and fluid equations tend to obscure what is going on at a microscopic, single-particle level. These motions can be counterintuitive, in large part because the magnetic field exerts a force in the direction perpendicular to a charged particle's velocity. In the absence of additional forces, ions and electrons follow helical trajectories, spiraling around field lines. On the other hand, in the presence of both electric and magnetic fields, particles undergo a constant "drift" motion in the $\mathbf{E} \times \mathbf{B}$ direction. The drift velocity is easily derived by time-averaging the Lorentz force equation over the fast cyclotron orbits in order to isolate the motion of the particle's "guiding center"

(here the subscript $\perp$ denotes the direction perpendicular to $\mathbf{B}$):

$$m_\sigma \langle \frac{d\mathbf{v}_{\sigma\perp}}{dt} \rangle = q_\sigma \left(\mathbf{E}_\perp + \langle \mathbf{v}_{\sigma\perp} \rangle \times \mathbf{B} \right) \tag{1.18}$$

$$0 = \mathbf{E}_\perp + \langle \mathbf{v}_{\sigma\perp} \rangle \times \mathbf{B} \tag{1.19}$$

$$\langle \mathbf{v}_{\sigma\perp} \rangle \equiv v_{E\times B} = \frac{\mathbf{E} \times \mathbf{B}}{B^2}. \tag{1.20}$$

In general, for any constant, spatially uniform force $\mathbf{F}$ acting on the particle, there is a drift velocity:

$$v_F = \frac{\mathbf{F} \times \mathbf{B}}{qB^2}. \tag{1.21}$$

$\mathbf{F}$ does not have to be a physical force like gravity; a particle undergoing helical cyclotron motion along a curved field line feels a centrifugal force that leads to a cross-field "curvature" drift, and the presence of a magnetic field gradient also leads to drift motion (known as the "grad-B" drift) because the Larmor radius varies over the course of a cyclotron orbit. Finally, a temporal change in any of the other drift velocities leads to an additional guiding center drift known as the polarization drift: $(-md\mathbf{v}_F/dt)$ is an effective force, so Eq. 1.21 gives

$$\mathbf{v}_p = -\frac{m}{qB^2} \frac{d\mathbf{v}_F}{dt} \times \mathbf{B}. \tag{1.22}$$

1.1.5 Plasma Waves

Wave phenomena are of significant importance in plasmas. Global oscillations are supported at the plasma frequency, $\omega_p \equiv \sqrt{\sum_\sigma \omega_{p\sigma}^2} \equiv \sqrt{\sum_\sigma n_\sigma q_\sigma^2/\epsilon_0 m_\sigma}$, and a wide variety of propagating wave modes can also exist. Some of these are similar to electromagnetic waves propagating in vacuum, others resemble sound waves, and many involve more complicated dynamics, with the oscillatory motions of electrons and ions coupled together by electric and magnetic fields.

Wave analysis [4, Chapter 4] is typically carried out by assuming that the perturbation to the equilibrium plasma state is small, so that a generic plasma parameter $h(\mathbf{x}, t)$ may be written as the sum of its equilibrium value $h_0(\mathbf{x}, t)$ and a perturbation $h_1(\mathbf{x}, t)$, where $h_1 \ll h_0$. The equations describing the system are re-written using this decomposition, discarding terms higher than first order in the perturbed quantities, and the equilibrium equations (with $h = h_0$ for all quantities) are subtracted off to yield the "linearized" system

of equations describing the plasma. The perturbed variables are assumed to vary as $h_1 \sim \exp(i\mathbf{k}\cdot\mathbf{x} - i\omega t)$, where ω is the angular frequency and $k = 2\pi/\lambda$ is the wavenumber, and the linearized system is solved to yield a "dispersion relation", which gives the relationship between ω and k for a single Fourier mode. In general ω may be complex, i.e., $\omega = \omega_r + i\omega_i$. $\omega_i < 0$ implies that the wave is damped in time, while $\omega_i > 0$ corresponds to spontaneous growth (instability). When the wave amplitude becomes large, the assumption that $h_1 \ll h_0$ breaks down, and a more complex nonlinear wave analysis must be used.

Waves for which the dispersion relation is independent of temperature are known as "cold" plasma waves, while waves with a temperature-dependent dispersion relation are called "hot" plasma waves. This terminology is somewhat misleading, since cold plasma waves can readily exist in a very hot plasma—the true meaning is that having a finite spread of particle velocities does not affect the wave behavior for cold waves, so the temperature could be set to zero without changing the wave. A complete analysis of warm plasma waves requires a kinetic approach, while cold plasma waves may be accurately described by fluid theories.

1.2 Magnetically Confined Fusion Power and Spheromaks

The production of energy through controlled nuclear fusion requires that a dense, extremely hot (~ 10 keV $\approx 10^8$ K for deuterium-tritium fusion) plasma be confined for long enough to allow a significant number of fusion reactions to occur. Stars accomplish this confinement using gravity, but for terrestrial applications the plasma mass is far too small, so magnetic confinement, inertial confinement using high-power lasers, and various hybrid approaches are being pursued. The majority of magnetic confinement fusion research to date has focused on the tokamak concept [6], in which ionized particles are confined on closed magnetic flux surfaces in a toroidal, or donut-shaped, geometry.

Defining a cylindrical coordinate system with the z-axis pointing through the donut hole, we typically label the ϕ direction "toroidal" and the r and z directions "poloidal". Plasma is confined in a tokamak by the pinch force produced by a toroidal current, which is driven either transiently by an external solenoid positioned along the axis of the torus or by other (potentially steady state) methods such as neutral beam injection, RF waves, and naturally arising "bootstrap current". A strong toroidal magnetic field, produced by

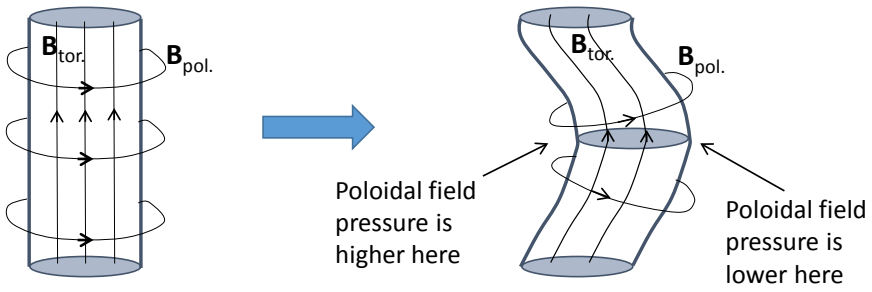

Figure 1.2: The kink instability for a straight current-carrying column (which approximates a small section of a toroidal plasma), explained in terms of magnetic pressure. A small helical perburbation leads to an inbalance in the poloidal field pressure on opposite sides of the plasma column, so the perturbation grows spontaneously if the toroidal magnetic field is not strong enough to provide stabilization.

external coils, is also necessary in order to avoid the MHD kink instability (illustrated in Fig. 1.2). The tendency of a current-carrying plasma to spontaneously kink can be understood qualitatively [4, Section 9.6] by noting from electrical circuit theory that the stored magnetic energy is $W_B = LI^2/2 = \Phi^2/2L$. Due to the frozen-in flux property of hot MHD plasmas, Φ is approximately constant, so the plasma can decrease its magnetic energy by evolving into a helical shape and increasing its inductance L. On the other hand, energy is required to deform the embedded toroidal field, so $B_{tor.}$ can provide stabilization against kinking. Stability is maintained if the "safety factor" $q \equiv aB_{tor.}/RB_{pol.} > 1$ everywhere in the plasma, where a is the minor radius and R is the major radius of the tokamak [4, Section 10.9]. This is called the Kruskal-Shafranov kink stability criterion.

After almost 60 years of research, tokamaks have progressed nearly to the point of net fusion energy production, and the upcoming ITER experiment [7] in France should achieve this goal[4]. However, in order to achieve good energy confinement tokamaks have to be large (ITER will have $R = 6.2$ m and $a = 2.0$ m) and consequently they are expensive (ITER's estimated cost is $20 billion USD and rising). Alternative confinement concepts may have a better chance at enabling a commercially viable reactor. One such concept is the spheromak [8], in which a torus-shaped plasma is confined in a simply connected (usually cylindrical) flux conserving vessel. The plasma is confined by the interaction of its internal currents with image currents in the walls.

[4]... if the project is not derailed by endlessly increasing costs and international political bickering.

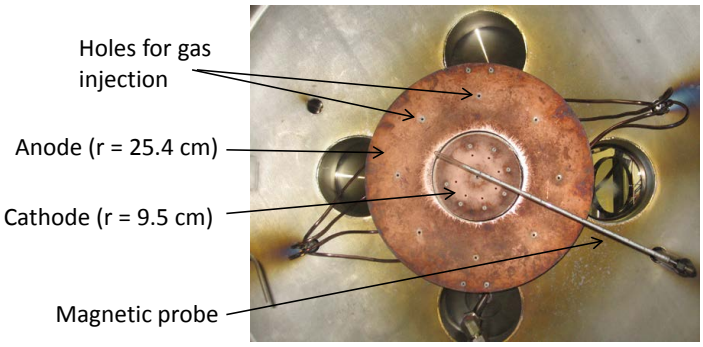

Figure 1.3: The original coaxial planar electrodes used to create spheromaks and MHD-driven jets in the Bellan plasma lab at Caltech.

Spheromaks do not need large external toroidal field coils (which are one of the most expensive parts of a tokamak); instead, the plasma is allowed to kink [5] [10] and undergo other instabilities, before finally settling into a nearly force-free equilibrium[6] with the magnetic field in the plasma satisfying

$$\nabla \times \mathbf{B} = \lambda \mathbf{B}, \tag{1.23}$$

where λ is a constant (i.e., spatially uniform). The process by which the plasma evolves toward a force-free state is called Woltjer-Taylor relaxation [12, 13]. The critical concept is conservation of global magnetic helicity, defined by:

$$K \equiv \int \mathbf{A} \cdot \mathbf{B} d^3 r, \tag{1.24}$$

where $\mathbf{A}$ is the magnetic vector potential. Helicity is a measure of the number of linkages or twists in the magnetic field. It is conserved in an ideal MHD plasma, since the magnetic topology remains constant due to frozen-in flux. On the other hand, in a plasma with finite resistivity, the helicity may change, but it is dissipated much more slowly than the magnetic energy $W_B = B^2/2\mu_0$ [4, Problem 11.2]. Therefore, it is a good approximation to assume that helicity is conserved as the plasma evolves toward a minimum energy state, in which case Eq. 1.23 can be derived using a variational argument [4, Section 11.3].

[5] Although the kink instability is not necessarily problematic for spheromaks, there are other global MHD instabilities and difficulties with poor energy confinement that must be reckoned with in order to develop a practical spheromak fusion reactor [9, Section 13.6].

[6] The equilibrium can only be truly force-free, with $\mathbf{J} \times \mathbf{B} = 0$, for a plasma with negligible thermal pressure, i.e., $\beta \equiv P/(B^2/2\mu_0) = 0$. Spheromaks that have been studied to date have all had low β, but for a fusion reactor it would be desirable to have β as high as possible (≥ 0.1) [11].

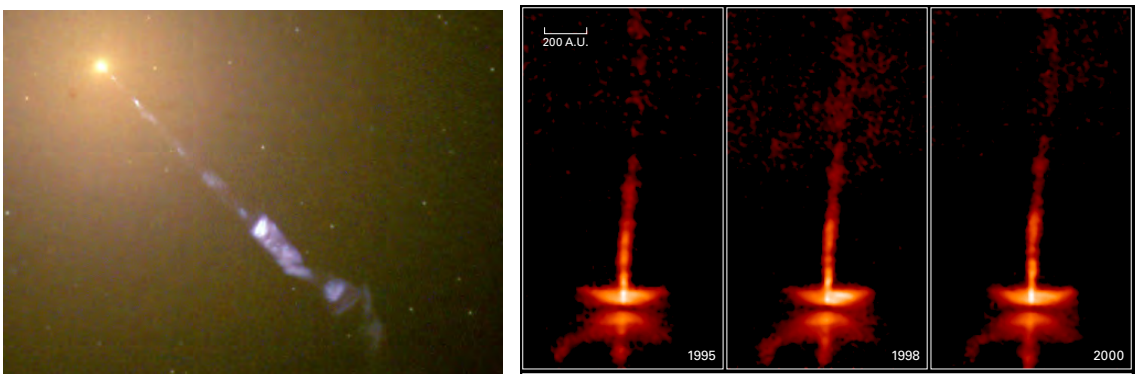

Figure 1.4: Left: Hubble Space Telescope photograph of the M87 AGN jet, constructed by combining images from several optical filters. The blue light is synchrotron radiation emitted by relativistic electrons. The jet is $\sim 5 \times 10^{19}$ m long when viewed in visible light, while its radio emission extends for $\sim 10^{21}$ m. It is believed to be driven by a $\sim 2 \times 10^9$ solar mass black hole at the center of the galaxy. Right: Hubble images showing the evolution of the HH 30 YSO jet over a five year period. The accretion disk surrounding the young star is visible at the bottom of the images. The visible jet length is $\sim 2 \times 10^{14}$ m, and its velocity is 40–270 km/s. Images from www.hubblesite.org, News Release numbers STScI-2000-20 and STScI-2000-32.

The theory of Woltjer-Taylor relaxation has been very successful at explaining the observed equilibrium properties of spheromaks (as well as those of reversed-field pinches [14] and many astrophysical plasmas); however, the relaxation process through which the plasma reaches its final state is not well understood. Spheromaks are usually created using a cylindrical coaxial plasma gun [15]; when the plasma emerges from the gun, relaxation has already begun and the spheromak is partially formed. On the other hand, the Caltech Spheromak Experiment (also called the Caltech MHD-Driven Jet Experiment) creates spheromaks using a novel planar coaxial plasma gun designed by Scott C. Hsu and Paul M. Bellan [16, 17]. This electrode design, shown in Fig. 1.3, allows for unrestricted diagnostic access in the formation region. Through high-speed imaging and magnetic probe measurements during the early stages of the plasma's evolution, new insights into the formation of spheromaks and related plasma structures have been obtained [10, 17].

1.3 Astrophysical Jets

Because low-β plasmas with helical magnetic fields tend to spontaneously relax toward a force-free state, spheromak-like plasmas are common in nature. One example is the

collimated supersonic jets commonly driven from astrophysical accretion disks on both stellar and galactic scales. Images of an active galactic nucleus (AGN) jet and a young stellar object (YSO) jet are shown in Fig. 1.4. Although these jets differ in scale by 6–7 orders of magnitude, the basic physical mechanisms that explain the jets' formation and their impressive collimation (i.e., nearly uniform axial cross sectional area along the length of the jet) are likely universal [18]. Astrophysical jets were once thought to be purely hydrodynamically driven, but models without magnetic fields have difficulty explaining many of the observed properties [19, 20], and it is now generally accepted that MHD forces are of dominant importance for launching and collimation [18, 21]. Several jet models have predicted a force-free magnetic field structure in some region of the jet [22, 23], and there is observational evidence of helical magnetic fields in AGN jets [22, 24], although there is some ambiguity in the interpretation of the measurements [25].

In addition to being beautiful and fascinating phenomena, jets are likely of fundamental importance to the evolution of the accretion disk and central object [18]. AGN jets can carry large amounts of energy from a central black hole to distant reservoirs (radio lobes), with the mass and power transported often composing a significant fraction of the total amount available [21, p. 2]. In order for a star to form, the material in the surrounding accretion disk must lose almost all of its angular momentum so that it can fall inwards. Instabilities and turbulence in the disk are typically invoked to explain outward angular momentum transport [26], but jets may also be important once the material approaches the inner magnetosphere of the star [21, p. 91–92].

The most promising models for MHD-driven astrophysical jets begin with a poloidal magnetic field linking the accretion disk and central object. The field is frozen into the nearly perfectly conducting disk plasma, and it becomes twisted up due to differential rotation. The resulting toroidal field component collimates the jet through the MHD pinch force (see Fig. 1.1). An influential model by Blandford and Payne [23] posits that low-β plasma above the disk is forced by the poloidal magnetic field to orbit at the same velocity as the underlying disk, which rotates at the local Keplerian velocity. If the field intersects the disk at an angle of less than 60 degrees, centrifugal forces will fling this material outward along the field lines. Higher up, the toroidal field collimates the outflow into a jet. Alternately, magnetic towers and related models [27, 28, 29] attribute the jet acceleration to an axial gradient in the toroidal magnetic field pressure (equivalently, this is a manifestation of the

hoop force due to a poloidal current; see the caption for Fig. 1.5).

High resolution observations of the central engines of jets have found that the outflows are only weakly collimated near the source. For instance, the M87 AGN jet was found to have an opening angle of $\sim 60^\circ$ at a distance of 100 Schwarzchild radii from the driving black hole, but several parsecs from the core the opening angle decreases to $< 10^\circ$ [30]. Similarly, Ray et al. [31] estimated that the initial opening angle of HH 30 was at least 60°, and other YSO jets also have large opening angles near the star [32]. These observations may favor a magnetocentrifugal launching mechanism like that proposed by Blandford and Payne, with collimation by the toroidal field or ambient gas pressure further from the disk.

However, Bellan [33] questioned the fundamental assumption made by Blandford and Payne (and most other jet theorists) that an accretion disk consists of an ideal MHD plasma undergoing Keplerian orbital motion around a central object, with the angular velocity of a fluid element at radius r proportional to $r^{-3/2}$ (for the ideal case of a circular orbit). In the presence of a gravitational force in the $-\hat{r}$ direction and a magnetic field in the poloidal ($\hat{r}/\hat{z}$) direction, an individual ion in the plane of the disk will undergo a guiding center drift in the toroidal ($\hat{\phi}$) direction, with a velocity given by Eq. 1.21. Since all ions at a given distance from the source are drifting at this velocity, which for typical field strengths is much smaller than the Keplerian orbit velocity at radius r, the center of mass of the plasma cannot be moving at the Kepler velocity[7]. In place of differential Keplerian rotation twisting up the magnetic field, Bellan proposed an alternate mechanism involving a dust-driven dynamo to produce the radial electric field necessary to drive the poloidal current believed to accelerate and collimate the jet.

The details of the jet launching and collimation mechanisms (and the extent to which they are universal across different types of accreting systems) remain open questions because sparse observational data exists to confirm or refute the predictions of the models. YSO jets are difficult to study because they are cool and weakly ionized and thus only emit detectable radiation from portions of the jet that have been heated by shocks, so images may not be indicative of the underlying jet structure. AGN jets are observed through the synchrotron radiation emitted by magnetized relativistic electrons, but the protons that may carry most of the flow energy remain invisible [21, p. 16–20]. Directly measuring the magnetic field

[7]Furthermore, the electrons drift in the $-\hat{\phi}$ direction, so there is a net toroidal current density in the plasma which produces a $\mathbf{J} \times \mathbf{B}$ force to keep the MHD fluid from falling inward.

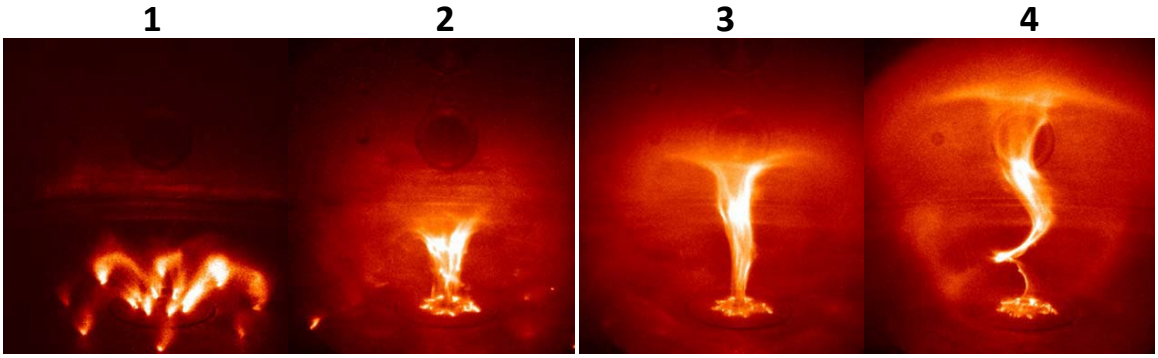

Figure 1.5: High-speed camera images (false color) showing the Caltech MHD-Driven Jet Experiment sequence for a plasma shot with intermediate λ_{gun}. 1) An external "bias" coil behind the inner electrode (cathode) creates an arched poloidal magnetic field linking the electrodes. Neutral gas is puffed into the chamber, then a radial electric field is created by applying a high voltage across the electrodes, breaking down the gas to form current-carrying plasma loops that follow the poloidal field. 2) The current loops expand due to the MHD hoop force, merging along the central axis because their parallel currents attract one another. 3) Driven by the $\mathbf{J} \times \mathbf{B}$ force (or equivalently, the toroidal magnetic field pressure gradient), the jet expands away from the electrodes and is collimated. A diffuse envelope completes the current path from the anode to the cathode. 4) The jet goes kink unstable, evolving toward a force-free equilibrium determined by the amount of helicity injected at the electrodes (i.e., the value of λ_{gun}). The images shown here are rotated 90 degrees relative to the actual experiment orientation illustrated in Fig. 1.6.

strength and direction in YSO jets is impossible except in special cases [34], such as when relativistic electrons from another source stream through the jet and emit synchrotron radiation [35]. The situation is somewhat better for AGN jets, as the polarization angle of the synchrotron emission as a function of frequency allows the magnitude of the field and its direction in the plane of the sky to be estimated [36], but relating the measurements to models still requires substantial interpretation and guesswork [21, p. 52]. In all cases, the vast distances involved mean that the jet launching region subtends an extremely small angle on the sky: < 0.1 arcsecond for the closest YSO jets [21, p. 120] and < 1 milliarcsecond for the closest AGN jets [30].

Because of these observational difficulties, there is ample opportunity for numerical simulations [28] and laboratory experiments to make useful contributions to our understanding of astrophysical jet physics. MHD-driven jets similar to astrophysical magnetic tower jets can be created at the Caltech Spheromak Experiment. The experiment's coaxial electrodes (see Fig. 1.3) have the same topology as an accreting system in astrophysics: the inner elec-

trode is analogous to the central star or black hole, and the outer electrode is analogous to the accretion disk. An initially poloidal magnetic field is created linking the electrodes, and gas is injected and ionized to form arches of plasma following the background field lines. A capacitor bank is used to drive poloidal current through these plasma loops, causing them to merge and form a jet (see Fig. 1.5). Three basic regimes exist for the experiment [10], depending on the value of the Woltjer-Taylor state eigenvalue λ imposed at the electrodes:

$$\lambda_{gun} = \frac{\mu_0 I_{gun}}{\psi_{gun}}, \tag{1.25}$$

where I_{gun} is the peak poloidal current and ψ_{gun} is the poloidal magnetic flux intercepting the inner electrode. For small λ_{gun}, a stable, straight MHD-driven jet forms, while for intermediate λ_{gun} the jet goes kink unstable. Both of these behaviors are relevant to astrophysical jets. For high λ_{gun}, the plasma quickly detaches from the electrodes.

1.4 Simulating Astrophysics in the Laboratory

Carrying out laboratory experiments to simulate astrophysical objects with dimensions ranging from astronomical units to megaparsecs is possible in principle because of the scalability of MHD. The MHD continuity equation (1.9), momentum equation (Eq. 1.10), and induction equation (Eq. 1.15) can be written in dimensionless form as

$$\frac{\partial \bar{\rho}}{\partial \tau} = -\bar{\nabla} \cdot \left(\bar{\rho}\bar{\mathbf{U}}\right) \tag{1.26}$$

$$\bar{\rho}\left(\frac{\partial}{\partial \tau} + \bar{\mathbf{U}} \cdot \bar{\nabla}\right)\bar{\mathbf{U}} = \left(\bar{\nabla} \times \bar{\mathbf{B}}\right) \times \bar{\mathbf{B}} - \beta \bar{\nabla} \bar{P} + \gamma \bar{\rho} \bar{\mathbf{g}} \tag{1.27}$$

$$\frac{\partial \bar{\mathbf{B}}}{\partial \tau} = \bar{\nabla} \times \left(\bar{\mathbf{U}} \times \bar{\mathbf{B}}\right) + \frac{1}{S}\bar{\nabla}^2 \bar{\mathbf{B}}, \tag{1.28}$$

where the induction equation has been simplified by assuming that η is spatially uniform. All variables with bars over them have been normalized to typical values in the plasma (denoted with a subscript 0) and are of order unity; the relative importance of the various terms is captured in the three dimensionless parameters:

$$\beta \equiv \frac{2\mu_0 P_0}{B_0^2} \quad ; \quad S \equiv \frac{\mu_0 L v_A}{\eta} \quad ; \quad \gamma \equiv \frac{g_0 L}{v_A^2}, \tag{1.29}$$

Quantity	AGN Jet	YSO Jet	Lab Jet (hydrogen)
L	10^{21} m	10^{14} m	0.3 m
n	10 m^{-3}	10^{10} m^{-3}	10^{22} m^{-3}
B	10^{-9} T	10^{-7} T	0.1 T
v_A	10^4 km/s	20 km/s	20 km/s
β	< 1?	0.4	0.1–1
S	$\ggg 1$	10^{15}	10–100

Table 1.1: Typical physical and dimensionless parameters for AGN jets, YSO jets, and laboratory jets. Densities and magnetic field strengths for AGN and YSO jets were taken from [21, p. 34]. To calculate β and S for YSO jets, a temperature of 1 eV was assumed [20]. The temperature for AGN jets is poorly constrained because we can only detect non-thermal synchrotron emission. Note that all of the values for astrophysical jets are very rough and may differ by orders of magnitude over the length of a given jet [34]. In particular, the jets may be low-β and Alfvénic in the acceleration region but high-β and super-Alfvénic ($v > v_A$) further from the source where the magnetic field is weaker.

where $v_A \equiv B_0/\sqrt{\rho_0 \mu_0}$ is the characteristic Alfvén velocity and S is called the Lundquist number. These dimensionless equations imply that plasmas that have the same values of β, S, and γ and the same geometry will behave identically if MHD is applicable. Note that the characteristic length scale L appears only in the definitions of S and γ; if the plasma is perfectly conducting so $S \to \infty$ (ideal MHD) and gravity is of negligible importance so $\gamma \to 0$, then the system of equations becomes scale invariant.

Ideal MHD is an excellent approximation for astrophysical plasmas (S is enormous because the length scale L is extremely large), except in certain localized regions where terms neglected in Eq. 1.16 become important. In these locations, the frozen-in flux condition breaks down and "magnetic reconnection" can occur, releasing magnetic energy and changing the global magnetic topology (but approximately conserving helicity, as discussed in Sec. 1.2). The Caltech MHD-Driven Jet Experiment also has $S \gg 1$ (although it is much smaller than in astrophysical systems), so ideal MHD is approximately valid, and $\beta < 1$, so magnetic forces are of dominant importance for the jet acceleration and collimation. Therefore, the laboratory jets should be governed by similar physics as accretion disk jets for regions far from the central star where $\gamma \ll 1$. Typical plasma parameters for the laboratory jets, YSO jets, and AGN jets are listed in Table 1.1.

The near-disk region in the experiment is subject to boundary effects due to the plasma interaction with the metal electrodes that do not exist in an accretion disk, and relativistic effects present in AGN jets cannot be seen in the experiment. The effects of radiative cool-

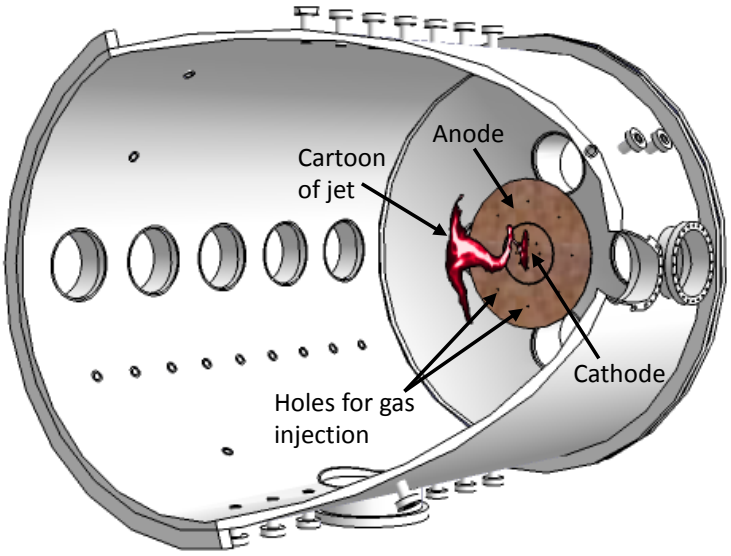

Figure 1.6: Cutaway view of the vacuum chamber for the MHD-Driven Jet Experiment.

ing may also differ between the laboratory and astrophysical jets. Despite these differences, the experiment reproduces key aspects of astrophysical jet dynamics and serves as a valuable testbed for jet models [28], while possessing some major advantages over astronomical observations, namely far superior diagnostic accessibility and the ability to actively tune the plasma parameters to test scaling relationships.

Another obvious difference between the laboratory and astrophysical systems is that the outer electrode in the experiment does not rotate. However, if we accept for the moment the usual picture of an accretion disk as a differentially rotating ideal MHD plasma, note that Eq. 1.16 implies that the interaction of the disk rotation with the poloidal magnetic field will create a radial electric field $E_r = -U_\phi B_z$ in the frame of the central object. This electric field drives a poloidal current that creates a toroidal magnetic field—the same process that was earlier described as the frozen-in poloidal field getting twisted up. In the experiment, an equivalent radial electric field is produced by the electrostatic voltage applied between the anode and cathode. The end result, helicity injection and a hoop force that drives jet expansion and collimation, is the same.

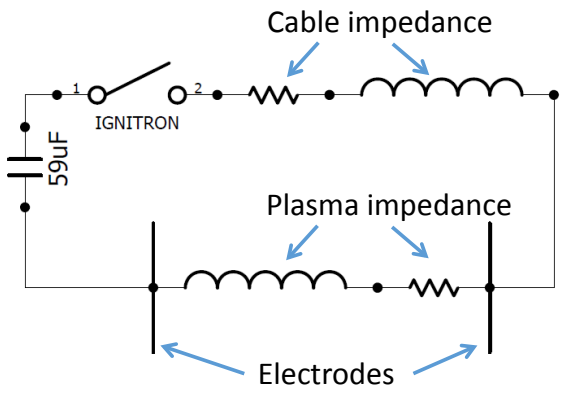

Figure 1.7: Main discharge circuit for the MHD-Driven Jet Experiment. The ignitron switch is described in Appendix A.

1.5 Overview of Experiment Setup

The experiments were carried out in a large stainless steel vacuum chamber with the coaxial planar electrodes mounted on one end, as shown in Fig. 1.6. The walls were far enough away from the electrodes that the plasma had minimal interaction with them and essentially expanded into free space, as in an astrophysical system. Numerous windows and ports gave access for optical diagnostics and probes. The diagnostic techniques used to study the laboratory jets and the RF plasmas used for pre-ionization will be described in detail in Secs. 6.1 and 3.1, respectively.

The jet plasma was an arc discharge, driven by a high voltage capacitor attached across the coaxial electrodes. The formation of plasma in front of the electrodes completed an underdamped series RLC circuit, as illustrated in Fig. 1.7. Additional pulsed capacitor discharge circuits were used to create the background poloidal magnetic field and to power the electromagnetic valves used for neutral gas injection—details are given in Secs. 1.6.3 and 1.6.4. A precision timing system, described in Sec. 1.6.5, was used to trigger the capacitor banks and diagnostics for the experiment.

Throughout this thesis, a cylindrical coordinate system will be used with the z axis aligned along the central axis of the chamber and the origin at the center of the electrodes. As in the discussions of toroidal fusion plasmas and astrophysical jets, the r and z directions will be called "poloidal" and the ϕ direction will be called "toroidal".

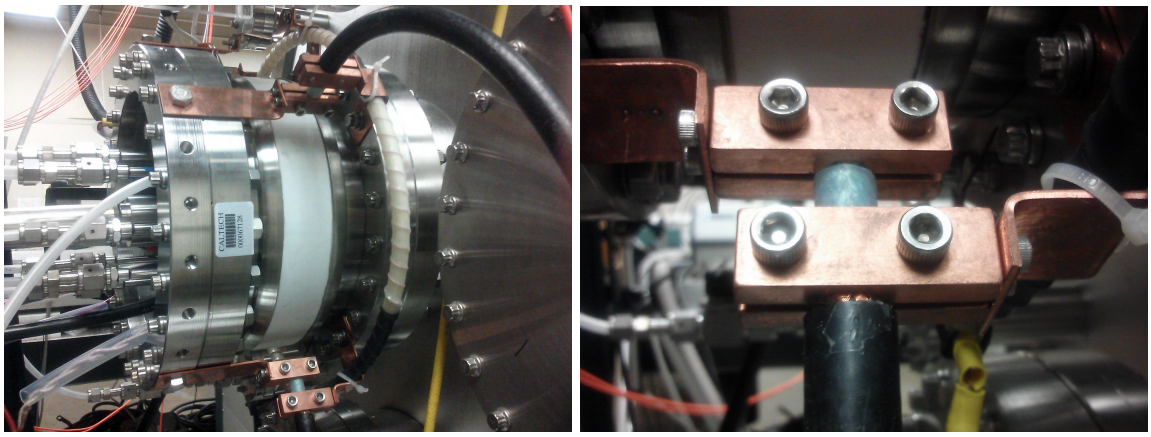

Figure 1.8: Left: Photo showing the electrical connections between the jet experiment and the coaxial cables leading to the main capacitor bank. The inner conductor of the coaxial cables was electrically connected to the inner electrode, while the outer conductor of the cables was attached to the chamber and the outer electrode. Right: Close-up of the copper cable clamp pieces, which were fabricated by the Caltech Aerospace (GALCIT) machine shop.

1.6 Experimental Hardware

This section contains a detailed description of the experimental hardware: the reader who is primarily interested in the big picture physics may skip to Sec. 1.7. The modules described here, with minor variations, are common to all of the pulsed power plasma experiments in the Bellan lab. Descriptions of the novel hardware and electronics that were unique to this thesis work will be deferred to Chapter 2 and the appendices.

1.6.1 Vacuum Chamber

The length of the stainless steel vacuum chamber was 114.3 cm, not counting the end domes, and the radius was 45.7 cm (earlier spheromak formation and MHD-driven jet experiments were carried out in a similar, larger chamber with length 163.0 cm and radius 68.6 cm). The chamber was pumped to a base pressure $< 5 \times 10^{-7}$ Torr by a Leybold TMP 1000 turbo pump backed by an Edwards XDS10 scroll pump. The electrodes were machined from 1/8" thick oxygen-free high conductivity (OFHC) copper by the Caltech Aerospace (GALCIT) machine shop.

1.6.2 Main Capacitor Bank

The main discharge circuit (see Fig. 1.7) consisted of an ignitron-switched 59 μF capacitor bank (containing an Aerovox type PX70D10 capacitor rated to 20 kV), high-voltage coaxial cables and cable clamping pieces (see Fig. 1.8), the electrodes, and the plasma itself. Examples of the discharge current and voltage waveforms during plasma shots are shown in Figs. 6.9 and H.6. The total energy stored by the capacitor was $\sim$ 1 kJ when it was charged to -6 kV, and the electrical power delivered to the plasma during the first 5 μs of the discharge could be as high as $\sim$ 100 MW.

The capacitor was charged by an Ultravolt 12C24-N125 12 kV, 125 W power supply. A system of relays disconnected the power supply from the capacitor before the bank was triggered to protect the supply from damage. After each plasma shot, another relay connected a pair of Kanthal 889AS series 300 Ω resistors in parallel across the capacitor to safely dissipate any residual charge.

Fast switching of discharge currents up to $\sim$ 60 kA was accomplished using a General Electric GL7703 ignitron (rated for up to 20 kV and 100 kA) [37] that was mounted on top of the capacitor in a low-inductance coaxial housing designed by Paul M. Bellan. As part of this thesis work, a new circuit was designed for rapidly triggering the ignitron—details are given in Appendix A.

1.6.3 Bias Field Coil and Bank

The bias field coil, which was used to produce the initial vacuum poloidal magnetic field, was wound using AWG 11 square heavy build magnetic wire onto a custom bobbin (machined from G-10 phenolic by the Caltech Aerospace (GALCIT) machine shop) by Coil Winding Specialist. The coil had 100 turns stacked 10 high and 10 deep, and the radius to the center of the windings was 7.91 cm. It was attached behind the inner electrode as shown in Fig. 2.2 using eight size #8 glass-filled nylon screws[8].

The bias coil current was provided by a 14.44 mF capacitor bank (consisting of 5 Kemet PEH200ZX4330MB2 aluminum electrolytic capacitors in parallel), switched by a silicon-controlled rectifier (SCR). The capacitors were charged by an Ultravolt 1/2C24-P125 500

[8]The original jet experiment had used four ordinary nylon screws; these once snapped during an experiment at a high bias bank voltage due to the strong repulsive force between the coil current and the opposing current induced in the inner electrode.

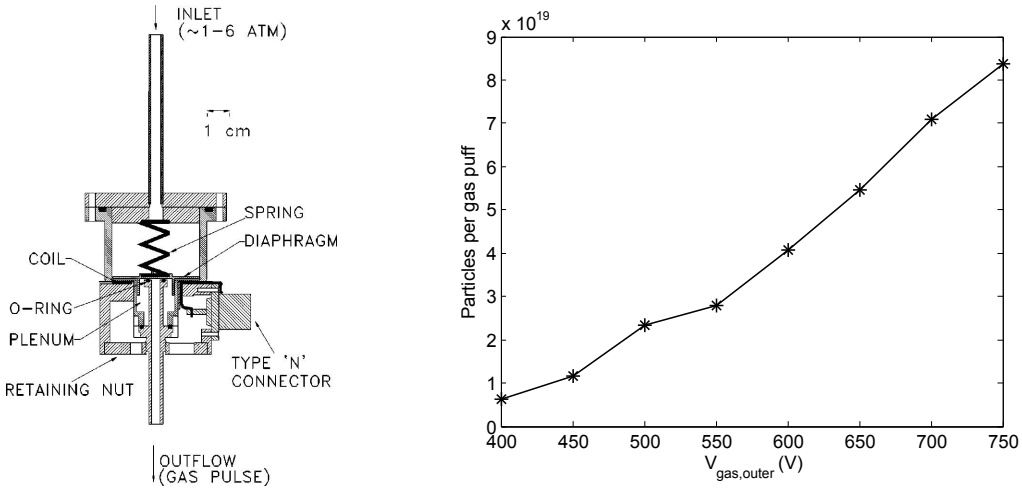

Figure 1.9: Left: Fast gas valve design (figure from [38]). Right: Total throughput for the outer electrode fast gas valve when operated with argon gas at 75 psig, measured by monitoring the pressure rise in the chamber after gas puffs with the turbo pump turned off and its exhaust valve closed.

V, 125 W power supply, which was itself powered by an Absopulse DIO 122-24/24-R4513 24 V DC power supply with 20 kV isolation, which allowed the entire capacitor bank to float electrically during plasma shots. The floating circuit was attached to the jet experiment cathode through a 15 Ω high pulse energy non-inductive resistor (Carborundum Co. 887AS series), so that it followed changes in the cathode voltage.

The bias coil inductance measured by a BK Precision Model 885 LCR/ESR meter at 100 Hz was 1.53 mH, while a fit to the measured series RLC circuit discharge gave $L_{coil} = 1.65$ mH and $R_{coil} = 260$ mΩ. The direction of the magnetic field produced by the coil could be reversed by opening or closing a relay in the capacitor bank. When the power switch for the bank was turned off, the capacitors were automatically discharged through a Kanthal 886AS series 60 Ω resistor.

1.6.4 Fast Gas Valves

Neutral gas was injected into the chamber through 8 holes in each of the inner and outer electrodes (see Fig. 1.3) by electromagnetically controlled fast pulsed gas valves [38] that were triggered 1–7 ms before the main capacitor bank (see Table 1.2). Transient gas injection was necessary to achieve high enough gas pressure directly in front of the electrodes to enable plasma breakdown ($p \sim 100$ mTorr was necessary in the absence of pre-ionization),

while retaining high vacuum in the remainder of the chamber so that the jet, once formed, could propagate into empty space. The location of the gas inlets determined the initial plasma geometry, the 8-loop "spider leg" configuration seen in Panel (1) of Fig. 1.5, which approximated the azimuthally symmetric initial condition for astrophysical jets.

The gas valves were triggered by driving a current through an internal coil located below a conducting diaphragm (see the left panel of Fig. 1.9), which induced an opposing current in the diaphragm and caused it to jump upward, releasing high-pressure (typically 60–100 psig) gas that had been confined in the plenum. The current pulse was provided by a capacitor bank consisting of a CSI Capacitors 50 μF, 1.5 kV rated thin film capacitor that was charged by an Ultravolt 1C20-P24 1 kV, 20 W power supply and switched by an SCR. A diode (type 85HF160) was installed in parallel with the capacitor to prevent the voltage from ringing negative and damaging the power supply as the underdamped RLC circuit discharged.

The capacitor bank for the gas valve attached to the high voltage inner electrode was installed beside the bias field bank, and both were powered by the same Absopulse isolation supply. When the bank was switched off, the 50 μF capacitor was discharged through an Ohmite AZ331KE 330 Ω ceramic non-inductive resistor rated for up to 2.8 kJ pulse energy. Additional 50 μF capacitor banks were used to power the other two fast gas valves used in the experiment.

The quantity of gas injected by each valve could be varied by adjusting the gas bank charging voltage V_{gas}. The total throughput of the gas valves increased approximately linearly with V_{gas} (see the right panel of Fig. 1.9). However, the relevant quantity for the experiment was the instantaneous gas density in front of the electrodes when the main bank was triggered, and there was strong evidence (see Fig. 5.3 and [38]) that this density scaled nonlinearly with V_{gas}. This may have been because above a certain gas bank voltage, further increases in V_{gas} caused the diaphragm to stay open longer but did not lead to a substantial increase in the rate of gas flow from the valve.

1.6.5 Data Acquisition and Timing Systems

Electrical data was digitized by a 40-channel VME (Versa Module Europa) system from Struck Innovative Systeme. The VME was controlled by an IDL program. Each channel had 50 Ω input impedance and accepted voltages from -500 mV to 500 mV with 11-bit

Gas species	Inner Electrode	Outer Electrode	RF Plasma Source
Hydrogen	-1.1 ms	-2.3 ms	-1.45 ms
Helium	-1.7 ms	-3.0 ms	-2.2 ms
Argon	-5.0 ms	-7.0 ms	-6.15 ms

Table 1.2: Standard timings for the fast gas valves that supplied gas to the 8 inner electrode inlets, to the 8 outer electrode inlets, and to the RF pre-ionization plasma source discharge tube. The gas travel distance between the fast gas valve and the plane of the electrodes was approximately 1.09 m, 1.70 m, and 1.78 m, respectively, for the three gas valves. Note that the outer electrode gas timing used with hydrogen was longer than would be expected based on the relative sound speeds and travel distances; however, this long delay was necessary to form a well-defined jet. A similarly anomalous outer electrode gas timing has always been used for hydrogen shots on the original MHD-driven jet experiment.

dynamic range (so the resolution was $\sim$ 0.5 mV). The standard sampling rate was 100 MHz.

Trigger pulses for the capacitor banks, VME, and other experiment components were provided by Quantum Composers Model 9518 programmable digital pulse generators. The triggers were converted to optical signals and then back to electrical using Avago Technologies fiber optic transmitters (HFBR-1414) and receivers (HFBR-2412), so that the timing system was isolated from the experiment in order to avoid false triggers caused by ground loops and other electrical pickup. Typically the bias bank was triggered 11 ms before the main capacitor bank, so that the bias field in front of the electrodes reached its peak value[9] at $t = 0$. Standard timings for the fast gas valves are listed in Table 1.2.

The time delay for breakdown was not consistent from shot-to-shot (although RF pre-ionization improved the situation–see Sec. 6.2). In order to obtain a consistent timing reference for the fast cameras and other diagnostics, the pulse generator that controlled the diagnostics was triggered by light emitted by the plasma itself at the time of breakdown, which was collected by an optical fiber attached to a collimating lens pointed at one of the inner electrode gas inlets.

[9]Although the bias bank discharge current peaked $\sim$ 7 ms after it was triggered, magnetic field measurements using Hall probes constructed by Bao N. Ha showed that the field in the chamber peaked $\sim$ 4 ms later due to diffusion through the copper electrodes.

1.7 Motivation for Pre-Ionization

Previous experiments in the Bellan plasma lab have yielded many interesting results, providing fundamental insights into the physics of spheromak formation [10, 39], demonstrating the importance of non-equilibrium, MHD-driven flows in the expansion and collimation of current-carrying flux tubes [40], and identifying a mechanism by which MHD plasmas may undergo fast magnetic reconnection as a result of a multiscale instability cascade [41]. However, the experiments have been limited to operating in a high density ($\geq 10^{21}$ m^{-3}) regime because of the requirements for achieving the initial plasma breakdown. If the plasma density could be decreased while keeping the level of electrical energy input unchanged, then we would expect to produce hotter, faster MHD-driven jets and spheromaks. These hotter plasmas would have increased relevance to fusion, and they would also be more similar to astrophysical jets. Specifically, the Lundquist number in the laboratory jets would be increased since it is proportional to $n_i^{-1/2}T_e^{3/2}$ (because $v_A \propto n_i^{-1/2}$ and $\eta \propto T_e^{-3/2}$ [4, p. 596]). Increasing the jet velocity would bring the experiment closer to the relativistic regime relevant to AGN jets, although achieving $v \sim 0.1c$ would require a factor of 1000 increase in velocity, which is probably impossible to realize in practice[10]. Another motivation for decreasing the plasma density is simply to broaden the accessible region of parameter space. Previous experience has shown that such exploration often leads to unforeseen breakthroughs; for example, increasing the jet experiment duration by installing a pulse forming network enabled the discovery of the aformentioned multiscale instability cascade [43].

The criterion for gas breakdown in a DC electric field is known as Paschen's law, after Friedrich Paschen, who discovered experimentally in 1889 that the minimum voltage required for breakdown was a function of the product of the gas pressure and the distance between the electrodes [45]. Lieberman and Lichtenberg [5, p. 544] present a rough derivation of the minimum breakdown voltage, which is given by

$$V_b = \frac{Bpd}{\ln(Apd) - \ln[\ln(1 + 1/\gamma_{se})]}, \tag{1.30}$$

[10]Since the jets are electromagnetically driven, we can estimate the velocity scaling by setting the kinetic energy density equal to the magnetic field energy density, i.e., $\rho v^2/2 = B^2/2\mu_0$. This yields $v = B/\sqrt{\mu_0\rho} = v_A$, so the jets are expected to be Alfvénic. In order to increase the velocity by a factor of 1000 while holding B constant, the density would have to be decreased by a factor of 10^6. Driving ~ 50 kA of current through a plasma with $n = 10^{16}$ m^{-3} would likely lead to kinetic instabilities [42] that would rapidly break up the jet (for further discussion, see Sec. I.1).

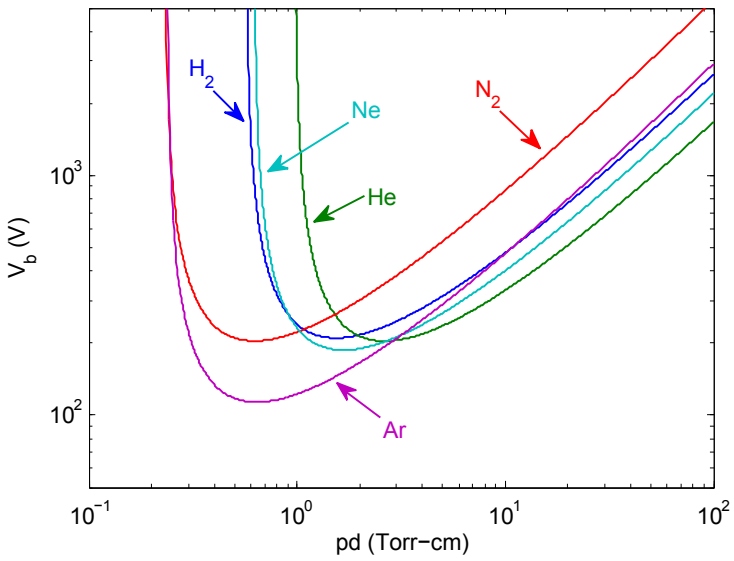

Figure 1.10: Paschen curves calculated from Eq. 1.30. The curves give the minimum DC voltage for breakdown of each gas as a function of pd. $\gamma_{se} = 0.07$ was assumed [44]. These curves are only rough estimates; in reality A and B in Eq. 1.30 are only constant over a limited range of electric field strengths, and γ_{se} is also energy-dependent above ~ 500 eV, so experimentally obtained Paschen curves will be more accurate.

where γ_{se} is the secondary electron emission coefficient for ions striking the cathode and A and B are empirically determined constants. Using values for A and B from [5, Table 14.1], Eq. 1.30 is plotted in Fig. 1.10 for several gases of interest.

The dependence on pd may be understood intuitively by realizing that breakdown occurs through electric impact ionization of neutral atoms. The mean free path for electron-atom collisions is $\lambda_{en} = (n_g \sigma_{en})^{-1}$, where n_g is the gas density and σ_{en} is the collision cross section. If pd is very small, then λ_{en} will be longer than the inter-electrode distance d, and too few ionizing collisions will occur to achieve breakdown. On the other hand, if pd is too large, λ_{en} will be very short compared to d, and electrons will tend to undergo randomizing collisions before they have been accelerated through a sufficient potential difference to attain the energy necessary for ionization. Breakdown is thus easiest to achieve at intermediate values of pd. Below a threshold pd at which the Paschen curve asymptotes to vertical, breakdown is not possible at any voltage. The Caltech experiments have typically operated near this low-pressure limit for breakdown, at the left-hand side of the Paschen curve. Therefore, unless the distance between the electrodes was increased, which was not practical, the quantity of gas injected (which ultimately determined the plasma density since the discharges were

nearly 100% ionized) could not be decreased.

However, if plasma is already present when a DC electric field is applied to a system, then the Paschen breakdown criterion does not apply. It is easier to sustain a gas discharge than it is to initiate one. The rest of this thesis describes the design and characterization of a radiofrequency (RF) pre-ionization system, and its application to the Caltech experiments. By ionizing plasma in a tube behind the electrodes and allowing it to flow into the chamber before the main capacitor bank was triggered, it was possible to make lighter, faster, hotter MHD-driven jets than could be created using Paschen breakdown alone. Independent of the pulsed power jet experiment, some interesting RF discharge behaviors were discovered and studied in detail—these investigations are the subject of Chapters 3, 4, and 5.

Chapter 2

Pre-Ionization System Design

2.1 RF Plasmas

Various technologies for achieving plasma pre-ionization exist, including triggered spark gaps, hot electron-emitting filaments, radiofrequency (RF) plasma sources, and microwave sources. Microwaves with frequency ~ 100 GHz have been used in many tokamaks to assist in start-up through electron cyclotron heating (ECH), and this method is planned for ITER [46, 47, 48]. RF pre-ionization has been used at the HIT-SI spheromak experiment at the University of Washington to achieve lower plasma densities [49], and also in tokamaks [50].

For the Caltech experiments, RF pre-ionization was chosen due to the modest cost and scale of the apparatus needed and the promise of high ionization efficiency with relatively low input power. Since the plasma density in the original MHD-driven jet experiment was around 10^{21}–10^{22} m^{-3}, the pre-ionization plasma source needed to be able to produce plasma with density on the order of 10^{17}–10^{20} m^{-3} in order to access an interesting new experimental regime. This density range is readily accessible in RF plasma sources with ~ 1 kW of input power [51, 52, 53].

Three means of transferring energy from an RF power source to a plasma exist: capacitive coupling, in which a large amplitude oscillatory voltage on an antenna or electrode creates a high voltage sheath at the edge of the plasma, driving RF currents that heat the plasma; inductive coupling, in which a time-varying current through an external coil or antenna induces electric fields which accelerate electrons in the plasma; and wave heating, in which waves excited by an antenna are damped and transfer their energy to the plasma as they propagate through it or along its surface [5]. Each type of RF discharge has important applications in the fabrication of integrated circuits (plasma processing) and for other

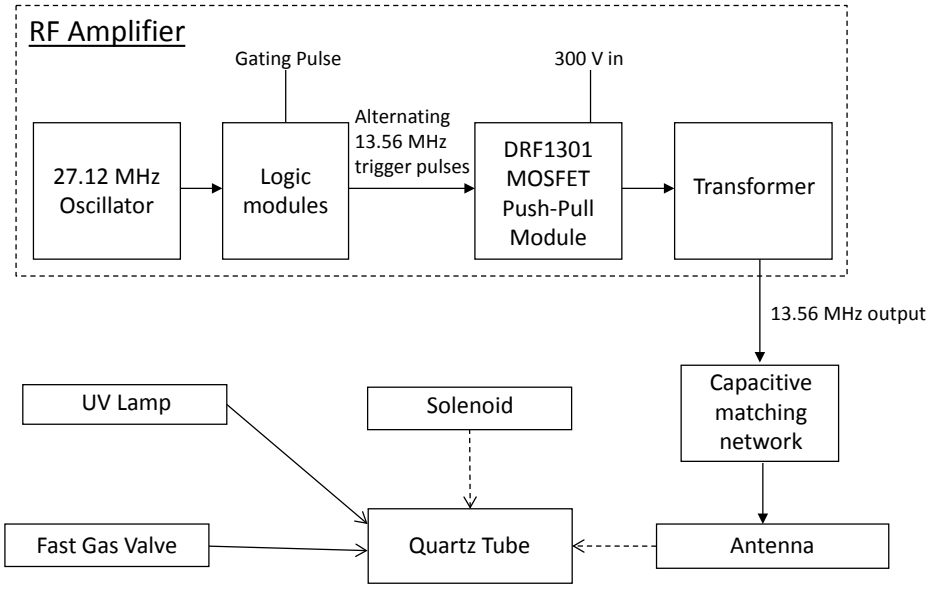

Figure 2.1: Block diagram for the RF plasma source, showing the main sections of the RF amplifier and the other key components described in the text.

surface processing of materials used in industry [5]. Usually a plasma source is designed to take advantage of a particular energy transfer mechanism, but in some cases all three coupling regimes have been observed in a single device as the RF input power was varied [54].

A particular class of wave heated discharges that operates with helicon waves has been found to be exceptionally efficient at producing a high plasma density with low input power [51]. The impressive properties of helicon sources [55, 56] made them an attractive candidate to use for pre-ionization in the Caltech experiments, so we designed our RF plasma source with helicon mode operation in mind. However, detailed density scaling measurements (described in Chapter 3) ultimately showed that wave heating was probably not important in our source; instead, the discharge was found to be primarily inductively coupled.

2.2 Pre-ionized Jet Experiment Overview

The original concept for the pre-ionized MHD-driven jet experiment was conceived by Paul M. Bellan, who also designed the RF amplifier and carried out initial tests and troubleshooting. The author joined the project at this stage and carried out the bulk of the pre-ionization system testing and optimization, along with the construction of the new jet experiment,

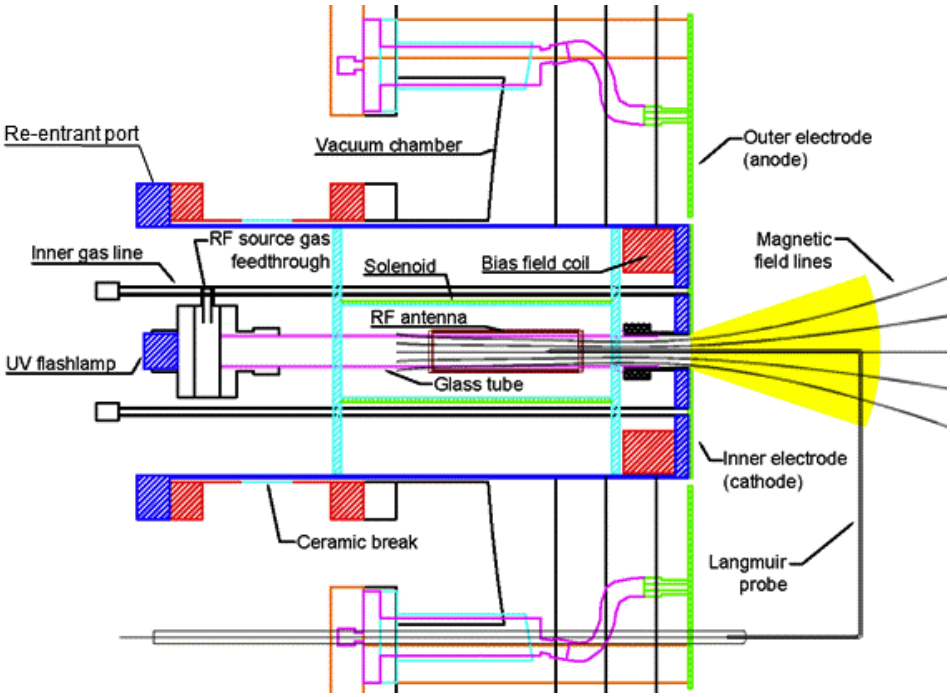

Figure 2.2: Schematic showing the pre-ionization plasma source installed on the MHD-driven jet experiment. Some minor elements of the source such as the coaxial cable leading to the RF antenna and the support structure holding up the gas feed flange have been omitted for clarity. The jet experiment's electrodes appear as thin rectangles at the right-hand side of the figure in this side-on, cross-sectional view. The anode was attached to the grounded vacuum chamber, while the cathode and all attached components, including the pre-ionization source, charged up to $(-3)-(-6)$ kV when the main capacitor bank was triggered. The RF plasma expanded into the chamber along the background magnetic field through a hole in the center of the cathode, as illustrated in the figure. The magnetic field lines shown were calculated using an IDL program written by Bao N. Ha.

with the aid of ongoing consultations with Professor Bellan. A block drawing of the main components of the RF plasma source is shown in Fig. 2.1, and a 2D CAD drawing of the final jet experiment setup is shown in Fig. 2.2. The coaxial planar electrodes shown in Fig. 1.3 were modified with a 1" diameter hole in the center of the cathode. A custom battery-powered RF amplifier was used to create plasma in a quartz tube behind the electrodes, and it flowed into the chamber through this hole, with radial confinement provided by an axial magnetic field.

The dimensions of the pre-ionization source were chosen so that the entire system could fit behind the cathode with minimal modification to the original plasma gun design [17]. The outer electrode supports, bias coil, and overall size and geometry of the "re-entrant

port" (consisting of a 10" CF flange welded to a 7.50" outer diameter [OD], 7.375" inner diameter [ID] stainless steel tube with a 3/8" thick circular stainless steel plate welded to the opposite end) were all unchanged. The ability to inject gas through 8 inlets on each of the inner and outer electrodes was retained, with the aim of allowing the experiment to access a full range of jet densities between the $\sim 10^{22}$ m^{-3} achieved using DC Paschen breakdown alone and the 10^{18}–10^{19} m^{-3} expected when only the pre-ionized plasma was used.

Three fast gas valves (see Sec. 1.6.4), one each for the inner electrode gas inlets, outer electrode gas inlets, and RF plasma source tube, were used for the experiment. Two of these were mounted on the chamber above the jet experiment gun, with 1/4" OD polyethylene tubing carrying the gas to the appropriate gas feeds, while the gas valve supplying the inner electrode inlets was suspended from the ceiling behind the gun[1]. Custom stainless steel pieces with Swagelok fittings were used to split a single gas line into eight for each of the inner and outer electrodes. These gas splitters, which were designed so that the flowing gas would never encounter a right angle turn where it would tend to reflect, were built by DV Manufacturing, as was the re-entrant port itself. Gas was delivered to the RF plasma source tube through a 2 3/4" CF double-sided flange (similar to MDC part number 140013) modified with a 1/4" Swagelok tube fitting welded onto one side. This flange was attached to a 2 3/4" flange with a 1" "quick-disconnect" welded on (MDC part number 412010) that slid onto the rear end of the tube as shown in Fig. 2.2.

The 33.0 cm long, 2.54 cm OD, $\sim$ 2.2 cm ID quartz discharge tube was blown by Rick Gerhart in the Caltech glass shop. The tube attached to the rear side of the jet experiment's cathode via a weldable 1-inch quick-disconnect (MDC part number 410010). It had a small raised ring about 1" from its end (known as a "maria" in glassblowing terminology) to prevent it from being pushed through the quick-disconnect into the chamber by the air-vacuum pressure difference.

The solenoid used to produce an axial magnetic field in the discharge tube was wound with Litz wire on a bobbin made of laser-cut 1/4" thick ABS plastic (custom-ordered from Pololu Robotics and Electronics). The solenoid had 78 turns spread over a 20.4 cm length, or $n = 382$ turns/meter. From Ampere's law and symmetry, the magnetic field strength inside

[1]This arrangement was adopted because it was found that argon gas would not break down in the standard jet experiment configuration with no RF pre-ionization if the gas travel distance between the fast gas valve and the inner electrode was too long.

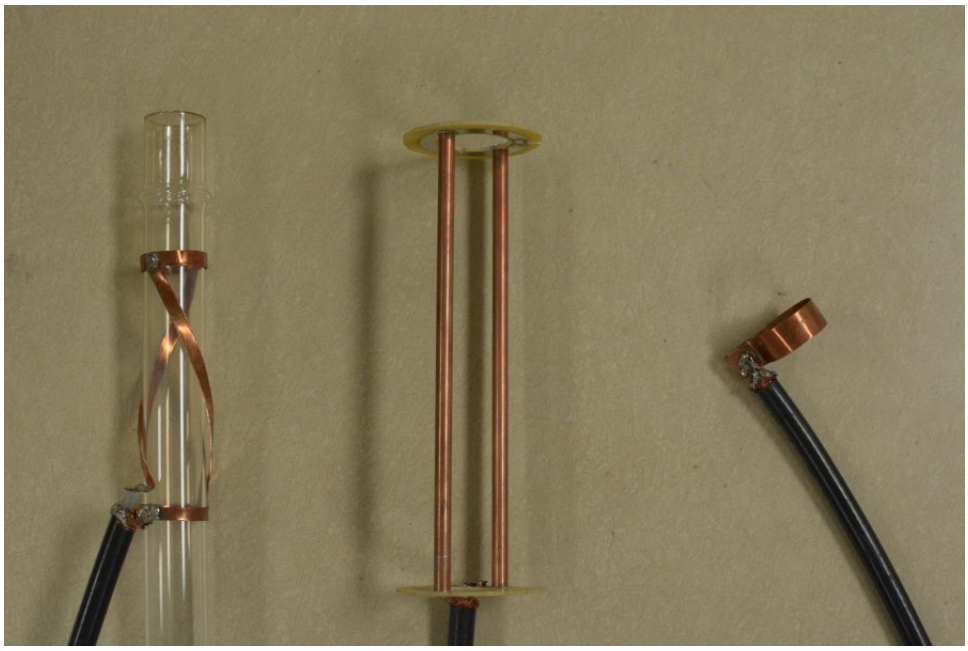

Figure 2.3: Antenna designs tested for the RF plasma source. Left: Half-turn helical "Shoji" (HTH) antenna [52] wound by hand directly onto the quartz discharge tube using thin copper strips soldered together. Center: Straight "Nagoya type III" (NIII) antenna [57] constructed from 1/4" OD copper tubing attached to small printed circuit boards. Right: Single loop $m = 0$ antenna wound by hand from a copper strip.

when a current I was passed through the windings was thus $B = \mu_0 n I = 4.8$ Gauss/Ampere.

The solenoid was powered by a floatable capacitor bank similar to those used to power the bias field coils and fast gas valves (see Sec. 1.5). The bank's 1.8 mF capacitance was provided by a single aluminum electrolytic capacitor rated to 450 V, and switching was accomplished with an SCR. With the leads between the bank and the solenoid twisted, calibration with a current monitor showed that the relationship between the charging voltage displayed on the bank's LED meter and the peak current through the solenoid was $I_{peak} \approx (2.44\ \text{A/V})\, V_{LED}$, or $B_{sol.} \approx (11.7\ \text{Gauss/V})\, V_{LED}$. The current peaked $\sim 650\ \mu$s after the bank was triggered.

RF power was transferred to the plasma using an antenna that fit snugly around the quartz discharge tube. We tested three different types of antennas known to excite helicon waves: a straight "Nagoya type III" (NIII) antenna [57], a [right-handed] half-turn helical "Shoji" (HTH) antenna [52], and a single loop antenna [58, 59]. Photos of the antennas are shown in Fig. 2.3. RF plasmas were successfully produced with all three antennas, but the

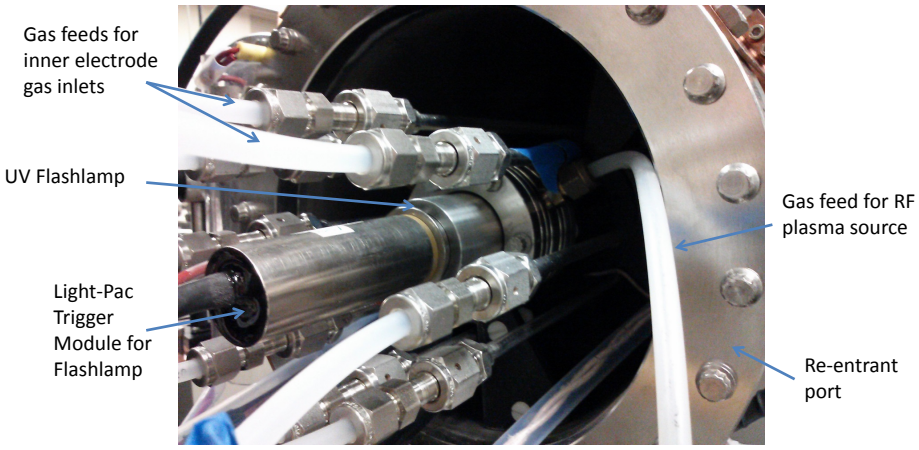

Figure 2.4: View from behind the pre-ionized MHD-driven jet experiment gun. The UV flashlamp was mounted on a custom 2 3/4" CF flange assembly (built by Mike Gerfen at Caltech Central Engineering) attached to the end of the quartz tube behind the gas feed—it emitted a burst of light directed down the tube at the beginning of each discharge.

highest level of ionization was obtained with the HTH antenna (see Sec. 3.4), so this design was ultimately used when the pre-ionization source was installed on the MHD-driven jet experiment.

In initial tests of the RF plasma source with argon gas[2], plasma breakdown was difficult to achieve, occurring only over a small range of gas pressures near 20 mTorr, and even within this range only after the RF amplifier was pulsed repeatedly for a minute or more with a 1 Hz rep rate. To remedy this problem, an ultraviolet (UV) flashlamp (Excelitas Technologies model FX-1165 Metal Can Xenon Flashlamp with Reflector, powered by Lite-Pac Trigger Module FYD-1150 and Power Supply PS-1120) was attached to the end of the quartz tube behind the gas feed connection (see Fig. 2.4). Firing the UV flashlamp at the time of RF turn-on produced enough seed ionization in the discharge tube to enable full plasma breakdown to occur consistently on every shot, with minimal temporal jitter.

A critical aspect of the RF pre-ionization system design was that all components could float electrically. This was important for safety because the source was installed inside the re-entrant port (see Fig. 2.2), which charged up to -3 to -6 kV along with the jet experiment's cathode when the electrodes were energized[3]. Floatable operation was accomplished

[2]The Nagoya type III antenna was used for these tests.

[3]The re-entrant port was isolated from the grounded vacuum chamber by a ceramic break (MDC part number 9632006), and the electrical connections to the main capacitor bank were made on either side of the break, as shown in Fig. 1.8. Referring to Fig. 2.2, it is notable that the re-entrant port fit tightly through the port on the end dome of the vacuum chamber, with only a small vacuum gap separating the conductors.

by powering the capacitor banks for the bias coil, solenoid, and fast gas valves through a 20 kV isolation power supply, as discussed in Sec. 1.5, and by designing the RF power amplifier and UV flashlamp power supply to run off of AA batteries. The batteries charged up capacitors to store up to ~ 2 J of energy per pulse for the RF amplifier and 0.16 J per pulse for the UV flashlamp. RF pulse durations of ≤ 1 ms were quite sufficient given the jet experiment's ~ 10 μs timescale, so 2 J of stored energy was enough to supply relatively high RF power levels (2–3 kW).

The "ground" references of the floating RF amplifier, capacitive matching network (which was isolated from the RF amplifier by the amplifier's output transformer, see Sec. 2.3), and floating capacitor banks for the bias coil, solenoid, and fast gas valves were all connected to a single node (to avoid ground loops), and this point was attached to the re-entrant port through a 15 Ω high pulse energy non-inductive resistor (Carborundum Co. 887AS series). The UV flashlamp and its circuit box were left floating, as were the fast gas valves themselves. The 15 Ω resistor value was chosen so that the RC time for the floating circuits to follow changes in the cathode voltage was $\ll 1$ μs (the total parallel capacitance to ground of the floating capacitor banks was measured to be ~ 1 nF), but it was desirable that R not be too small so that the peak current flowing between the cathode and the floating circuits was limited.

2.3 RF Power Amplifier

Although commercial high power RF amplifiers are readily available, they are typically designed for continuous (CW) operation and thus have costly cooling systems built in that were not necessary for our pulsed application. Furthermore, a high-voltage, high-power transformer would have been required to isolate such an RF supply from the AC main line to allow it to float at the high voltage of the MHD-driven jet experiment's electrodes (the Absopulse isolation supply used for the floating capacitor banks described in Sec. 1.5 could only output 120 W, whereas ≥ 1 kW was needed for the RF amplifier). These factors meant that building a compact, pulsed, battery-powered RF amplifier from scratch was a more attractive alternative than buying a commercial RF supply.

Even though the re-entrant port was charged to -3 to -6 kV during plasma shots and the chamber was grounded, breakdown did not occur in this gap because there was no gas present, and thus *pd* was too small for the Paschen criterion to be satisfied (see Sec. 1.7).

Figure 2.5: Photo of 3 kW RF amplifier, which was mounted on a 3" x 7.5" printed circuit board, and the AA batteries that powered it. The wires connecting the batteries to the board were twisted and passed through ferrite RF chokes to reduce interference between the amplifier's high voltage output stage and low voltage pulse generation stage.

2.3.1 Amplifier Circuit

The RF amplifier operated at 13.56 MHz, a frequency commonly used in both industry and research. Its design, which may be categorized as a transformer-coupled voltage-switching (TCVS) class D configuration [60], was based on a circuit described in a Microsemi Application Note by G. Choi [61], which we modified for pulsed operation. The central component was the Microsemi DRF1301 power MOSFET hybrid [62], a compact 1" x 2" module containing two power MOSFETs[4] (rated for $BV_{DSS} = 1000$ V and $I_D = 15$ A and capable of 30 MHz switching), along with high power gate drivers. A photo of the amplifier is shown

[4]MOSFET stands for "Metal-Oxide-Semiconductor Field-Effect-Transistor". MOSFETs have three terminals, called the "gate", "drain", and "source"—analogous to the base, collector, and emitter, respectively, of a bipolar junction transistor. For an n-channel MOSFET, a voltage drop from the gate to the source leads to a current into the drain. However, unlike in a BJT, in a MOSFET the gate is electrically insulated from the source-drain circuit, so there is no DC gate current and the gate affects the output only through its electric field. There is also a fourth terminal, known as the "body", which can be used to alter the threshold gate-source voltage for a drain current to start to flow. In the DRF1301, the body is internally connected to the source, and both are grounded in our circuit.

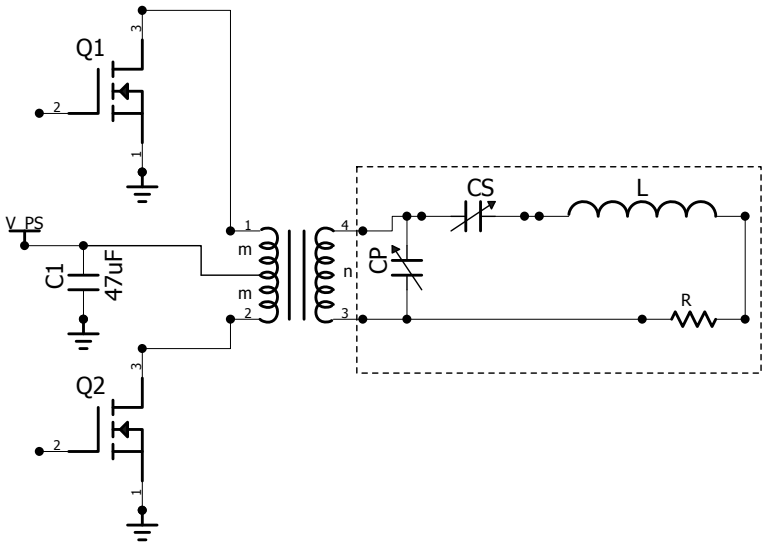

Figure 2.6: Schematic of the RF amplifier output stage. $Q1$ and $Q2$ are the power MOSFETs located inside the DRF1301. The dashed box surrounds the load, consisting of the antenna, plasma, and impedance matching capacitors (see Sec. 2.4).

in Fig. 2.5, and a full circuit diagram is given in Appendix B.

A schematic showing the key components of the RF amplifier's output stage is given in Fig. 2.6. The MOSFETs are operated as switches (this is the definition of a class D RF amplifier) controlled by trigger signals from the low-voltage pulse generation stage described below. The two input pulse trains are roughly 180 degrees out of phase, so the MOSFETs $Q1$ and $Q2$ are switched on and off alternately. When $Q1$ is on and $Q2$ is off, current flows from the 47 μF capacitor $C1$ (charged by the AA batteries through an EMCO Q03-12 miniature proportional DC power supply to $V_{ps} \leq 300$ V) through the upper half of the center-tapped primary winding of the transformer and through $Q1$ to ground. If the MOSFET behaves as an ideal switch, then the on-state voltage drop across it is 0, and thus the full V_{ps} drop must occur across the upper half of the transformer primary. Assuming that the transformer is also ideal, each half of the primary links the same magnetic flux, and the voltage drop across the lower half of the primary is also V_{ps}, so the drain of $Q2$ (terminal 3 in the figure) rises to $2V_{ps}$. The voltage across the primary is transformed to $(n/2m)\,(2V_{ps}) = (n/m)\,V_{ps}$ on the secondary, where n is the number of secondary turns and $2m$ is the total number of primary turns. Over the second half cycle, $Q1$ is off and $Q2$ is on, and the polarity of the output voltage across the transformer secondary reverses.

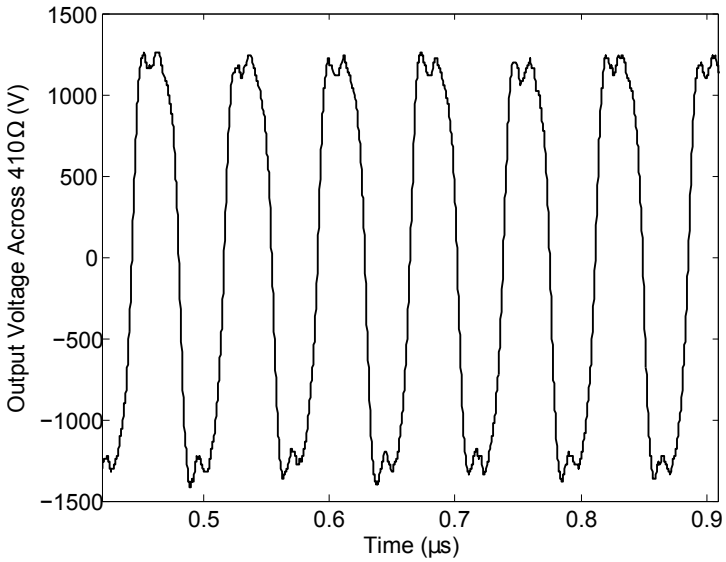

Figure 2.7: RF amplifier output voltage into a 410 Ω load with $n/m = 6/1$. The output power calculated from this waveform is $P = \langle V^2 \rangle / R = 2.70$ kW.

The result is a 13.56 MHz square wave voltage output across the load. It must be noted that this idealized description is only a rough approximation of what actually happens; in reality the MOSFETs cannot switch on and off instantaneously (the switching time is 3-4 ns according to the DRF1301 datasheet [62]), and parasitic inductance, capacitance, and resistance in the circuit cause substantial distortions of the output signal due to the high frequency of operation. The measured output waveform across a 410 Ω resistive load with $n/m = 6/1$ is shown in Fig. 2.7. A derivation of the output power of an ideal class D RF amplifier into several types of loads in given Appendix C.

The pulse generation circuit that sends trigger pulses to turn on the MOSFETs is shown in Fig. 2.8. The 27.12 MHz oscillator $U2$ runs continuously when the amplifier's batteries are connected. The RF output is enabled by an optical gating signal received by $U1$, which turns off the NPN transistor $Q1$ and causes the pin $2D$ of the flip-flop IC $U3$ to go to a high logic level. The left side of $U3$ (pins 1–7) is used to split the 27.12 MHz signal from the oscillator into two 13.56 MHz pulse trains (output at pins $1Q$ and $1\overline{Q}$) that are 180 degrees out of phase, while the right side (pins 8–14) allows the user to optimize the amplifier's performance by varying the pulse width and phase delay of one pulse train. To understand these functions, refer to the truth table for $U3$ shown in Table 2.1. The pin $1\overline{CLR}$ is held high, so at each rising edge of the 27.12 MHz clock waveform received at $1CLK$, the voltage

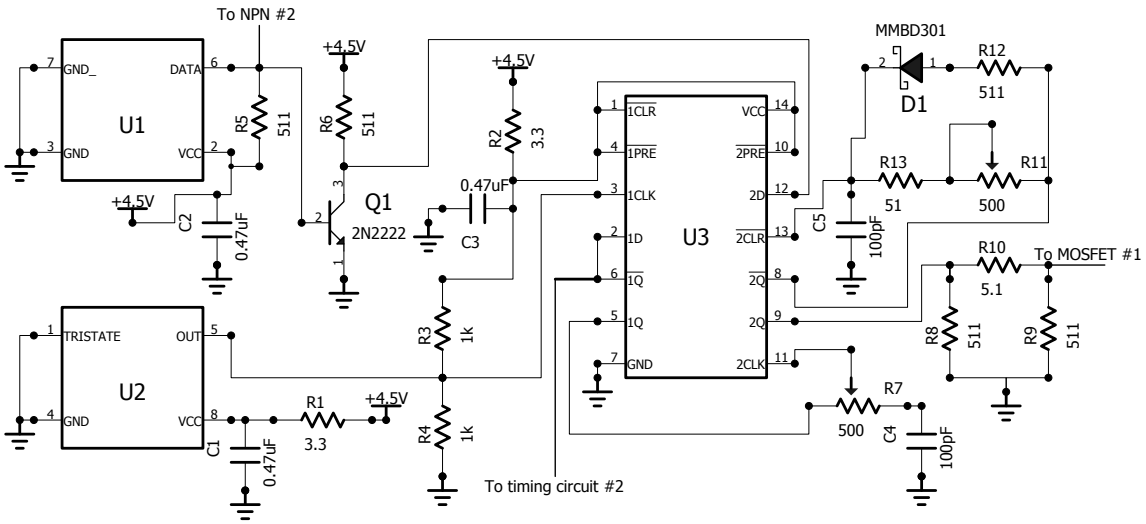

Figure 2.8: Partial circuit diagram for the RF amplifier's pulse generation stage. $U1$ is a fiber optic receiver (Avago Technologies HFBR-2412), $U2$ is a 27.12 MHz crystal oscillator (Ecliptek EP1100HSTSC-27.120MHZ), and $U3$ is a dual flip-flop logic IC (Texas Instruments SN74ACT74). The traces labeled "To NPN #2" and "To timing circuit #2" lead to the other half of the pulse generation stage circuit; both halves are shown together in Fig. B.1.

at $1D$ is transferred to $1Q$, and $1\overline{Q}$ takes on the opposite logic level. Since $1D$ is connected to $1\overline{Q}$, this flips the logic level at $1D$, and the output voltages reverse at the next clock trigger.

The output at $1Q$ is transferred to $2CLK$, but $U3$ only registers a rising edge trigger after a delay interval that is controlled by the adjustable RC timing circuit containing the potentiometer $R7$. $2D$ is held high, so when $2\overline{CLR}$ is high, the output trigger sent to MOSFET #1 from $2Q$ is a high level, and the MOSFET turns on. The low level at $2\overline{Q}$ is transferred to $2\overline{CLR}$ after a delay interval that can be modified by adjusting the potentiometer $R11$, at which point $2Q$ goes low, so the MOSFET turns off. The resulting high level at $2\overline{Q}$ is transferred to $2\overline{CLR}$ after a time delay set by $R12$ and $C5$, and the cycle repeats.

The output from pin $1\overline{Q}$ of $U3$ goes to a second SN74ACT74 logic IC (not shown in Fig. 2.8, but see Fig. B.1 for a full diagram of the other half of the circuit) that produces a series of pulses at 13.56 MHz to trigger the second MOSFET. Pins 8–14 of this IC are connected to a timing circuit that is identical to that attached to the right side of $U3$ in Fig. 2.8, except that the phase adjustment potentiometer $R7$ is replaced by a fixed 220 Ω

Inputs			Outputs	
$\overline{\text{CLR}}$	CLK	D	Q	$\overline{Q}$
L	X	X	L	H
H	↑	H	H	L
H	↑	L	L	H

Table 2.1: Partial truth table for the SN74ACT74 flip flop, valid when the $P\bar{R}E$ input is held high. 'H' stands for a high logic level, 'L' for a low level, and ↑ is a rising edge trigger.

resistor.

A detailed analysis of the variable RC circuits containing the 500 Ω potentiometers $R7$ and $R11$ reveals that the phase delay between the trigger pulses for the two MOSFETs may theoretically be adjusted between approximately 13 ns and 68 ns, and the pulse widths should be adjustable between approximately 7 ns and 76 ns under ideal conditions (the RF frequency 13.56 MHz corresponds to a period of ∼ 74 ns). In practice, switching delays in the logic ICs reduced the accessible range of pulse widths to be ∼ 12–72 ns, and a circuit layout error limited the phase shift between the two pulse trains to fall in a much smaller range between ∼ 37–42 ns. It was found experimentally that operating each MOSFET at somewhat less than 50% duty cycle (so with trigger pulse widths less than 37 ns) was ideal, with the trigger signals roughly 180 degrees out of phase. If the trigger pulses were too short, then both MOSFETs were turned off for a significant portion of the RF cycle and the output power suffered; if they were too long, there were times when both MOSFETs were turned on simultaneously, and the output became unstable. Examples of the pulse generation stage output pulses are shown in Fig. 2.9. For most experiments described in this thesis, $R11 = 70\ \Omega$ was used (corresponding to a ∼ 22 ns pulse duration sent to MOSFET #1) and the corresponding potentiometer value in the trigger circuit for MOSFET #2 was 113 Ω (corresponding to a ∼ 27 ns pulse duration). The asymmetry in pulse widths compensated for asymmetries in the output stage layout and possibly within the DRF1301 itself.

Both sections of the RF amplifier were mounted together on a 3" x 7.5" printed circuit board (see Fig. 2.5). Because of the compact size of the board, it was critical to use surface mount rather than through-hole components for the low-voltage circuitry to avoid excessive inductive pickup from the high voltage output stage. Another key practical consideration was the construction of the high-frequency center-tapped transformer, which was wound

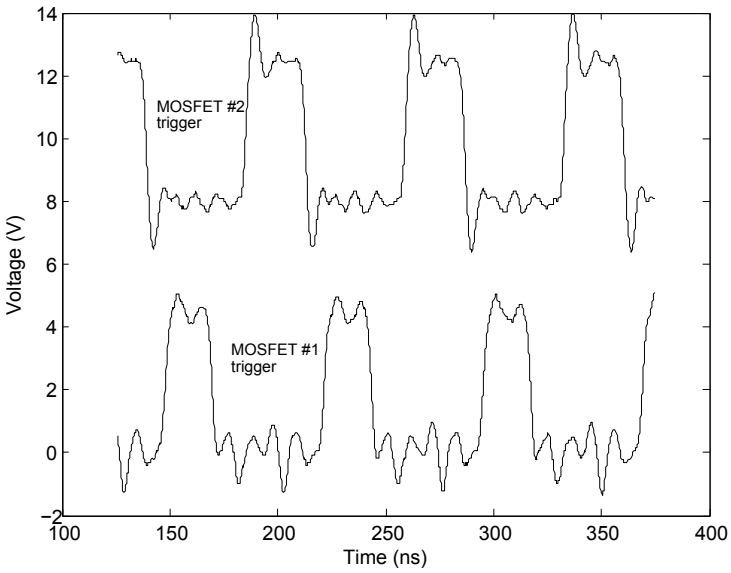

Figure 2.9: Trigger pulses delivered to the two MOSFETs by the RF amplifier's pulse generation stage. The differences in ringing amplitude in the two waveforms are due to the different oscilloscope probes used to make the two measurements and are not intrinsic to the circuit.

with 16 AWG wire on an Amidon FT240-61 ferrite toroid. Each half of the primary had a single turn composed of 8 windings in parallel in order to reduce resistive losses in the windings. The number of secondary turns was adjustable from 1 to 6, and multiple windings in parallel were again used when space permitted.

The amplifier required a total of 3 AA batteries for the pulse generation stage, 8–9 AA batteries for the driver stage (which consisted simply of a voltage supplied directly to the DRF1301 driver power supply inputs through 0.25 Ω resistors), and 1–8 AA batteries for the output stage, depending on the desired value of V_{ps}. The DRF1301s tended to develop a fault in which they would draw excessive steady-state current into the driver stage, so the driver stage batteries were used to charge up a 2 mF capacitance through a 150 Ω resistor in order to keep the batteries from being drained too fast in between RF amplifier pulses. The quiescent current drawn by the driver stage through this limiting resistor was $\sim$ 25 mA, so assuming the useful output capacity of each battery was 500 mAh = 1800 C (alkaline batteries rated for 2750 mAh were typically used, but the output voltage was too low to power the driver over much of the rated battery lifetime), the amplifier could be left on for $\sim$ 20 hours before the driver batteries needed to be replaced. This estimate agrees well with

the observed performance. The lifetime of the final stage batteries was similar; in typical operation with the amplifier pulsed roughly once per minute, the dominant energy sink was the ~ 0.2 W continuously dissipated in the 500 kΩ safety bleeder resistor installed across the 47 μF output stage capacitor, rather than the 1–2 J stored energy needed for each RF pulse. If our RF amplifier design were used for a portable application for which battery lifetime was an important concern, this bleeder resistor could be made larger or eliminated, enabling the amplifier to be pulsed several thousand times without replacing or recharging the final stage batteries.

2.4 Impedance Matching and Output Power

"Impedance matching" is a term frequently heard in discussions of high-frequency electronics. It actually encompasses at least two separate but related concepts [63]:

1. The power transfer from a source with fixed output impedance $Z_S = R_S + iX_S$ to a load with impedance Z_L is maximized if $Z_L = Z_S^* = R_S - iX_S$.

2. In a system with a transmission line between the source and the load, there will be no signal reflected from the load if the load impedance is equal to the characteristic impedance of the transmission line, i.e., $Z_L = Z_{line}$.

Concept (1) is known as the "maximum power transfer theorem". To prove it, consider a single Fourier mode of the source output voltage, $V_{S,\omega}(t) = |V_{S,\omega}|e^{i\omega t}$. With the source and load impedances in series with the voltage source, the current in the circuit is

$$I = \frac{V_{S,\omega}}{Z_S + Z_L} = \frac{|V_{S,\omega}|e^{i\omega t}}{(R_S + iX_S) + (R_L + iX_L)}. \tag{2.1}$$

The power delivered to the load is thus

$$P_L = \langle I^2 \rangle R_L = \frac{1}{2}|I|^2 R_L \tag{2.2}$$

$$= \frac{|V_{S,\omega}|^2 R_L}{2\left((R_S + R_L)^2 + (X_S + X_L)^2\right)}, \tag{2.3}$$

where angle brackets denote a time average. For a given choice of R_L, it is clear that P_L will always be maximized with $X_L = -X_S$, since this minimizes the denominator. With

the load reactance chosen to satisfy this condition, the power becomes simply

$$P_L = \frac{|V_{S,\omega}|^2 R_L}{2\left(R_S + R_L\right)^2}. \tag{2.4}$$

Maximizing with respect to R_L, we find

$$0 = \frac{\partial P_L}{\partial R_L} = \frac{|V_{S,\omega}|^2}{2}\left(\frac{1}{\left(R_S + R_L\right)^2} - \frac{2R_L}{\left(R_S + R_L\right)^3}\right) \tag{2.5}$$

$$0 = 1 - \frac{2R_L}{R_S + R_L} \tag{2.6}$$

$$R_L = R_S. \tag{2.7}$$

Thus the power delivered to the load is maximized when $Z_L = Z_S^*$. Since the load reactance must be capacitive ($X_L = -\left(\omega C_L\right)^{-1}$) for an inductive source reactance ($X_S = \omega L_S$), and vice versa, this condition cannot be satisfied at multiple frequencies simultaneously unless $X_S = 0$. If $X_S \neq 0$, then for an arbitrary periodic source voltage waveform that is the sum of multiple Fourier modes, the best one can do is to adjust the load impedance for maximum power transfer at the fundamental frequency.

Note that the maximum power transfer theorem assumes that the source output impedance is fixed. If Z_S can be adjusted, then making R_S smaller will increase P_L for a given R_L (this is apparent from Eq. 2.4). In many situations it is desired to maximize the efficiency of a source rather than the power transferred to the load. In this case, for a fixed source impedance the load resistance should be made as large as possible, while still satisfying some minimum power transfer requirement, since

$$\epsilon = \frac{P_L}{P_S + P_L} = \frac{\langle I^2 \rangle R_L}{\langle I^2 \rangle R_S + \langle I^2 \rangle R_L} = \frac{R_L}{R_S + R_L}. \tag{2.8}$$

For our RF amplifier, the primary goal was to deliver the highest possible power to the plasma; efficiency and the amount of reflected power were relatively unimportant. Thus the aim was to set $Z_L = Z_S^*$. However, while commercial RF power amplifiers are typically designed to have output impedances that are purely real, usually equal to 50 Ω, the output impedance of our RF amplifier was unknown and complex. An ideal class D RF amplifier with instantaneous switching has zero output impedance and thus can operate with 100% efficiency, since the product $IV = 0$ in each transistor at all times, but in a real system

dissipation exists that leads to finite Z_S. The MOSFETs in the DRF1301 have an on-state resistance equal to $\sim 1\ \Omega$ and a finite output capacitance[5] that had to be charged and discharged during each cycle [60], with an associated energy dissipation equal to $CV_C^2 = 4CV_{ps}^2$. There were also losses in the output transformer, as discussed in the previous section.

A rough estimate for the source impedance may be obtained by comparing the output power into different resistive loads. Tests of an RF amplifier prototype that used a Microsemi DRF1300 instead of a DRF1301[6] and had $n/m = 6/1$ implied that $|Z_S| \approx 11\ \Omega$ (see Fig. C.1). However, since the MOSFETs in the DRF1301 have a higher on-state resistance, the magnitude of the source impedance was expected to be larger in the final version of the RF amplifier (which used a DRF1301 and had $n/m = 1$), and indeed, optimal power transfer to the plasma was typically achieved with $|Z_L| = 20$–$25\ \Omega$ (see Fig. 2.12, for example).

When using the RF amplifier to create plasma, the impedance matching circuit shown in Fig. 2.6 was used [64]. The antenna and plasma are represented by the series inductor L and resistor R within the dotted box. We may roughly model the loading of the antenna by the plasma as a radiation resistance [65] defined by $P_{RF} = \langle I_{ant.}^2 \rangle R_{rad.}$ that adds to the antenna resistance.[7] The antenna had a radiation resistance even when there was no plasma present, but its magnitude was small, specifically

$$R_{rad.} \approx \frac{\mu_0 A^2 \omega^4}{12\pi c^3} = 6 \times 10^{-7}\ \Omega, \tag{2.9}$$

where the antenna area $A \approx .003\ \text{m}^2$ and only the magnetic dipole term in the multipole expansion of the antenna vector potential has been retained [66, p. 454]. With plasma present, the radiation resistance became roughly $R_{rad.} = P/\langle I_{ant.}^2 \rangle \approx (2\ \text{kW})\,/\,(30\ \text{A})^2 \approx 2\ \Omega$.

[5]The nominal output capacitance of each MOSFET is $C_{OSS} = 335$ pF [62], but this value decreases as the drain-source voltage increases [60].

[6]The DRF1300 and DRF1301 are similar, but the MOSFETs in the DRF1300 are rated for a lower peak drain-source voltage ($BV_{DSS} = 500$ V) and have lower on-state resistance ($R_{ON} \approx 0.24\ \Omega$).

[7]Note that although the representation of the antenna and plasma as a fixed inductor and variable radiation resistance is useful for a qualitative discussion of the impedance matching condition, it is not strictly correct if there is capacitive or inductive coupling between the antenna and plasma. In this case, the presence of the plasma will modify the effective antenna reactance as well as its effective resistance [5, p. 467]. For inductive coupling, the effect is similar to the modification of a coil's inductance when a conducting object is placed near it, which is the principle used in metal detectors. Since the source impedance was unknown in our experiment, a careful calculation of the load impedance was not particularly useful, and the matching network was simply adjusted empirically to obtain optimal power transfer.

Figure 2.10: Binary arrays of capacitors used to implement the variable capacitors C_p and C_s for the matching circuit. Removable copper jumpers were used to connect the desired capacitors into the circuit.

Since the effective antenna impedance depended upon the plasma conditions, the overall impedance of the load needed to be adjustable, so that it could be set to satisfy the conjugate matching condition for maximum power transfer for a variety of experimental setups and plasma parameters. This flexibility was achieved through the inclusion of the variable capacitors C_p and C_s, which provided two degrees of freedom for adjusting Z_L. Adjusting the RF amplifier's output transformer turns ratio provided another degree of freedom for setting $|Z_L|$; since the transformer stepped up the output voltage by a factor (n/m) and stepped down the current by a factor (m/n), the effective impedance seen by the source was $|Z_{eff}| = |V_S|/|I_S| = (m/n)^2 |V_L|/|I_L| = (m/n)^2 |Z_L|$. The effective impedance of the load seen by the RF amplifier was thus

$$Z_{eff} = \left(\frac{m}{n}\right)^2 \left(i\omega C_p + \frac{1}{R + i\omega L + \frac{1}{i\omega C_s}}\right)^{-1}. \tag{2.10}$$

Instead of using expensive high-voltage variable capacitors, the matching capacitances were implemented with binary arrays of fixed-value ceramic capacitors (American Technical Ceramics 100 E Series and AVX HQCE Hi-Q Series) that could be switched into or out of the circuit. The capacitances used were 1.0 pF, 2.0 pF, 3.9 pF, ... In a few cases the desired capacitance value to fill the approximately binary series was not readily available, and two smaller capacitances adding up to roughly the needed value were used instead. The

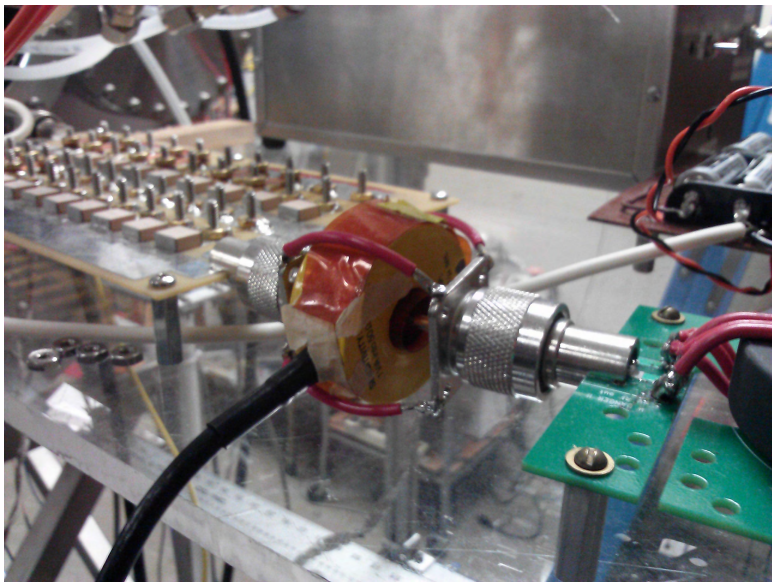

Figure 2.11: Ion Physics CM-100-M current monitor used to measured the RF amplifier output current. A single 16 AWG wire carried the RF signal through the current monitor, and four wires soldered around the outside of the current monitor carried the return current, approximating a short coaxial transmission line.

capacitors were mounted on a printed circuit board with removable copper strips used to connect each one into the circuit (see the photo in Fig. 2.10). Taking into account the stray capacitances on the circuit board, the binary arrays could be adjusted to obtain nearly any capacitance value up to 886 pF for C_s and 2604 pF for C_p with ~ 2 pF resolution.

Since the load resistance R was small when plasma was not present, the series capacitor and the antenna formed a high-Q resonant circuit, and a very high voltage across the antenna (roughly 3 kV amplitude with $n/m = 6/1$) could be obtained if C_s was set such that $\omega = 2\pi \times 13.56$ MHz $= 1/\sqrt{LC_s}$. A similar voltage amplitude would exist across C_s, so capacitors rated for ≥ 3.6 kV were chosen. The initial version of the circuit board suffered from high voltage arcing around the capacitors, within the Type N connector at the output side of the board, and even around the edge of the board from the top to bottom conductors. To solve the problem, a new board was ordered with larger distances between the components, the Type N connector was filled with RTV162 silicon adhesive, and insulating varnish was painted over the sharp edges of the copper pours on the board in areas that were prone to arcing.

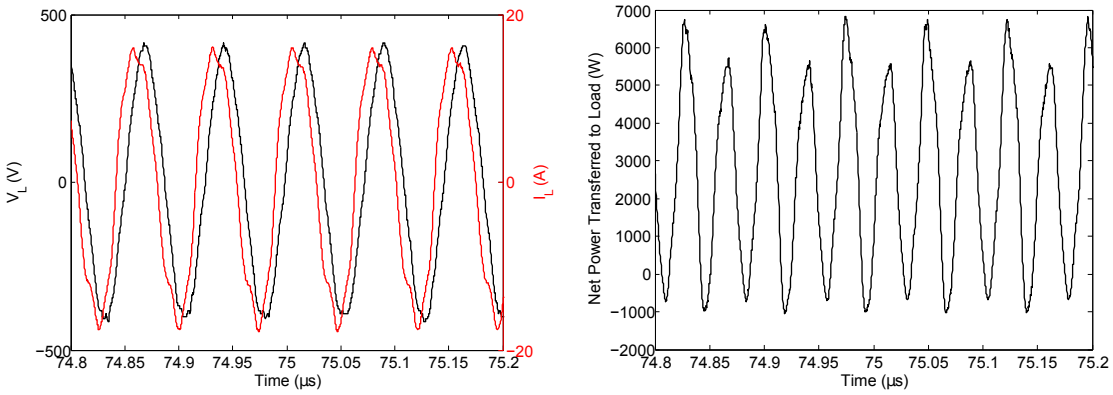

Figure 2.12: Left: RF amplifier output voltage and current during an argon shot with the NIII antenna and no magnetic field. Right: $P_L = I_L V_L$ delivered to the load during this shot. The average power transferred was $P_L \approx 2.67$ kW, the phase shift between I_L and V_L was $\phi \approx 7$ ns, and the magnitude of the load impedance was $|Z_L| = |V_L|/|I_L| \approx 24\ \Omega$. $n/m = 1/1$ was used in this case; in general, setting $n/m \leq 2$ was necessary to achieve efficient power transfer to the load and high plasma density.

Having a high voltage across the antenna was beneficial for achieving the initial plasma breakdown, but the matching capacitances needed to maximize the power delivered to the plasma were not necessarily the same as those needed to tune to the LC resonance. In CW RF plasma experiments, the matching network elements may be adjusted gradually while monitoring the plasma density in order to maximize the power transfer to the plasma, but this was not possible in our pulsed experiment. We tested a setup with two RF amplifiers used in tandem (feasible because of the low cost and compact size of each amplifier), with one matching network tuned to maximize the antenna voltage for plasma breakdown and density build-up[8] and the other tuned to set $Z_L = Z_S^*$ with high-density plasma present. Ultimately, the plasma density achieved using this method (monitored with optical emission spectroscopy and Langmuir probes, as described in Chapter 3) was no higher than that achieved with a single RF amplifier tuned for maximum power transfer; typically the UV flashlamp pulse was sufficient to start the discharge with only a moderate antenna voltage.

The power transferred to the load was determined by directly measuring the RF amplifier output voltage and current at the secondary of the transformer, and then multiplying these waveforms together numerically to determine $\langle I_L V_L \rangle$ averaged over several RF periods. The

[8]It is believed that all RF discharges start out in a capacitively-coupled mode, for which a high antenna voltage is beneficial, before the density has built up enough to support inductively coupled or wave-heated modes of operation.

current was measured with an Ion Physics CM-100-M current monitor, inserted into the circuit at the amplifier output as shown in Fig. 2.11, and the voltage was measured with a Tektronix P6015A high voltage probe. I_L and V_L were measured simultaneously on a single oscilloscope to determine the phase difference between them, taking into account the difference in length between the cables leading to the oscilloscope (for example, in the typical setup the current monitor cable was 1.83 m long while the high voltage probe cable was 3.05 m long, so given the signal propagation velocity $v = 2c/3 = 2 \times 10^8$ m/s in the cables, the necessary correction to the phase shift was $\sim$ 6 ns). It was found that the apparent amplitude of the V_L signal was inflated if I_L was measured simultaneously due to coupling of the signals either within the oscilloscope or nearby (the effect of the V_L signal the I_L waveform was not as great, likely because the amplitude of the current monitor signal was $\sim$ 15 V, while the amplitude of the 1000x high voltage probe signal was only 200-500 mV). An effort was made to divert any RF ground currents on the current monitor cable using the procedure described in [67], but the distortion of the voltage signal persisted, so a procedure was adopted in which the relative phase shift was first determined by measuring I_L and V_L simultaneously, and then the experiment was repeated while measuring each one individually with the other cable unplugged in order to determine the correct signal amplitudes.

An example of an output power measurement is shown in Fig. 2.12. Optimal power transfer was always achieved with I_L leading V_L, meaning that the load impedance had a negative imaginary part (i.e., it was capacitive). Therefore, the maximum power transfer theorem implies that the RF amplifier output impedance was somewhat inductive.

Chapter 3

RF Discharge Properties

This chapter will describe the overall RF discharge behavior, and in particular the plasma parameters achieved inside the antenna. Discussion of the downstream transport and the pre-ionized plasma properties in the vicinity of the jet experiment electrodes will be deferred to the following chapter. The experiments described in this chapter were carried out with an approximately uniform gas pressure in the chamber, with gas supplied by a Granville-Phillips Series 203 variable leak valve (the fast gas valves were not used). Unless otherwise noted, the working gas was argon.

3.1 RF Plasma Diagnostics

3.1.1 Langmuir Probes

Electrostatic probes were perhaps the original plasma diagnostic, invented by Irving Langmuir and colleagues in the 1920s [68, 69], and they were the workhorse tool for studying our RF plasma. The technique involves inserting a small biased electrode into the plasma and measuring the current collected (the biasing and measurement circuit used is shown in Fig. 3.1). By scanning the probe potential over a range of voltages, the "I-V characteristic" is determined, and plasma parameters such as the density, electron temperature, and plasma potential (V_{plasma}) may be extracted. There are three main segments of the I-V curve (see the sample probe data in Fig. 3.2):

1. For $V_{probe} \ll V_{plasma}$, electrons are repelled from the probe and only ions are collected. The current collected in this regime is known as the ion saturation current, and its magnitude is roughly $I_{sat.} \approx 0.6 n_i e c_s A$, where $c_s = \sqrt{k_B T_e / m_i}$ is the ion acoustic or

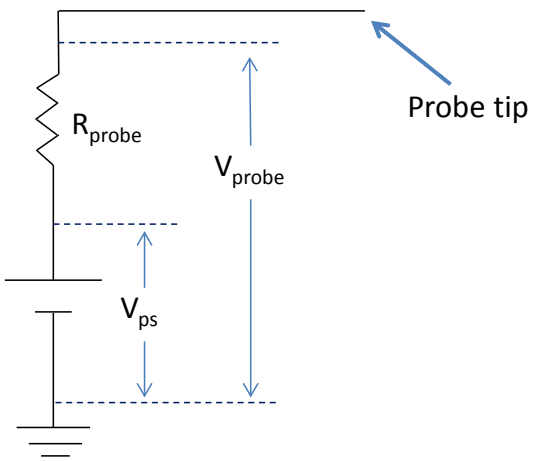

Figure 3.1: Circuit used to bias the Langmuir probes and measure the current collected. The measurement resistor was placed between the probe tip and the power supply, and two oscilloscope probes were used to simultaneously measure V_{probe} and V_{ps}, with the probe current given by $I_{probe} = (V_{probe} - V_{ps})/R_{probe}$. Although it would have been convenient to place the resistor on the ground side of a floating power supply and measure V_R with a single oscilloscope probe, it was found that the measurement had poor time resolution in this configuration because of the power supply's internal capacitance to ground (hundreds of nF), which was effectively in parallel with R_{probe}.

Bohm velocity and A is the exposed surface area of the probe [70].

2. For $V_{probe} < V_{plasma}$, the electron current grows exponentially as V_{probe} is increased (if the electron velocity distribution is Maxwellian), because only electrons with kinetic energy sufficient to overcome the potential barrier are collected. The slope of a plot of $\ln|I_e|$ vs. V_{probe} is $e/k_B T_e$.

3. For $V_{probe} > V_{plasma}$, the electron current stops growing exponentially, and negligible ion current is collected. The current collected in this regime, the electron saturation current, is much larger in magnitude than the ion saturation current since $v_{Te} \gg c_s$.

Details of the analysis procedure that was used to determine T_e, V_{plasma} and n_i from the Langmuir probe I-V curves are given in Appendix D. Accurate electron temperature measurements were only possible after the RF power was turned off, because the probes used did not have RF compensation (see Appendix D). Furthermore, for measurements inside the glass discharge tube, the plasma may not have been in good contact with a ground potential reference, meaning that the probe tip itself could modify the plasma potential[1],

[1]To see that this is possible, suppose that the capacitance to ground of the plasma is 10 pF. If the probe draws 10 mA of current from the plasma, then the rate of change of the plasma potential would be

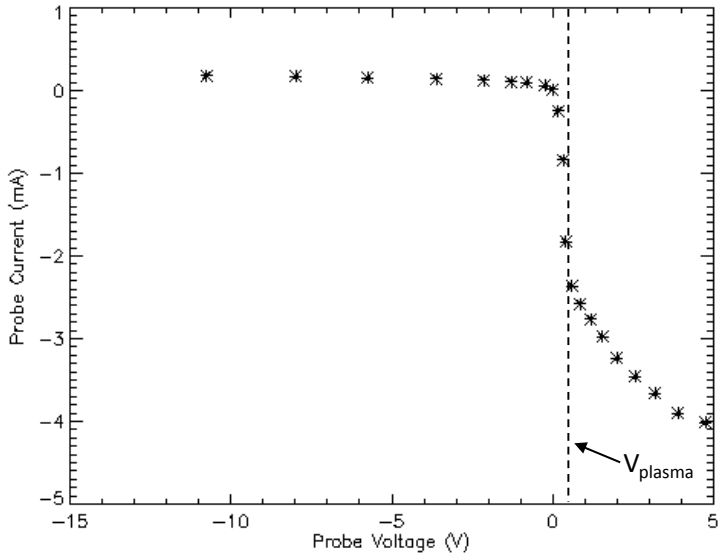

Figure 3.2: Sample Langmuir probe I-V curve for a cold afterglow plasma. Ion saturation current is collected for $V_{probe} \lesssim -2$ V, the electron current grows exponentially for -2 V $\lesssim V_{probe} \lesssim 0.5$ V, and electron saturation current is collected for $V_{probe} > V_{plasma} \approx 0.5$ V.

invalidating the temperature measurement [71]. Fortunately, the plasma density was the main property of interest. For most measurements presented in this chapter and in Chapter 4, only the ion saturation current was measured, and $n_e \approx n_i$ was calculated from Eq. D.9 by plugging in the T_e predicted by the global discharge model described in Sec. 3.3. Only for measurements taken out in the main vacuum chamber during the afterglow (described in Chapter 5) was the full I-V curve was analyzed.

Three Langmuir probes were constructed by threading lengths of .085" OD semi-rigid coaxial cable (purchased from Cross RF) through cylindrical stainless steel (SS) probe shafts. Vacuum epoxy (Torr Seal Low Vapor Pressure Resin) was used to make a vacuum tight attachment between the semi-rigid cable and the SS tube (the interfaces between the conductors and insulation of a semi-rigid cable are generally vacuum tight, enabling this simple probe-construction strategy). The shield and dielectric were stripped off the end of the cable to expose a probe tip with $L \approx 3$ mm and $R \approx 0.25$ mm.

The first Langmuir probe, shown in Fig. 3.3, was used for the initial optimization of the RF plasma source carried out on a small test vacuum chamber. The semi-rigid cable extended all the way through the short SS probe shaft and was terminated with a BNC

$dV_p/dt = (dQ/dt)/C = -1$ V/ns, if there is no other net current flowing to/from the plasma.

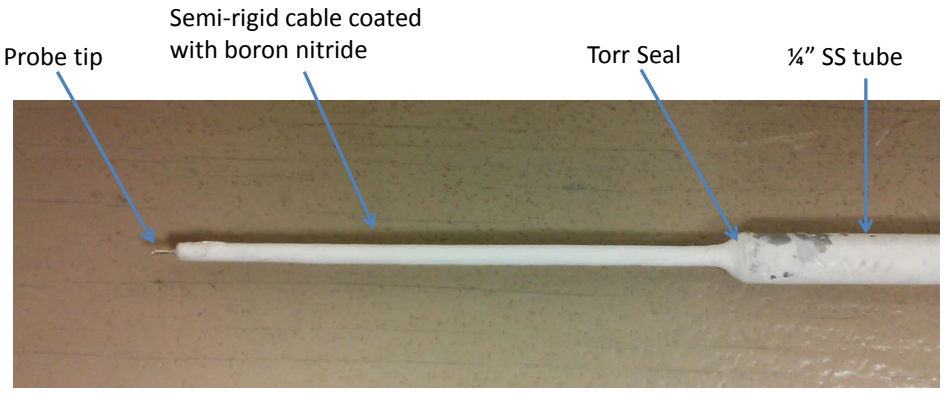

Figure 3.3: Photo of a Langmuir probe constructed using semi-rigid coaxial cable. In this photo, taken after the probe was pulled out of the discharge tube through the 1/4" quick-disconnect, some of the boron nitride insulating coating had rubbed off, exposing the stainless steel probe shaft.

connector, and the grounded cable shield and SS tube were coated with boron nitride aerosol spray (from ZYP Coatings) to insulate them from the plasma and avoid drawing large amounts of current, which would have perturbed the plasma excessively. The probe was inserted into the plasma through a 1/4" quick-disconnect welded to a 2 3/4" CF flange (MDC part number 412003) attached to the end of the quartz discharge tube, so that the axial position of the probe tip was adjustable. A similar Langmuir probe with a longer shaft was subsequently used once the source was installed on the main vacuum chamber. The probe was inserted through a 1/4" quick-disconnect on one of the chamber's 2 3/4" side ports, allowing it to slide radially at a distance $z = 3.8$ cm in front of the electrodes.

Finally, in order to make measurements inside the quartz discharge tube in the final experiment configuration, a third probe was constructed by bending semi-rigid cable into a U-shape using a tubing bender (see Figs. 2.2 and 3.4). The 3/8" OD SS probe shaft was inserted through a 3/8" quick-disconnect welded onto a 2 3/4" CF flange (MDC part number 412005) mounted on one of the chamber's end dome ports. The probe could slide axially and make measurements between $z \approx 30$ cm and $z \approx -9$ cm (i.e., 9 cm into the RF source tube).

It was found that the boron nitride coating on the straight probe was being eroded when the jet experiment was run (even though the probe was not used for measurements during jet experiment shots and was pulled as far out of the chamber as possible), so the U-shaped probe was designed differently, with the outer conductor of the semi-rigid cable isolated

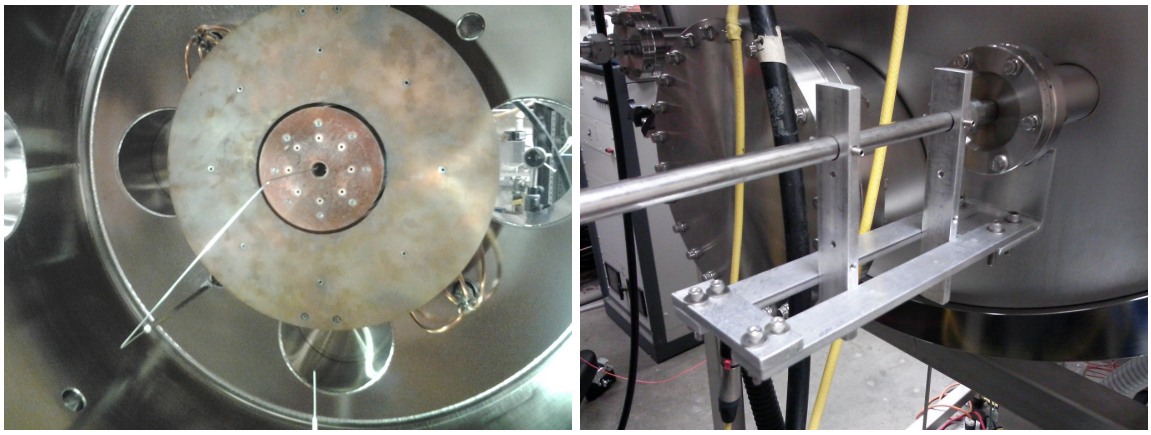

Figure 3.4: Left panel: Photo of the U-shaped Langmuir probe installed in the chamber. The straight Langmuir probe coated with white boron nitride is also visible at the bottom of the photo (when in use, it would be slid upwards so that the probe tip was at or near the chamber's central axis). Right panel: Guide structure used to prevent the U-shaped probe from rotating when it was being moved axially. The vertical bars were clamped onto the probe shaft with set screws and fit tightly into the groove at the bottom of the structure.

from the grounded probe shaft. This was accomplished by cutting off the semi-rigid cable near the Torr Seal vacuum interface and using a normal wire with an insulating jacket to carry the signal the rest of the way out of the probe shaft; the short length of semi-rigid cable inside the probe shaft was covered with heat shrink. This design ensured that the probe tip was the only conductor drawing current from the RF plasma; the downside was that the semi-rigid cable's outer conductor did not provide shielding.

In order to reduce the RF signal picked up from the nearby RF amplifier, the exposed portion of the wire near the power supply and oscilloscope was wrapped in aluminum foil, and the foil was clamped to the end of the probe shaft to form a continuous conducting shield. RF currents on the foil were diverted to ground using the procedure developed by Perkins and Bellan [67]: the wire with its foil shield was passed through a ferrite choke near the point of connection to the probe resistor and power supply, and the foil was explicitly grounded just upstream of the ferrite by taping it firmly to the cart carrying the RF amplifier and other experimental apparatus. This procedure reduced the RF signal picked up by the long wire enough that the signal picked up by the probe within the plasma dominated, allowing temporal and spatial variations in RF fluctuations in V_{probe} to be measured (see Fig. 3.5).

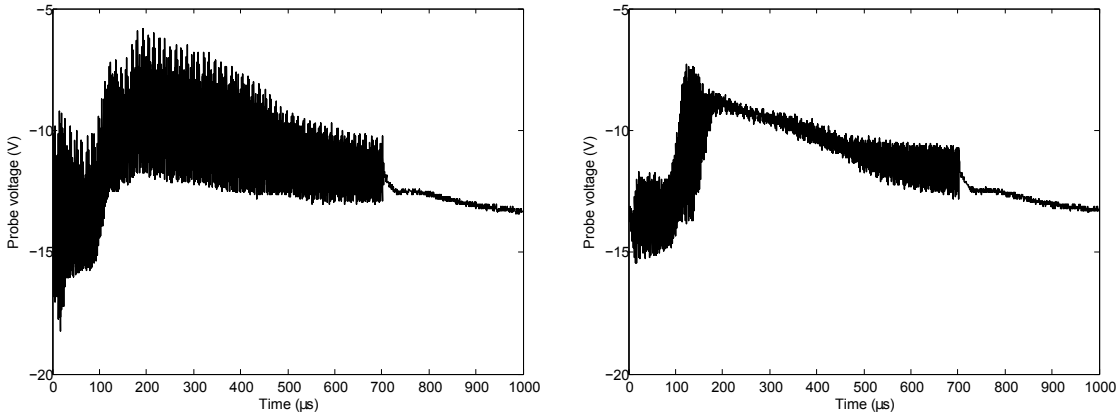

Figure 3.5: Left: Langmuir probe voltage measured with a 1x oscilloscope probe with no shielding on the Langmuir probe's signal wire (probe tip at $z = -4.2$ cm, $R_{probe} = 270\ \Omega$, measuring ion saturation current). The RF oscillations are mostly pickup from the high voltage RF amplifier output coupled into the signal line outside the vacuum chamber. Right: Probe voltage under the same conditions measured with aluminum foil shielding on the probe wire and the scheme from [67] used to prevent RF ground currents from coupling to the signal line. With this setup, the RF oscillations are mostly picked up by the section of the probe within the plasma. Dramatic temporal variations in the amplitude of the RF oscillations are seen that do not correspond to any changes in the RF amplifier's output voltage or current; these must reflect changing plasma properties, but the mechanism is not yet fully understood.

3.1.2 Optical Emission Spectroscopy

Passive optical emission spectroscopy was used to track the populations of atomic excited states and make non-invasive, mostly qualitative/comparative measurements of the ionization fraction and electron temperature. The spectroscopy system setup and initial measurements were carried out with the assistance of Hannah V. Willett, a Summer Undergraduate Research Fellowship (SURF) student from Cambridge University [72]. Light was collected by an optical fiber (Ocean Optics part number P200-10-UV-VIS, 200 μm core diameter) and was coupled into a Jarrell-Ash 82-092 0.5 meter Ebert scanning spectrometer using a lens. The spectrometer was operated as a monochromator, with a Hamamatsu R928 photomultiplier tube (PMT) used as a detector. The PMT output current was recorded on an oscilloscope with an 8 kΩ terminating resistor; the time resolution, determined by the RC time of the cable capacitance and the measurement resistor, was approximately (100 pF) $\times$ (8 kΩ) $\approx$ 1 μs. The PMT power supply was operated at 1 kV, and the spectrometer entrance slit width was 400 μm. With this setup, the full width at half maximum

of the Ar II 434.8 nm emission line (measured by adjusting the monochromator wavelength away from the line center until the measured signal level was half of the peak value) was ~ 0.8 nm, so only lines separated by $\Delta\lambda \gg 1$ nm could reliably be distinguished from one another. Wavelength calibration of the monochromator was carried out by observing a set of known atomic emission lines from hydrogen, oxygen, and argon spectral lamps [72].

During initial optimization of the RF plasma source, the plasma properties were monitored as the experiment setup was varied by observing neutral argon (Ar I) emission lines at 696.5 nm (electron transition: $4p \rightarrow 4s$; upper level energy $\equiv E_k = 13.36$ eV ; transition rate $\equiv A_{ki} = 6.4 \times 10^6$ s^{-1}) and 703.0 nm ($6s \rightarrow 4p$; $E_k = 14.88$ eV ; $A_{ki} = 2.7 \times 10^6$ s^{-1}) and a singly ionized argon (Ar II) emission line at 434.8 nm ($4p \rightarrow 4s$; $E_k = 19.55$ eV ; $A_{ki} = 1.2 \times 10^8$ s^{-1})[2]. Quantitative interpretation of the spectroscopic data, which would have required a detailed numerical calculation (usually known as a "collisional-radiative" model) since the plasma density was expected to fall in between the low-density coronal and high-density local thermodynamic equilibrium (LTE) regimes [74], was not attempted. However, it was still possible to draw useful qualitative conclusions from the relative line intensities.

The intensity of an emission line is proportional to the population density of the upper level of the corresponding atomic transition times the rate for spontaneous transitions from the upper level to the lower level, i.e., $I_{ki} \propto n(k)\, A_{ki}$, where A_{ki} is a property of the atom or ion that can be calculated from quantum mechanics alone. In a low density plasma, the level k is populated primarily by collisional excitation from the ground state, and the equilibrium value of $n(k)$ is determined by balancing this excitation rate with the rate of depopulation to all other levels through spontaneous emission (this is the coronal equilibrium regime). At higher densities, collisional de-excitation and collisional excitation out of levels other than the ground state become important. Furthermore, recombination of ions and electrons can lead to enhanced population densities in the upper atomic energy levels, as electrons recombine into high energy levels and then cascade to the ground state through a series of spontaneous transitions.

Fujimoto [75] showed that for any plasma, the population density of an energy level k in ionization stage j may be expressed as the sum of a term proportional to the ground

[2]Atomic data cited here and elsewhere in this thesis are from the National Institute of Standards and Technology (NIST) [73].

state population density of the ion j and a term proportional to the ion density in the next ionization stage $j+1$, i.e.,

$$n_j(k) = Z_j(k)\, r_0(k)\, n_{j+1} n_e + \left[Z_j(k)\,/Z_j(1)\right] r_1(k)\, n_j(1)\,, \tag{3.1}$$

where $r_0(k)$ and $r_1(k)$ are temperature- and density-dependent coefficients that encapsulate the detailed atomic physics. $Z_j(k)$ is the Saha-Boltzmann coefficient:

$$Z_j(k) = \frac{g(k)}{2g_j}\left(\frac{h^2}{2\pi m k_B T_e}\right)^{3/2} \exp\left(\frac{-\chi(k)}{k_B T_e}\right), \tag{3.2}$$

where $g(k)$ and g_j are the statistical weights for the level k and the ion j, and $\chi(k)$ is the energy of the level k relative to the ionization energy (so $\chi(k) < 0$). A plasma in which the term involving r_1 dominates is labeled an "ionizing" plasma, while a plasma in which the term containing r_0 dominates is labeled a "recombining" plasma. These terms refer solely to the dominant mechanism populating the atomic energy levels and do not necessarily imply that the ionization balance of the plasma is changing in time. For example, many laboratory plasmas are in the "ionizing" regime because recombination is negligible in comparison to charged particle losses to the walls, and it is these diffusive losses that are balanced by ionization in the steady state (see Sec. 3.3). This was the case in our pre-ionization source when power was being supplied to sustain the plasma.

For an ionizing phase plasma, neglecting the detailed dependence of $r_1(k)$ on T_e and n_e, we see that the population density of level k roughly scales as

$$n_j(k) \sim \left[Z_j(k)\,/Z_j(1)\right] n_j(1) = \frac{g(k)}{g(1)} \exp\left(\frac{E(1) - E(k)}{k_B T_e}\right) n_j(1)\,, \tag{3.3}$$

where $E(k)$ is now defined relative to the ground state energy (i.e., it is equal to $\chi(k) + \chi_j$, where χ_j is the ionization potential) for consistency with the upper level energies given above for specific argon lines. The ratio of the population of a level k to a different level m of the same ionization stage scales roughly as

$$\frac{n_j(k)}{n_j(m)} \sim \frac{g(k)}{g(m)} \exp\left(\frac{E(m) - E(k)}{k_B T_e}\right). \tag{3.4}$$

If $E(k) > E(m)$, then at low electron temperatures, the population of level k will be negligi-

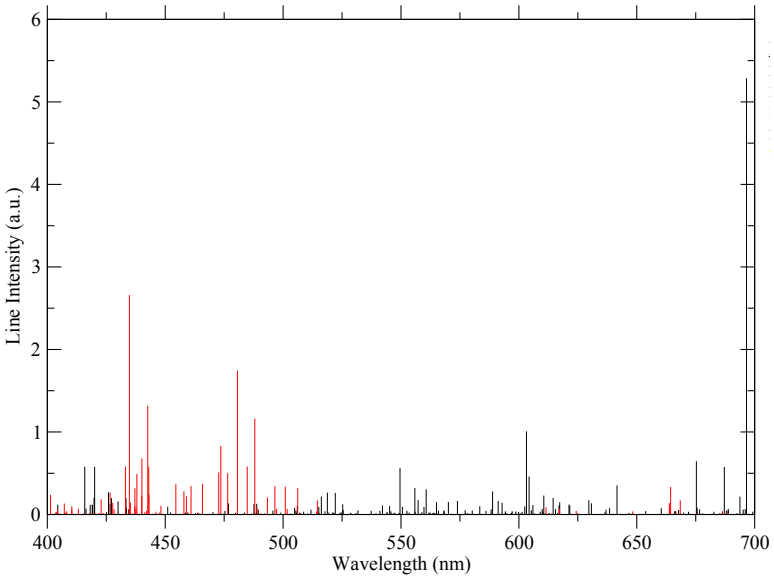

Figure 3.6: Theoretical argon optical emission spectrum [73], with Ar I lines shown in black and Ar II lines shown in red. The spectrum was calculated under the local thermodynamic equilibrium (LTE) approximation, assuming $T_e = 1$ eV and $n_e = 10^{21}$ m^{-3}. These parameters are not relevant to our RF plasma, but were chosen so that the Ar I and Ar II line intensities would be comparable in order to demonstrate the clustering of ion lines at blue/violet wavelengths and neutral lines at yellow/red wavelengths. The visible Ar I emission is dominated by the 696.5 nm line, and there are a number of additional strong lines in the infrared (not shown).

ble compared to the population of level m. For higher temperatures, the ratio $n_j(k)\,/n_j(m)$ will tend to increase, along with the ratio of the intensity of any emission line with upper level k to the intensity of any other line with upper level m. This principle was applied to use the measured [Ar I 703.0 nm] / [Ar I 696.5 nm] ratio as a qualitative temperature diagnostic (to use the ratio as a quantitative diagnostic, the detailed form of $r_1(n_e, T_e)$ for each line's upper level would have to be known). Since the upper level energy of the 703.0 nm line is higher than that of the 696.5 nm line by 1.52 eV, the line ratio is sensitive to temperature in the $T_e = 1$–5 eV regime relevant to RF discharge plasmas.

The [Ar II 434.8 nm] / [Ar I 696.5 nm] line ratio was used to qualitatively track the ionization fraction in the pre-ionization plasma[3]. It is clear intuitively, and from the factor $n_j(1)$ in Eq. 3.3, that the population density of a level k is proportional to the overall population density n_j of the ionization stage. However, the exponential factor in Eq. 3.4

[3]Both line intensity ratios studied were corrected for the wavelength-dependent quantum efficiency of the PMT, but this constant correction factor was of little consequence since only variations in the line ratios were of interest.

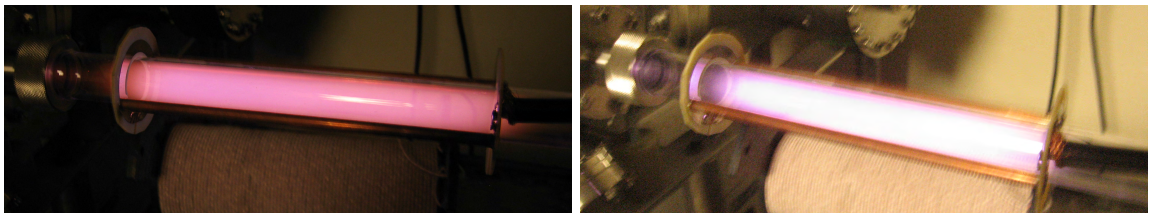

Figure 3.7: Photos of the RF plasma during preliminary experiments on the test chamber using the Nagoya type III (NIII) antenna. The solenoid was removed for these photos. Left: Discharge with mostly neutral argon (Ar I) emission. Right: Discharge with a higher level of ionized argon (Ar II) emission.

leads to a strong temperature dependence in the [Ar II 434.8 nm] / [Ar I 696.5 nm] ratio (independent of the temperature dependence of the ionization balance itself) because the upper level energy for the 434.8 nm line is 6.19 eV higher than that of the 696.5 nm line. Thus having an independent T_e measurement from the [Ar I 703.0 nm] / [Ar I 696.5 nm] ratio was important for decoupling the two effects.

The measured line ratios may have been modified by re-absoprtion of 696.5 nm emission. Based on the population density of the 4s metastable state calculated by the global discharge model described in Sec. 3.3 (see Fig. 3.11), the mean free path for 696.5 nm photons was $\sim$ 2–4 cm (see Eq. E.7). This is longer than the discharge tube radius but shorter than the axial length of the antenna, so spectroscopic measurements made with a line of sight along the axis were possibly affected. Although the quantitative values of the line ratios may have been moderately altered by this effect, the basic qualitative conclusions presented in Sec. 3.4.2 should not have been affected.

An interesting feature of argon plasmas is that the strongest ion emission lines are concentrated toward the blue end of the visible spectrum, while the strongest neutral lines are in the red and near infrared (see Fig. 3.6). Thus one can make a quick visual determination of how much Ar II is present simply by looking at the color of the plasma. Examples are shown in Fig. 3.7.

3.1.3 Visible/Infrared Photodiode

After the pre-ionization source was installed on the jet experiment, a photodiode (United Detector Technology PIN-10DP) was used to measure the overall time-dependent optical and near infrared emission from the RF plasma. Typically the photodiode was mounted near

the UV flashlamp (see Fig. 2.2), pointing toward the antenna region. The photocurrent was recorded by measuring the voltage across a 50 Ω terminating resistor with an oscilloscope. When necessary, the photodiode surface was covered with one or more layers of painter's tape in order to attenuate the incident light intensity so that the device would remain in the linear regime (it was necessary to keep the photocurrent below ~ 5 mA to avoid saturation). Although coarse, this simple diagnostic turned out to be extremely useful for determining the gas pressure in the discharge tube (see Sec. 5.1) and for making comparisons between model predictions and experiments.

3.1.4 Fast Camera

A fast intensified charge-coupled device (ICCD) camera (Cooke Corporation, with CamWare v1.21 software) with a Nikon f/1.4 lens was used to photograph the visible light emission from the RF plasma as it entered the chamber through the hole in the center electrode (these images are discussed in Chapter 4). This camera could only take a single image during each plasma shot; however, it was preferred over the 14-frame Imacon 200 movie camera described in Sec. 6.1 for photographing the relatively dim expanding RF plasma because it had 12-bit dynamic range compared to 10-bit for the Imacon camera, and it also gathered roughly 8 times more light due to the 8-way beam splitter inside the Imacon camera. Typically images were taken with the lens aperture fully open (f/1.4), the microchannel plate (MCP) gain set to 80 (on a scale of 100), the analog gain set to +6 dB, and a 10 μs exposure time.

3.2 Helicon Waves

As discussed in Sec. 2.1, energy can be transferred from an RF power supply to a plasma by capacitive coupling, inductive coupling, or wave damping. Our pre-ionization plasma source was originally designed to excite helicon waves, so a brief overview of the theory of helicon sources will now be given. However, many details will be omitted because our experiments ultimately showed that the source was probably not operating in a helicon wave-heated mode.

Helicon waves [56] are circularly polarized magnetized plasma waves that propagate in a bounded cylindrical container; the analogous waves in an unbounded volume are known as whistlers. They exist in the frequency regime $\omega_{LH} < \omega < \omega_{ce}$, where $\omega_{ce} = eB/m_e$ is

the electron cyclotron frequency and $\omega_{LH} = \omega_{ci}^2 + \omega_{pi}^2/\left(1 + \omega_{pe}^2/\omega_{ce}^2\right)$ is the "lower hybrid" frequency. In this regime, the electron cyclotron motion is too fast to affect the wave behavior, and ion motion is slow enough relative to the wave frequency that it can be ignored. Thus the wave current is produced by the $\mathbf{E} \times \mathbf{B}$ guiding center drift of electrons in the wave electric field and the background magnetic field.

The reason for the high ionization efficiency of helicon sources is complicated and is still an active area of research. The expected damping rate of the waves by Coulomb collisions is roughly 1000 times too slow to account for the heating observed in experiments at low gas pressure [51]. Collisionless (Landau) damping was proposed as the energy transfer mechanism in a classic paper on helicon theory by Chen [56], but later studies by Chen [76] and others [77, 78] cast doubt on this hypothesis, suggesting instead a process in which helicons couple to a related wave called the Trivelpiece-Gould mode, and these waves are rapidly absorbed.

The helicon wave fields vary in the axial, radial, and azimuthal directions and can be written in the form

$$\mathbf{B}(r, \theta, z, t) = \mathbf{B}(r)\, e^{i(m\theta + k_z z - \omega t)} \tag{3.5}$$

$$\mathbf{E}(r, \theta, z, t) = \mathbf{E}(r)\, e^{i(m\theta + k_z z - \omega t)}. \tag{3.6}$$

Among the antennas tested in our experiments (see Fig. 2.3), the straight Nagoya type III (NIII) antenna should in principle have excited the $m = +1$ and $m = -1$ azimuthal helicon wave modes together, while the half-turn helical Shoji (HTH) antenna could excite either the $m = +1$ or $m = -1$ mode depending on the orientation of the background magnetic field, and the single loop antenna should have excited the $m = 0$ mode. The wave magnetic fields were not measured in this work, but other researchers have found that in practice the operation of these antennas differs from the theoretical expectation, with the $m = +1$ mode preferentially excited by both the NIII and HTH antennas for reasons that are not yet fully understood [57, 79].

If the discharge tube is long and narrow, so $\lambda_z \gg \lambda_\perp$ and $k_z \ll k_\perp$, then the helicon dispersion relation for the $m = 0$ and $m = \pm 1$ modes has a simple form:

$$\frac{\omega}{k_z} \approx \frac{B_0 Z_1}{\mu_0 e n_0 a}, \tag{3.7}$$

where Z_1 is a zero of the Bessel function $J_1(x)$ (equal to 3.83 for the first radial mode, 7.02 for the second radial mode, etc.). ω is imposed by the frequency of the RF source, and the preferred k_z is typically set by the length of the antenna or some other geometrical constraint, so the wave phase velocity ω/k_z in a given helicon source is approximately fixed. Thus the plasma density that allows for efficient helicon wave launching is directly proportional to the strength of the background magnetic field. A rough scaling of discharge density with field strength has been observed in many helicon experiments [80, 55], with transitions between different axial or radial modes leading to jumps in the n_0 vs. B_0 relation. Helicon sources can generally operate in capacitively coupled (CCP) and inductively coupled (ICP) modes in addition to the efficient wave-heated (WHP) mode, with only the former modes of operation possible at low RF power levels. Transitions between the modes as the power is increased are accompanied by dramatic jumps in the plasma density [80, 54, 81].

Considering the axial currents they induce, the NIII and HTH antennas are both half-wavelength structures [54], so a reasonable assumption was that the helicon wavelength would be roughly $\lambda_z \approx 2L_{ant.}$ [51, 56]. For the HTH antenna, setting $Z_1 = 3.83$ for the first radial mode, Eq. 3.7 then gives $n_0 = \left(6.1 \times 10^{20}\right) B_0$ in S.I. units. Thus with $B_0 = 100$ G, we anticipated that a plasma density $n_0 \approx 6 \times 10^{18}$ m^{-3} would be required for efficient helicon propagation, while at $B_0 = 500$ G, $n_0 \approx 3 \times 10^{19}$ m^{-3} was expected to be required. This density range was expected to be accessible in our source, so it was anticipated that helicon mode operation would be possible.

3.3 Global Discharge Model

We will interpret our results with the aid of a global steady state discharge model, in which particle and energy inputs and losses are balanced in order to derive the equilibrium electron temperature (T_e) and density (n_e) in an argon discharge. The starting point is the two-fluid equations (see Sec. 1.1.2). In general, the source and sink terms on the right-hand side of the continuity equation (Eq. 1.6) may encompass a diverse set of processes including electron-impact ionization and three-body recombination, photoionization and radiative recombination, ionization of neutrals due to collisions with fast ions, and ionization resulting from collisions between two excited neutrals ("pooling ionization", see Sec. 5.2). However, most of these processes were of negligible importance in our experiment while the

RF power was turned on, and it will be sufficient to consider only electron-impact ionization and ignore the rest[4]. Therefore, the steady-state ion continuity equation becomes simply

$$\nabla \cdot (n_i \mathbf{u}_i) = \nu_{iz} n_e, \tag{3.8}$$

where ν_{iz} is the ionization frequency, which in general may depend on both T_e and n_e.

The term $\nabla \cdot (n_i \mathbf{u_i})$ represents a steady diffusion of plasma away from regions with a high ionization rate and toward the walls. The flow velocity $\mathbf{u}_i$ is governed by the electron and ion equations of motion (Eq. 1.7). In weakly ionized RF discharges, the magnetic force and convective terms can often be ignored [5, Section 2.3], and collisions with neutrals are more important than Coulomb collisions in mediating plasma diffusion because the mean electron and ion fluid velocities must be the same in order to maintain quasineutrality[5]. Thus in the steady state, Eq. 1.7 reduces to

$$0 = q_\sigma n_\sigma \mathbf{E} - \nabla P_\sigma - m_\sigma n_\sigma \nu_{\sigma n} \mathbf{u}_\sigma, \tag{3.9}$$

where the neutral fluid is assumed to be nearly at rest.

If $|\mathbf{u}_\sigma| \ll v_{T\sigma}$, then $\nu_{\sigma n} = n_g \sigma_{\sigma n} v_{T\sigma}$ is independent of $\mathbf{u}_\sigma$, and it is straightforward to combine Eqs. 3.8 and 3.9 to derive the ambipolar diffusion equation (this approach is taken in Sec. 4.4.1). However, in the low-to-intermediate pressure regime in which the ion-neutral mean free path satisfies $(T_e/T_i)\,\lambda_{in} \gtrsim R, L$ (where R and L are the discharge radius and length[6]), $|\mathbf{u}_i| \gtrsim v_{Ti}$, so $\nu_{in} \propto |\mathbf{u}_i|$ and the diffusion equation becomes nonlinear (see Sec. 4.4.1 and [5, Section 5.3]). In this regime, the density profile is relatively flat in the

[4] As one example, consider three-body recombination, with rate coefficient $K_{rec} \approx \left(1.1 \times 10^{-39}\right) T_{eV}^{-9/2}$ m^6/s (see Eq. 4.27). For an argon plasma with $T_e = 3$ eV, $n_e = 5 \times 10^{19}$ m^{-3}, and $n_g = 10^{21}$ m^{-3}, the recombination rate is $K_{rec} n_e^2 \approx 2 \times 10^{-2}$ s^{-1}. Meanwhile, from [5, Table 3.3], the rate of collisional ionization out of the ground state is $K_{gi} n_g \approx 10^5$ s^{-1}, so recombination can be neglected by comparison.

[5] This statement is only strictly true for an unmagnetized plasma—in a magnetized plasma the electrons may diffuse primarily along $\mathbf{B}$ and the ions primarily across $\mathbf{B}$ in such a way that quasi-neutrality is preserved [5, p. 154]. However, this situation can only persist if the plasma is enclosed in a conducting container so that currents can flow in the walls.

[6] We will assume that the discharge volume is bounded by the antenna length, which is a reasonable approximation in the unmagnetized case. Thus for experiments with the HTH antenna, $L = 10.5$ cm and $R = 1.1$ cm. In RF plasmas, power from the source is coupled mainly to the electrons; they transfer energy to the ions through collisions, but this energy transfer is very inefficient since $m_e/m_i \ll 1$, so the ions tend to be near room temperature (0.025 eV), and $T_i/T_e \sim 0.01$–0.1. Assuming $T_e = 3$ eV and $T_i = 0.05$ eV, and using $\sigma_{in} \approx 5 \times 10^{-19}$ m^2 [5, Figure 3.15], we find $(T_e/T_i)\,\lambda_{in} \geq R$ for $p \lesssim 320$ mTorr and $(T_e/T_i)\,\lambda_{in} \geq L$ for $p \lesssim 35$ mTorr .

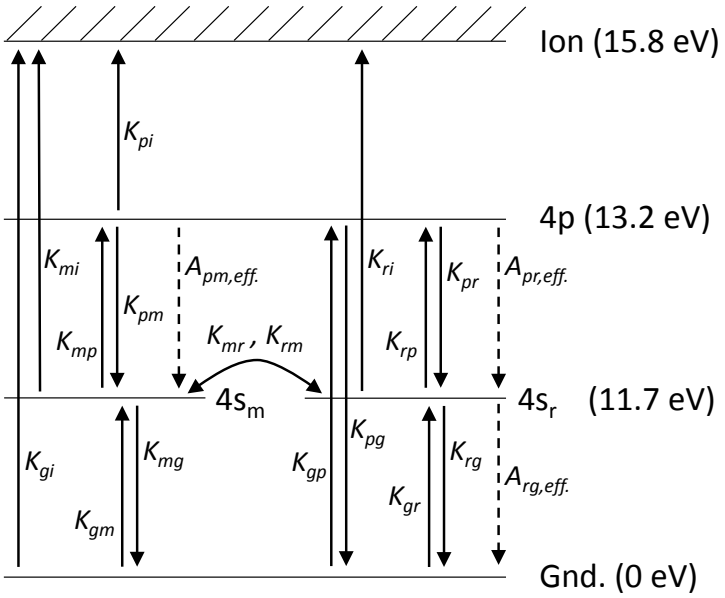

Figure 3.8: Illustration of the Ar I energy level structure (not to scale) and the collisional and radiative transitions included in the global discharge model. Solid arrows indicate electron-impact excitations and de-excitations with rate coefficients $K_{\alpha\beta}$, and dotted lines indicate spontaneous transitions with absorption-corrected transition rates $A_{\alpha\beta,eff.}$.

center and steep near the edges, and the plasma can be approximated as having a uniform density almost everywhere, with a sharp drop-off near the sheaths at the boundaries (see Appendix D for more discussion of sheaths). The ratio of the density at the radial sheath edge (defined as the location where the mean ion velocity toward the wall is equal to c_s) to the peak density at the center of the plasma is given approximately by the formula

$$h_R \equiv \frac{n_{sR}}{n_{i0}} \approx 0.80 \left(4 + \frac{R}{\lambda_{in}}\right)^{-1/2}, \tag{3.10}$$

which was derived through an empirical fit to analytical diffusion solutions [5, Section 5.3]. The corresponding estimate for the density at the axial sheath edge is

$$h_L \equiv \frac{n_{sL}}{n_{i0}} \approx 0.86 \left(3 + \frac{L}{2\lambda_{in}}\right)^{-1/2}. \tag{3.11}$$

We will find that the plasma is $< 15\%$ ionized at the gas pressures and RF power levels of interest, so only singly charged ions (Ar II) and neutrals (Ar I) need to be included in the model. However, because of the relatively high plasma density in our source, it is critical to

Process	Rate Coefficient Formula	Energy
e + Ar elastic scattering	$K_{el.} = \left(2.3 \times 10^{-14}\right) T_e^{1.61} \exp\left(0.06\left(\ln T_e\right)^2 - 0.12\left(\ln T_e\right)^3\right)$	$3\frac{m_e}{m_i} k_B T_e$
e + Ar(g) $\rightarrow$ Ar^+ + e	$K_{gi} = \left(2.34 \times 10^{-14}\right) T_e^{0.59} \exp\left(-17.44/T_e\right)$	15.76
e + Ar(4s) $\rightarrow$ Ar^+ + e	$K_{mi} = K_{ri} = \left(6.8 \times 10^{-15}\right) T_e^{0.67} \exp\left(-4.2/T_e\right)$	4.11
e + Ar(4p) $\rightarrow$ Ar^+ + e	$K_{pi} = \left(1.8 \times 10^{-13}\right) T_e^{0.61} \exp\left(-2.61/T_e\right)$	2.59
e + Ar(g) $\rightarrow$ Ar(4s) + e	$K_{gm} = K_{gr} = \left(2.5 \times 10^{-15}\right) T_e^{0.74} \exp\left(-11.56/T_e\right)$	11.65
e + Ar(4s) $\rightarrow$ Ar(g) + e	$K_{mg} = K_{rg} = \left(4.3 \times 10^{-16}\right) T_e^{0.74}$	-11.65
e + Ar(g) $\rightarrow$ Ar(4p) + e	$K_{gp} = \left(1.4 \times 10^{-14}\right) T_e^{0.71} \exp\left(-13.2/T_e\right)$	13.17
e + Ar(4p) $\rightarrow$ Ar(g) + e	$K_{pg} = \left(3.9 \times 10^{-16}\right) T_e^{0.71}$	-13.17
e + Ar(4s) $\rightarrow$ Ar(4p) + e	$K_{mp} = K_{rp} = \left(8.9 \times 10^{-13}\right) T_e^{0.51} \exp\left(-1.59/T_e\right)$	1.52
e + Ar(4p) $\rightarrow$ Ar(4s) + e	$K_{pm} = K_{pr} = \left(1.5 \times 10^{-13}\right) T_e^{0.51}$	-1.52
e+Ar($4s_m$) $\rightarrow$ Ar($4s_r$)+e	$K_{mr} = \left(2 \times 10^{-13}\right)$	0
e+Ar($4s_r$) $\rightarrow$ Ar($4s_m$)+e	$K_{rm} = \left(2 \times 10^{-13}\right)$	0

Table 3.1: Electron collisional processes included in the global discharge model. The rate coefficients [5, Table 3.3] are given in units of m^3/s, and T_e is in eV in the formulas. The third column gives the energy in eV lost by the electron fluid as a result of each process (negative values imply that the free electrons gain energy from the collision).

include excited atomic states (in contrast, many models of lower-density plasma discharges [5, Section. 10.2], [82] assume that all ionizations occur out of the ground state). Following the approach previously used by Ashida, Lee, and Lieberman [83] and other authors [84, 85], we group the Ar I excited states into three effective energy levels, consisting of the two $4s$ metastable states (labeled by a subscript m)[7], the two $4s$ resonant states (labeled r), and the ten $4p$ states (labeled p). The corresponding statistical weights ($g_\alpha = \sum 2J + 1$, where J is the total angular momentum quantum number) are $g_m = g_r = 6$ and $g_p = 36$. The neutral and ionized ground states (labeled g and i, respectively) are also included in the model, while neutral bound states above the $4p$ level and excited ion states are neglected. The ground state neutral density is calculated as $n_g = n_{total} - (n_i + n_m + n_r + n_p)$, where $n_{total} \propto p_{Ar}$ is the total number of argon atoms in the discharge volume, assumed to be constant. Here and throughout this section, $n_e = n_i$ is assumed, and the two will be used interchangeably. The energy level groupings and atomic transitions considered in the model are illustrated in Fig. 3.8.

The steady state balance between ionization and diffusive losses, specified locally by Eq.

[7] Among the four neutral argon excited states that have an electron in the $4s$ level, the states with total angular momentum $J = 0$ and $J = 2$ are metastable, meaning that spontaneous radiative transitions to the ground state are forbidden, while the two states with $J = 1$ are resonant, meaning that spontaneous transitions to the ground state are allowed. This is because the ground state has $J = 0$, and according to the quantum mechanical selection rules, only transitions with $\Delta J = 0, \pm 1$ are allowed, but $J = 0 \rightarrow J = 0$ is forbidden.

3.8, can be written globally as

$$\pi R^2 L n_e \left(K_{gi} n_g + K_{mi} n_m + K_{ri} n_r + K_{pi} n_p\right) = c_s \left(2\pi R L n_{sR} + 2\pi R^2 n_{sL}\right). \tag{3.12}$$

The terms on the left-hand side account for ion creation by electron-impact ionization out of the neutral argon ground state and excited states, while the right-hand side represents radial and axial losses. $K_{\alpha\beta}(T_e) = \langle \sigma_{\alpha\beta} v_e \rangle$ denotes the rate coefficient for collisional transitions from state α to state β (units of m^3/s). Lieberman and Lichtenberg's formulas [5, Table 3.3] were used for the temperature dependence of all rate coefficients in the model—these are reproduced in Table 3.1. The electron velocity distribution was assumed to be Maxwellian, with T_e spatially uniform.

We may write a similar equation that balances the RF power input with the various processes that remove energy from the electron fluid (the energy content of the ion fluid can be neglected since $T_i \ll T_e$):

$$P_{RF} = \pi R^2 L n_e \Bigg[K_{gi} n_g E_{gi} + K_{mi} n_m E_{mi} + K_{ri} n_r E_{ri} + K_{pi} n_p E_{pi} + \sum_{\alpha,\beta} K_{\alpha\beta} n_\alpha E_{\alpha\beta} + K_{el.} n_g E_{el.} \Bigg] + c_s \left(2\pi R L n_{sR} + 2\pi R^2 n_{sL}\right) \left[\left(eV_s + \frac{1}{2} k_B T_e \right) + 2 k_B T_e \right]. \tag{3.13}$$

The first four terms in the first square bracket represent electron energy losses from ionizing collisions with neutrals, the summation accounts for electron energy losses and gains due to excitations and de-excitations of neutral atoms, and the final term represents elastic scattering of electrons off neutrals. $E_{\alpha i}$ is the ionization energy out of a given level—for example, $E_{mi} = E_{ri} = 4.05$ eV $= 6.49 \times 10^{-19}$ J—and the energies for excitations and de-excitations are defined similarly (see Table 3.1). The mean energy transfer per elastic electron-neutral collision is $E_{el.} = (3m_e/M_i)\, k_B T_e$ [5, p. 81].

The term proportional to c_s on the second line of Eq. 3.13 represents the energy carried to the walls by particles that diffuse out of the plasma. It can be shown [5, p. 37] that for a Maxwellian velocity distribution, the mean kinetic energy carried to the wall by each electron is $2k_B T_e$. The mean kinetic energy of each ion lost is $(k_B T_e/2 + eV_s)$, where V_s is the sheath voltage drop ([5, p. 332], and see Eq. D.2). This term must be included in the electron energy equation because the energy that accelerates the ions toward the wall is extracted from the potential difference between V_{plasma} and the wall potential (equal to the

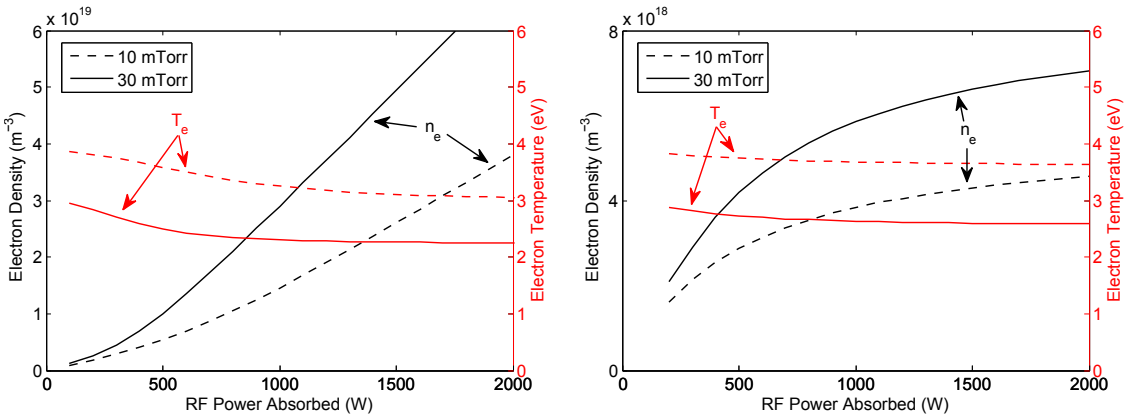

Figure 3.9: T_e and n_e calculated by the global model for unmagnetized argon ICPs (left) and CCPs (right) with $L = 10.5$ cm and $R = 1.1$ cm.

floating potential V_f), which arises as a result of finite T_e (see Eq. D.11 and the discussion of sheaths and the floating potential in Appendix D).

The sheath voltage drop is $V_s \approx 4.7 k_B T_e/e$ for argon inductively coupled plasmas (ICPs) and wave-heated plasmas (WHPs), but it is much larger for capacitively coupled plasmas (CCPs), approximately 40% of the applied RF voltage amplitude [5, Sec. 10.2]. As a result, for a given RF power level, CCPs cannot produce plasma densities as high as ICPs and WHPs, because too much energy is carried to the walls by ions falling into the deep sheath potential well.

The steady state argon excited state population densities are determined by balancing the rates of bound electron transitions into and out of each energy level (see Fig. 3.8). For the $4s$ metastable state, we have

$$K_{gm} n_g n_e + K_{rm} n_r n_e + (K_{pm} n_e + A_{pm,eff.})\, n_p = (K_{mr} + K_{mp} + K_{mg} + K_{mi})\, n_e n_m, \quad (3.14)$$

where the left-hand side accounts for processes that increase n_m while the right-hand side includes processes that decrease n_m. The loss rate of metastable atoms by diffusion to the walls [83] is smaller than the collisional depopulation rate by at least two orders of magnitude in our discharge and can be neglected. The analogous balance equations for the

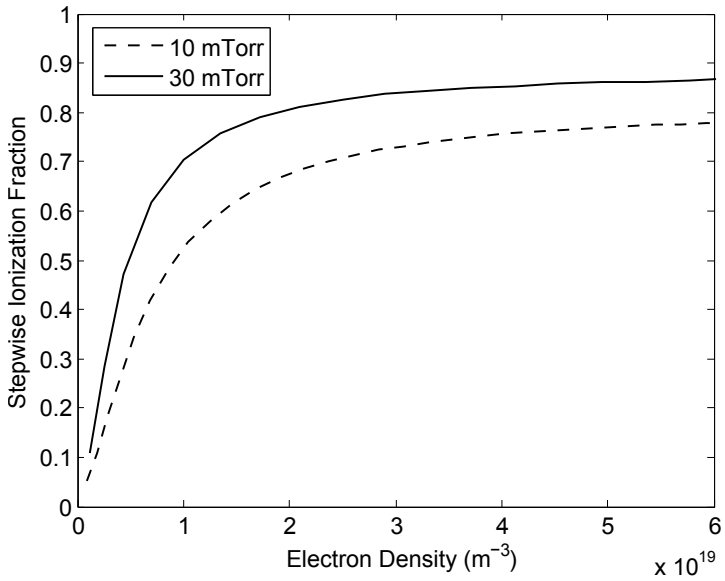

Figure 3.10: Fraction of the total ionization occurring out of excited states, calculated by the global model for unmagnetized ICPs with $L = 10.5$ cm and $R = 1.1$ cm.

$4s$ resonant and $4p$ states are

$$K_{gr} n_g n_e + K_{mr} n_m n_e + (K_{pr} n_e + A_{pr,eff.})\, n_p = ((K_{rm} + K_{rp} + K_{rg} + K_{ri})\, n_e + A_{rg,eff.})\, n_r \tag{3.15}$$

$$K_{gp} n_g n_e + K_{mp} n_m n_e + K_{rp} n_r n_e = ((K_{pm} + K_{pr} + K_{pg} + K_{pi})\, n_e + A_{pm,eff.} + A_{pr,eff.})\, n_p. \tag{3.16}$$

The $A_{\alpha\beta,eff.}$ are effective spontaneous transition rates (units of s^{-1}) that take into account re-absorption of emitted line radiation. We follow Ashida, Lee, and Lieberman [83] and assume that all photons emitted at a distance $d > l_{mfp}$ from the edge of the plasma are re-absorbed, while those emitted within one absorption mean free path l_{mfp} of the walls escape. The details of the calculation of the $A_{\alpha\beta,eff.}$, which depend on the lower and upper level population densities n_β and n_α, are provided in Appendix E.

The equilibrium discharge properties are found by numerically solving the system of nonlinear Eqs. 3.12, 3.13, 3.14, 3.15, and 3.16 for T_e, n_e, n_m, n_r, and n_p. Since the absorption-corrected spontaneous emission rates depend on the ground state and excited state population densities, which are not known a priori, an iterative solution procedure is employed: the model is first solved using initial guesses for $A_{rg,eff.}$, $A_{pm,eff.}$, and $A_{pr,eff.}$,

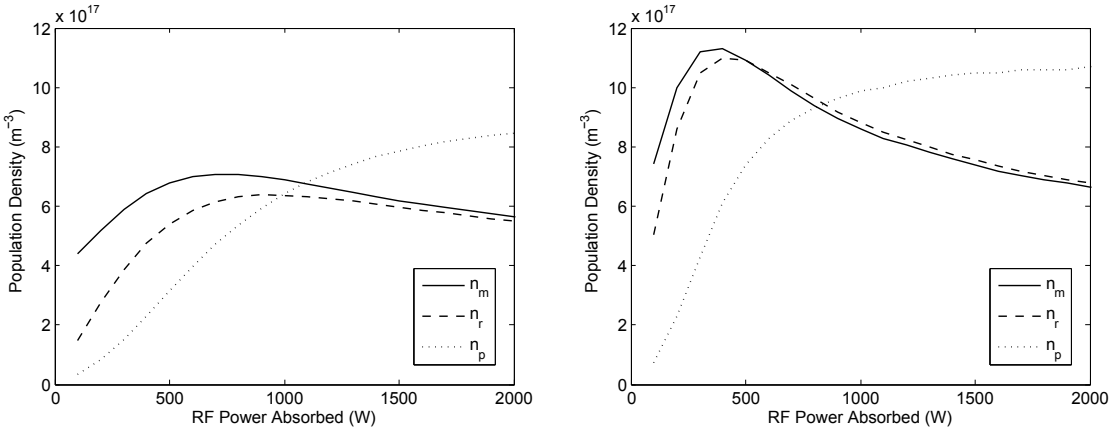

Figure 3.11: Ar I excited state population densities calculated by the global model for unmagnetized argon ICPs at 10 mTorr (left) and 30 mTorr (right) with $L = 10.5$ cm and $R = 1.1$ cm.

then these values are updated using the calculated n_g, n_m, n_r, and n_p, and the calculation is repeated until it converges to a self-consistent solution.

In Fig. 3.9, the electron density and temperature calculated by the model are plotted as a function of P_{RF} for unmagnetized ICPs and CCPs at 10 mTorr and 30 mTorr. For the capacitively coupled calculation, $V_s = 0.4V_{antenna}$ was assumed; from experimental measurements, $V_{antenna} \approx .37P_{RF}$ (S.I units) for the HTH antenna, so $V_s = .15P_{RF}$ was used in the model. From the plots, we see that n_e is an increasing function of P_{RF} as expected, but the curves are concave up for ICPs and concave down for CCPs. For ICPs, multistep ionization out of excited states becomes increasingly important at high RF power, lowering the average collisional energy loss (from ionizing, exciting, and elastic collisions) per ionization event, so n_e rises faster than linearly with P_{RF}. The critical role that stepwise ionization plays at high n_e is illustrated explicitly in Fig. 3.10. Qualitatively, stepwise ionization becomes important when the electron-neutral collision frequency exceeds the effective spontaneous transition rate out of excited states; this condition is satisfied over most of the parameter regime of interest for our discharge[8]. Stepwise ionization also becomes important at high n_e in CCPs, but its impact on the plasma density is more than canceled out by the increase in V_s and the consequent large diffusive energy losses at high RF power, which limit the rate of increase of n_e with P_{RF}.

[8]It is interesting to note that because $K_{pi} \gg K_{mi}, K_{ri}$ (see Table 3.1), the vast majority of stepwise ionizations occur out of the $4p$ state in this model.

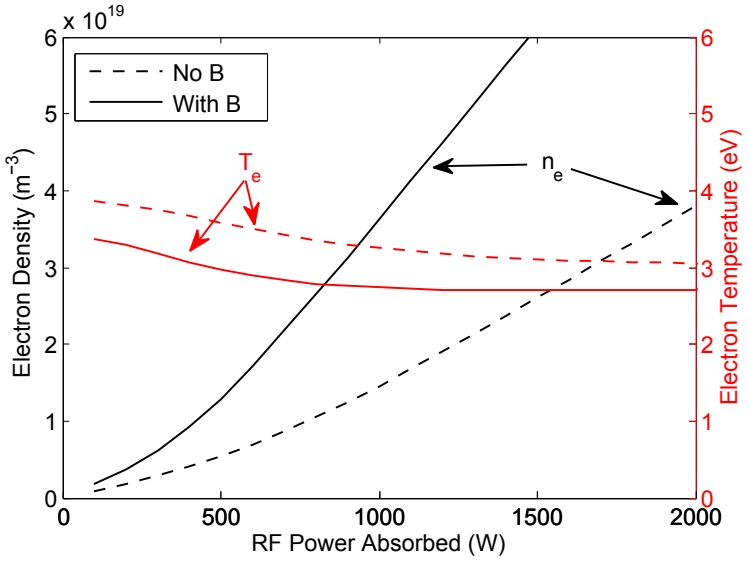

Figure 3.12: Qualitative illustration of the effect of an axial magnetic field on the equilibrium T_e and n_e. Model results are shown for ICPs at 10 mTorr with $L = 10.5$ cm and $R = 1.1$ cm. The "With B" simulation had h_R set to half of the normal value specified by Eq. 3.10.

The electron temperature in a steady state gas discharge adjusts itself to the value that allows the particle and energy balance equations (Eqs. 3.12 and 3.13) to be satisfied simultaneously. Because the ionization rate coefficients listed in Table 3.1 are increasing functions of T_e, the temperature depends inversely on the gas pressure, as shown in Fig. 3.9 (at higher p_{Ar} electron-neutral collisions are more frequent, so lower T_e is needed to provide a high enough ionization rate to balance losses). In weakly ionized discharges, T_e nearly always falls in the range 1.5 eV $< T_e <$ 6 eV [5, Figure 10.1]—increasing P_{RF} leads to more ionization and higher n_e rather than to higher T_e. The situation is similar to boiling a pot of water: ionization of neutral atoms is analogous to the liquid-gas phase transition, which uses up all of the energy input to the water and clamps the temperature at 100° C.

The excited state population densities n_m, n_r, and n_p are plotted for ICPs in Fig. 3.11. Unlike the electron density, n_m and n_r do not increase monotonically with P_{RF}. Examining the simulation results in detail to understand this behavior, we find that the dominant process depopulating the $4s$ metastable level is collisional excitation to the $4p$ state, and the dominant processes populating the metastable level are collisional de-excitation and spontaneous transitions from the $4p$ level. Extracting the relevant terms from Eq. 3.14, we

have

$$K_{pm} n_p n_e + A_{pm,eff.} n_p \approx K_{mp} n_m n_e \tag{3.17}$$

$$n_m \approx \left(\frac{K_{pm}}{K_{mp}} + \frac{A_{pm,eff.}}{K_{mp} n_e} \right) n_p. \tag{3.18}$$

At low n_e (or equivalently, low RF power), $A_{pm,eff.} \gg K_{pm} n_e$ and spontaneous transitions are the dominant process acting to increase n_m. As n_e rises, however, the term $A_{pm,eff.}/K_{mp} n_e$ becomes smaller[9], so n_m will decrease with increasing P_{RF} unless n_p is increasing rapidly, which is not the case at high powers in Fig. 3.11. Similar logic can be applied to explain the observed dependence of n_r on P_{RF}, although spontaneous transitions to the ground state are also an important depopulating mechanism for the $4s$ resonant state when n_e is low.

Another (perhaps) surprising prediction of the model is that the $4s$ metastable and $4s$ resonant states have similar population densities[10], even though there is no radiative decay pathway to depopulate the metastable state. This occurs because most of the resonant line emission is re-absorbed (at 30 mTorr, $A_{rg,eff.} \approx A_{rg}/500$), and as a result the frequent electron-impact transitions between the resonant and metastable states keep their populations nearly equal (in mathematical terms, $K_{rm} n_e \gg A_{rg,eff.}$).

The model presented here can only give quantitatively accurate results for unmagnetized discharges. However, a qualitative sense of how magnetic confinement affects the plasma properties may be obtained by decreasing the parameter h_R defined in Eq. 3.10 in order to artificially suppress the radial diffusive loss rate. The results of such a calculation are shown in Fig. 3.12, which demonstates that applying an axial magnetic field causes T_e to decrease and n_e to increase. Note, however, that the model assumption of uniform T_e may not be accurate in this case since the field inhibits radial electron heat transport, and also the plasma volume, previously assumed to be bounded by the antenna length, can increase as a result of magnetic confinement, but this effect was not accounted for in Fig. 3.12.

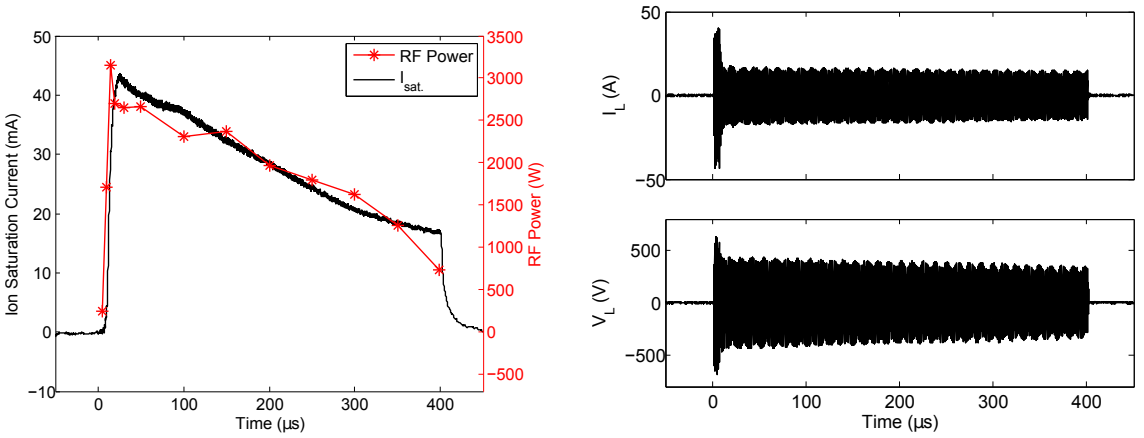

Figure 3.13: Left: Time-dependent ion saturation current and net RF power delivered to the load for a set of discharges with the HTH antenna used, $B = 340$ G, $p_{Ar} = 30$ mTorr, and an RF pulse length of 400 μs. Right: Time-dependent current and voltage at the RF amplifier output. The power declines faster than the I_L and V_L amplitudes due to a gradual increase in the phase shift ϕ. The apparent oscillations in the amplitudes are an artifact (aliasing) arising because of undersampling of the RF waveform by the oscilloscope.

3.4 Results and Discussion

During initial experiments on the small test vacuum chamber, the pre-ionization source performance was diagnosed using optical emission spectroscopy, as described in Sec. 3.1.2. For a given gas pressure and magnetic field strength, it was found that the level of Ar II 434.8 nm emission peaked at or near the same matching network tuning that maximized the net power transferred to the load. The initial RF amplifier configuration had a high output transformer turns ratio ($n/m = 6/1$) in order to produce a high antenna voltage for breaking down the neutral gas, but the maximum power transfer theorem was not satisfied with this setup (see Eq. 2.10), so the plasma density was low. Reducing the turns ratio to $n/m = 2/1$ or $n/m = 1/1$ led to greatly improved ionization performance.

Among the three antenna designs tested (see Fig. 2.3), the ionization efficiency (as measured by the axially line-integrated intensity of Ar II 434.8 nm emission) achieved by the HTH antenna was greater than that of the NIII antenna, which in turn performed better than the single loop antenna. Therefore, the HTH antenna was used exclusively when the pre-ionization system was installed on the MHD-driven jet experiment. However, a number

[9]This simple analysis ignores the relatively weak temperature dependence of $K_{mp}(T_e)$ and also neglects the dependence of $A_{pm,eff.}$ on n_m and n_p (see Appendix E).

[10]In fact, $n_r > n_m$ for $P_{RF} > 500$ W at 30 mTorr due to slight differences between $A_{pr,eff.}$ and $A_{pm,eff.}$.

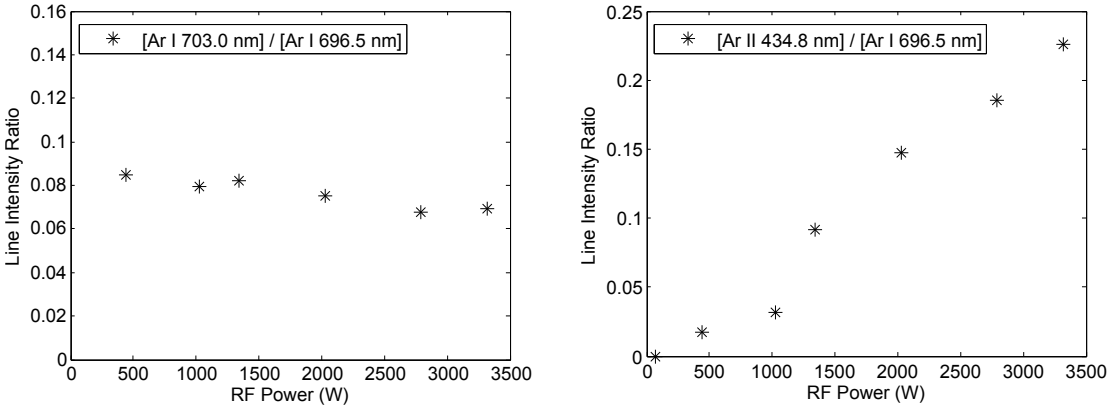

Figure 3.14: Measured argon optical emission line ratios vs. RF power delivered to the load (P_L was varied by changing the number of batteries powering the final stage of the RF amplifier). The NIII antenna was used, the gas pressure was 16 mTorr, and there was no magnetic field. The line of sight was along the axis of the discharge tube through a window on the test chamber. Here and in Figs. 3.15 and 3.16, the RF power was measured at $t = 75$ μs, and the line intensities were averaged over the interval $t = 100$–200 μs and also averaged over 5 shots for each line.

of early scaling measurements were carried out using the NIII antenna (see Figs. 3.14, 3.15, and 3.16).

3.4.1 Time-Dependent Discharge Behavior

The time-dependent behavior of the pre-ionization source with the HTH antenna installed is illustrated in Fig. 3.13. For these measurements and all others presented in this chapter, the U-shaped Langmuir probe was positioned along the tube axis, with the probe tip 1.4 cm inside the antenna. If the probe was inserted deeper into the tube so that the probe tip was at the antenna center, fast camera images indicated that the presence of the 0.085" OD probe shaft along the axis was perturbing the plasma formation.

The RF amplifier was turned on and the UV flashlamp was pulsed to produce seed ionization at $t = 0$ μs in Fig. 3.13. Initially, the source and load were mismatched, so the net power delivered to the load was low. At $t \sim 10$ μs, the plasma density had risen sufficiently to load the antenna and improve the impedance match, and P_L increased, allowing the discharge to transition to a much higher density mode of operation. The subsequent rapid density increase lagged the power rise by ~ 3 μs. The duration of the initial low-density phase could be altered by adjusting the matching capacitance C_s to vary the unloaded

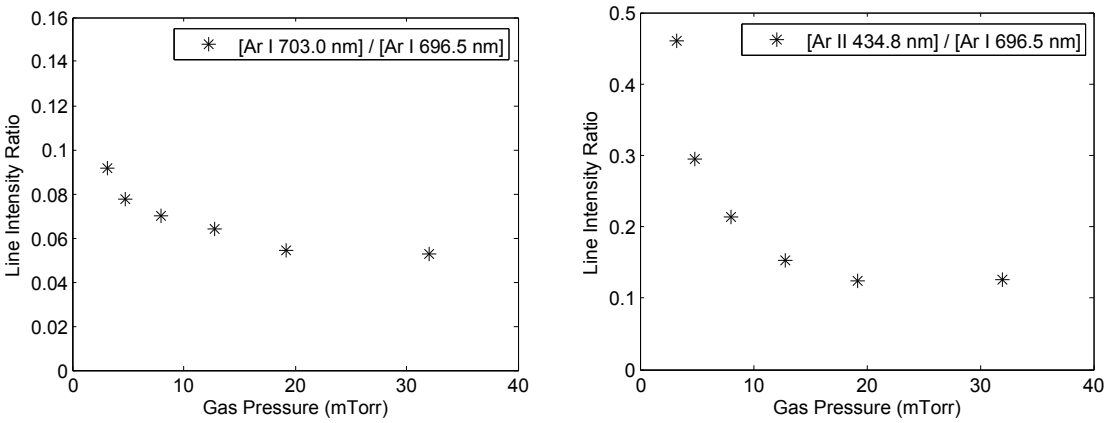

Figure 3.15: Measured argon optical emission line ratios vs. gas pressure. The NIII antenna was used, the RF power output was 2.73 ± 0.14 kW (an effort was made to adjust the matching network tuning to keep the RF power constant as the gas pressure was varied, but it was not possible to do this perfectly), and there was no magnetic field.

antenna voltage.

The power output of the RF amplifier gradually decreased in time as the 47 μF output stage capacitor discharged, with a proportional decline in the measured $I_{sat.}$. Since the timescale for these changes was much longer than the timescale for particle and energy losses from the discharge (a few μs), the discharge may be considered to have been in a quasi-steady state from t = 30–400 μs, with particle and energy balance satisfied, so the model of Sec. 3.3 is applicable.

3.4.2 Plasma Parameters Achieved, Scalings Measurements, and Energy Coupling Mechanism

Qualitative scaling measurements made spectroscopically during experiments with the NIII antenna are shown in Figs. 3.14, 3.15, and 3.16. In the left panel of Fig. 3.14, the temperature-dependent [Ar I 703.0 nm] / [Ar I 696.5 nm] line intensity ratio decreases gradually with increasing RF power, in agreement with the prediction of the global discharge model (see Fig. 3.9). The [Ar II 434.8 nm] / [Ar I 696.5 nm] ratio shown in the right panel is roughly proportional to P_{RF}, indicating that the ionization fraction increased at higher powers as expected.

The dependence of the line ratios on p_{Ar}, shown in Fig. 3.15, is also consistent with the

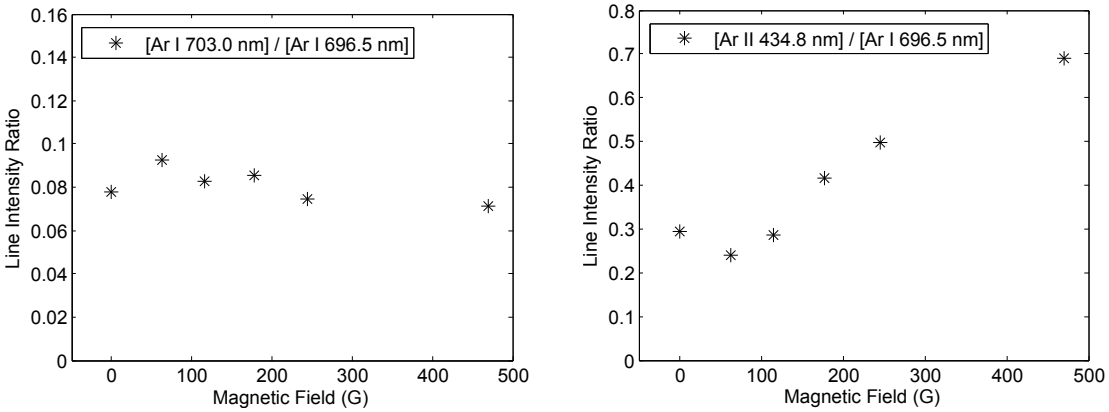

Figure 3.16: Measured argon optical emission line ratios vs. axial magnetic field strength. The NIII antenna was used, the gas pressure was 6 mTorr, and the RF power output was $\sim 2.11 \pm 0.27$ kW.

model predictions[11]. The [Ar I 703.0 nm] / [Ar I 696.5 nm] ratio (left panel) shows that T_e fell at higher pressures. The interpretation of variations in the [Ar II 434.8 nm] / [Ar I 696.5 nm] ratio (right panel) is ambiguous in this case. The observed decrease in the line ratio at high pressures could be due solely to the strong temperature dependence arising because of the 6.19 eV difference in the upper level energies for the two lines, or it might be partially explained by a decrease in the ionization fraction at large n_g (the model predicts that n_i will rise but n_i/n_g will decrease as p_{Ar} is increased).

The scaling of the line ratios with the background magnetic field strength, shown in Fig. 3.16, was of particular interest, since our initial goal was to deliver power to the plasma via helicon waves. The measurements implied that the electron temperature was approximately constant as a function of B (left panel), although it is possible that there was some variation in T_e that could not be resolved by the [Ar I 703.0 nm] / [Ar I 696.5 nm] line ratio, which has relatively weak temperature dependence. With T_e held constant, the [Ar II 434.8 nm] / [Ar I 696.5 nm] line ratio is proportional to the ionization fraction, so the right panel shows that as the field strength was increased, $n_i/n_g \propto n_i$ first decreased and then increased.

More precise scaling measurements were made for experiments with the HTH antenna

[11]For all argon gas pressure measurements in the range 1–1000 mTorr reported in this thesis, a gas species correction factor of 1.6 was applied to the thermocouple gauge measurement. For example, when the thermocouple read 10 mTorr, the true pressure was $p_{Ar} \approx 16$ mTorr. The magnitude of this correction factor was chosen based on recommended values in the range 1.5–1.7 found in documentation for various thermocouple and Pirani gauges manufactured by Duniway, Pfeiffer, Kurt J. Lesker, and Arun Microelectronics. The factor 1.6 was also confirmed by direct calibration of the thermocouple on the main vacuum chamber using a capacitance manometer from the Caltech ice dusty plasma experiment [86].

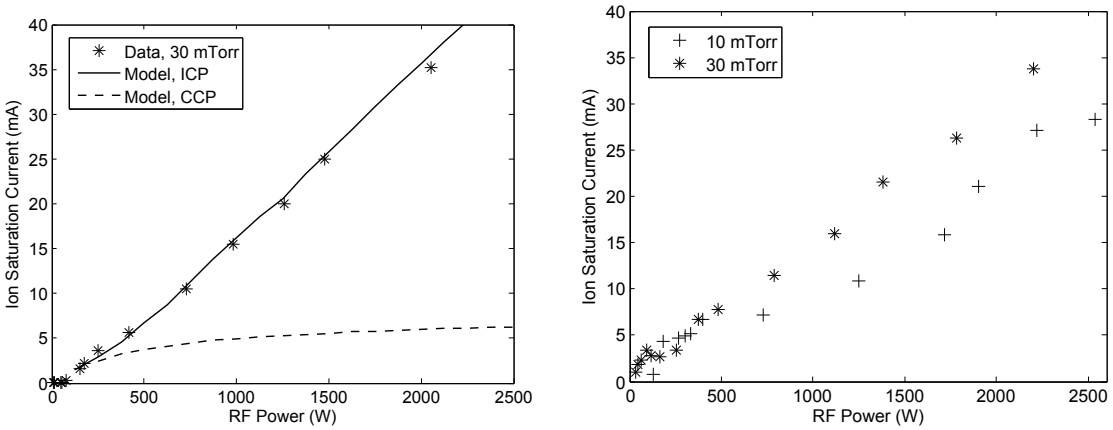

Figure 3.17: Langmuir probe ion saturation current vs. RF power with $B = 0$ G (left) and $B = 340$ G (right). The HTH antenna was used for both sets of measurements, and P_{RF} and $I_{sat.}$ were measured at $t = 100$ μs, except in the lowest power cases, for which the discharge only reached a quasi-steady state at a later time. In panel (a), the solid and dotted lines show the model predictions for inductively coupled and capacitively coupled discharges, respectively, at 30 mTorr, assuming that 80% of the RF power delivered to the load was absorbed by the plasma.

using the Langmuir probe, which was also capable of measuring the magnitude of n_i if the model prediction for T_e was used along with the measured ion saturation current in Eq. D.9. The measured $I_{sat.}$ as a function of RF power and magnetic field is shown in Figs. 3.17 and 3.18. Data was taken at both 10 and 30 mTorr in the magnetized cases, while with $B = 0$, the discharge could only be initiated at $p_{Ar} \gtrsim 20$ mTorr. $I_{sat.} \propto n_i T_e^{1/2}$, so it was a good proxy for density given that T_e varied over a relatively narrow range as P_{RF} and B were adjusted (see Figs. 3.9 and 3.12).

In the left panel of Fig. 3.17, the data is compared with model predictions for $I_{sat.}$ (derived from the results shown in Fig. 3.9 using Eq. D.9) for discharges with low voltage (ICP) and high voltage (CCP) sheaths. We only measured the net RF power delivered to the load as a whole; the fraction of this power that was actually absorbed by the plasma (rather than dissipated in the impedance matching capacitors and antenna resistance) is not known, but adopting a reasonable value of 80% for the model calculation gives good agreement between the data and the ICP model. The $I_{sat.}$ values predicted by the CCP model, on the other hand, are far too low, indicating that the discharge could not have been primarily capacitively coupled.

Numerical values for the ion density in several representative cases are listed in Table 3.2

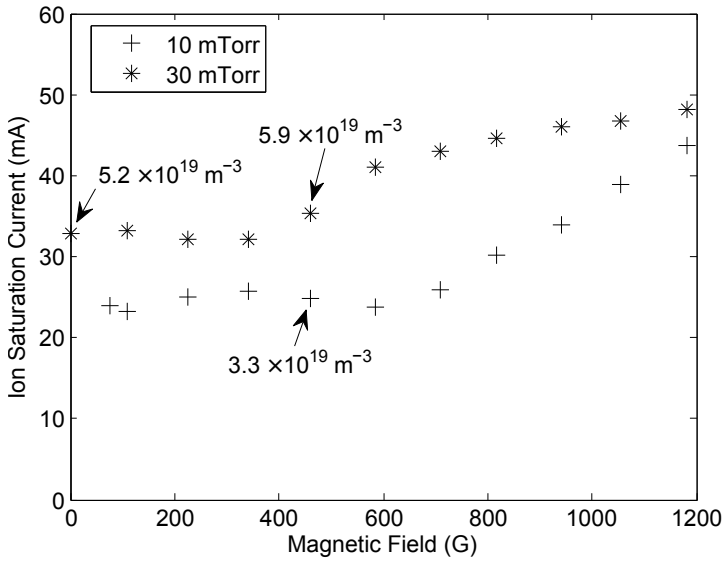

Figure 3.18: Ion saturation current vs. axial magnetic field strength with $P_{RF} = 2.40 \pm 0.20$ kW. The HTH antenna was used and $I_{sat.}$ was measured at $t = 100$ μs. The calculated values of n_i at several points are labeled for reference (also see Table 3.2).

and labeled on Fig. 3.18. The table also shows the corresponding model predictions for ICPs and CCPs; comparing the model and data confirms that the energy transfer mechanism in unmagnetized discharges using the HTH antenna was mostly inductive, while discharges that used the NIII antenna likely operated with a mix of capacitive and inductive coupling.

In discharges with an axial magnetic field applied, the additional possibility of wave heating by helicons existed. However, there were several pieces of indirect evidence that damping of these waves or the related Trivelpiece-Gould mode [77, 76] was not the primary mechanism for energy transfer to the plasma in our experiment:

- The plasma densities obtained with and without a magnetic field were similar (compare the 30 mTorr data between the left panel and the right panel of Fig. 3.17). Helicon sources can typically create plasma more efficiently than unmagnetized ICPs; this is thought to be because wave-particle interactions reduce the collisional energy loss per ionization event to near the ionization potential [56, 51]. However, we did not see the expected degree of improvement when the magnetic field was turned on, which should have increased the density both by improving confinement and by allowing for helicon wave propagation.

Antenna	p	B (G)	Expt. n_e	Model T_e (ICP)	Mod. n_e (ICP)	Mod. n_e (CCP)
NIII	11	0	8.3×10^{18}	3.04 eV	2.2×10^{19}	2.9×10^{18}
NIII	11	470	2.1×10^{19}	2.60 eV	5.4×10^{19}	6.0×10^{18}
HTH	30	0	5.2×10^{19}	2.26 eV	6.2×10^{19}	6.7×10^{18}
HTH	10	470	3.3×10^{19}	2.72 eV	8.6×10^{19}	9.4×10^{18}
HTH	30	470	5.9×10^{19}	2.05 eV	1.5×10^{20}	1.5×10^{19}

Table 3.2: Comparison of measured densities with global discharge model predictions for inductively coupled (ICP) and capacitively coupled (CCP) discharges, assuming 80% of the RF power delivered to the load was absorbed by the plasma. All densities are given in m^{-3}, and pressures are in mTorr. The experimental densities were calculated from the measured ion saturation currents using the T_e values predicted by the model, as discussed in Appendix D. As in Fig. 3.12, approximate model calculations for discharges with $B = 470$ G were carried out by assuming that the radial loss rate (parameterized by $h_R \equiv n_{sR}/n_{i0}$) was a factor of 2 lower than in the unmagnetized case.

- In experiments with the HTH antenna, n_e was nearly constant as a function of B for $B \leq 500$ G, and increased only gradually at higher fields (see Fig. 3.18). When the NIII antenna was used, the ionization fraction increased significantly at $B \gtrsim 200$ G, but n_e was lower at $B \sim 100$ G than at $B = 0$ (see Fig. 3.16). In contrast, a rough linear scaling of density with field strength has been observed in many helicon experiments [51, 87, 55] due to the proportionality between n_e and B_0 in Eq. 3.7. The mode jumps that are often seen in plots of n_e vs. B for helicon sources [80] were also absent in our experiments.

- As the RF power was increased in magnetized experiments with the HTH antenna (see the right panel of Fig. 3.17), no density jump indicating a transition from a CCP or ICP mode to the helicon mode was seen, unlike in other helicon sources [54, 88]. There was a notable jump in the [Ar II 434.8 nm] / [Ar I 696.5 nm] line ratio at $P_{RF} \sim 1200$ W in the experiments with the NIII antenna (see the right panel of Fig. 3.14), but this could not have been due to a helicon mode transition because no magnetic field was applied in this case.

- The effectiveness of the HTH antenna at producing plasma was unchanged when the direction of the magnetic field was reversed, in contrast to the behavior of other experiments in which helicon mode operation has been demonstrated [52, 79].

Evidence of helicon mode operation was likewise absent in a limited set of experiments

with the single-loop antenna (see Fig. 2.3). Therefore, we may conclude that inductive coupling rather than wave heating was the dominant energy transfer mechanism in our RF plasma source. It is natural to ask why helicon mode operation was not achieved, even though our source operated with values of ω, k_z, B, and n_e (see Eq. 3.7) typical of helicon sources, and three standard helicon antennas were tested. One possible explanation was that the RF pulse length was too short: other pulsed helicon experiments have found that it took anywhere from ~ 500 μs [89] to > 2 ms [90] for a steady state to be reached. In order to test this hypothesis, we increased the RF amplifier's output stage capacitance from 47 μF to 188 μF; with this modification, > 2 ms RF pulses were possible, and the output power declined by less than 15% over the first 1 ms of the pulse. However, no mode transitions were observed in experiments with longer RF pulses; the plasma density simply decreased in time as in the left panel of Fig. 3.13, but at a more gradual rate. Therefore, we concluded that the short pulse length was not to blame for the lack of helicon mode operation.

Even if our RF pulse length was in principle long enough, and the power high enough, for the source to transition to a helicon mode, there may not have been a path through parameter space to reach this mode of operation. Carter et al. [91] attributed the observed difficulty in achieving helicon source operation with light ions (H and He) to this practical constraint. In experiments with argon, Boswell's group [54, 92] observed density jumps when the magnetic field was increased only after dramatically adjusting the matching network tuning, as the radiation resistance of the antenna was lower in the helicon mode than in an inductively coupled mode. However, in many of Boswell's experiments the RF supply was pulsed on a ms timescale [51, 93], implying that the impedance matching did not have to be adjusted while the plasma was present in order to achieve helicon mode jumps. An extensive effort was made to explore different tunings and find a helicon mode of operation in our pre-ionization source, but no efficiency improvement over the typical ICP mode of operation was observed.

A third possibility is that our discharge tube radius was too narrow. Chen [87] carried out extensive studies on helicon sources with 1 cm and 2 cm tube radii and found that discharges in the smaller tube did not follow standard helicon scalings; the plasma densities achieved with $R = 1$ cm were no higher than those achieved with $R = 2$ cm with the same RF input power, and the density did not rise significantly as the magnetic field strength was increased (similar to our results shown in Fig. 3.18). The discharge became turbulent for

$B \gtrsim$ 100–200 G. Chen concluded that electrostatic charging of the tube walls was playing an important role in the discharge behavior, and also found that the boundary conditions at the end of the tube were important. Other helicon experiments with $R < 2$ cm include the work of Toki et al. [94], Kerdtongmee et al. [95], Kuwahara et al. [96], Shinohara et al. [97], and Batishchev [98]. Although all of these authors called their plasma a helicon source, the presence of propagating helicon waves was not directly verified in any of the experiments. Kerdtongmee et al. and Toki et al. did not observe a jump to helicon mode operation in plots of n_e vs. P_{RF}. Kuwahara et al. did measure such a mode jump, but the density below the jump was low enough ($\sim 10^{17}$ m^{-3}) that the transition could have been from a CCP to an ICP mode. Batishchev observed a dramatic increase in Ar II optical emission when a strong magnetic field was applied but did not directly measure n_e. Only Shinohara et al. [97] identified two separate mode transitions from a CCP mode to an ICP mode and then to helicon mode. Kuwahara et al. found that higher RF power was needed to achieve $n_e \approx 10^{19}$ m^{-3} with $R = 0.5$ cm than with $R = 1$ cm, and with $R = 1$ cm a higher density inside the antenna was achieved with $B = 0$ than with finite B.

Based on the trend of non-ideal helicon performance in experiments with small discharge tubes, we suspect that the narrow tube radius was to blame for the lack of helicon mode operation in our source. However, this conclusion has not been verified experimentally and remains speculative. Most small helicon experiments, including ours, were designed with a specific application in mind such as pre-ionization or electric propulsion [94, 97] and thus were not optimized for studying fundamental helicon physics. Since there are a number of practical uses for small RF plasma sources [95, 96, 98], there is a clear need for well-designed, dedicated experiments to explore the scaling of helicon source operation with tube radius, building on the work of Shinohara's group [97]. Diagnostic accessibility is intrinsically challenging in small radius discharges, but measurements of n_e, T_e, and wave magnetic fields in a larger chamber downstream of the source tube can provide useful insights. Since perturbation of the plasma by probes is difficult to avoid in small radius discharges, the use of non-invasive measurement techniques such as interferometry, spectroscopy, and laser-induced fluorescence can be valuable.

3.4.3 High Density Inductively Coupled Plasma

In Sec. 3.3, we computed the scaling of n_e vs. P_{RF} for argon ICPs (see Fig. 3.9) by balancing ion creation and losses, energy input and losses, and population and de-population of Ar I excited states. However, the details of the mechanism by which energy was inductively coupled to the plasma were ignored. Lieberman and Lichtenberg [5, p. 466–470] show that for a coil driving azimuthal current in a cylindrical plasma, in the parameter regime typical of ICPs used in industrial plasma processing, the power absorbed by the plasma scales as $P_{RF} \propto I_{RF}^2 n_e^{-1/2}$ at high densities. This relationship between power input and density must be satisfied along with the particle and energy balance conditions, and it tends to limit the density obtainable in practice in this type of discharge to $n_e \sim 10^{18}$ m^{-3}. Higher densities can only be achieved if the coil current I_{RF} is made very high, but this lowers the efficiency of the source due to increased resistive dissipation in the coil.

The reason for the inverse scaling of power absorption with density is that the power absorption in an ICP occurs within a skin layer of thickness δ at the edge of the plasma, which becomes narrower as the density rises [54]. Expressing the current density profile in the plasma as $J_\phi(r) = J_{\phi 0} \exp\left(-\left(R-r\right)/\delta\right)$, the time-averaged power absorbed is

$$P_{RF} = \int \langle \mathbf{J}(t) \cdot \mathbf{E}^*(t) \rangle dV = \frac{\langle J_{\phi 0}^2 \rangle}{\sigma_{eff}} 2\pi L \int_{R-\delta}^{R} e^{-2(R-r)/\delta} r dr, \tag{3.19}$$

where $\sigma_{eff} = n_e e^2 / m_e \nu_{eff}$ is the effective conductivity, with $\nu_{eff} \approx \nu_{en} + \nu_{ei} + \nu_{stoc}$ an effective collision frequency that takes into account stochastic heating. Integrating and using $\delta \ll R$ yields

$$P_{RF} \approx \frac{\langle J_{\phi 0}^2 \rangle}{\sigma_{eff}} \pi L R \delta. \tag{3.20}$$

The total current induced in the plasma is

$$I_p = L \int_0^R J_{\phi 0} e^{-(R-r)/\delta} dr \approx J_{\phi 0} L \delta. \tag{3.21}$$

The plasma acts like the secondary of a transformer, with the external coil serving as the primary, so $I_p \propto I_{RF}$. Thus we have

$$P_{RF} \approx \frac{\langle I_p^2 \rangle \pi R}{\sigma_{eff} \delta L} \propto \frac{\langle I_{RF}^2 \rangle}{\sigma_{eff} \delta}. \tag{3.22}$$

In the regime typical of semiconductor processing ICPs, the collisionless skin depth scales as $\delta_p \propto n_e^{-1/2}$, while $\sigma_{eff} \propto n_e$ because electron-neutral collisions are of dominant importance, leading to the $P_{RF} \propto I_{RF}^2 n_e^{-1/2}$ scaling described above. Our RF plasma source, on the other hand, is in the anomalous skin effect regime [99], in which $\delta_a \propto n_e^{-1/3}$. Stochastic heating [5, p. 709] dominates over Ohmic heating; roughly $\nu_{stoc} \propto 1/\delta_a \propto n_e^{1/3}$, so $\sigma_{eff} \propto n_e^{2/3}$. Thus

$$P_{RF} \propto I_{RF}^2 n_e^{-1/3}. \tag{3.23}$$

The inverse dependence of P_{RF} on n_e is gentler than in the typical case, perhaps helping to explain the high densities we have been able to achieve through inductive coupling. Additionally, since we used a half-turn helical antenna rather than a multi-turn coil, the threshold current at which resistive losses in the antenna would have become important should have been much higher than for typical ICPs. However, the scalings derived here may not apply at all, since the assumption that plasma currents are driven only azimuthally is clearly inappropriate for our long, narrow antenna.

In any case, the regime in which our pre-ionization source operates has rarely been explored (we know of only one other experiment [96] in which $n_e > 10^{19}$ m^{-3} was achieved in a low pressure RF plasma source operating in an unmagnetized ICP mode). The density of power input in our source is very high: considering that ~ 2 kW of power is deposited in a skin layer of width $\delta \approx 3$ mm, outer radius 1.1 cm, and length 10.5 cm, the power density is $P_{RF}/V \approx 100$ MW/m^3. That this power density can be achieved using a low cost RF amplifier powered by AA batteries is a testament to the capabilities of pulsed power systems. Small, high density ICPs such as ours can serve as interesting testbeds for studying the fundamentals of plasma discharge operation.

3.4.4 Importance of Gas Species

High-density ICPs could readily be created in our source using a variety of noble gases (helium, neon, argon, and krypton were tested). However, difficulties were encountered when operating with hydrogen and nitrogen. With a uniform fill pressure in the chamber, the time-dependent source behavior with these gases was similar to that shown in Fig. 3.13. However, when a fast gas valve was used to transiently inject gas into the discharge tube, as in the final jet experiment setup, the plasma failed to transition from the initial very low-

density (likely capacitively-coupled) mode to a higher density ICP mode, and the antenna loading remained negligible. Exhaustive scans were made of the gas bank voltage and RF matching network tuning, but a good operating regime could not be found with these gases.

Strangely, if the chamber was pre-filled to a gas pressure at which high-density hydrogen or nitrogen operation would normally have been possible, pulsing the fast gas valve prior to turning on the RF source was observed to inhibit the usual mode transition. Various setups were investigated to change the spatiotemporal dependence of the gas density delivered by the fast gas valve (for instance, inserting a large gas reservoir halfway along the gas line between the fast gas valve and the source tube), but these did not enable high-density operation. This phenomenon remains a mystery that is worthy of further study.

3.4.5 Applications and Future Work

Our RF plasma source should be widely applicable to other experiments in which the requirements for Paschen breakdown are incompatible with the desired plasma parameters. Since the source is battery-powered, it can float at arbitrary voltages in a pulsed power system without risk of damage. The RF amplifier can also be used as a stand-alone power source; the combined weight of the amplifier, matching network, and batteries is ~ 1 kg, making it well suited for a variety of portable applications. With cooling added as described in [61], the amplifier could be operated as a CW 3 kW RF source, or it may be easily modified to operate at much lower power. This has been done for a small dusty plasma experiment at Caltech [86] that operates with 1-3 W of power capacitively coupled to the plasma. Small, high-density RF plasma sources also have applications in space propulsion [94, 100], industrial surface processing [96], and bioengineering [95].

Several outstanding research questions regarding the pre-ionization source warrant future study. Additional experiments to investigate the conditions necessary for helicon mode operation would likely yield very interesting results. High-frequency magnetic probes could be used to determine if helicon waves are being excited in the plasma, as in other helicon experiments [51, 57, 54]. The discharge tube radius could be increased to test our hypothesis that the small radius was responsible for inhibiting wave heating of the plasma.

If operation with a 1-inch OD discharge tube is to be studied further, it would be beneficial to design a new experimental setup with better diagnostic access. The solenoid could be replaced by two or more discrete coils (e.g., in a Helmholtz coil arrangement),

and the quartz tube could be broken into several segments with probe feedthroughs in between, as in [87]. A probe inserted through a gap in the side of the tube would perturb the plasma much less than one inserted along the axis and would allow for measurements of radial variations in plasma parameters. If possible, the magnetized region should extend for several times the antenna length in order to study downstream plasma properties and limit the influence of end boundary conditions on the discharge.

With the current experimental setup, more thorough experiments could be done with helium, neon, krypton, hydrogen, and nitrogen, and the global discharge model of Sec. 3.3 could be modified with an appropriate energy level structure and set of rate coefficients for each gas. If good agreement were found between the data and model for these gases, it would further validate our modeling framework for unmagnetized high density RF discharges.

Finally, additional study of the high density ICP regime could prove fruitful. It would be interesting to replace the helical antenna with a multi-turn helical coil for which the model of Sec. 3.4.3 is more directly applicable and compare the plasma properties and source efficiency achieved with the quantitative predictions of generally accepted theories of ICP operation (e.g., [5, Chapter 12]).

Chapter 4

Downstream Transport of the RF Plasma

In order for the RF plasma source to be useful in the MHD-driven jet experiment, the pre-ionized plasma needed to flow down the source tube from the antenna region into the main vacuum chamber. Experiments were carried out to determine the downstream density and the timing of the plasma's arrival into the region in front of the coaxial electrodes. The transport phenomena observed were surprisingly complex and interesting, with unexpected time and spatial dependences. These behaviors are the subject of this chapter.

A simple picture of plasma expansion is as follows: since quasi-neutrality must be obeyed except at the plasma edges, the electron and ion fluids should flow at the same rate. The kinetic energy per unit volume available for expansion is equal to the sum of the mean electron and ion thermal energies in one direction, which from statistical mechanics is

$$E/V = \frac{1}{2}nk_BT_e + \frac{1}{2}nk_BT_i \approx \frac{1}{2}nk_BT_e, \tag{4.1}$$

where $T_e \gg T_i$ was assumed. Meanwhile, when the electrons and ions are flowing outwards together at velocity u, their total kinetic energy density is

$$E/V = \frac{1}{2}nm_iu^2 + \frac{1}{2}nm_eu^2 \approx \frac{1}{2}nm_iu^2. \tag{4.2}$$

Equating these two expressions, we find

$$u = \sqrt{\frac{k_BT_e}{m_i}} \equiv c_s, \tag{4.3}$$

so the plasma should expand at roughly the ion acoustic speed.

While appealing, this energy argument is too oversimplified to describe reality. In the pressure regime of interest for our experiment, ion-neutral collisions slow down the expansion and make it diffusive in nature. Collisionless plasmas at low pressure likewise do not expand uniformly at the ion acoustic speed; instead, the expansion is self-similar with the low-density leading edge of the plasma moving faster than c_s and a "rarefaction wave" propagating backwards into the ambient plasma [101, 102, 103]. Understanding the physics of low-pressure expanding plasmas is important for inertial confinement fusion [101] and also for research on the ionosphere and on wakes created by moving bodies such as planets and satellites in space [102]. In inductively-coupled and wave-heated plasma sources used for integrated circuit fabrication, the wafer is typically located some distance from the source region [5, p. 19], and thus transport of plasma downstream from the source is a critical aspect of the operation of plasma processing tools.

4.1 Time Evolution of Fast Camera Images

The Cooke Corporation ICCD camera described in Sec. 3.1.4 was initially used to confirm that some RF plasma was reaching the main chamber and to determine the best time to trigger the main capacitor bank to create a jet. In these experiments, a fast gas valve (see Sec. 1.6.4) was used to supply gas to the RF discharge tube. Unless otherwise noted, the gas valve power supply was set to $V_{gas,RF} = 550$ V, and the delay between the triggering of the fast gas valve and the initiation of the RF discharge was $t_{gas,RF} = -6.0$ ms. The gas pressure in the tube at this time was not precisely known, but a method was discovered for indirectly determining the pressure by comparing photodiode measurements of the time-dependent light emission during these experiments with measurements taken during shots with a known uniform gas pressure in the tube. Details are given in Sec. 5.1. The inferred pressure with $V_{gas,RF} = 550$ V and $t_{gas,RF} = -6.0$ ms was $p_{Ar} \approx 460$ mTorr (see Fig. 5.3).

The half-turn helical (HTH) antenna, which was used for all experiments described in this chapter, was mounted with its front end located 5.9 cm behind the plane of the electrodes (i.e., at $z = -5.9$ cm). Therefore, if the RF plasma flowed out of the source tube along the bias magnetic field at the ion acoustic speed, it would have emerged from the tube roughly 27 μs after the source transitioned to the high-density inductively coupled (ICP)

mode (assuming $T_e \approx 2$ eV, so $c_s \approx 2.2$ km/s). After 120 μs, the plasma would have filled the region within ~ 20 cm of the center electrode, and it would have been a good time to trigger the main capacitor bank. However, the actual behavior observed was very different from this. Examples for three different RF plasma source configurations are shown in Figs. 4.1, 4.2, and 4.3.

In all three image series, the plasma expansion into the chamber appears to be unsteady, with two or more phases in which different behaviors are evident. A region of bright emission appears in front of the RF plasma source tube output within 50 μs after RF turn-on—the spatial extent of this region is greater for cases with the bias coil and solenoid turned on[1] (Figs. 4.1 and 4.2) than for the case shown in Fig. 4.3 with no magnetic field. It appears in frames 2–3 of Figs. 4.1 and 4.2 that the emitting region is expanding away from the source tube and into the chamber; however, around $t = 150$ μs it rapidly dims. In Fig. 4.1, in which the RF power was turned off at $t = 200$ μs, a new cloud of plasma emerges from the source tube at around this time, expanding far into the chamber roughly following the bias magnetic field lines and gradually dimming at late times. In Fig. 4.2, on the other hand, in which the RF power was left on until $t = 400$ μs, no plasma expansion is visible from $t = 200$–400 μs—the expansion appears to be inhibited somehow by continued application of RF power back at the antenna region. Meanwhile, in Fig. 4.3, which also used a 400 μs RF pulse but had $B = 0$, an expanding cone of plasma is readily visible from $t = 200$–300 μs. In both Figs. 4.2 and 4.3, an additional relatively dim puff of plasma appears to emerge from the source tube soon after the RF power is turned off. In all cases in which a cloud of plasma appears be expanding into the chamber, the velocity inferred from the images is on the order of 1 km/s.

4.2 Interpretation of Observed Visible Emission Patterns

It soon became clear that camera images alone were insufficient to study this complex behavior, and additional diagnostics were employed. The U-shaped Langmuir probe described in Sec. 3.1.1 was installed in order to make detailed measurements of $n_i(z,t)$, and the spectroscopy system described in Sec. 3.1.2 was used to detect argon line emission from RF plasma in front of the electrodes. These diagnostics ultimately showed that interpreting

[1]For all magnetized discharges described in this chapter, unless otherwise noted, the capacitor banks powering the bias coil and solenoid were charged to $V_{bias} = 80$ V and $V_{sol.} = 60$ V, respectively.

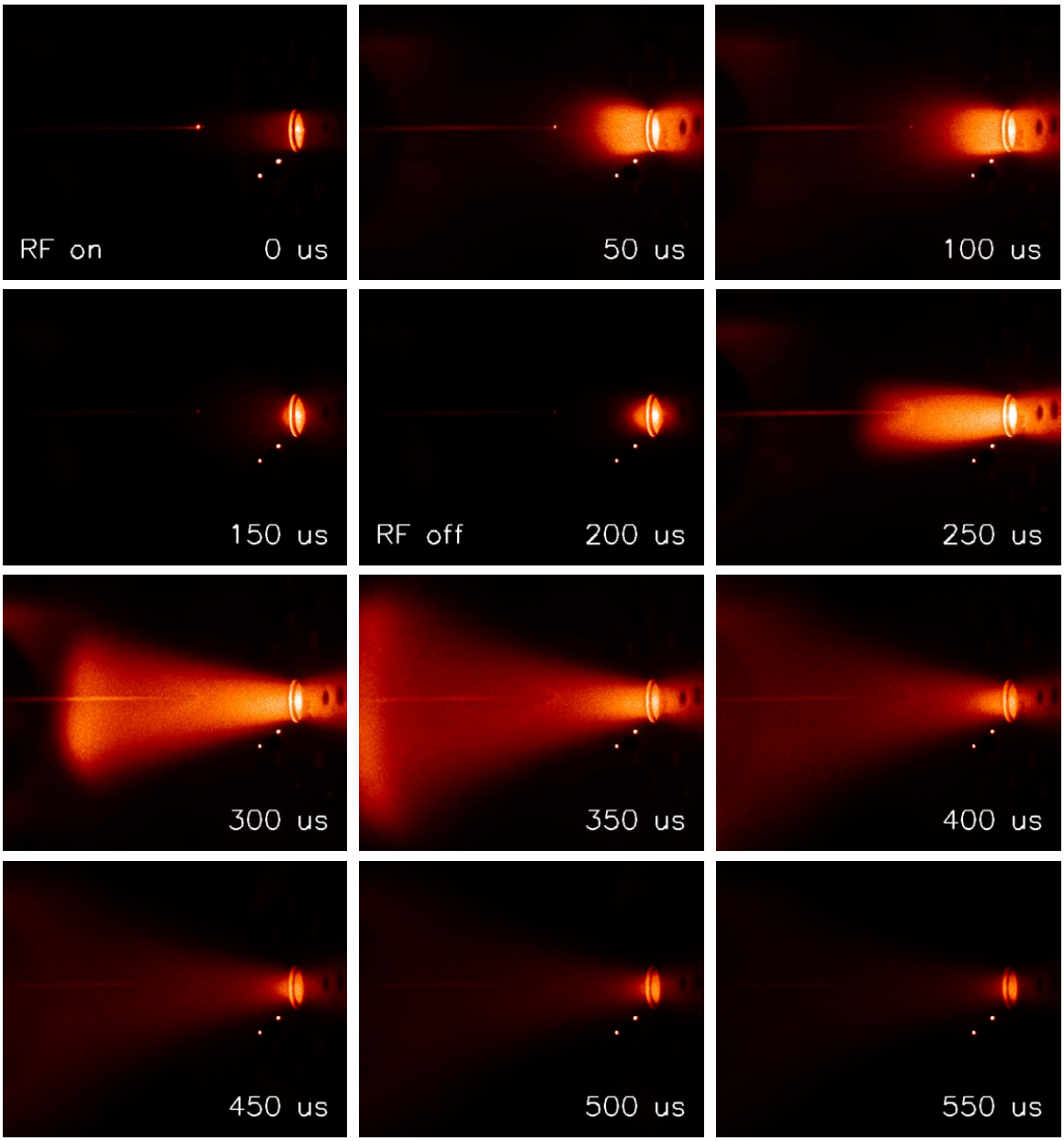

Figure 4.1: Fast camera images of RF plasma expansion into the main vacuum chamber for shots with the RF power on for 200 μs and the bias field coil and solenoid turned on. False color is used to indicate overall light intensity, with the brightest regions shown in white and dimmer areas in red. The orientation of the images is flipped with respect to the source schematic in Fig. 2.2—here the RF source tube and antenna are located to the right of the field of view. The images were each taken on separate shots, but since the discharge behavior was extremely consistent and reproducible for a given set of experimental parameters, they can be interpreted as a movie of RF plasma expansion. The images suggest that there are two phases to plasma expansion: at early times there is bright emission near the source tube output, but this dims before the RF source is turned off at $t = 200$ μs, and only after RF turn-off does the plasma fully expand into the chamber. However, as discussed in Sec. 4.2, Langmuir probe measurements (see Fig. 4.4) revealed that the brightness of optical emission by the plasma was not always proportional the local plasma density; in fact, some aspects of the images are highly deceiving.

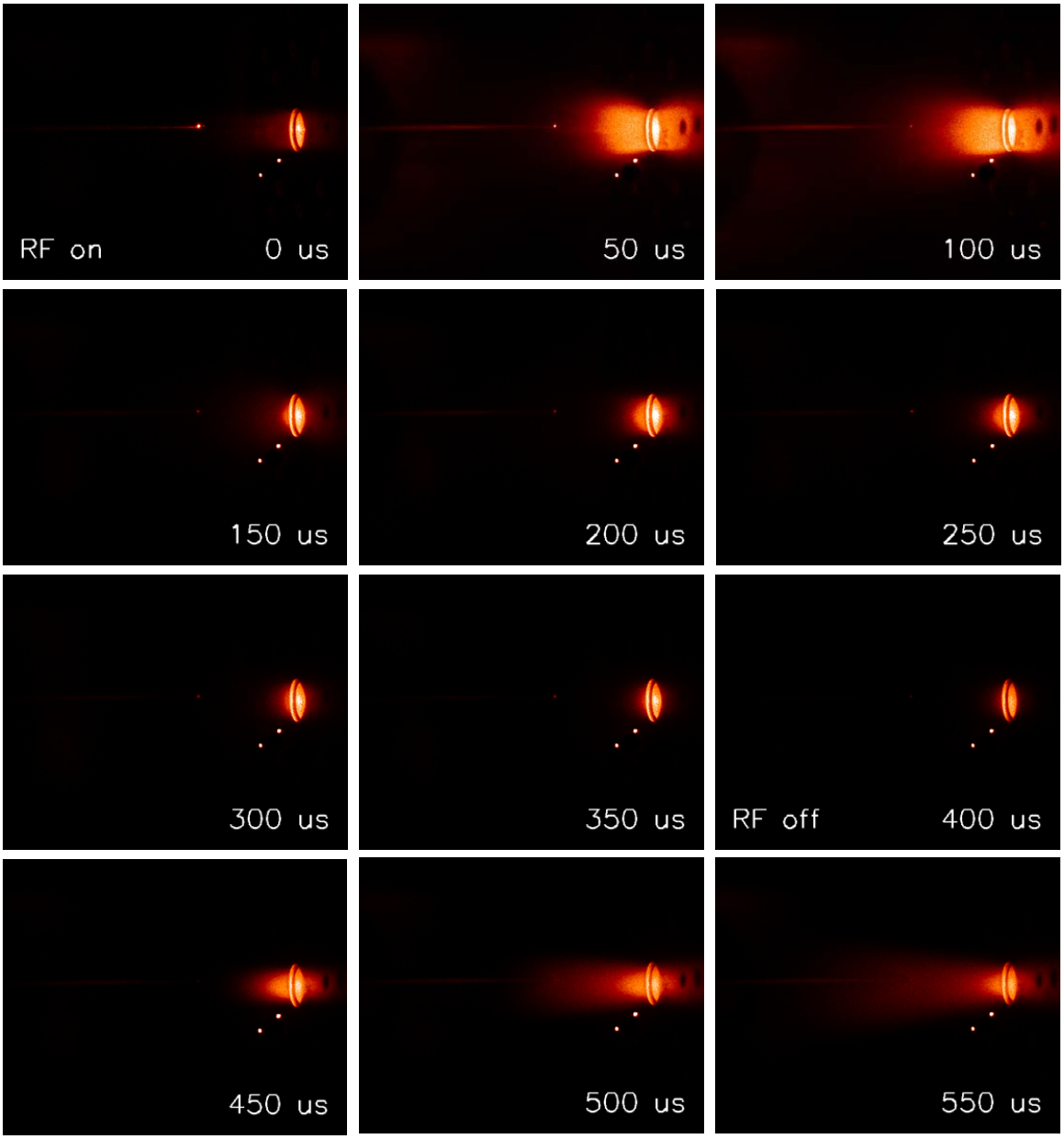

Figure 4.2: Fast camera images of RF plasma expansion into the main vacuum chamber for shots with the RF power on for 400 μs and the bias field coil and solenoid turned on. The 1" diameter RF plasma source tube output is visible toward the right side of each frame—it appears as a bright narrow oval due to the nearly side-on camera viewing angle. The two bright dots directly to the lower left of the source tube output are an artifact due to a damaged portion of the ICCD detector. These images are identical to those in Fig. 4.1 for $t < 200$ μs, as expected; however, from $t = 200$–400 μs, very little light emission is seen in the chamber. Only after RF turn-off at $t = 400$ μs does plasma appear to expand unimpeded into the chamber. Once again, however, some features of these images are deceptive—see Sec. 4.2 for a detailed analysis.

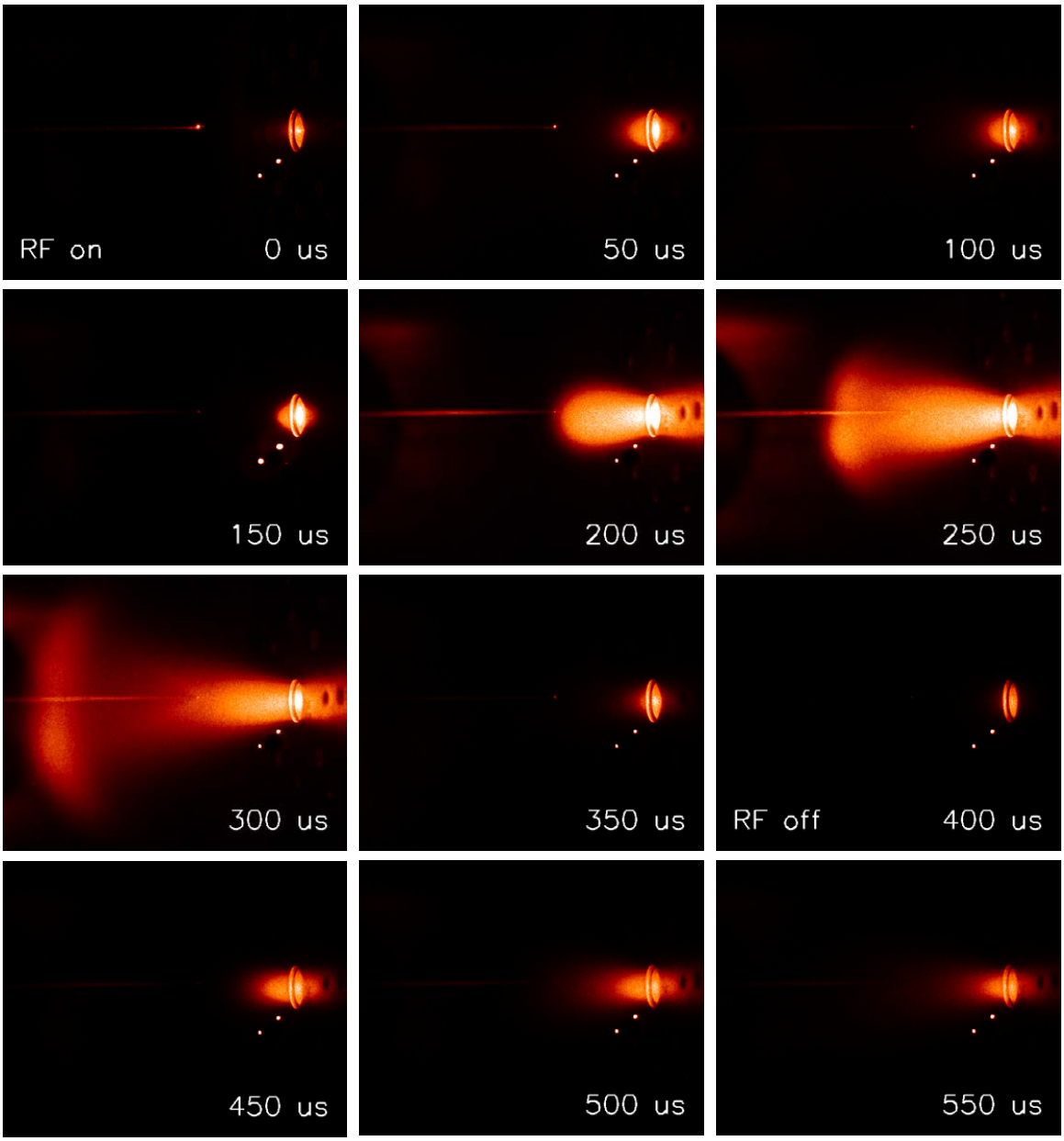

Figure 4.3: Fast camera images of RF plasma expansion into the main vacuum chamber for shots with the RF power on for 400 μs and the magnetic field coils turned off. The exposure time for these images and those in Figs. 4.1 and 4.2 was 10 μs. The axially moveable Langmuir probe shown in Fig. 3.4 is visible along the center axis of the chamber in some frames here and in Figs. 4.1 and 4.2; the probe tip was located at $z = 6$ cm in front of the jet experiment electrodes. Compared to Figs. 4.1 and 4.2, the size of the initial emitting region at early times is much smaller with $B = 0$, and in stark contrast to the case in Fig. 4.2 with the magnetic field on, it appears that a cone of plasma successfully expands out into the chamber between $t = 150$–300 μs, while the RF power is still on. However, Langmuir probe measurements (see Fig. 4.4 and Sec. 4.2) ultimately told a different story about the relative conditions with the magnetic field on and off. In these images, the emission dims rapidly between $t = 300$–350 μs, and after RF turn-off another cloud of plasma appears to emerge from the source tube, as in Fig. 4.2.

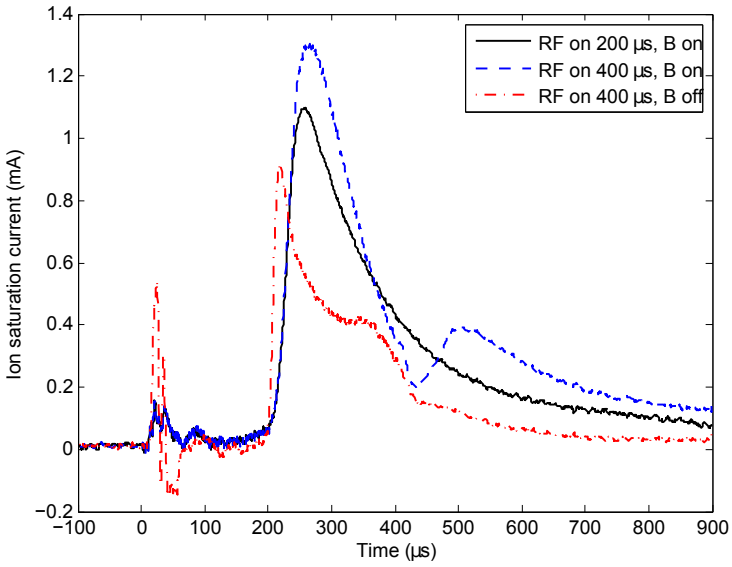

Figure 4.4: Ion saturation current measured with $V_{probe} = -15.3$ V at $z = 6$ cm during the discharges photographed in Figs. 4.1, 4.2, and 4.3 (the probe tip may be seen glowing just to the right of the center of the first image in each series). The negative current collected at $t = 20$–60 μs in the "RF on 400 μs, B off" case indicates that the probe was collecting some electron current at this time because the plasma was hotter than usual at the probe location; at later times, however, the current measured should truly be ion saturation current, proportional to $n\sqrt{T_e}$. The electron temperature is expected to change drastically only immediately after RF turn-off—at other times, changes in $I_{sat.}$ should closely correspond to variations in the plasma density.

the images was not at all straightforward. In essence, due to the existence of several different regimes for atomic processes producing visible and infrared line emission in a partially ionized plasma, the images were a relatively poor indicator of "where the plasma was" at a given time.

Because the gas pressure was > 100 mTorr for these experiments, ion-neutral collisions in the pre-sheath reduced the ion saturation current collected by the Langmuir probe to below the value predicted by collisionless theories, and the magnitude of the ion density could not be measured accurately (see Sec. D.2 for details). However, for experiments at a given gas pressure, the measured $I_{sat.}$ still scaled linearly with n_i, so using $I_{sat.}$ measurements to track temporal variations in density or compare densities between different discharges was still a valid approach.

Fig. 4.4 shows $I_{sat.}(t)$ in front of the electrodes (at $z = 6$ cm) during the discharges shown in the image series in Figs. 4.1, 4.2, and 4.3. Consider first the initial 100 μs of

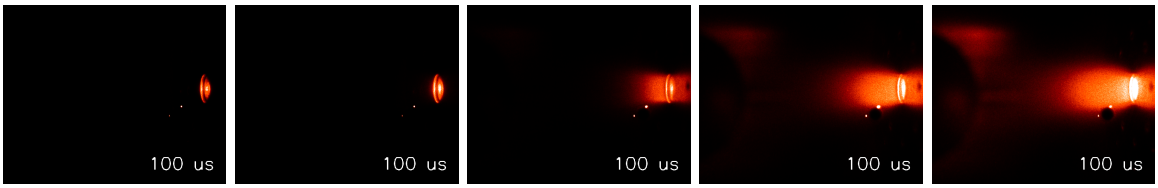

Figure 4.5: Fast camera images of the emission in front of the source tube output at $t = 100$ μs for five different argon fast gas valve delays. From left to right: $t_{gas,RF} = [-4.5 \text{ ms}, -5.0 \text{ ms}, -5.5 \text{ ms}, -6.0 \text{ ms}, -6.5 \text{ ms}]$, where $t = 0$ μs is the time at which the UV flashlamp was triggered and the RF was turned on. For longer fast gas valve delays, the neutral gas had propagated further into the chamber by $t = 0$ μs, and thus the emitting region, which corresponded mostly to the neutral gas glowing as it was bombarded by fast electrons accelerated near the RF antenna, was larger. The small black circle to the lower left of the brightest part of each image is an artifact caused by a damaged portion of the ICCD detector.

each discharge. During this time interval in Figs. 4.1 and 4.2 (the first three frames), there is a bright cloud of emission in front of the source tube that reaches the location of the probe tip. However, Fig. 4.4 shows that the plasma density at the probe was low at this time (with the highest early spike in density in fact measured for the case with $B = 0$, corresponding to Fig. 4.3). This implies that the emission was produced mostly by neutral gas that was already present in front of the source tube output at $t = 0$, not by plasma that flowed into the chamber from the antenna region. Further evidence is provided by the images in Fig. 4.5, which show that the size of the emitting region varied when the fast gas valve delay relative to RF turn-on was adjusted to be longer or shorter than the usual $t_{gas,RF} = -6.0$ ms.

The cause of the emission was probably fast electrons streaming out of the antenna region and colliding with the pre-existing neutral gas cloud, exciting the argon atoms, which then produced line radiation. Some of these atoms got ionized, leading to the small density increase measured by the Langmuir probe at very early times in Fig. 4.4. With no magnetic field, the fast electrons were not confined radially and few made it out of the source tube, explaining the smaller size of the initial emitting region in Fig. 4.3 compared to Figs. 4.1 and 4.2. In Fig. 4.6, a series of images taken around the time of RF turn-off with 1 μs exposure time demonstrates that the initial emission in front of the source tube dimmed extremely rapidly when the RF was turned off, in only 1–2 μs. This is in contrast to the much slower dimming that occurs in the last few frames of Figs. 4.1, 4.2, and 4.3. If this rapid dimming

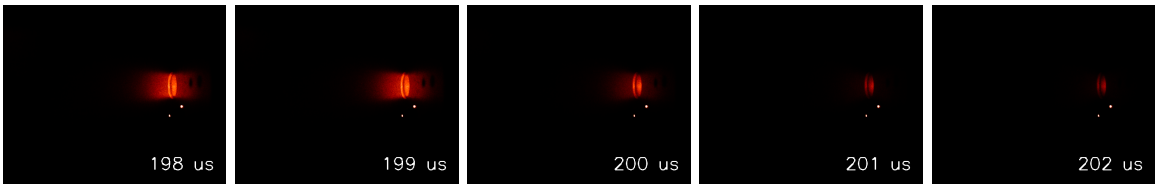

Figure 4.6: Fast camera images of the initial emitting region in front of the source tube output, taken with a 1 μs exposure time, for magnetized discharges with the RF power turned off at $t = 200$ μs. The rapid dimming after RF turn-off, which was too fast to be explained by plasma flowing out of the region in front of the electrodes, provides additional evidence that the emission was caused by fast electrons from the antenna region colliding with a pre-existing neutral gas cloud. Note that the RF amplifier was set up differently when these images were taken than it was for Figs. 4.1 and 4.2 (the driver stage battery voltage was lower), and as a result the transition from the initial low-density discharge mode to a high-density inductively coupled (ICP) mode (see Fig. 3.13) occurred later. The different time-evolution in this case meant that the initial emitting region was still glowing brightly at $t = 199$ μs, while in Figs. 4.1 and 4.2 it had begun to dim by $t = 150$ μs for a reason unrelated to RF turn-off, discussed in the text.

were due to plasma flowing out of the region of interest, which had a radius of ~ 2 cm, the bulk ion flow velocity would have to have been ~ 20 km/s; however, since $c_s \leq 4$ km/s, this is too fast to be feasible based on the energy considerations discussed in the chapter introduction. On the other hand, an electron with enough energy to collisionally excite an argon atom (~ 10 eV) can travel ~ 2 m in 1 μs, so these were lost from the system very rapidly after the RF power was turned off, and the glowing neutral gas dimmed accordingly.

In Figs. 4.1 and 4.2, the initial emitting region actually dims and shrinks before RF turn-off, around $t = 150$ μs. Then at $t \approx 200$ μs in Fig. 4.1, a bright cone of plasma emerges from the source tube, expanding into the chamber in the subsequent frames. No such expanding plasma is visible from $t = 200$–400 μs in Fig. 4.2, but surprisingly, the Langmuir probe data in Fig. 4.4 shows that there in fact *was* a high density plasma in the chamber at this time! The peak $I_{sat.}$ at $t \approx 260$ μs was actually higher for the case with the RF power still turned on (corresponding to Fig. 4.2) than for the case in which the RF was turned off at $t = 200$ μs (corresponding to Fig. 4.1); however, the electron temperature was likely lower for the discharge in which the RF had already been turned off, so we cannot determine which of the two had a higher peak density from the data shown.

Before seeking to explain the observed behavior from $t = 200$–400 μs, let us consider the reason for the dimming of the emission in front of the source tube at $t \approx 150$ μs.

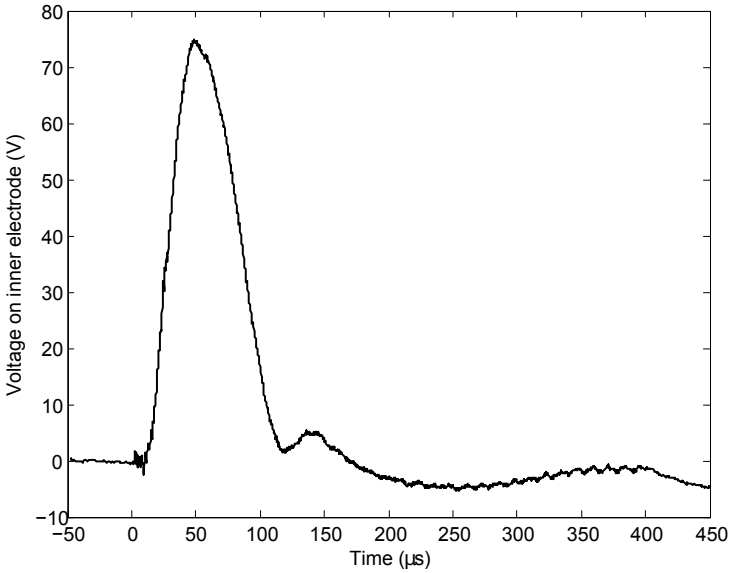

Figure 4.7: Voltage (floating potential) measured on the jet experiment's inner electrode during a discharge with $V_{bias} = 80$ V, $V_{sol.} = 60$ V, $V_{gas,RF} = 550$ V, $t_{gas,RF} = -6.0$ ms, and the RF power on for 400 μs (the same conditions as in Fig. 4.2).

There are two plausible explanations. The mean free path for electron-electron collisions is $\lambda_{ee} = (n_e \sigma_{90})^{-1}$, where σ_{90} is the effective cross section for 90 degree scattering due to the cumulative effect of small angle colllisions, given by [4, p. 16]:

$$\sigma_{90} = \frac{1}{2\pi} \left(\frac{e^2}{\epsilon_0 \mu v_R^2} \right)^2 \ln \Lambda, \tag{4.4}$$

where $\mu = m_e/2$ is the reduced mass, v_R is the relative velocity between the two colliding particles, and $\ln \Lambda \approx 10$. Plugging in the numbers for a 10 eV electron colliding with lower energy thermal electrons, we find that $\sigma_{90} \approx 5 \times 10^{-18}$ m^2. Langmuir probe measurements (see Fig. 3.18) showed that the plasma density inside the antenna was $n_e > 5 \times 10^{19}$ m^{-3} in experiments at $p_{Ar} = 30$ mTorr, and the data (Figs. 3.17 and 3.18) and the global discharge model (Figs. 3.9 and 3.12) also showed that the density was an increasing function of gas pressure. If we therefore assume that the density upstream of the antenna in experiments with the fast gas valve was at least $n_e \sim 10^{19}$ m^{-3}, then the mean free path of an electron accelerated toward the main chamber from the antenna region with $E \sim 10$ eV was $\lambda_{ee} \lesssim$ 2 cm. Thus it is possible that the dimming of the emission in front of the source tube output around $t = 150$ μs was due to the increasing quantity of plasma near the front of

the tube, which prevented most of the primary electrons accelerated at the antenna from making it out of the tube before losing their energy through collisions[2].

Another possibility is that the importance of capacitive coupling in the RF plasma source operation diminished after $t \approx 100$ μs, and at later times there were no large electrostatic potentials in the antenna region to accelerate primary electrons to high energies. Evidence supporting this hypothesis is shown in Fig. 4.7. When the jet experiment's inner electrode and the attached conductors (including the quick-disconnect piece holding the quartz tube—see Fig. 2.2) were left electrically floating[3], they would charge up to $\sim$ 75 V and then discharge during the first $\sim$ 100 μs of the RF pulse. This rise and fall of the floating potential indicates that some plasma with a high plasma potential was contacting these conductors during the early part of the discharge, and then the plasma potential fell at later times. This likely happened because of stray capacitive coupling between the antenna and plasma [5, p. 464], which existed even though the source was operating primarily in an ICP mode after $t \approx 20$ μs. For some reason the capacitive coupling may have become less important at $t > 100$ μs, leading to a decrease in the number of electrons accelerated to $E \geq 10$ eV, and consequently to a drop in the visible light emission in the chamber.

Returning to our discussion of the $t = 200$–400 μs interval in Figs. 4.1, 4.2, 4.3, and 4.4: emission line intensities measured with the spectrometer provide some clues regarding how to reconcile the images with the probe $I_{sat.}$ measurements. The spectroscopic data was taken with the optical fiber viewing the MHD-driven jet experiment electrodes at a roughly 45 degree angle through a window at the midplane of the vacuum chamber, with a collimating lens used to restrict the line of sight to a narrow column. Initially, the lens was aligned so that the line of sight intersected the chamber axis at $z \approx 5$ cm; however, the signals with this setup were too weak to reliably calculate line intensity ratios, so the

[2]Note that although the mean free path for 90 degree scattering of a 10 eV electron by collisions with neutrals at $p = 460$ mTorr ($n_g = 1.5 \times 10^{22}$ m^{-3}) is $\lambda_{en} \approx 7 \times 10^{-4}$ m (using $\sigma_{en} \approx 1 \times 10^{-19}$ m^2 from [5, Figure 3.13]), the time for the electron to lose most of its energy in these collisions is slower than the 90 degree scattering time by roughly a factor $m_i/4m_e \approx 2 \times 10^4$ [4, p.18], so if magnetic confinement keeps it from being lost to the walls, the electron will still have most of its energy when it emerges from the tube after a number of collisions with neutrals, enabling the bright emission seen in the first 100 μs of the discharge in Figs. 4.1 and 4.2.

[3]Conversely, during most other experiments in which only the RF plasma was being studied and the main bank was not fired, the inner electrode was explicitly grounded by attaching a copper short between one of the cable attachments on the re-entrant port and the vacuum chamber (see Fig. 1.8), in order to have a fixed potential reference contacting the plasma for Langmuir probe measurements. Whether or not the inner electrode was grounded had a negligible effect on the time evolution of the RF plasma emission as monitored by camera images.

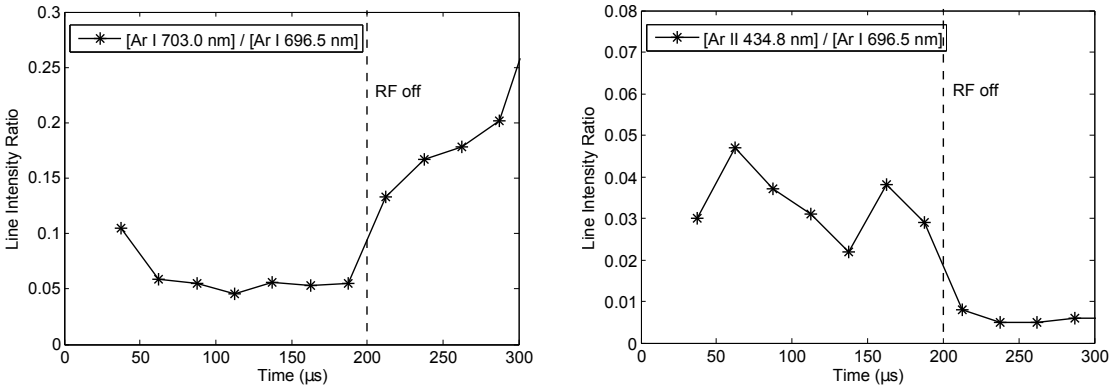

Figure 4.8: Argon emission line intensity ratios measured near the front of the RF source tube ($z \approx -1$ cm) with the bias and solenoid fields on and the RF amplifier pulsed for 200 μs. The data was averaged over 20 shots for each line and binned in 25 μs intervals.

alignment was adjusted so that the line of sight just barely grazed the near side of the 1" diameter source tube output hole and intersected the $r = 0$ axis at $z \approx -1$ cm. With this setup, the spectrometer may have collected some light that was emitted deeper in the source tube and reflected off of the quick-disconnect piece.

As in Sec. 3.4.2, the Ar I 696.5 nm, Ar I 703.0 nm, and Ar II 434.8 nm lines were observed. The measured line intensity ratios for experiments with the magnetic fields turned on and the RF amplifier pulsed for 200 μs (corresponding to Fig. 4.1) are shown in Fig. 4.8. In Secs. 3.1.2 and 3.4.2, we saw that the [Ar I 703.0 nm] / [Ar I 696.5 nm] line ratio was an increasing function of electron temperature, while the [Ar II 434.8 nm] / [Ar I 696.5 nm] was proportional to the plasma density, but also depended on T_e. In the right panel of Fig. 4.8, the [Ar II 434.8 nm] / [Ar I 696.5 nm] ratio is roughly constant in time while the RF power is on, then drops rapidly after RF turn-off, consistent with the expectation that the temperature and density should fall after the power source is removed. Analysis of the time-dependent particle and energy balance equations (see Sec. 4.4.2 and in particular Fig. 4.22) shows that T_e falls much faster than n_e after RF turn-off, so the rapid decrease in the [Ar II 434.8 nm] / [Ar I 696.5 nm] ratio at $t = 200$ μs was probably due mostly to the temperature drop.

In light of the expected temperature decrease after RF turn-off, the sudden *increase* in the [Ar I 703.0 nm] / [Ar I 696.5 nm] ratio at $t = 200$ μs visible in the left panel of Fig.

4.8 seems surprising[4]. However, the experimental results can be understood by recalling the distinction between "ionizing phase" and "recombining phase" plasmas [75] discussed in Sec. 3.1.2. When the RF power was turned on, the plasma inside the antenna was in the ionizing phase, which in this context means that the second term in Eq. 3.1 was of dominant importance in determining the atomic energy level population densities, and does not necessarily imply that the ionization balance was changing in time. On the other hand, after RF turn-off the plasma may be categorized as an "afterglow", expected to be in the recombining phase [104], which means that the first term in Eq. 3.1 was dominant. In general, at a given electron temperature, the population density of high energy levels is much higher in recombining phase plasmas than in ionizing phase plasmas; in particular, above certain density and temperature thresholds, the population density of a level with effective principle quantum number p scales as $n(p)/g(p) \propto p^{-6}$ for an ionizing phase plasma but as $n(p)/g(p) \propto e^{-E(p)/k_B T_e}$ (Boltzmann distribution) for a recombining phase plasma [105], where $g(p)$ is the statistical weight. Thus one cannot compare line ratios measured in the two different phases and draw conclusions about the relative values of T_e—the dominant physical processes populating the energy levels are very different in the two cases, and thus different scalings with temperature apply. Because of the enhanced atomic upper level populations in the recombining phase, some emission lines will be brighter in the afterglow than during the main discharge [105, 106, 107], and if the gas pressure is high enough, the overall visible and infrared light emission after power turn-off may even exceed the main discharge brightness, as we will see in Sec. 5.1.

The rise in optical emission during the afterglow phase explains why the expanding cone of plasma in the magnetized RF discharges was visible in camera images during the 200–400 μs interval when the RF power was turned off at $t = 200$ μs (Fig. 4.1), but not when it was left on until $t = 400$ μs (Fig. 4.2), even though the ion saturation current measured by the Langmuir probe (Fig. 4.4) was similar in both cases. Spectroscopy is also helpful for understanding the differences between Figs. 4.2 and 4.3. In Fig. 4.9, the [Ar I 703.0 nm] / [Ar I 696.5 nm] ratio is shown during discharges with a 500 μs RF pulse for

[4]To confirm the validity of this result, several other line intensity ratios were measured. The Ar I 703.0 nm line is produced by an electron transition from the $6s$ to $4p$ level; to rule out some anomaly in the population of the $6s$ state, three lines with $4d$ upper levels (Ar I 675.3 nm, Ar I 687.1 nm, and Ar I 735.3 nm) were observed, and their intensities were compared to those of two other lines (Ar I 738.4 nm and Ar I 763.5 nm) that have $4p$ upper levels like the Ar I 696.5 nm line. For each ratio a similar phenomenon was observed in which the relative intensity of the line with the higher upper level energy increased after RF turn-off.

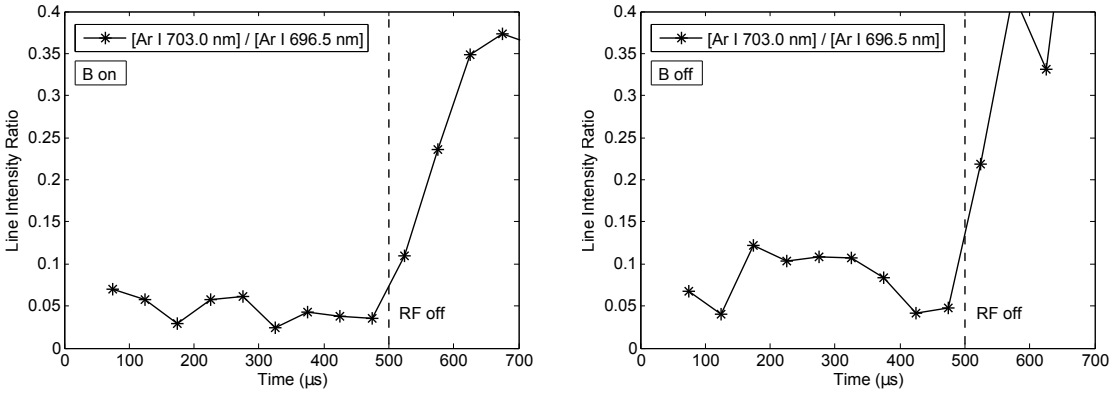

Figure 4.9: [Ar I 703.0 nm] / [Ar I 696.5 nm] line intensity ratio measured near the front of the RF source tube ($z \approx -1$ cm) with the RF amplifier pulsed for 500 μs and the bias and solenoid magnetic fields either on (left) or off (right).

cases with the magnetic field on or off. During the 200–400 μs interval, the line ratio was twice as high for the discharge with $B = 0$ (right panel) than for the discharge with finite B (left panel). This result could explain why the expanding plasma, known to be present in all cases from the probe data in Fig. 4.4, could be seen in camera images of discharges with a long RF pulse and no magnetic field (Fig. 4.3), but not in discharges with finite B (Fig. 4.2). We hypothesize that in the case with $B = 0$, the cloud of plasma in the chamber was effectively somewhat disconnected from the power source because hot electrons coming from the antenna region were not well confined and most were lost to the walls of the tube. Thus this plasma was closer to being in the recombining phase than the plasma expanding along a confining field, and as a result it radiated more visible light. An alternate explanation is that both plasmas were still in the ionizing phase, but the electron temperature was higher in the case with no magnetic field (as predicted by Fig. 3.12), and this led to the enhanced upper level populations and the observed high level of optical emission.

The preceding discussion highlights ways in which camera images of low temperature, weakly ionized plasmas can be deceptive, in the sense that the visible brightness is not necessarily proportional to the plasma density. This is also true, incidentally, for high temperature fusion plasmas and for the solar corona, but for a different reason: these plasmas have such high T_e that the atoms are either fully ionized (for hydrogen isotopes) or exist in high ionization stages that mostly emit line radiation in the UV and x-ray portions of the spectrum (for other ion species). As discussed in Sec. 1.3, the study of protostellar

(YSO) jets is complicated by the fact that regions of the jet that have been heated by shocks tend to radiate much more than cooler regions, so our telescope images, whether taken in the optical portion of the spectrum or in some other bandpasses, may not be indicative of the true jet structure [21]. A major advantage for laboratory plasma experiments over astrophysical observations, then, is that when faced with potentially misleading images or spectroscopic data, the laboratory experimentalist can turn to other diagnostics such as Langmuir probes and magnetic probes to clarify the situation. Astrophysicists, on the other hand, are restricted to only collecting photons, and occasionally high energy particles, and while they have developed many clever ways of teasing complex understanding from limited data, their task is inevitably more challenging.

4.3 Density Profiles in Experiments Using the Fast Gas Valve

A more complete picture of the RF plasma expansion is obtained by considering Langmuir probe measurements taken at several different axial locations. These are shown in Fig. 4.10 for discharges with a 500 μs RF pulse. Several interesting features are apparent in the ion saturation current curves. The peak $I_{sat.}$ near the antenna (which was located at $z \leq -5.9$ cm) was higher for the case with $B = 0$ (right panel) than for the case with finite B (left panel); this may reflect the relative ion densities in the two cases, or it could be due to the electron temperature being higher in the unmagnetized case, as predicted by Fig. 3.12. Some caution is warranted in interpreting this result and those that follow, given that the gas pressure was a factor of ~ 8 too high for collisionless probe theory to be applicable (see Sec. D.2).

Out in the main chamber at $z \approx 6.5$ cm, the peak $I_{sat.}$ was surprisingly only marginally higher with a confining field than without one, confirming the impression given by the images in Fig. 4.3 that a substantial amount of plasma was able to make it out of the source tube even with $B = 0$ (this was also demonstrated in Fig. 4.4). The relatively sharp bump in the $B = 0$, $z = 6.5$ cm $I_{sat.}$ curve at its peak (around $t = 220$ μs) likely corresponds to the shock-like structure visible at $t = 250$–300 μs in Fig. 4.3. Understanding the cause of this feature, which only appeared when there was no applied magnetic field, will require further study.

There was a surprising degree of time-dependence in $I_{sat.}$ measured near the antenna—

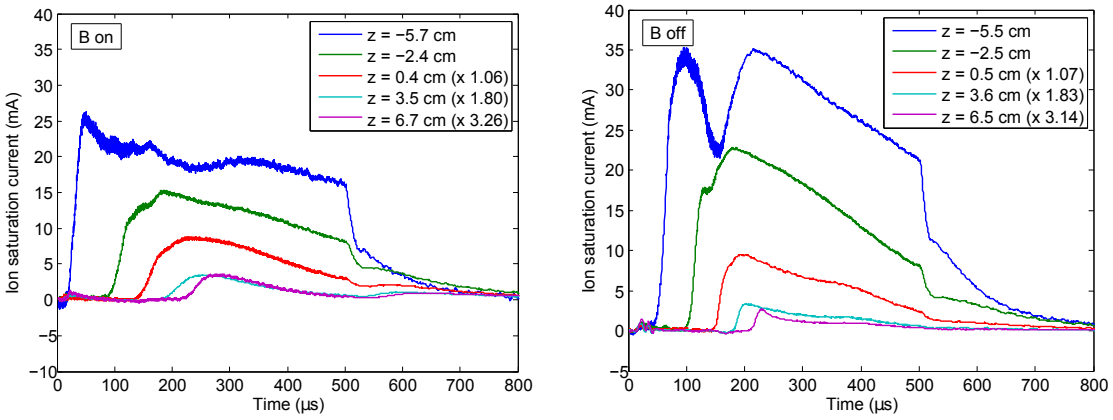

Figure 4.10: Langmuir probe ion saturation current measured at five different locations on axis ($r = 0$) for cases with the bias field coil and solenoid on (left) and off (right). The RF power was on from $t = 0$–500 μs, and the fast gas valve was used with the usual settings ($V_{gas,RF} = 550$ V, $t_{gas,RF} = -6.0$ ms). The $I_{sat.}$ curves for locations beyond the end of the ~ 1.1 cm inner radius discharge tube ($z > 0$ cm) have been multiplied by the ratio of the cross-sectional area of the expanding plasma at the axial location of interest to the cross-sectional area at $z = 0$, in order to facilitate a clear comparison of the amount of plasma present at different axial locations (this rescaling corrects for the $\partial I_{sat.}/\partial z$ due solely to the fact that the plasma was expanding along a diverging field, allowing us to focus on the changes in $I_{sat.}$ due to diffusion and ionization). The cross-sectional area as a function of z was determined for the case with finite B by assuming that the plasma was expanding along the magnetic field lines; the field profile was calculated using an IDL program written by Bao N. Ha. The same scaling function was used for the data taken with no magnetic field, since camera images (Figs. 4.1 and 4.3) indicated that the opening angle of the expanding plasma cone was similar with B on and off.

the dip around $t = 150$ μs in the unmagnetized case is particularly striking. Such features were absent from data taken at lower gas pressures. Note that the power output by the RF amplifier was gradually decreasing during the 500 μs interval shown (see Fig. 3.13). Upon RF turn-off at $t = 500$ μs, $I_{sat.}$ near the antenna dropped dramatically; as discussed in Sec. 4.2, this feature was probably primarily due to the rapid decrease of T_e in the afterglow.

If we interpret the intervals between the times that $I_{sat.}$ first began to rise at each successive probe location to be indicative of the expanding plasma's velocity, then both panels of Fig. 4.10 imply that the plasma was accelerating as it moved away from the antenna. This result is inconsistent with the simple model of expansion at the ion acoustic speed described in the chapter introduction (presumably T_e did not increase moving away from the power source), but it is consistent with diffusive transport in a neutral gas background if $\partial n_g/\partial z < 0$ (the ambipolar diffusion coefficient is inversely proportional to n_g—see Eq.

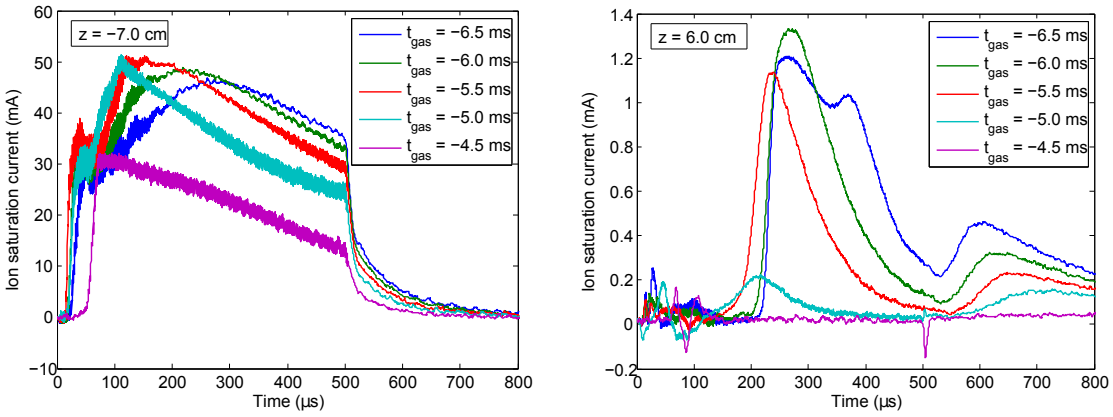

Figure 4.11: Langmuir probe ion saturation current measured at $z = -7.0$ cm (left) and at $z = 6.0$ cm (right) during experiments with the fast gas valve triggered at five different times. The bias field coil and solenoid were turned on, and the RF power was on from $t = 0$–500 μs. The rise in $I_{sat.}$ after RF turn-off at $z = 6.0$ cm is noteworthy; this behavior will be analyzed in detail in Sec. 5.2.

4.12), which was expected to be the case when the fast gas valve was used.

The diffusive nature of the RF plasma expansion will be further established in Sec. 4.4. A key feature was the importance of continuous ionization in the downstream region. In Fig. 4.11, $I_{sat.}$ measurements at $z = -7.0$ cm (well inside the RF antenna) and at $z = 6.0$ cm are shown for experiments with fast gas valve trigger times ranging from $t_{gas,RF} = -6.5$ ms to $t_{gas,RF} = -4.5$ ms. For large $|t_{gas,RF}|$, the gas had time to fill the entire discharge tube and the region in front of the jet experiment electrodes before the RF discharge was initiated, while with small $|t_{gas,RF}|$ the gas had only barely reached the antenna region at $t = 0$, and the plasma expanded into a low density gas background (the spatial extent of the neutral gas cloud, which glowed at early times in the discharge, is visible in the images in Fig. 4.5). The left panel of Fig. 4.11 shows that a high density plasma would form inside the antenna with any of the five gas timings tested. However, the peak density in front of the electrodes at $z = 6.0$ cm (right panel) was low for $t_{gas,RF} = -5.0$ ms, and negligible for $t_{gas,RF} = -4.5$ ms. This shows that despite the radial confinement provided by the magnetic field, axial transport of plasma created inside the antenna was insufficient to achieve a reasonable density in front of the electrodes; there also had to be ionization of pre-existing neutral gas in the expansion path to replenish the plasma against losses to the walls of the discharge tube.

4.4 RF Plasma Transport Models

The RF plasma transport can be analyzed using the two-fluid model described in Sec. 1.1.2. Some simplifications will be necessary, however, in order to make the problem tractable. We will focus on unmagnetized discharges and seek to develop a model valid in the pressure range $p_{Ar} \sim 30$–300 mTorr. Although the pressure in the discharge tube was higher than this during some experiments using the fast gas valve (for example, we estimated $p_{Ar} \approx 460$ mTorr for $V_{gas,RF} = 550$ V and $t_{gas,RF} = -6.0$ ms), the lower pressure regime is more straightforward to model using the framework described here. In order to determine which terms in the two-fluid equations may be safely neglected, we will estimate the magnitude of each term by assuming that the characteristic length scale for the problem is $l_{char.} = 5$ cm, the characteristic timescale is $t_{char.} = 20$ μs (so $f_{char.} = 50$ kHz and $\omega_{char.} \approx 3 \times 10^5$ rad./s), the characteristic temperatures are $T_{e,char.} = 2$ eV and $T_{i,char.} = 0.05$ eV, and the pressure is $p_{Ar} = 100$ mTorr (so the argon density is $n_{total} = 3.33 \times 10^{21}$ m^{-3}).

We will first present a simple analytical diffusion model that gives some insight into the qualitative features of the plasma expansion. In the following section, a more complex numerical model will be developed, yielding excellent quantitative agreement with the experimental data over a limited range of gas pressures.

4.4.1 Isothermal Diffusion Solution

As in Sec. 3.3, assume electron-impact ionization dominates over all other ionization and recombination processes. Thus the ion continuity equation (Eq. 1.6) becomes

$$\frac{\partial n_i}{\partial t} + \nabla \cdot (n_i \mathbf{u}_i) = \nu_{iz} n_e. \tag{4.5}$$

The ratio of the inertial term to the collisional drag term in the two-fluid momentum equation (Eq. 1.7) is

$$\frac{\left| n_\sigma m_\sigma \left(\frac{\partial}{\partial t} + \mathbf{u}_\sigma \cdot \nabla \right) \mathbf{u}_\sigma \right|}{\left| \nu_{\sigma n} m_\sigma n_\sigma \mathbf{u}_\sigma \right|} \sim \frac{\omega_{char.}}{\nu_{\sigma n}} = \frac{\omega_{char.}}{n_g \sigma_{\sigma n} v_{T\sigma}}, \tag{4.6}$$

where the collisions were assumed to occur with low-velocity neutral atoms (as in Sec. 3.3, electron-ion collisions are unimportant because the two charged species move together with the same mean fluid velocity $\mathbf{u}_e = \mathbf{u}_i \equiv \mathbf{u}$). Using the characteristic parameters defined

above, along with $\sigma_{en} = 5 \times 10^{-20}$ m^2 and $\sigma_{in} = 5 \times 10^{-19}$ m^2 [5, Figures 3.13 and 3.15], we find $\omega_{char.}/\nu_{en} \approx 2 \times 10^{-3}$ and $\omega_{char.}/\nu_{in} \approx 0.37$. Thus the inertial term in the electron momentum equation is negligible and can be dropped. Following the standard approach for deriving "ambipolar diffusion" [5, Section 5.1], we will also neglect the inertial term in the ion momentum equation, even though its magnitude is within a factor of 3 of the magnitude of the collisional term for the assumed discharge parameters. This approximation will limit the ability of the model to capture high-frequency phenomena. With the magnetic force term also neglected, the momentum equation is reduced to the form given in Eq. 3.9. Solving for the electric field:

$$\mathbf{E} = -\frac{\nabla P_e}{ne} - \frac{m_e \nu_{en}}{e}\mathbf{u} = \frac{\nabla P_i}{ne} + \frac{m_i \nu_{in}}{e}\mathbf{u}, \tag{4.7}$$

where $n_e = n_i \equiv n$ was used.

The ion momentum equation can also be solved for the ion flux:

$$\mathbf{\Gamma}_i \equiv n\mathbf{u} = \frac{ne\mathbf{E} - \nabla P_i}{m_i \nu_{in}} = -\left(\frac{\nabla P_e + m_e \nu_{en} n\mathbf{u} + \nabla P_i}{m_i \nu_{in}}\right). \tag{4.8}$$

$P_e/P_i = T_e/T_i \gg 1$ and $m_e\nu_{en}/m_i\nu_{in} \ll 1$, so this reduces to

$$\mathbf{\Gamma}_i \approx -\frac{\nabla P_e}{m_i \nu_{in}}. \tag{4.9}$$

Plugging into Eq. 4.5, we have

$$\frac{\partial n}{\partial t} - \frac{1}{m_i \nu_{in}} \nabla^2 P_e = \nu_{iz} n. \tag{4.10}$$

If the electrons are isothermal, then we can pull $k_B T_e$ out of the Laplacian to get the usual form of the ambipolar diffusion equation:

$$\frac{\partial n}{\partial t} - D_a \nabla^2 n = \nu_{iz} n, \tag{4.11}$$

where the ambipolar diffusion coefficient is

$$D_a \approx \frac{kT_e}{m_i \nu_{in}} \approx \frac{T_e}{2T_i} \lambda_{in}^2 \nu_{in}. \tag{4.12}$$

This has the standard form of $D \sim (\text{step size})^2 / (\text{time step})$ for a random walk process,

modified by the temperature ratio.

This derivation assumed that ν_{in} was a constant equal to $n_g \sigma_{in} v_{Ti}$ (or equivalently, v_{Ti}/λ_{in}), which is only true when the ions are isothermal and $v_{Ti} \gg |\mathbf{u}|$. Within the context of this model we have, from Eq. 4.9,

$$|\mathbf{u}| \approx \frac{|\nabla P_e|}{n m_i \nu_{in}} \sim \frac{kT_e}{l_{char.} m_i n_g \sigma_{in} v_{Ti}} = \frac{1}{2}\frac{T_e}{T_i}\frac{\lambda_{in}}{l_{char.}} v_{Ti}. \tag{4.13}$$

Therefore, the condition $|\mathbf{u}| \ll v_{Ti}$ is only satisfied when $\lambda_{in}/l_{char.} \lesssim T_i/T_e$. For longer ion-neutral mean free paths (i.e., at lower gas pressure), the ion momentum equation is nonlinear in $|\mathbf{u}|$, and the plasma density can be approximated as constant across most of the discharge volume with a rapid drop at the sheath boundaries [5, Section 5.3], as in Sec. 3.3. In our RF discharge, the characteristic length in the radial direction ($l_{char.} \sim R$) is much shorter than the characteristic length in the axial direction ($l_{char.} \sim L$). As a result, at pressures between 30 and 300 mTorr, the uniform density approximation applies in the radial direction, while the linear diffusion equation (Eq. 4.10 or 4.11) is valid in the axial direction.

To derive an analytical solution describing the plasma expansion, we will approximate the electrons as isothermal and treat the axial transport as a one-dimensional problem. Although we found in Sec. 3.3 that the ionization frequency depended on the excited state populations (see Eq. 3.12) and was thus a function of both T_e and n, here we will assume that ν_{iz} depends on T_e alone, so that Eq. 4.11 is linear in n. In light of these approximations, quantitative agreement with the experimental data is not expected, but some useful qualitative insights may be gained.

In order to convert the problem to 1D, we replace $\nabla^2 n$ by $\partial^2 n/\partial z^2$ in Eq. 4.11. We will account for the radial loss rate of plasma to the walls by adding an extra sink term on the right-hand side of the equation. The flux into the radial sheath at an axial location z is $\Gamma_i(z) = n_{sR}(z)\, c_s = h_R n(z)\, c_s$, where $n(z)$ is the density on axis and the radial sheath edge density $n_{sR}(z)$ is given by Eq. 3.10[5]. Since the total rate of radial losses over a length dz of the tube is $\Gamma_i(z)\,(2\pi R dz)$, the loss rate per unit volume is $\Gamma_i(z)\,(2\pi R dz)\,/\,\left(\pi R^2 dz\right) =$

[5]Eq. 3.10 was derived by solving a steady-state diffusion equation [5, Section 5.3]; however, it has been used by other authors in time-dependent problems [83]. In our case, since $L \gg R$, it is reasonable to assume that radial equilibrium is reached quickly in comparison to the axial diffusion timescale, so using steady-state radial density profile solutions is reasonable.

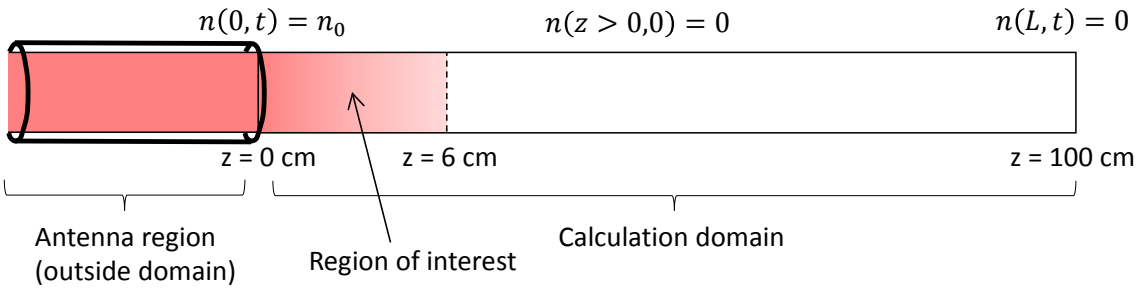

Figure 4.12: Illustration of the domain, boundary conditions, and initial condition for the analytical 1D isothermal diffusion calculation. In this figure and in Eq. 4.16, the edge of the RF antenna is defined as $z = 0$ cm, whereas elsewhere in this thesis $z = 0$ usually refers to the plane of the jet experiment electrodes (the electrodes are located at $z \approx 6$ cm here).

$2\Gamma_i(z)/R = 2h_R c_s n(z)/R$. Thus the ambipolar diffusion equation becomes

$$\frac{\partial n}{\partial t} - D_a \frac{\partial^2 n}{\partial z^2} = \left(\nu_{iz} - \frac{2h_R c_s}{R}\right) n = \nu_{i-l} n, \tag{4.14}$$

where we define the "effective frequency for ionization minus losses" by

$$\nu_{i-l} \equiv \nu_{iz} - \frac{2h_R c_s}{R}. \tag{4.15}$$

Since the ionization rate is an exponentially increasing function of temperature (see Table 3.1), ν_{i-l} will be negative at low T_e and positive at high T_e.

We will use the plasma density at the antenna edge as a boundary condition, taken to be constant in time for this approximate calculation, and solve Eq. 4.14 for $n(z,t)$ in the downstream region of the discharge tube. The calculation domain and boundary conditions are illustrated in Fig. 4.12. The tube is assumed to extend axially for a long distance (the main chamber region beyond the tube, where the plasma can expand radially, is not considered), and the density falls to 0 at the end of the tube (at $z = L$, where L was chosen to be 1 meter). Varying L does not affect the solution much as long as $z \ll L$ and $t \ll L^2/D_a$ for the region of interest. Adopting the initial condition $n(z > 0, t = 0) = 0$ (plasma forms only inside the antenna at first and then diffuses down the tube), a solution

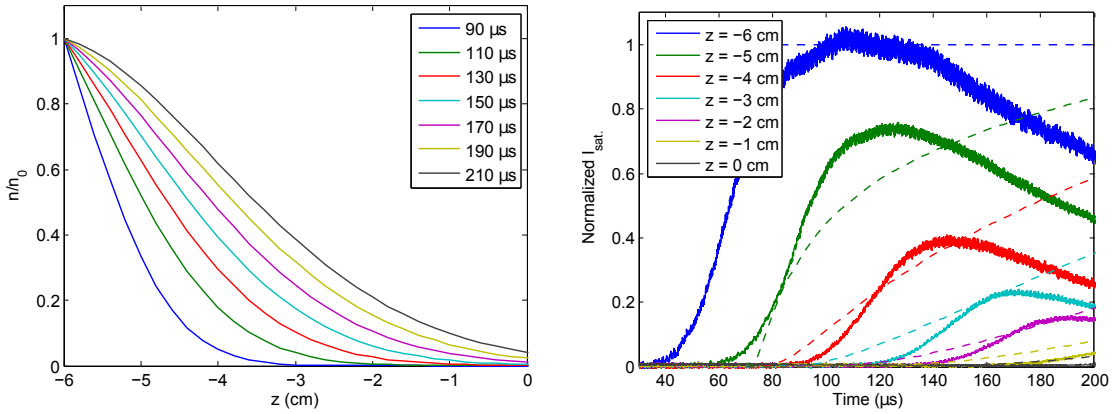

Figure 4.13: Plots of the analytical diffusion solution (Eq. 4.16) with $D_a = 2.5$ m^2/s and $\nu_{i-l} = 5 \times 10^3$ s^{-1}. Left: Calculated density profiles as a function of z at seven different times. The times have been shifted by 70 μs and the locations have been shifted by -6 cm relative to the (z,t) used in Eq. 4.16 in order to make comparisons with the Langmuir probe data. Right: Calculated density profiles as a function of time (dotted lines), superimposed on the $I_{sat.}$ data (solid lines) for unmagnetized discharges with $p_{Ar} = 240$ mTorr. The edge of the antenna was at $z = -5.9$ cm in the experiments.

of Eq. 4.14 is

$$n(z,t) = n_0\left(1-\frac{z}{L}\right) + 2n_0\sum_{m=1}^{\infty}\left(\frac{\nu_{i-l}}{(m\pi)\left(D_a\left(\frac{m\pi}{L}\right)^2-\nu_{i-l}\right)} - \frac{e^{\left(\nu_{i-l}-D_a\left(\frac{m\pi}{L}\right)^2\right)t}}{\left(m\pi-\frac{\nu_{i-l}L^2}{D_a m\pi}\right)}\right)\sin\left(\frac{m\pi z}{L}\right). \quad (4.16)$$

The derivation of this result is given in Appendix F.

In order to facilitate straightforward comparisons between the experiments and the models described here and in the following section, $I_{sat.}(z,t)$ was measured with the Langmuir probe during discharges with a uniform gas pressure in the chamber supplied by a leak valve. The additional complexity introduced by our ignorance of the detailed spatial pressure profile produced by the fast gas valve was thereby avoided. We will compare the predictions of Eq. 4.16 with data taken at $p_{Ar} = 240$ mTorr. From Eq. 4.12, with $T_e = 2$ eV and $T_i = 0.05$ eV we have $D_a \approx 2.5$ m^2/s. In Fig. 4.13, the analytical solution for $n(z,t)$ is plotted for a case with the ionization rate exceeding the radial loss rate ($\nu_{i-l} = 5 \times 10^3$ s^{-1} was assumed). In the right panel, the model predictions are overlaid on probe data taken at 1 cm intervals along the tube axis during a set of unmagnetized discharges. The model does a reasonable job of reproducing the initial density rise at each location, although the

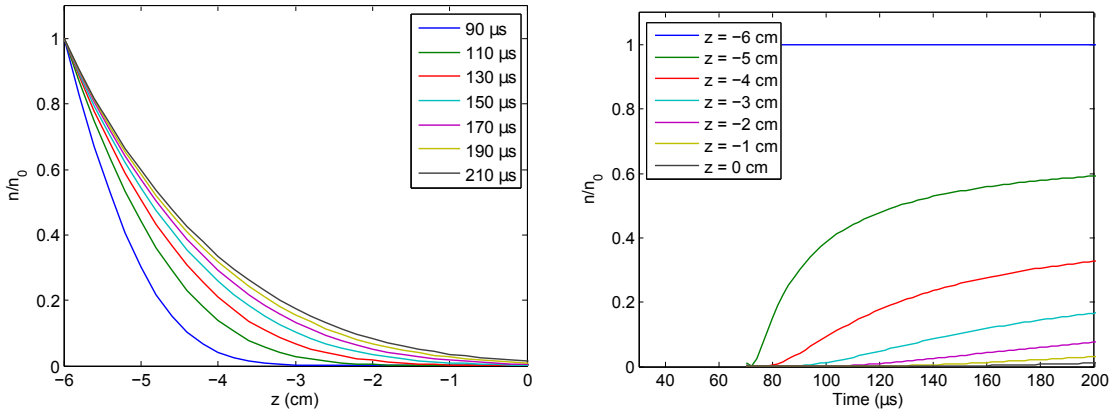

Figure 4.14: Plots of the analytical diffusion solution (Eq. 4.16) with $D_a = 2.5$ m^2/s and $\nu_{i-l} = -5 \times 10^3$ s^{-1}. Left: Calculated density profiles as a function of z at seven different times. Right: Calculated density profiles as a function of time at seven axial positions. As in Fig. 4.13, the times have been shifted by 70 μs and the locations have been shifted by -6 cm relative to the (z, t) used in Eq. 4.16.

detailed time dependence of the solution differs from the data. However, the measured $I_{sat.}(t)$ at each location stops rising after $\sim$ 50 μs, while the model $n(t)$ curves increase indefinitely.

On the other hand, if ν_{i-l} is chosen to be negative (see Fig. 4.14), then $n(t)$ at each location asymptotes to a constant value, as the density in the experiment would if the RF power input were constant (the temporal decrease of P_{RF} was not taken into account in the model). However, the rate of the density rise at each location is too slow to match the data (this was true to some extent in Fig. 4.13 as well). We can make $\partial n/\partial t$ larger by choosing ν_{i-l} to be large and positive, as shown in Fig. 4.15, but the downstream density soon exceeds the density at the antenna edge. Examining Eq. 4.16, we see that the fundamental ($m = 1$) mode of the analytical diffusion solution will grow without bound whenever $\nu_{i-l} > D_a \pi^2 / L^2$. This behavior cannot occur in reality because each ionization of a neutral atom removes energy from the electron fluid, so T_e (and consequently ν_{i-l}) must decrease as n rises until the ionization rate no longer exceeds the loss rate. Clearly, the isothermal approximation must be abandoned in order to derive a more accurate model of the RF plasma transport.

Nevertheless, the qualitative trend visible in Fig. 4.15 is useful for understanding the plasma expansion data shown in Fig. 4.10[6]. Comparing the two panels of Fig. 4.10, it is

[6]As discussed in the paragraph following Eq. 4.13, the model is not strictly applicable at the high gas pressure used in Fig. 4.10 because the approximation of a flat radial density profile breaks down; however, the simple qualitative comparison of ν_{i-l} values discussed here should still be valid.

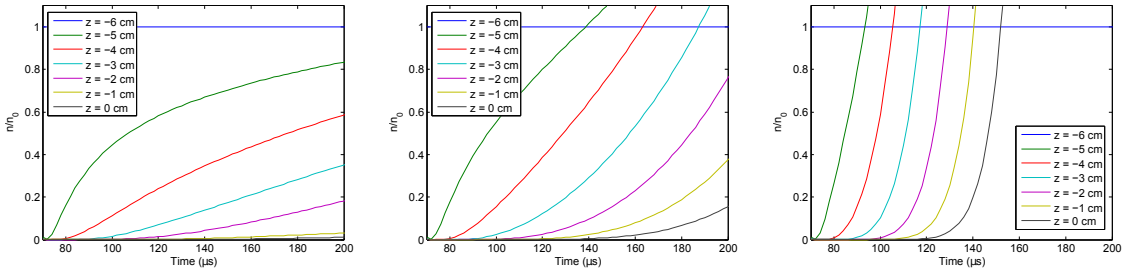

Figure 4.15: Plots of density vs. time from Eq. 4.16 with $D_a = 2.5$ m^2/s and $\nu_{i-l} = 5 \times 10^3$ s^{-1} (left), $\nu_{i-l} = 2 \times 10^4$ s^{-1} (center), and $\nu_{i-l} = 8 \times 10^4$ s^{-1} (right). As in Fig. 4.13, the times have been shifted by 70 μs and the locations have been shifted by -6 cm relative to the (z, t) used in Eq. 4.16.

apparent that $I_{sat.}$ rises more suddenly (greater $\partial I_{sat.}/\partial t$) at each location in the case with $B = 0$ (right panel) than in the case with finite B (left panel). This probably implies that ν_{i-l} was higher in the unmagnetized case. Although the loss rate, proportional to h_R, should have been higher with no confining field, we also expect that T_e was higher with $B = 0$ because of the need to balance ionization and losses inside the antenna (see Fig. 3.12), so this conclusion is plausible. The analytical model shows how the RF plasma expansion involved both ambipolar diffusion and the propagation of an ionization front; together these effects enabled a relatively high plasma density ($n \geq 10^{18}$ m^{-3} at $z = 6$ cm) to be achieved out in the main vacuum chamber even with no magnetic confinement.

4.4.2 1D Time-Dependent Numerical Discharge Model

4.4.2.1 Model Derivation

In this section, we will construct a 1D time-dependent numerical model of the unmagnetized ICP discharge, building upon the isothermal diffusion calculation from the previous section and the steady state global model that was used to predict the plasma properties inside the antenna in Sec. 3.3. The Ar I energy level structure shown in Fig. 3.8 and the rate coefficients for electron-impact transitions giving in Table 3.1 will again be used. The simulation domain and boundary conditions are illustrated in Fig. 4.16. As in the analytical model, we consider a long discharge tube with uniform radius R; the antenna region is now included at the center of the domain, and the plasma density falls to 0 far from the antenna[7]. We assume

[7]In practice, a low, non-zero value was used for the boundary density $n_e(0, t) = n_e(L, t)$ in order to maintain numerical stability.

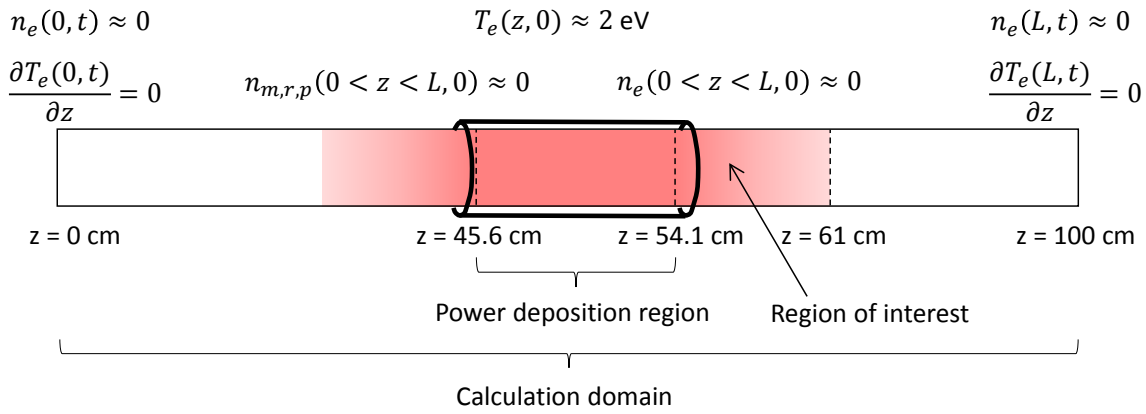

Figure 4.16: Illustration of the simulation domain, boundary conditions, and initial condition for the numerical 1D time-dependent discharge model. The jet experiment electrodes were located at $z = 61$ cm in the simulation—this location is re-defined to be $z = 0$ cm in the following figures showing the calculation results for consistency with the convention used throughout this thesis.

that RF power is deposited uniformly within a region inside the antenna, with no power absorbed elsewhere. The model has two free parameters: the total power absorbed by the plasma (which cannot exceed the measured power output by the RF amplifier), and the ion temperature, which is assumed to be spatially uniform and equal to the neutral gas temperature. All other variables are solved for in a self-consistent manner.

Rewriting the overall ionization rate ν_{iz} in terms of the ionization rates out of each individual energy level group, the 1D diffusion equation with non-uniform T_e becomes

$$\frac{\partial n_i}{\partial t} - \frac{1}{m_i \nu_{in}} \frac{\partial^2 P_e}{\partial z^2} = \left(K_{gi} n_g + K_{mi} n_m + K_{ri} n_r + K_{pi} n_p - \frac{2 h_R c_s}{R} \right) n_e \tag{4.17}$$

(see Eqs. 4.10 and 4.14, and also Eq. 3.12). The electron pressure $P_e = n_e k_B T_e$ evolves according to the electron energy equation (Eq. 1.8):

$$\frac{\partial}{\partial t}\left(\frac{3}{2} P_e\right) + \nabla \cdot \left(\frac{3}{2} P_e \mathbf{u}\right) + P_e \nabla \cdot \mathbf{u} = p_{RF} - \nabla \cdot \mathbf{q}_e + m_e n_e \nu_{en} u^2 - \left(\frac{\partial W}{\partial t}\right)_{Een}, \tag{4.18}$$

where p_{RF} is the RF power input per unit volume. As discussed in Sec. 1.1.2, in order to use this equation we need an approximate expression for the microscopic heat flux $\mathbf{q}_e$. For a collisional plasma with $\lambda_{ee} \ll l_{char.}$, the Braginskii closure for the two-fluid equations [108]

may be used. In cgs units, the heat flux [79] is then given by

$$\mathbf{q}_e = -\kappa_\parallel \nabla \left(k_B T_e\right) \quad ; \quad \kappa_\parallel = 3.2 \frac{n_e k_B T_e}{m_e} \tau_e \quad ; \quad \tau_e = 1.7 \times 10^{23} \frac{\left(k_B T_e\right)^{3/2}}{n_e \ln \Lambda}. \tag{4.19}$$

Combining these expressions, plugging in the constants, and converting to S.I. units, with T_e in eV and the Coulomb logarithm assumed to be $\ln \Lambda \approx 10$, the expression for the heat flux is

$$\mathbf{q}_e \approx -C_q \nabla \left(T_{eV}^{7/2}\right) \quad ; \quad C_q \equiv 900 \text{ kg m s}^{-3} \text{ eV}^{-3.5}. \tag{4.20}$$

Following the same line of reasoning used to derive Eq. 4.14, we will convert the energy equation to 1D by rewriting the radial energy transport terms in terms of an effective energy sink term. The rate of radial energy loss is equal to the loss rate of charged particles times the energy carried to the walls by each electron-ion pair, equal to $(eV_s + 5k_B T_e/2)$ (see Eq. 3.13). Since the discharge was found to be inductively coupled in Sec. 3.3, a low-voltage sheath with $eV_s = 4.7 k_B T_e$ is assumed. Defining the loss frequency $\nu_{loss} \equiv 2h_R c_s / R$ (see Eq. 4.15), the energy loss rate per unit volume is

$$\left(\text{Radial Energy Losses}\right) = n_e \nu_{loss} \left(eV_s + \frac{5}{2} k_B T_e\right). \tag{4.21}$$

The 1D version of Eq. 4.18 is then

$$\frac{3}{2}\frac{\partial P_e}{\partial t} + \frac{3}{2}\frac{\partial}{\partial z}\left(P_e u_z\right) + P_e \frac{\partial u_z}{\partial z} = p_{RF} - \frac{\partial q_{ez}}{\partial z} + m_e n_e \nu_{en} u^2 - \left(\frac{\partial W}{\partial t}\right)_{Een} - n_e \nu_{loss} \left(eV_s + \frac{5}{2} k_B T_e\right). \tag{4.22}$$

Assuming the same characteristic parameters as in the previous section, we will estimate the magnitude of each term in this equation. From Eq. 4.13, the characteristic fluid velocity in the axial direction is $u_{z,char.} \approx 120$ m/s. Typical radial diffusion velocities will be faster than this, on the order of the ion thermal velocity $v_{Ti} \approx 500$ m/s. Since the frictional heating term involves energy transfer from the neutrals to the electrons, which is not captured in the radial loss term, we should evaluate this term using the larger flow velocity u_r:

$$m_e n_e \nu_{en} u^2 \approx m_e n_e \nu_{en} u_r^2 \sim 2 \times 10^3 \text{ W/m}^3, \tag{4.23}$$

where $n_e \sim 5 \times 10^{19}$ m^{-3} was taken as a typical density value. On the other hand, the magnitude of the axial heat flux term is

$$-\frac{\partial q_{ez}}{\partial z} = C_q \frac{\partial^2}{\partial z^2}\left(T_{eV}^{7/2}\right) \sim \frac{C_q T_{eV}^{7/2}}{l_{char.}^2} \sim 4 \times 10^6 \text{ W/m}^3, \tag{4.24}$$

so the frictional heating term is negligible by comparison. The ratio of the sum of the spatial derivative terms on the left-hand side of Eq. 4.22 to the time derivative term is

$$\frac{\frac{3}{2}\frac{\partial}{\partial z}\left(P_e u_z\right) + P_e \frac{\partial u_z}{\partial z}}{\frac{3}{2}\frac{\partial P_e}{\partial t}} \sim \frac{5}{3}\frac{u_{z,char.}}{\omega_{char.} l_{char.}} \sim 10^{-2}, \tag{4.25}$$

so the spatial derivative terms can be neglected. Thus Eq. 4.22 is simplified to

$$\frac{3}{2}\frac{\partial P_e}{\partial t} = p_{RF} + C_q \frac{\partial^2}{\partial z^2}\left(T_{eV}^{7/2}\right) - \left(\frac{\partial W}{\partial t}\right)_{Een} - n_e \nu_{loss}\left(eV_s + \frac{5}{2}k_B T_e\right). \tag{4.26}$$

$(\partial W/\partial t)_{Een}$, the collisional energy transfer from electrons to neutrals, includes the same ionization, excitation/de-excitation, and elastic collision terms listed in Eq. 3.13. Additionally, in order to better fit the data after RF power turn-off, we will include a term for three-body recombination, which becomes important once T_e falls to near room temperature in the afterglow. This process involves an interaction between an ion and two free electrons—one electron recombines with the ion, while the other electron carries away the excess energy that exists in the center of mass frame. We will use the formula for the recombination rate ν_r from Celik et al. [109], which takes into account the effects of both finite electron temperature and the Stark effect in determining the highest atomic energy level into which recombination can occur:

$$\nu_r = \frac{C' E_{gi}^{7/2}}{7\eta^{7/2} k_B^{7/2}} \frac{n_e^2}{T_e^{9/2}} \left(1 + \left(\frac{E_{gi}}{\eta k_B T_e}\right)\left(\frac{n_e}{n_{IT}}\right)^{4/15}\right)^{-7/2}, \tag{4.27}$$

where $C' = 6.74 \times 10^{-38}$ m^6 K s^{-1} and $n_{IT} = 10^{29.19}$ m^{-3}. Recombination occurs most frequently into highly excited states [109, 106]; the excited atoms are subsequently de-excited by collisions with free electrons, until the bound electron reaches a threshold "bottleneck" level below which spontaneous emission takes over as the dominant de-excitation process. The position of the bottleneck is parameterized by the dimensionless parameter η in Eq. 4.27, whose value has been estimated to be between 1 and 4 by different authors [109] (note

that η is not the same as the principle quantum number of the bottleneck level) . We will adopt the value $\eta = 2$ here. Changing η by a factor of 2 alters the recombination rate by an order of magnitude, so the uncertainty in this parameter is potentially a significant source of error in the calculation.

Since the highest energy level in our model is the $4p$ state, we will assume that all recombinations occur into this level, with each recombination transferring an energy $E_{pi} = 1.53$ eV to the free electrons. This would be an excellent approximation of reality if the true bottleneck level were at or below the $4p$ level, since the cascade of collisional de-excitations following recombination would ultimately lead to an equivalent 1.53 eV of energy transfer to the free electrons. However, the bottleneck state is expected to be higher than the $4p$ level[8], so our rough treatment of three-body recombination overestimates the reheating of the electrons. Fortunately, the contribution of recombination to the overall energy balance is small—see Fig. 4.26.

With the collisional energy loss terms written out and recombination included, the electron energy equation takes the form:

$$\frac{3}{2}\frac{\partial P_e}{\partial t} = p_{RF} + \frac{C_q}{k_B^{7/2}}\frac{\partial^2}{\partial z^2}\left(\frac{P_e^{7/2}}{n_e^{7/2}}\right) - n_e\nu_{loss}eV_s - \frac{5}{2}\nu_{loss}P_e + \nu_r n_e E_{pi}$$
$$- n_e\left(K_{gi}n_g E_{gi} + K_{mi}n_m E_{mi} + K_{ri}n_r E_{ri} + K_{pi}n_p E_{pi} + \sum_{\alpha,\beta} K_{\alpha\beta}n_\alpha E_{\alpha\beta} + K_{el.}n_g E_{el.}\right). \tag{4.28}$$

As in Eq. 3.13, the summation over α and β includes collisional transitions between the $4s$ resonant, $4s$ metastable, and $4p$ excited states. In the heat flux term, $k_B = 1.6\times10^{-19}$ J/eV should be used if C_q is evaluated in the units given in Eq. 4.20. With a sink term added for recombination, the ambipolar diffusion equation (Eq. 4.17) is updated to read

$$\frac{\partial n_e}{\partial t} - \frac{1}{m_i\nu_{in}}\frac{\partial^2 P_e}{\partial z^2} = \left(K_{gi}n_g + K_{mi}n_m + K_{ri}n_r + K_{pi}n_p - \nu_r - \frac{2h_R c_s}{R}\right)n_e \tag{4.29}$$

[8]Neglecting re-absorption, which quickly becomes unimportant in the afterglow as n_m and n_r fall, the spontaneous transition rate out of the $4p$ state is $A_{ps} \approx 3\times10^7$ s^{-1} (this can be calculated from Table E.1 by summing all of the transition rates for the individual lines, weighted by the upper level statistical weights), while from Table 3.1, assuming $T_e = 0.1$ eV and $n_e = 5\times10^{19}$ m^{-3} in the afterglow, the rate of collisional de-excitation to the $4s$ levels is $(K_{pr} + K_{mr})\,n_e \sim 5\times10^6$ s^{-1}. Thus spontaneous emission is the dominant de-population mechanism for the $4p$ level, and the "bottleneck" energy level for which the collisional and spontaneous de-excitation rates are equal must be higher than $4p$.

The equations for the evolution of the excited state populations are similar to Eqs. 3.14, 3.15, and 3.14. Axial diffusion of excited neutrals is neglected[9]; however, we will include a term in each equation to account for radial losses of these atoms to the walls. The rate for this process is much lower than the collisional de-excitation rate in the region of interest near the center of the simulation domain (see Fig. 4.16), but it can be important for preventing an unphysically high metastable population density from building up far from the antenna, where n_e is low and thus the metastable state is rarely depopulated by electron impacts. The loss rate [83, 110] can be approximated by

$$\nu_{loss,exc.} \approx \frac{D_{eff.}}{\Lambda^2}, \tag{4.30}$$

where the effective diffusion length is $\Lambda = R/\chi_{01} = R/2.405$ (χ_{01} is the first zero of the Bessel function $J_0(x)$) and we will adopt Lee and Chung's [110] formula for the effective diffusion coefficient:

$$D_{eff.} = \frac{1.0 \times 10^{20}\ \mathrm{m}^2/\mathrm{s}}{n_g}. \tag{4.31}$$

The population equation for the $4s$ metastable state is

$$\frac{\partial n_m}{\partial t} = K_{gm} n_g n_e + K_{rm} n_r n_e + \left(K_{pm} n_e + A_{pm,eff.}\right) n_p - \left[\left(K_{mr} + K_{mp} + K_{mg} + K_{mi}\right) n_e + \frac{D_{eff.}}{\Lambda^2}\right] n_m, \tag{4.32}$$

the equation for the $4s$ resonant state is

$$\frac{\partial n_r}{\partial t} = K_{gr} n_g n_e + K_{mr} n_m n_e + \left(K_{pr} n_e + A_{pr,eff.}\right) n_p - \left[\left(K_{rm} + K_{rp} + K_{rg} + K_{ri}\right) n_e + A_{rg,eff.} + \frac{D_{eff.}}{\Lambda^2}\right] n_r, \tag{4.33}$$

and the equation for the $4p$ state is

$$\frac{\partial n_p}{\partial t} = K_{gp} n_g n_e + K_{mp} n_m n_e + K_{rp} n_r n_e + \nu_r n_e - \left[\left(K_{pm} + K_{pr} + K_{pg} + K_{pi}\right) n_e + A_{pm,eff.} + A_{pr,eff.} + \frac{D_{eff.}}{\Lambda^2}\right] n_p. \tag{4.34}$$

[9]Including axial diffusion terms in Eqs. 4.32, 4.33, and 4.34 would significantly increase the computation time for the model because implicit time-advance methods are required for such terms, as discussed in Appendix G.

The absorption-corrected spontaneous transition rates $A_{\alpha\beta,eff.}$ are calculated at each position and time using the procedure described in Appendix E.

In preparation for a numerical solution, we will rewrite Eqs. 4.28, 4.29, 4.32, 4.33, and 4.34 in dimensionless form by defining $\tau \equiv \nu_{in}t$, $\bar{z} \equiv z/z_0$, $\bar{n}_\alpha \equiv n_\alpha/n_0$, and $\bar{P}_e \equiv P_e/P_{e0} = n_e T_e/n_0 T_{e0}$. The electron pressure $P_e = n_e k_B T_e$ is chosen as a primary simulation variable rather than T_e because it makes the calculation simpler overall, but $T_e(z,t)$ will also be calculated at each timestep so that the various temperature-dependent quantities (rate coefficients, etc.) in the equations can be evaluated. We also define the following dimensionless parameters:

$$A \equiv \frac{k_B T_{e0}}{m_i \nu_{in}^2 z_0^2} \quad ; \quad B(T_e) \equiv \frac{\nu_{loss}(T_e)}{\nu_{in}} \quad ; \quad C \equiv \frac{2}{3}\frac{C_q T_{e0}^{5/2}}{\nu_{in} n_0 k_B z_0^2} \tag{4.35}$$

$$D(T_e) \equiv \frac{2}{3}\frac{\nu_{loss}(T_e)\, eV_s(T_e)}{\nu_{in} k_B T_{e0}} \quad ; \quad E(T_e) \equiv \frac{5}{3}\frac{\nu_{loss}(T_e)}{\nu_{in}} \tag{4.36}$$

$$\bar{K}_{\alpha\beta}(T_e) \equiv \frac{K_{\alpha\beta}(T_e)\, n_0}{\nu_{in}} \quad ; \quad \bar{K}_{E\alpha\beta}(T_e) \equiv \frac{2}{3}\frac{K_{\alpha\beta}(T_e)\, n_0 E_{\alpha\beta}}{\nu_{in} k_B T_{e0}} \quad ; \quad \bar{A}_{\alpha\beta} \equiv \frac{A_{\alpha\beta,eff.}}{\nu_{in}} \tag{4.37}$$

$$\bar{p}_{RF} \equiv \frac{2}{3}\frac{p_{RF}}{\nu_{in} n_0 k_B T_{e0}} \quad ; \quad \bar{D}_{eff.} \equiv \frac{D_{eff.}}{\Lambda^2 \nu_{in}} \quad ; \quad \bar{\nu}_r \equiv \frac{\nu_r(T_e)}{\nu_{in}} \quad ; \quad \bar{\nu}_{Er} \equiv \frac{2}{3}\frac{\nu_r(T_e)\, E_{pi}}{\nu_{in} k_B T_{e0}}. \tag{4.38}$$

Here T_{e0} is in eV and k_B is in J/eV, but $E_{\alpha\beta}$ is in J. With these definitions, the five equations that must be solved for the unknowns $\bar{n}_e$, $\bar{P}_e$, $\bar{n}_m$, $\bar{n}_r$, and $\bar{n}_p$ are

$$\frac{\partial \bar{n}_e}{\partial \tau} = A\frac{\partial^2 \bar{P}_e}{\partial \bar{z}^2} - B\bar{n}_e + \left(\bar{K}_{gi}\bar{n}_g + \bar{K}_{mi}\bar{n}_m + \bar{K}_{ri}\bar{n}_r + \bar{K}_{pi}\bar{n}_p - \bar{\nu}_r\right)\bar{n}_e \tag{4.39}$$

$$\begin{aligned}\frac{\partial \bar{P}_e}{\partial \tau} = {} & \bar{p}_{RF} + C\frac{\partial^2}{\partial \bar{z}^2}\left(\frac{\bar{P}_e^{7/2}}{\bar{n}_e^{7/2}}\right) - D\bar{n}_e - E\bar{P}_e + \bar{\nu}_{Er}\bar{n}_e \\ & - \bar{n}_e\left(\bar{K}_{Egi}\bar{n}_g + \bar{K}_{Emi}\bar{n}_m + \bar{K}_{Eri}\bar{n}_r + \bar{K}_{Epi}\bar{n}_p + \sum_{\alpha,\beta}\bar{K}_{E\alpha\beta}\bar{n}_\alpha + \bar{K}_{Eel.}\bar{n}_g\right)\end{aligned} \tag{4.40}$$

$$\begin{aligned}\frac{\partial \bar{n}_m}{\partial \tau} = {} & \bar{K}_{gm}\bar{n}_g\bar{n}_e + \bar{K}_{rm}\bar{n}_r\bar{n}_e + \left(\bar{K}_{pm}\bar{n}_e + \bar{A}_{pm}\right)\bar{n}_p \\ & - \left[\left(\bar{K}_{mr} + \bar{K}_{mp} + \bar{K}_{mg} + \bar{K}_{mi}\right)\bar{n}_e + \bar{D}_{eff.}\right]\bar{n}_m\end{aligned} \tag{4.41}$$

$$\frac{\partial \bar{n}_r}{\partial \tau} = \bar{K}_{gr}\bar{n}_g\bar{n}_e + \bar{K}_{mr}\bar{n}_m\bar{n}_e + \left(\bar{K}_{pr}\bar{n}_e + \bar{A}_{pr}\right)\bar{n}_p - \left[\left(\bar{K}_{rm} + \bar{K}_{rp} + \bar{K}_{rg} + \bar{K}_{ri}\right)\bar{n}_e + \bar{A}_{rg} + \bar{D}_{eff.}\right]\bar{n}_r \quad (4.42)$$

$$\frac{\partial \bar{n}_p}{\partial \tau} = \bar{K}_{gp}\bar{n}_g\bar{n}_e + \bar{K}_{mp}\bar{n}_m\bar{n}_e + \bar{K}_{rp}\bar{n}_r\bar{n}_e + \bar{\nu}_r\bar{n}_e - \left[\left(\bar{K}_{pm} + \bar{K}_{pr} + \bar{K}_{pg} + \bar{K}_{pi}\right)\bar{n}_e + \bar{A}_{pm} + \bar{A}_{pr} + \bar{D}_{eff.}\right]\bar{n}_p. \quad (4.43)$$

As in Sec. 3.3, $\bar{n}_g = n_{total}/n_0 - (\bar{n}_e + \bar{n}_m + \bar{n}_r + \bar{n}_p)$.

The numerical algorithm used to advance these equations forward in time is described in detail in Appendix G. A low, non-zero initial electron density (10^{14}–10^{15} m^{-3}) was specified in order to ensure numerical stability of the energy equation, and the RF power was ramped up from 0 to its maximum value over a period of 3 μs. The initial electron temperature was chosen to be $T_e \sim 2$ eV, but much higher or lower values could be used without any noticeable effect on the simulation results at $t \gg 1$ μs. The boundary conditions on $\bar{P}_e$ at the edges of the simulation domain (see Fig. 4.16) were derived from the requirement $\partial T_e/\partial \bar{z} = 0$ for zero heat flux at the boundaries (see Eq. 4.19)—refer to Appendix G for details. No boundary conditions were necessary for n_m, n_r, and n_p because there are no spatial derivatives in Eqs. 4.41, 4.42, and 4.43.

4.4.2.2 Ion Saturation Current

In order to validate the model, the numerical results for $n_e(z,t)$ and $T_e(z,t)$ were used in Eq. D.9 to calculate the model prediction for the ion saturation current, assuming the same Langmuir probe geometry and bias voltage used in the experiments. The model $I_{sat.}(z,t)$ was compared with data taken during discharges with uniform argon fill pressures of 30, 60, 120, and 240 mTorr. The peak RF power level and the rate of decay of the absorbed power (P_{RF} decreased in time in the experiment due to the gradual discharging of the RF amplifier's final stage capacitor—see Figs. 2.6 and 3.13) was adjusted so that the model $I_{sat.}(t)$ matched the data at $z = -7$ cm, the furthest location inside the antenna at which data was taken. The accuracy of the model was then judged by the extent to which the predicted $I_{sat.}(t)$ downstream at $z = -6$ cm to $z = -0$ cm matched the measurements.

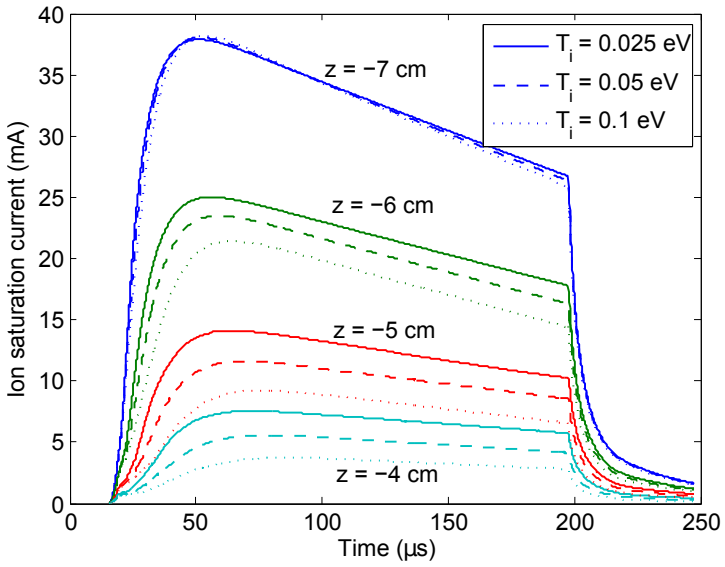

Figure 4.17: $I_{sat.}(z,t)$ calculated by the 1D time-dependent model for three different ion temperatures. The gas pressure was $p_{Ar} = 60$ mTorr, and a 10.5 cm long RF power deposition region was assumed, with total absorbed power $P_{RF} = 1190$ W.

The temperature of the neutral atoms and ions was left as a free parameter, which was adjusted within the plausible range 0.025 – 0.25 eV for the best fit to the data. Changing $T_i = T_g$ affected the ambipolar diffusion rate through the dependence of the ion-neutral collision frequency ν_{in} on v_{Ti} (see Eq. 4.29) and also altered the cross sections for re-absorption of line emission (see Eq. E.7). The overall impact of varying T_i on the simulation results was modest—in general, with higher T_i the predicted $I_{sat.}$ rose more slowly at each location, and the ultimate quasi-steady state density downstream of the antenna was lower, as illustrated in Fig. 4.17.

The best-fit model results for $p_{Ar} = 30$ mTorr are shown overlaid on the Langmuir probe data in Fig. 4.18. RF power absorption was assumed to occur only within the inner 8.5 cm of the 10.5 cm-long antenna. A simpler assumption would have been to set the length of the power absorption region equal to the antenna length, as in Sec. 3.3. However, in the data shown in Fig. 4.18 there is a delay of several μs between the initial density rise at $z = -7$ cm and the time at which the density begins to rise at $z = -6$ cm, implying that plasma had to be transported to $z = -6$ cm rather than being created there initially (the front edge of the antenna was located at $z = -5.9$ cm, so $z = -6$ cm was just inside the

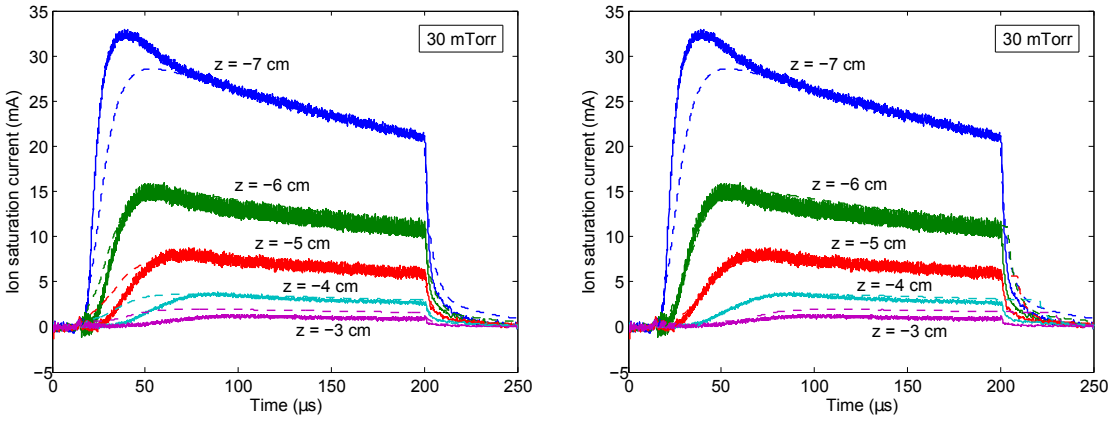

Figure 4.18: Model $I_{sat.}$ predictions (dashed curves) overlaid on Langmuir probe data (solid curves) for unmagnetized discharges at $p_{Ar} = 30$ mTorr. The RF power deposition region was assumed to extend from $z = -15.4$ cm to $z = -6.9$ cm (the boundaries of the antenna in the experiment were at $z = -16.4$ cm and $z = -5.9$ cm). The best fit between the model and data was achieved with $T_i = 0.1$ eV and $P_{RF} = 1600$ W, with the time-dependence of the RF power input after the initial ramp-up period modeled as $P_{RF}(t) = P_{RF,peak}\left[1 - (t - t_{peak})\,/\,(700\ \mu\text{s})\right]$ up until $t = 200$ μs, at which time the RF power was instantaneously switched off. $t = 0$ μs for the model was set to coincide with the timing of the initial fast density rise at $z = -7$ cm in the experiment, which occurred at $t \approx 16$ μs on the plots. In the left panel, the raw model results are shown, while in the right panel, the downstream model curves ($z = -6$ cm to $z = -3$ cm) have been shifted in time to match the measured timing of the initial density rise at each location in order to demonstrate the excellent agreement in the calculated and measured $\partial I_{sat.}/\partial t$ (the model curves at $z = -6$ cm through $z = -4$ cm are barely visible on this figure because they precisely overlap with the data).

antenna).

There are four main properties of the experimental $I_{sat.}$ curves that a model should ideally reproduce: the time delay before the density begins to rise at each axial location, the rate of increase $\partial I_{sat.}/\partial t$ during the density rise, the final quasi-steady state axial $I_{sat.}(z)$ profile, and the rate of decrease of $I_{sat.}$ after RF power turn-off. As seen in Fig. 4.18, our model performed admirably by the second and third measures, and reasonably well by the fourth. The quasi-steady state $I_{sat.}(z)$ profile matched the data extremely closely, and the rate at which $I_{sat.}$ rose at each location was predicted nearly perfectly as well. In the region where the plasma density was high, the predicted rate of $I_{sat.}$ decline in the afterglow was too slow, but excellent agreement with the measured $I_{sat.}$ decay rate was obtained at some downstream locations.

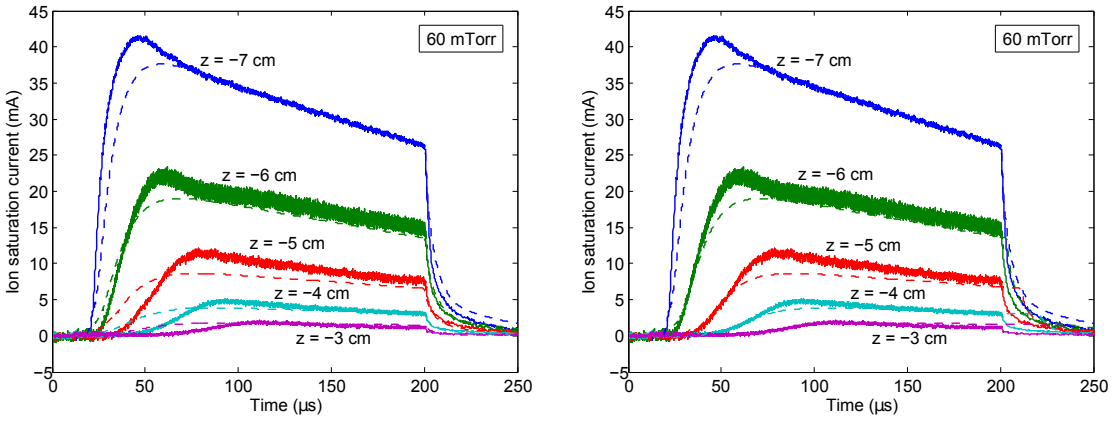

Figure 4.19: Model $I_{sat.}$ predictions (dashed curves) overlaid on Langmuir probe data (solid curves) for unmagnetized discharges at $p_{Ar} = 60$ mTorr. The left panel shows the raw model results, while in the right panel the downstream model curves ($z = -6$ cm to $z = -3$ cm) have been shifted in time to match the measured timing of the initial density rise at each location. The RF power deposition region was assumed to extend from $z = -15.4$ cm to $z = -6.9$ cm, and the best fit between the model and data was achieved with $T_i = 0.05$ eV and $P_{RF} = 1400$ W.

There was, however, one major discrepancy between the model and data, illustrated in the left panel of Fig. 4.18: in the simulation, the plasma density both within the antenna and downstream began to rise soon after the RF power was turned on, while in reality there was a delay of $\sim$ 5–10 μs before $I_{sat.}$ began to rise at each successive axial location. Only if the model $I_{sat.}(t)$ curves are artificially translated in time, as in the right panel of Fig. 4.18, is the excellent agreement in $\partial I_{sat.}/\partial t$ at each location demonstrated. The reason for the immediate downstream density rise in the model can be seen from the detailed results presented in Sec. 4.4.2.3. At the beginning of the discharge, the plasma density is low, and the high level of RF power input causes T_e to become high inside the antenna. The resulting gradient in T_e leads to a large axial heat flux (see Eqs. 4.20 and 4.28) that quickly raises the temperature downstream (see Fig. 4.22). With $T_e \sim 5$ eV, the rate coefficient for ionization out of the ground state is $K_{gi} \sim 2 \times 10^{-15}$ m^3/s (see Table 3.1). Then with $n_g \approx 10^{21}$ m^{-3}, the ionization rate is $K_{gi} n_g \sim 2 \times 10^6$ s^{-1}. This is much larger that the radial loss rate $\nu_{loss} = 2h_R c_s/R \sim 2 \times 10^5$ s^{-1}, so Eq. 4.29 approximately reduces to $\partial n_e \partial t \approx K_{gi} n_g n_e$, implying that n_e grows exponentially with a time constant[10] of $\sim$ 500 ns until the electrons

[10]This argument neglects stepwise ionization out of excited states, so the actual e-folding time would be even shorter.

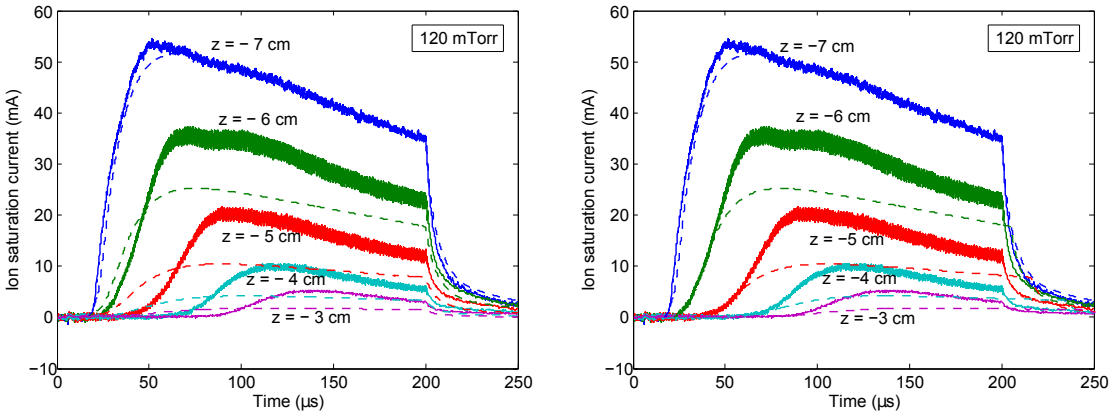

Figure 4.20: Model $I_{sat.}$ predictions (dashed curves) overlaid on Langmuir probe data (solid curves) for unmagnetized discharges at $p_{Ar} = 120$ mTorr. The left panel shows the raw model results, while in the right panel the downstream model curves ($z = -6$ cm to $z = -3$ cm) have been shifted in time to match the measured timing of the initial density rise at each location. The RF power deposition region was assumed to extend from $z = -15.4$ cm to $z = -6.9$ cm, and the best fit between the model and data was achieved with $T_i = 0.025$ eV and $P_{RF} = 1230$ W.

have cooled enough to reduce the ionization rate.

This sequence of events probably did not occur in the experiments because the electron heat flux q_{ez} could not actually be high in regions where there was little or no plasma present. The Braginskii heat flux expression (Eq. 4.20) is independent of n_e, but it was derived under the assumption that the electron-ion collision mean free path was much smaller than the characteristic length scale for the problem, and thus it is not valid in the region out in front of the expanding plasma. However, it is not clear what expression for the heat flux should be used instead of Eq. 4.20 in this region; more work is needed to determine whether this aspect of RF plasma transport can be accurately modeled within a two-fluid framework.

The times at which the density began to rise at each location in the experiment may be used to infer an "expansion velocity" $v_{exp.}$ for the RF plasma. We find $v_{exp.} \approx 1380$ m/s at 30 mTorr (Fig. 4.18), $v_{exp.} \approx 1210$ m/s at 60 mTorr (Fig. 4.19), $v_{exp.} \approx 850$ m/s at 120 mTorr (Fig. 4.20), and $v_{exp.} \approx 780$ m/s at 240 mTorr (Fig. 4.21). If the expansion velocity were proportional to the ambipolar diffusion coefficient, it would approximately scale with p_{Ar}^{-1} (see Eq. 4.12), but this was not the case, probably because the expansion involved a combination of both diffusion and ionization of pre-existing neutral gas. However, the

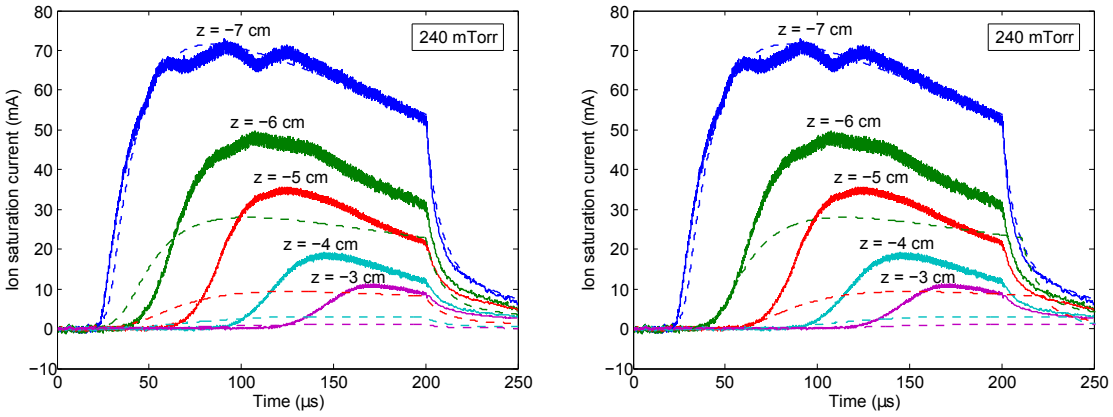

Figure 4.21: Model $I_{sat.}$ predictions (dashed curves) overlaid on Langmuir probe data (solid curves) for unmagnetized discharges at $p_{Ar} = 240$ mTorr. The left panel shows the raw model results, while in the right panel the downstream model curves ($z = -6$ cm to $z = -3$ cm) have been shifted in time to match the measured timing of the initial density rise at each location. The RF power deposition region was assumed to extend from $z = -15.4$ cm to $z = -6.9$ cm, and the best fit between the model and data was achieved with $T_i = 0.025$ eV and $P_{RF} = 1100$ W.

details of the physics at the expansion front are not yet understood.

Consider now the calculated and measured $I_{sat.}(z,t)$ at $p_{Ar} = 60$ mTorr, shown in Fig. 4.19. Once again, the model accurately predicts the ultimate quasi-steady state $I_{sat.}(z)$ profile and the time-dependence of $\partial I_{sat.}/\partial t$ during the initial density rise at each location and during the afterglow. The corresponding results for $p_{Ar} = 120$ mTorr and $p_{Ar} = 240$ mTorr are shown in Figs. 4.20 and 4.21, respectively. At these higher pressures, although the model matches the measured rise and fall rates of $I_{sat.}$ well, the predicted quasi-steady state $I_{sat.}(z)$ declines far too quickly moving away from the power deposition region. Therefore, there must be some physical process missing from the model that is relatively unimportant at $p \lesssim 60$ mTorr but becomes critical for achieving a high downstream density at $p \gtrsim 120$ mTorr. Many approximations were made in developing the model, so there are numerous possible candidates ranging from axial radiative transport (re-absorption of emitted photons changes the excited state population densities non-locally) to some exotic collisional atomic process. The main culprit has yet to be conclusively identified, however. Interestingly, while the measured downstream density profile was not fit well by the model at $p_{Ar} \geq 120$ mTorr, the initial $\partial I_{sat.}/\partial t$ inside the power deposition region at $z = -7$ cm

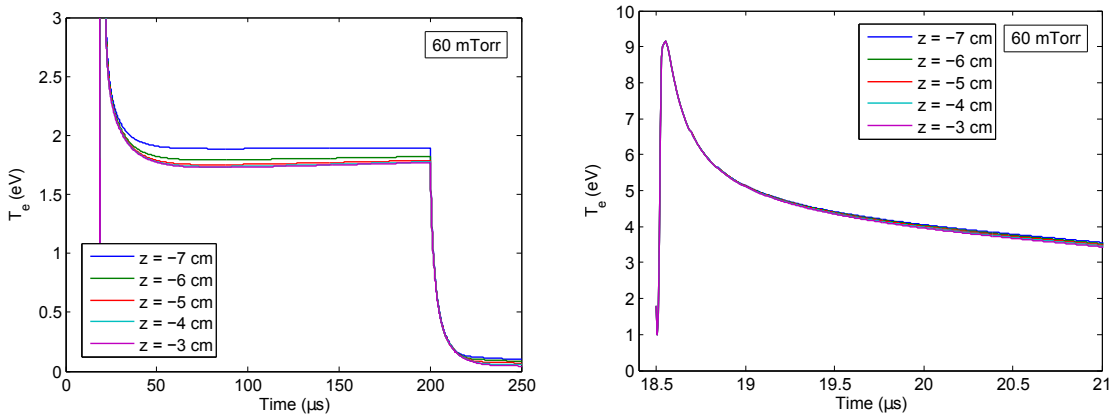

Figure 4.22: Electron temperature vs. time calculated by the 1D numerical discharge model with $p_{Ar} = 60$ mTorr. The same simulation parameters were used as in Fig. 4.19. The right panel zooms in on the first 2.5 μs of the simulation, which was started at $t = 18.5$ μs to facilitate comparison with the data in Fig. 4.19.

was predicted more accurately in Figs. 4.20 and 4.21 than at lower pressures[11].

The best fits between the model and data were achieved by setting $T_i = 0.1$ eV for the 30 mTorr calculation, $T_i = 0.05$ eV for the 60 mTorr calculation, and $T_i = 0.025$ eV for the 120 mTorr and 240 mTorr calculations. It makes sense intuitively that $T_i = T_g$ should have been lower at high p_{Ar}, since the ions and neutrals were heated by electric impacts, and the ratio of the number of electrons to the number of heavy particles was lower at high pressure.

The RF power level that was necessary to make the model $I_{sat.}(t)$ fit the Langmuir probe data at $z = -7$ cm was also pressure-dependent, ranging from $P_{RF} = 1600$ W at $p_{Ar} = 30$ mTorr to $P_{RF} = 1100$ W at $p_{Ar} = 240$ mTorr. On the other hand, the measured RF power delivered to the load as a whole at $t = 100$ μs was $P_L = 2290$ W at 30 mTorr and $P_L = 2100$ W at 240 mTorr. The more drastic pressure dependence in the absorbed powers inferred from the model was probably not physically meaningful, but rather arose because the ion saturation current measured by the probe was depressed at high pressures due to collisional effects (see Sec. D.2 for more discussion). This non-ideal probe behavior was not taken into account when using Eq. D.9 to convert the model results for $n_e(z,t)$ and

[11]Note that while the time dependence of $P_{RF}(t)$ used in the model was adjusted to fit the gradual decay in $I_{sat.}$ at later times due to the decreasing power output from the RF amplifier, there was no fine-tuning to fit the initial $I_{sat.}$ rise rate—the RF power was always ramped up linearly to reach its maximum value 3 μs after the start of the simulation.

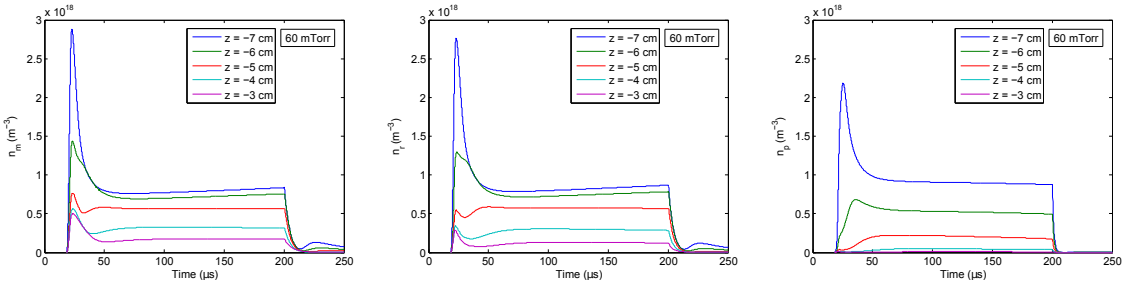

Figure 4.23: Ar I excited state population densities vs. time calculated by the model with $p_{Ar} = 60$ mTorr. The same simulation parameters were used as in Fig. 4.19. The left panel shows the $4s$ metastable state population density, the center panel shows the $4s$ resonant state population density, and the right panel shows the $4p$ state population density.

$T_e(z,t)$ into a predicted ion saturation current.

4.4.2.3 Detailed Model Results at 60 mTorr

If the model could only reproduce the experimental results, it would already have some value, as the demonstrated close agreement between the predicted $I_{sat.}$ and the probe data at $p_{Ar} \leq 60$ mTorr provides confidence that the key physical processes in this pressure range are well understood. However, the simulation results also contain a wealth of information about plasma properties and atomic processes that could not be measured with the available diagnostics. Some examples will be shown from the calculations at 60 mTorr—qualitatively similar results were obtained at 30 mTorr.

Fig. 4.22 shows the time evolution of the electron temperature. When the power is turned on, T_e rises rapidly to ~ 9 eV everywhere and then gradually falls to an equilibrium value of 1.7–2.0 eV. Axial heat flux keeps the plasma nearly isothermal, but the slight temperature gradient is important for establishing the quasi-steady state density profile observed in Fig. 4.19. After RF power turn-off at $t = 200$ μs, T_e falls very quickly to < 0.2 eV.

The calculated excited state population densities for the same discharge conditions are shown in Fig. 4.23. The high electron temperature at early times leads to a high rate of collisional excitation that quickly raises n_m, n_r, and n_p, enabling a high stepwise ionization rate that builds up the plasma density (the evolution of $n_i = n_e$ basically follows the ion

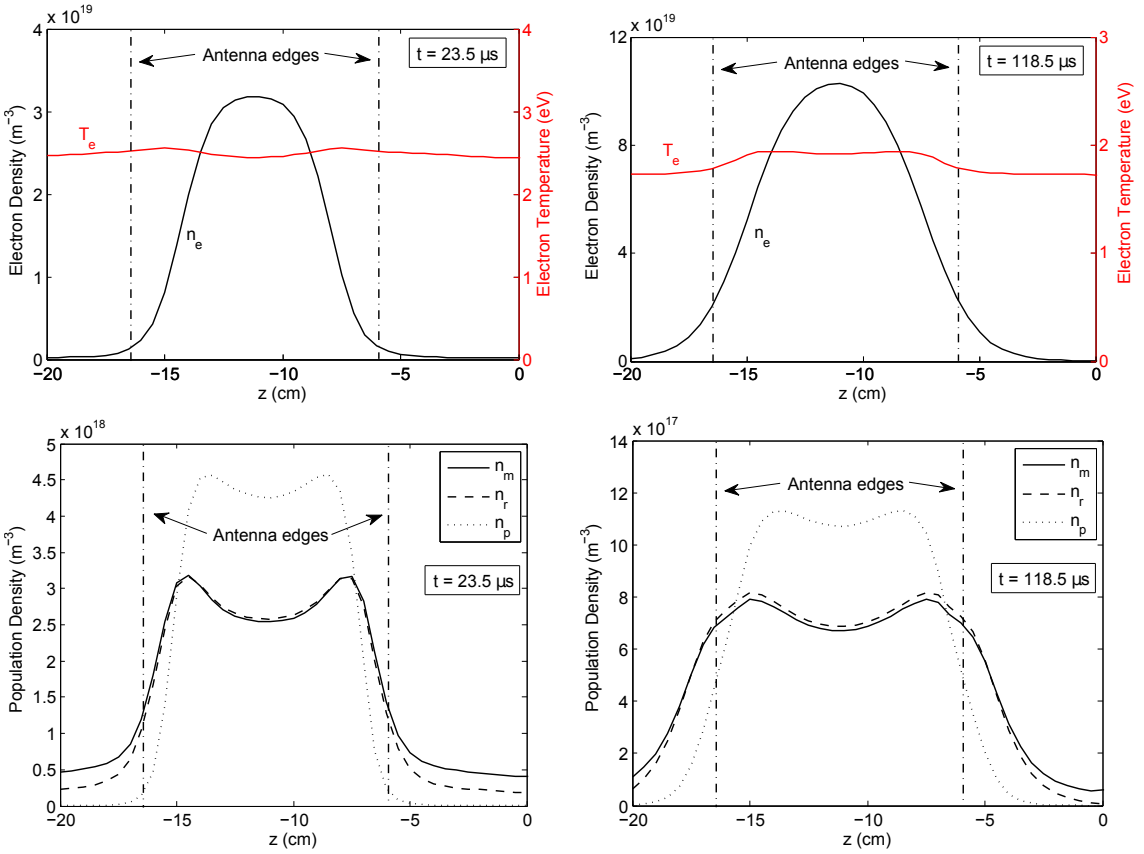

Figure 4.24: Spatial dependence of n_e, T_e, n_m, n_r, and n_p calculated by the 1D numerical discharge model at $p_{Ar} = 60$ mTorr. The same simulation parameters were used as in Fig. 4.19. The density and temperature profiles are plotted at $t = 23.5$ μs (i.e., 5 μs after the start of the simulation) and at $t = 118.5$ μs, during the quasi-steady state phase.

saturation current curves shown in Fig. 4.19). The excited state populations fall moving away from the power deposition region. As in Fig. 3.11, the $4s$ metastable and $4s$ resonant manifolds have similar population densities because the collisional transition rate between these states is high (see Table 3.1) and most of the resonant line emission is re-absorbed. In the quasi-steady state, the $4p$ level has a higher population density than the $4s$ levels inside the antenna, but n_p decreases more rapidly moving downstream. It is interesting that even though three-body recombination was assumed to occur exclusively into the $4p$ level, it is the $4s$ levels whose population densities peak in the afterglow at around $t \approx 225$ μs: this is because the effective radiative decay rate for the $4p$ state ($A_{ps,eff.} \sim 3 \times 10^7$ s^{-1}) far exceeds the three-body recombination rate ($\nu_r \sim 10^2$–10^4 s^{-1}). Balancing the population

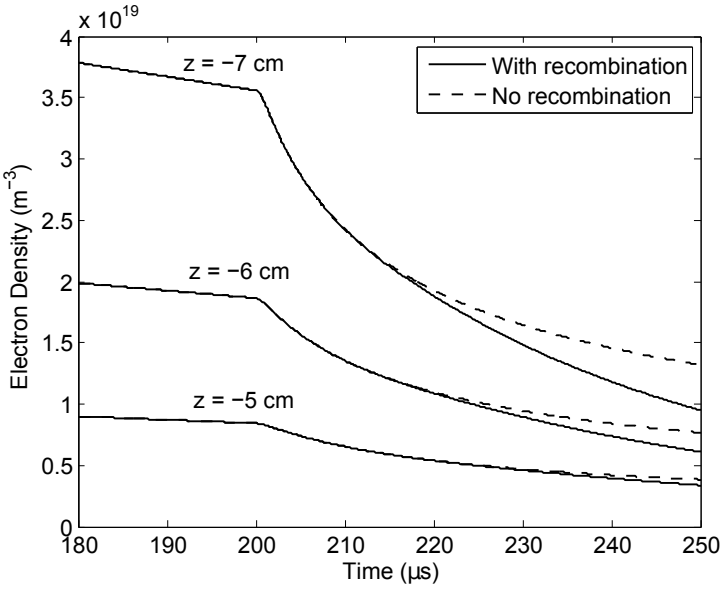

Figure 4.25: Electron density decay in the afterglow from 1D discharge model calculations with and without three-body recombination included. The calculation parameters used were otherwise the same as in Fig. 4.19.

and depopulation rates per unit volume for the $4p$ state yields $n_p/n_e \approx \nu_r/A_{ps,eff.}$, so the $4p$ population density in the afterglow is lower than the electron density by 3–5 orders of magnitude. On the other hand, $A_{rg,eff.} \approx 5 \times 10^5$ s^{-1}, so the resonant and metastable state population densities can rise to $n_r \approx n_m \approx (\nu_r/A_{rg,eff.})\, n_e \sim 0.01 n_e$ when these energy levels are populated from above by spontaneous decays from the $4p$ state following recombination.

The spatial profiles of the plasma density, electron temperature, and excited state population densities are plotted for two representative times in Fig. 4.24. After the initial transient phase of the discharge, T_e is approximately uniform inside the power deposition region and approximately uniform far downstream, but there is a relatively steep temperature gradient in the transition regions around $z \sim -15.5$ cm and $z \sim -7$ cm that drives heat flux away from the antenna. Interestingly, n_m, n_r, and n_p peak near the edges of the power deposition region and are lower at the center of the antenna due to the complex balance of populating and de-populating processes included in Eqs. 4.32, 4.33, and 4.34. It is also notable that there is a substantial population density of metastable excited atoms far from the antenna region.

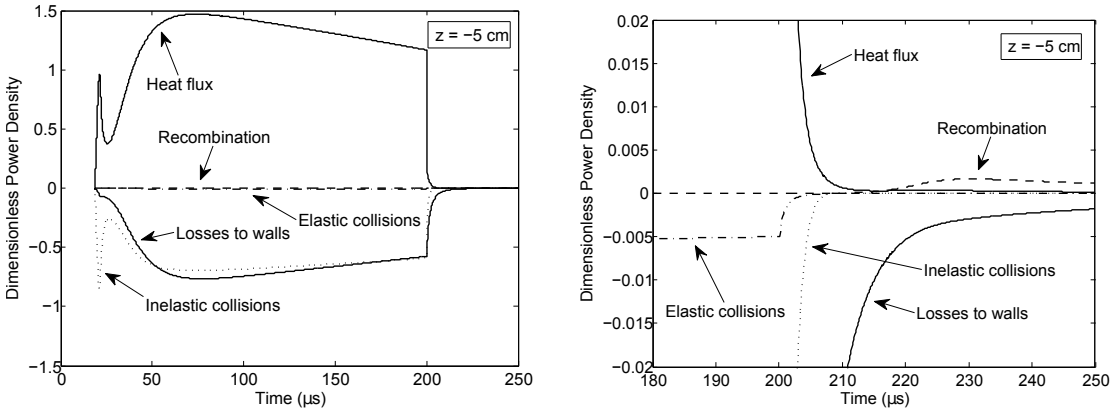

Figure 4.26: Relative contributions of the processes included in Eq. 4.40 to the overall change in the dimensionless electron pressure at $z = -5$ cm, just downstream of the power deposition region. The right panel zooms in on the afterglow period ($t > 200$ μs). The same simulation parameters were used as in Fig. 4.19.

A useful feature of numerical modeling is the ability to artificially turn off physical processes in order to explicitly see their impact on the plasma evolution. For example, Fig. 4.25 illustrates the effect of turning off three-body recombination by setting $\nu_r = 0$. The simulation results are unchanged for $t \leq 215$ μs, indicating that recombination was of negligible importance during the main power-on period ($t \leq 200$ μs), as expected. However, later in the afterglow, the density decreases too slowly when recombination is not included, particularly near the antenna where n_e was high initially (the recombination rate per unit volume is approximately proportional to n_e^3—see Eq. 4.27).

We can also plot the magnitude of each term in the model equations as a function of time or position in order to monitor their relative importance. One example is given in Fig. 4.26, which illustrates the contributions of the various terms in Eq. 4.40 to the overall rate of change of the dimensionless electron pressure at $z = -5$ cm. The left panel shows that heat flux from the antenna region is approximately balanced by the sum of diffusive energy losses to the walls (the terms involving D and E in Eq. 4.40) and electron energy losses due to inelastic collisions (the ionization and excitation/de-excitation terms in Eq. 4.40) during the main discharge. In the afterglow, diffusive losses to the walls (i.e., evaporative cooling) are the dominant energy loss mechanism, and three-body recombination provides some reheating of the electrons. The effect of elastic electron-neutral collisions is negligible

during both periods.

4.5 Future Work

The time-dependent 1D discharge model calculations that have already been carried out contain a large amount of information that can be further dissected as in Fig. 4.26 to identify the key physical processes in the RF discharge during the initial density build-up, the quasi-steady state period, and the afterglow. Much insight into the discharge physics at $p_{Ar} \leq 60$ mTorr may be garnered through continued detailed investigations into these simulation results.

The original aim of the analytical and numerical modeling was to better understand the emission patterns and plasma density behavior observed in the experiments with the fast gas valve described in Secs. 4.1, 4.2, and 4.3, but little contact has been made with these data as of yet. Since the estimated gas pressure in the discharge tube was 400–500 mTorr when the most interesting phenomena were seen in the camera images and ion saturation current data (see, for example, Figs. 4.1–4.3 and 4.10), the top priority for future work is to understand the reason for the inaccuracy of the numerical model at $p \geq 120$ mTorr. Once the proper physics for high pressure discharges is included in the model, it would be straightforward to implement a spatially non-uniform gas pressure such as that produced by the fast gas valve. It is uncertain if the plasma parameters could be accurately calculated unless the actual gas distribution in the experiment were measured and used as an input for the simulation, but it may be possible to estimate $p_{Ar}(z)$ using a relatively simple fluid dynamics calculation.

Ideally, the ion and neutral temperatures in the simulation should be calculated independently as a function of time and space in a self-consistent manner. This is a non-trivial undertaking, however, and it is not likely to have a significant impact on the results at high gas pressure, where T_i and T_g are both expected to be near room temperature. Likewise, the neglect of axial diffusion of excited neutral atoms is probably not the main cause of inaccuracy in the model at high pressures, since the diffusion rate is inversely proportional to p_{Ar} (see Eq. 4.31).

On the experimental side, spectroscopic measurements of additional Ar I emission lines would be useful for continuing to build understanding of the time-dependent emission seen in the camera images (Figs. 4.1, 4.2, and 4.3). Measuring the relative population densities of a number of different argon energy levels would help to confirm and flesh out the interpretations of the observed emission patterns given in Sec. 4.2. It would also be very valuable to make electron temperature measurements out in the main chamber (i.e., at $z \geq 0$ cm) using an RF compensated Langmuir probe (see Sec. D.5). In contrast to the behavior inside the source tube, at $z = 6$ cm the measured ion saturation current did not drop suddenly when the RF power was turned off (compare the left and right panels of Fig. 4.11), suggesting that T_e may have already been very low at this location.

Chapter 5

Afterglow Emission and Density Peaks

In Chapter 4, there were hints that the afterglow period of the RF discharge (i.e., after the power was turned off) was not simply an uninteresting decay phase but featured mysterious plasma behaviors that were worthy of study in their own right. For instance, the fast camera images in Figs. 4.2 and 4.3 exhibited a burst of visible emission in the main chamber region downstream of the source after RF turn-off, Figs. 4.8 and 4.9 showed a large increase in the relative populations of highly excited argon atoms in the afterglow, and Fig. 4.11 featured an unexpected increase in the ion saturation current ($I_{sat.}$) measured by a Langmuir probe at $z = 6.0$ cm after the power was turned off. This chapter will examine the light emission and plasma density evolution in the afterglow in more detail, revealing an unforeseen application and a hidden source of free energy in the plasma.

5.1 Indirect Gas Pressure Measurements Using the Afterglow Emission Peak

It is well known that decaying plasmas emit intense visible and infrared (IR) radiation as they recombine [111]. The so-called emission "afterpeak" in argon pulsed inductively coupled plasmas and pulsed DC glow discharges has been studied in detail [106, 112, 113] due to the applications of these plasmas for sample analysis using mass spectrometry and optical emission spectroscopy [114] and also in semiconductor processing and other industries [83, 112]. However, there is still controversy regarding whether the high level of afterglow

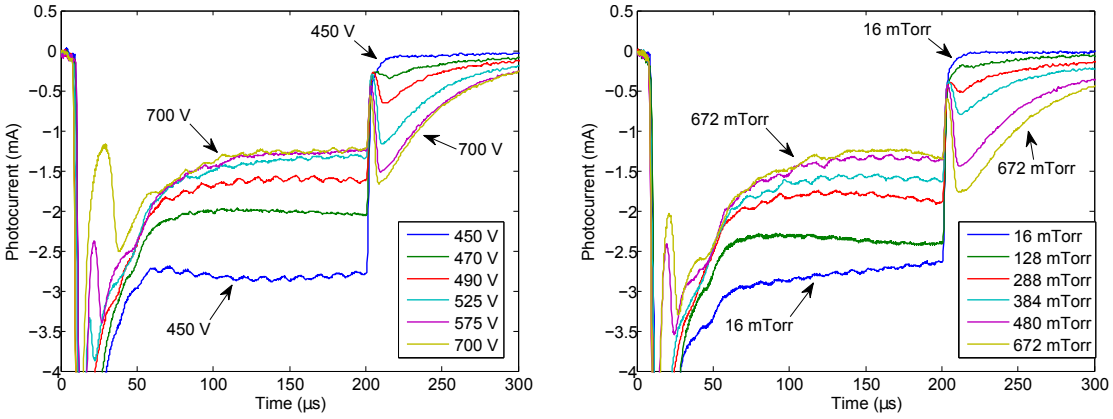

Figure 5.1: Optical and infrared emission measured by a photodiode viewing the rear side of the source tube during argon discharges with the RF power on from t = 0–200 μs. The photocurrent was always negative, with its magnitude proportional to the incident brightness. The bias magnetic field was turned on for these experiments (V_{bias} = 80 V, $V_{sol.}$ = 0 V), but similar results were also obtained with $B = 0$. Left: Photodiode signal during experiments with the fast gas valve used (the legend shows the gas bank voltage $V_{gas,RF}$). The gas bank was triggered at $t_{gas,RF} = -6.0$ ms for all experiments discussed in this section. Right: Photodiode signal during experiments with a uniform pressure in the discharge tube.

emission in experiments at $p_{Ar} \sim 0.2$–2 Torr can be accounted for by plausible three-body recombination rates [112, 113] or whether electron-ion dissociative recombination involving positive molecular ions ($Ar_2^+ + e^- \rightarrow Ar^* + Ar$, where Ar^* denotes an excited argon atom) must play a critical role [106].

We measured the overall level of optical and IR emission in our RF discharge using the photodiode described in Sec. 3.1.3, which was mounted inside the re-entrant port between the UV flashlamp / gas feed assembly and the end of the solenoid bobbin (see Fig. 2.2), at $z \approx -29$ cm. The line of sight was toward the rear end of the HTH antenna. The time-dependent emission during experiments with argon gas supplied by a fast gas valve (see Sec. 1.6.4) is shown for a range of gas bank voltages in the left panel of Fig. 5.1. The plasma brightness dropped rapidly after the RF power was turned off at t = 200 μs, but at higher gas bank voltages it rose again a few μs later, exhibiting a strong afterpeak. For $V_{gas,RF} \gtrsim 550$ V, the peak afterglow brightness exceeded the quasi-steady state main discharge brightness recorded at $t \approx$ 100–200 μs.

Similar emission patterns were produced during experiments with a uniform gas pressure

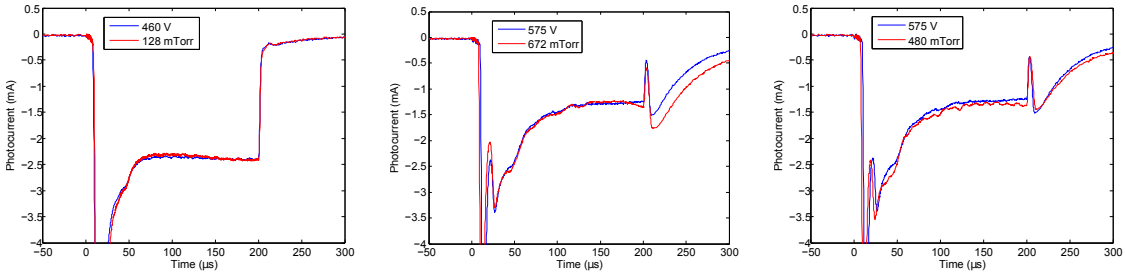

Figure 5.2: Examples of the close correspondence between photodiode signals obtained during experiments with the fast gas valve used and with a uniform pressure in the discharge tube. Left: The time-dependence and brightness of the emission with a gas bank voltage $V_{gas,RF} = 460$ V was closely reproduced with a uniform pressure of $p_{Ar} = 128$ mTorr. Center and right: For $V_{gas,RF} = 575$ V, the best match to the emission during the RF on period ($t < 200$ μs) was obtained with $p_{Ar} = 672$ mTorr, while the best match to the afterpeak brightness was obtained with $p_{Ar} = 480$ mTorr.

in the discharge tube (a leak valve was used to feed in argon gas at the midplane of the main vacuum chamber), shown in the right panel of Fig. 5.1. In fact, as illustrated in Fig. 5.2, an extremely close correspondence existed between the magnitude and time-dependence of the photodiode signal obtained at a given fast gas valve bank voltage and the signal recorded at some uniform gas pressure. The match between the measured emission patterns was so precise that the plasma conditions, and in particular the argon gas pressure, must have been nearly identical between the pairs of shots shown in Fig. 5.2. Therefore, we may interpret the time-dependent optical and IR emission as giving an indirect measurement of the pressure produced in the discharge tube by the fast gas valve. Knowledge of the neutral gas density was very important for determining the appropriate transport and collisional-radiative regimes for analyzing the RF discharge behaviors discussed in Chapter 4 and Sec. 5.2, so this was a valuable measurement[1]. The technique could be applied even though the detailed excited state population densities that produced the observed line emission were not known; in fact, the complexity of the emission processes was advantageous, as this made it very unlikely that a close match between the overall time-dependent emission patterns in two different discharges could have been obtained if the gas pressures were not equal. This

[1]Ideally, one would measure the time-dependent gas pressure produced by a fast gas valve puff directly using a fast ion gauge [43, Appendix B], but it would have been difficult to build one that could be inserted into the narrow discharge tube, and in any case such a gauge inserted into the tube would have significantly perturbed the gas flow.

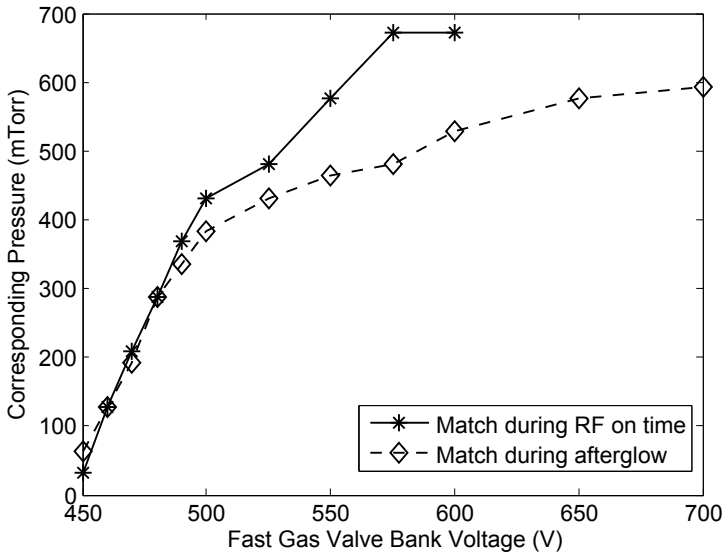

Figure 5.3: Pressure in the discharge tube as a function of gas bank voltage, as determined from matching photodiode traces between experiments that used the fast gas valve and experiments that had uniform gas pressure. The two curves show the best fit pressure from emission comparisons during the RF on time (as in the center panel of Fig. 5.2) and in the afterglow (as in the right panel of Fig. 5.2).

method for inferring the gas pressure could also be useful in other experiments that employ a fast gas valve to feed gas to an RF plasma source, such as the helicon pre-ionization source at the University of Washington's HIT-SI experiment [49].

As shown in the left panel of Fig. 5.2, at low gas bank voltages the correspondence between the emission produced during experiments with the fast gas valve and during uniform pressure experiments was nearly exact at all times, while at higher bank voltages a somewhat different uniform pressure was needed to match the emission during the main discharge period versus during the afterglow. A plausible explanation involves re-absorption of line emission, which was shown to be important in our discharge in Secs. 3.3, 4.4.2, and E. The 1D time-dependent discharge model in Sec. 4.4.2 showed that the Ar I $4s$ and $4p$ excited state population densities fell drastically after RF power turn-off (see Fig. 4.23), so re-absorption of visible and IR emission (which arose from electron transitions between excited states) was negligible in the afterglow but may have played a role while the power was on. Therefore, the emission detected by the photodiode during the afterglow may have come from a location deeper into the discharge tube, on average, than the emission

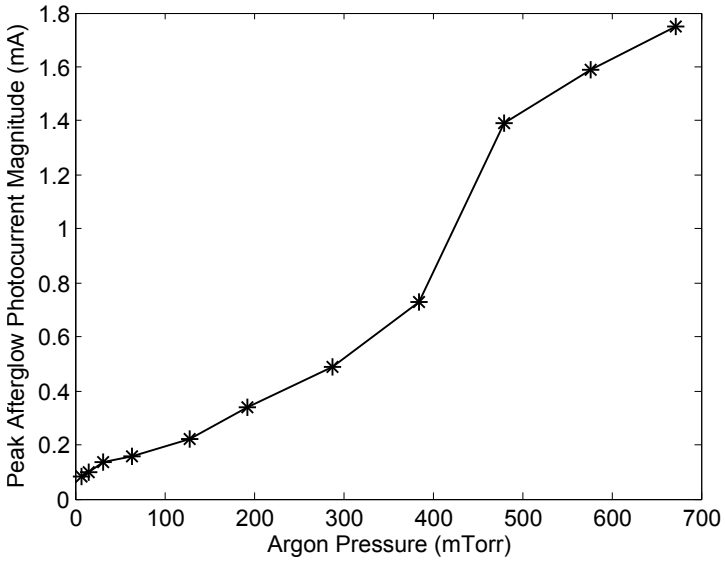

Figure 5.4: Measured photocurrent magnitude at $t = 210$ μs, around the time of the peak afterglow emission, from the data shown in the right panel of Fig. 5.1.

detected during the main discharge period. The gas pressure produced by the fast gas valve was probably higher near the gas inlet at the rear of the discharge tube (see Fig. 2.2), i.e., near the photodiode, than closer to the jet experiment electrodes, so the pressure inferred from the emission comparison was higher during the RF on time than during the afterglow. Since the pressure toward the front of the discharge tube near the electrodes was of the most interest for interpreting the data in Chapter 4 and Sec. 5.2, the pressure measurement using the afterglow emission was preferred.

The inferred pressures produced by the fast gas valve as a function of bank voltage are shown in Fig. 5.3. The pressure increased rapidly with $V_{gas,RF}$ between $V_{gas,RF} =$ 450–500 V, but then nearly leveled out at higher gas bank voltages. This nonlinear behavior is in stark contrast to the results of total throughput measurements (see Fig. 1.9), which showed a roughly linear dependence of the time-integrated gas valve output on bank voltage. Apparently the time dependence of the gas puff was quite different above and below $V_{gas} =$ 500 V.

According to Fig. 5.3, the pressure in the pre-ionization source tube for the most commonly used fast gas valve bank settings, $V_{gas,RF} = 550$ V and $t_{gas,RF} = -6.0$ ms, was

$p_{Ar} \approx 460$ mTorr. To estimate whether this is reasonable, note that when the fast gas valve plenum ($V = 2.3 \times 10^{-6}$ m^3 [43, Appendix B]) was filled with argon at a pressure 60 psig above atmospheric pressure, the total number of gas particles in the plenum was $\sim 3 \times 10^{20}$. However, from Fig. 1.9, only $\sim 5 \times 10^{19}$ of these particles actually made it into the chamber when the fast gas valve was triggered at $V_{gas,RF} = 550$ V. If all of these particles were in the quartz tube at the same time, at room temperature[2], then the pressure in the tube ($V \approx 1.4 \times 10^{-4}$ m^3) would have been ~ 1 Torr. Thus the inferred pressure of 460 mTorr corresponds to roughly half of the particles from the gas puff being in the tube simultaneously, which is plausible based on the ~ 1 ms gas travel time down the length of the tube (using the tube length $L \approx 35$ cm and the room temperature sound speed for argon, $c \approx 320$ m/s) and the results of fast ion gauge measurements in a similar experiment [43, Appendix B], which showed that the pressure rise time associated with a fast gas valve puff was a few ms.

The peak brightness of the afterglow emission in uniform gas pressure experiments is shown as a function of p_{Ar} in Fig. 5.4. The afterpeak brightness increased approximately linearly with argon pressure up to 384 mTorr, then jumped higher at 480 mTorr, perhaps indicating a transition to a different regime in which the dominant mechanism populating the argon excited states changed. Some insight into the underlying physics may be obtained from the 1D time-dependent discharge model developed in Sec. 4.4.2. A quantitative prediction of the time-dependent afterglow emission is beyond the scope of the model, since it does not track the population densities of argon excited states above the $4p$ level, which are a major source of afterglow emission, as illustrated in Figs. 4.8 and 4.9. However, if three-body recombination was the primary source of excited argon atoms in the afterglow, then assuming that the spontaneous emission timescale was short compared to the timescales for changes in the electron density and temperature, the visible brightness of the afterglow should have approximately scaled with the recombination rate. The model prediction for

[2]The gas may have been colder than room temperature due to adiabatic cooling as it expanded out of the fast gas valve, in which case the true pressures were lower than those stated here. However, it was the gas particle density rather than the pressure that actually mattered for the RF discharge, so the uncertainty in the gas temperature prior to initiating the discharge is unimportant—pressure values at 300 K have simply been calculated in order to facilitate comparison (for example, in Fig. 5.3) between the number densities produced by the fast gas valve and those present with uniform gas fills.

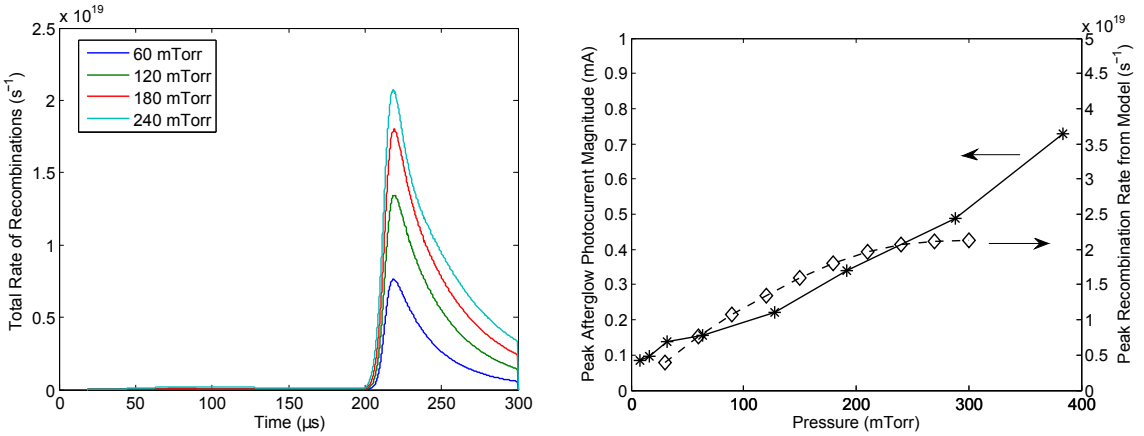

Figure 5.5: Left: 1D time-dependent discharge model calculations (see Sec. 4.4.2) of the total three-body recombination rate $\int \nu_r n_e dV$. Right: Peak recombination rate from the model as a function of pressure, overlaid on the measured afterpeak brightnesses at $p_{Ar} < 400$ mTorr. The model calculations all assumed $P_{RF} = 1600$ W, $T_i = 0.05$ eV, and an 8.5 cm-long power deposition region. The model is valid for unmagnetized plasmas, while the bias field was applied in the experiments shown, but similar photocurrents were measured in experiments with no magnetic field.

the total recombination rate $\nu_r n_e$ (where $\nu_r(n_e, T_e)$ was calculated from Eq. 4.27) integrated over the discharge volume is shown for four different argon pressures in the left panel of Fig. 5.5. These curves are qualitatively similar to the measured afterpeaks visible in Fig. 5.1. In the right panel of Fig. 5.5, the peak recombination rate in the model as a function of pressure is overlaid on the measured peak afterglow brightnesses. The predicted recombination rate increases approximately linearly with p_{Ar} below 100 mTorr, but levels out at higher pressures, in contrast to the measured afterpeak brightness. This may indicate that some other process in addition to three-body recombination became important for producing enhanced excited state population densities at $p_{Ar} \gtrsim 200$ mTorr[3]. However, it is difficult to draw firm conclusions without more detailed modeling specifically tailored to understanding the afterglow emission, such as has been carried out by Bogaerts [106] and Kang et al. [112].

Another interesting aspect of the photodiode data in Fig. 5.1 is that the quasi-steady state visible/IR brightness during the RF on time scaled inversely with p_{Ar}, even though

[3]Although it was shown in Sec. 4.4.2.2 that the model became less accurate at $p_{Ar} \geq 120$ mTorr, this applied primarily during the RF on time—the simulations at $p_{Ar} = 120$–240 mTorr fit the measured rate of ion saturation current decline in the afterglow quite well, as shown in Figs. 4.20 and 4.21.

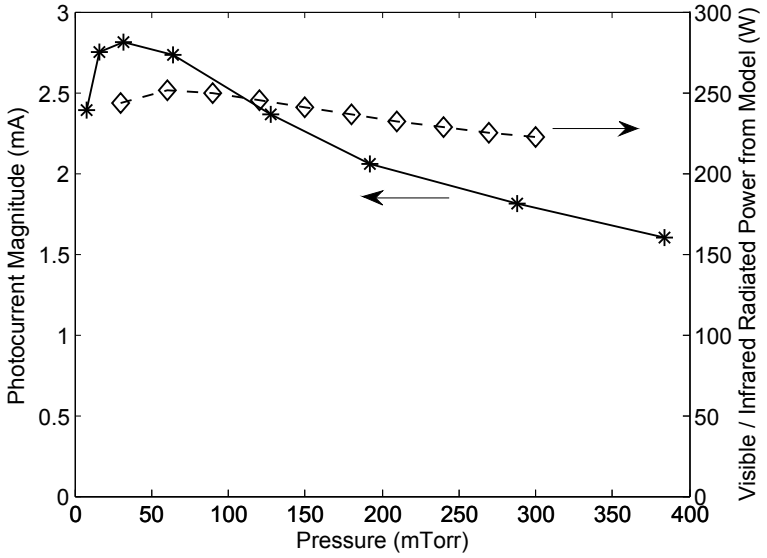

Figure 5.6: Measured photodiode signals averaged from $t = 100$–200 μs (solid line), compared with the average visible and IR radiated power over the same interval predicted by the 1D discharge model using Eq. 5.1 (dashed line). The model calculations all assumed $P_{RF} = 1600$ W, $T_i = 0.05$ eV, and an 8.5 cm-long power deposition region.

the plasma density was higher at higher pressures (see the ion saturation current data in Sec. 4.4.2.2). We can roughly estimate the level of visible and IR emission predicted by the 1D discharge model by assuming that it is proportional to the rate of Ar I $4p \rightarrow 4s$ transitions, corrected for re-absorption, i.e.,

$$P_{vis./IR} \approx n_p \left(A_{pm,eff.} + A_{pr,eff.} \right) E_{ps} \pi R^2 L \tag{5.1}$$

(see Sec. 3.3 for definitions of the quantities on the right hand side). This formula accounts for most of the emission that would be detected by the photodiode because transitions between the $4s$ resonant level and the ground state produced UV photons ($\lambda \approx 106$ nm), and emission lines produced by transitions originating from levels above $4p$ were relatively weak compared to the strongest lines produced by $4p \rightarrow 4s$ transitions while the RF power was on (see Figs. 4.8 and 4.9). Fig. 5.6 shows the quasi-steady state photodiode signal as a function of pressure, along with the total visible/IR radiated power predicted by Eq. 5.1. The model reproduces the basic result that the level of emission decreases with increasing pressure

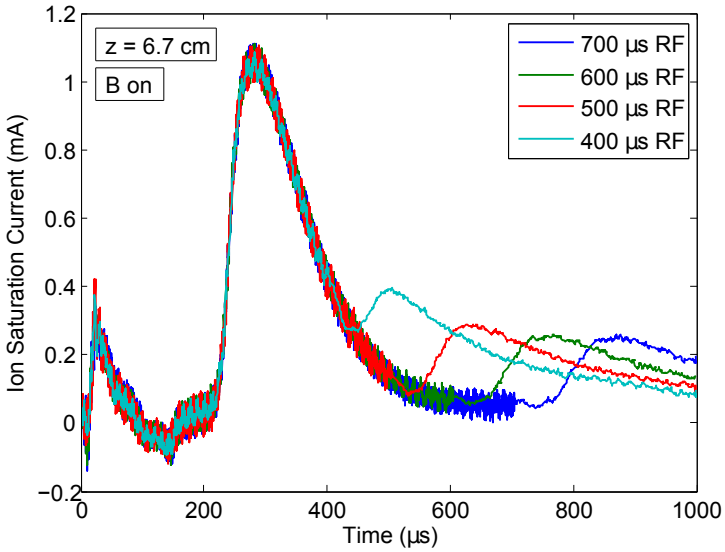

Figure 5.7: Langmuir probe ion saturation current measured at $z = 6.7$ cm for discharges with the RF amplifier turned off at four different times. The fast gas valve was used with $V_{gas,RF} = 550$ V, and the bias field coil and solenoid were turned on.

for $p_{Ar} \gtrsim 50$ mTorr, although the predicted pressure dependence is gentler than what was observed. Although one might have expected the excited state population densities, and consequently the radiated power, to be higher in discharges with high p_{Ar} and n_e, this was not the case in the simulation—the electron temperature was lower at higher pressures, partially negating the effect of higher n_e on the collisional excitation rates, and the balance of collisional and radiative populating and depopulating processes (see Eqs. 4.32, 4.33, and 4.34) ultimately caused n_m, n_r, and n_p to be nearly independent of pressure in the 30–300 mTorr range.

5.2 Plasma Density Peak in the Afterglow

5.2.1 Experimental Observations

Far more mysterious than the afterglow emission peak was the increase in the downstream ion saturation current that was also observed after RF power turn-off under some discharge conditions (for example, see Figs. 4.4, 4.10, and 4.11). Straightforward analytical estimates [5, Section 10.6] as well as numerical calculations (see Figs. 4.18–4.22) predict that $I_{sat.} \propto$

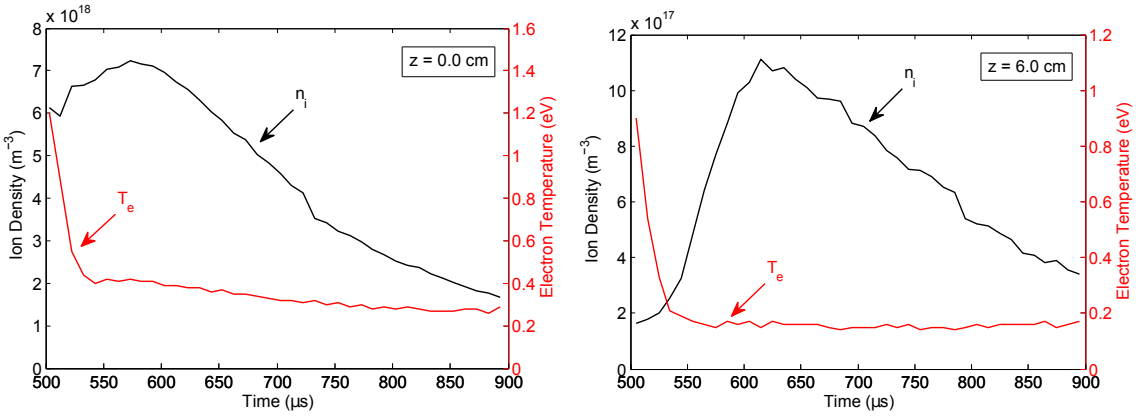

Figure 5.8: $n_i(t)$ and $T_e(t)$ at $z = 0.0$ cm (left) and $z = 6.0$ cm (right) during the afterglow, measured by analyzing the full Langmuir probe I-V curve. The RF power was turned off at $t = 500$ μs. The fast gas valve was used with $V_{gas,RF} = 550$ V, and the bias field coil and solenoid were turned on.

$n_e\sqrt{T_e}$ should decrease monotonically in the afterglow of an RF discharge. However, it was apparent from the probe data that some exotic process not considered in these models was important in our pre-ionization source. The effect is illustrated in Fig. 5.7, which shows $I_{sat.}(t)$ at $z = 6.7$ cm (out in the main vacuum chamber in front of the jet experiment electrodes) measured during discharges with four different RF pulse lengths. After an initial burst of ionization at the initiation of the discharge, the plasma density was low at the probe location until $t \sim 220$ μs, when the bulk of the expanding plasma reached the probe. After the main density peak, $I_{sat.}$ decayed, but in all four cases it rose again after RF turn-off to 20–40% of its original peak value.

Fig. 5.8 confirms that the afterglow $I_{sat.}$ rise was due to an increase in the ion density rather than the electron temperature—T_e fell rapidly to < 0.5 eV in the first ~ 30 μs after RF turn-off and did not rise again. For the case with a 500 μs RF pulse shown in Fig. 5.8, the density at $z = 6.0$ cm increased by more than a factor of 5 from its minimum value at $t = 500$ μs. The relative increase at $z = 0.0$ cm (at the output of the RF source tube) was smaller, but the absolute magnitude of the density increase was $\sim 1 \times 10^{18}$ m^{-3} at both locations[4].

[4]Given that we found in Sec. 5.1 that the gas pressure in the antenna region was $p_{Ar} \approx 460$ mTorr when the fast gas valve was used with $V_{gas,RF} = 550$ V, it seems likely that the pressure was greater than 60 mTorr at $z = 0.0$ cm, and possibly at $z = 6.0$ cm as well. Therefore, the Langmuir probe measurements may have underestimated n_i due to collisional effects (see Sec. D.2), so the density values shown in Fig. 5.8

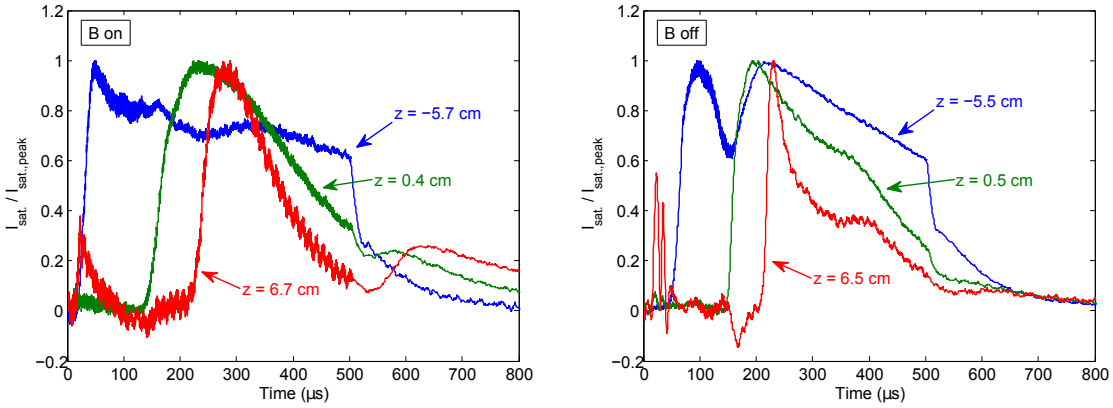

Figure 5.9: Ion saturation current near the RF antenna (blue), at the end of the discharge tube (green), and out in the main chamber (red), normalized to its peak value at each location, for discharges with the bias and solenoid fields on (left) and off (right). The RF power was turned on from $t = 0$–500 μs, and the fast gas valve was used with $V_{gas,RF} = 550$ V.

There are two basic possible explanations for the observed behavior: either plasma was confined deep in the discharge tube during the main discharge period and then released when the RF power was turned off, or new plasma was created during the afterglow. The confinement interpretation was initially favored, based in part on the fast camera images shown in Figs. 4.2 and 4.3, which gave the impression that plasma was flowing out of the discharge tube after RF turn-off, and also on the apparent lack of an energy source to power new ionization. However, we showed in Sec. 4.2 that the camera images could be deceptive, and indeed, no confinement mechanism could be identified that was consistent with the data. Furthermore, there was in fact a substantial amount of energy stored in excited neutral atoms—potentially enough to account for the observed density rise, as we will see in Sec. 5.2.2.

One candidate process that could have caused confinement was the ponderomotive force [4, p. 501], a nonlinear effect that pushes plasma away from regions where there is a high RF electric field. If for some reason there had been a peak in the RF field near the front of the discharge tube (at the end of the antenna, for example), then the plasma might have been confined in the tube while the RF power was on, and then allowed to escape once the power was turned off. Ponderomotive plasma confinement has been used to reduce axial losses in

should be taken as a lower limit on the true density.

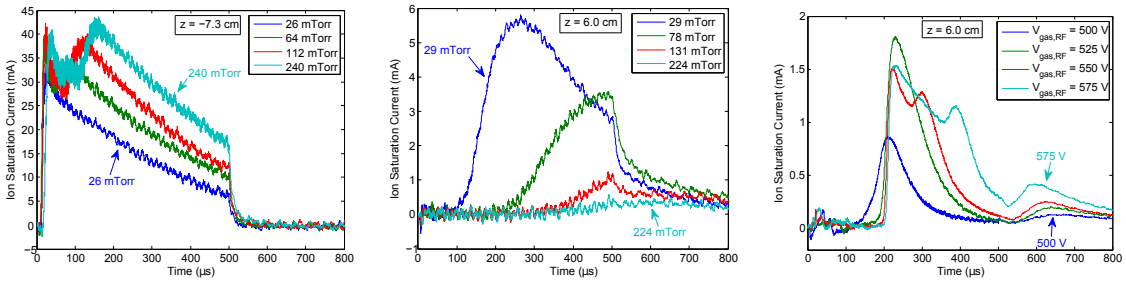

Figure 5.10: Left and Center: Ion saturation current inside the RF antenna ($z = -7.3$ cm) and out in the main chamber ($z = 6.0$ cm) during experiments with a uniform argon gas pressure. Right: $I_{sat}(t)$ at $z = 6.0$ cm during experiments with the fast gas valve used. In all cases, the RF power was turned on from $t = 0$–500 μs, and the bias magnetic field was applied ($V_{bias} = 80$ V, $V_{sol.} = 0$ V).

open-ended magnetic confinement fusion devices such as mirror machines (the technique is often called "RF plugging") [115, 116]. The expression for the ponderomotive force for each species in a magnetized plasma has a resonance near $\omega = \omega_{c\sigma}$ [117], so the effect can be quite strong if the applied RF frequency is chosen to be near the cyclotron frequency. In our experiment, however, the RF frequency $\omega \approx 8.5 \times 10^7$ rad./s was near neither the ion ($\sim 2.4 \times 10^5$ rad./s) nor the electron ($\sim 1.8 \times 10^{10}$ rad./s) cyclotron frequency (assuming $B \approx 0.1$ T near the center of the bias field coil), so the resonant effect was not expected to play a role. The Langmuir probe was used to look for a peak in the RF electric field by measuring the amplitude of the RF signal (as in Fig. 3.5) at many different axial locations; however, no obvious peak was found, so ponderomotive confinement was ruled out as a likely cause of the observed downstream density rise after RF turn-off.

Several observed trends were relevant for understanding the cause of the afterglow density rise. Fig. 5.9 shows a subset of the data from Fig. 4.10, rescaled to show the magnitude of the afterglow density rise (if present) relative to the peak density obtained at each location while the RF power was on. The relative size of the density rise was larger out in the main vacuum chamber (positive z) than inside the discharge tube (negative z), and $I_{sat.}(t)$ near the antenna region (blue curves in Fig. 5.9) decreased monotonically after RF turn-off. A slight afterglow density rise was visible at $z = 6.5$ cm in the unmagnetized discharges shown in the right panel, but it was much smaller than the corresponding effect in discharges with the bias field turned on (left panel).

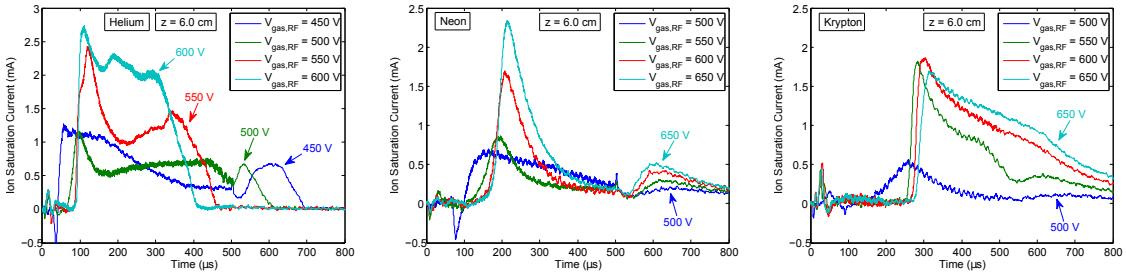

Figure 5.11: Ion saturation current at $z = 6.0$ cm for helium (left), neon (center), and krypton (right) plasmas. In all cases, the RF power was turned on from $t = 0$–500 μs, the fast gas valve was used, and the bias magnetic field was applied ($V_{bias} = 80$ V, $V_{sol.} = 0$ V).

No clear afterglow density increase was measured in experiments with a uniform gas pressure in the chamber, as shown in Fig. 5.10. Apparently the nonuniform pressure distribution set up by the fast gas valve was critical for enabling the phenomenon to occur. The right panel of Fig. 5.10 shows $I_{sat.}(t)$ during discharges with a range of fast gas valve voltages used, for comparison with the uniform pressure data[5].

When the fast gas valve was used, an afterglow density peak could also be seen in plasmas formed using helium, neon, or krypton gas instead of argon. Examples are shown in Fig. 5.11. Interestingly, in helium the effect was only visible for low $V_{gas,RF}$, while the opposite was true for the other gases (high $V_{gas,RF}$ was required). Experiments were also carried out with hydrogen, deuterium, and nitrogen, but a high-density plasma could not be created when the fast gas valve was used, as noted in Sec. 3.4.4, and thus no afterglow density increase was observed. It is possible that the same physical process responsible for the afterglow density peak was also critical for allowing the discharge to transition from its initial low-density mode of operation to a high-density inductively coupled mode (see Sec. 3.4.1), and this process may have occurred only in noble gases.

[5] Although the lowest gas bank voltage shown in the right panel of Fig. 5.10 ($V_{gas,RF} = 500$ V) produced a pressure $p_{Ar} \sim 380$ mTorr in the RF discharge tube (see Fig. 5.3), which is higher than any of the uniform pressures tested, the pressure out in the main chamber at $z = 6.0$ cm was almost certainly less than half of this value due to radial expansion of the gas puff exiting the discharge tube. Therefore, comparison between the data shown in the center and right panels of Fig. 5.10 is justified.

5.2.2 Pooling Ionization

The electron-impact ionization rate was extremely low in the afterglow because the electron temperature was below 0.5 eV (see Figs. 5.8 and 4.22), and the ionization rate coefficients depended exponentially on T_e (see Table 3.1). However, ionization can also occur as the result of a collision between two excited neutral atoms if the sum of their energies above the ground state exceeds the ionization energy. The most common example of this process, which is known as "energy pooling", is metastable-metastable ionization:

$$\mathrm{Ar_m} + \mathrm{Ar_m} \rightarrow \mathrm{Ar^+} + \mathrm{Ar} + \mathrm{e^-} + 7.5\ \mathrm{eV}, \tag{5.2}$$

where the excess energy is carried away by the free electron.

Pooling ionization is always taking place in an argon gas discharge, but it is relatively unimportant compared to electron-impact ionization as long as the electrons are being heated to several eV by an external power source. However, unlike electron-impact ionization, energy pooling can continue to produce new ions even after the power source has been turned off, thanks to the long-lived nature of metastables. Furthermore, since the ambipolar diffusion coefficient is proportional to T_e (see Eq. 4.12), the loss rate of plasma to the walls falls dramatically in the afterglow. It is then possible for the pooling ionization rate to temporarily exceed the loss rate, in which case the density grows. This effect was first observed in helium and neon microwave discharges at 1.6–3.1 Torr by Biondi [118], and afterglow density rises have since been observed in RF discharges at 0.1–1 Torr by several other authors [119, 120, 121]. These studies measured $n_e(t)$ using a variety of techniques including microwave interferometry, Langmuir probes, and monitoring changes in the resonant frequency of a cavity containing the plasma, so it is clear that the measured density increases were real and could not simply be attributed to anomalous probe performance in the afterglow. Density rises in the afterglow have been most commonly observed in helium discharges: Greenberg and Hebner [119] and Overzet and Kleber [121] both saw n_e increase by a factor of ~ 3 after RF turn-off with helium but saw little or no density rise with argon. Gamez and Bogaerts [122] found that n_e decreased monotonically in the afterglow of pulsed argon glow discharges at $p_{Ar} = 1$–3 mTorr. However, Ohtsu et al. [120] did see afterglow

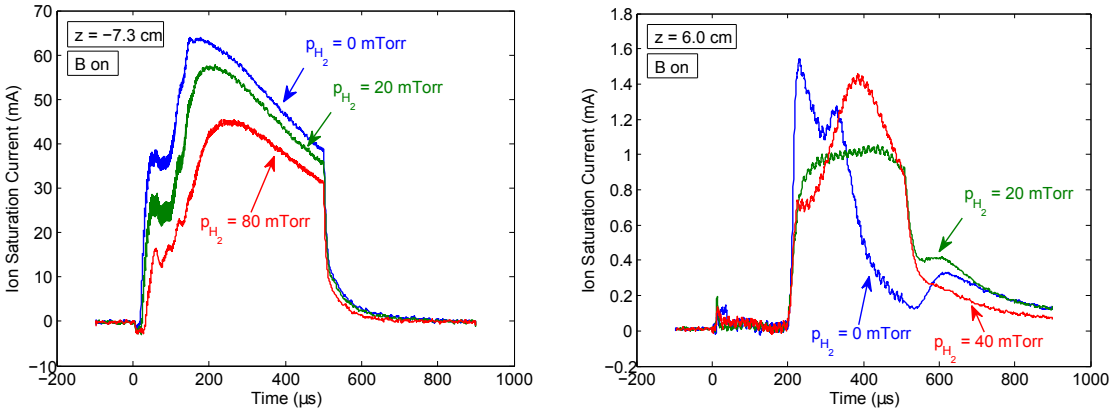

Figure 5.12: Ion saturation current inside the RF antenna (left) and out in the main vacuum chamber (right) during experiments with a uniform hydrogen backfill and argon supplied to the RF discharge tube using the fast gas valve ($V_{gas,RF} = 550$ V). The RF power was turned on from $t = 0$–500 μs, and the bias magnetic field was applied ($V_{bias} = 80$ V, $V_{sol.} = 0$ V).

density increases of up to an order of magnitude in argon discharges.

In order to test whether pooling ionization could be responsible for the afterglow density rise in our RF discharge, we tried introducing various amounts of hydrogen gas into the chamber while also supplying argon to the RF discharge tube using the fast gas valve. Kenty [111] suggested that the presence of H_2 in an argon discharge will tend to depopulate the Ar metastable state, a fact that was confirmed in more recent numerical simulations by Bogaerts [123], who found that adding a hydrogen concentration of only 5% to a glow discharge with $p_{Ar} = 560$ mTorr reduced the peak n_m by a factor of ~ 10. The rate coefficients for de-excitation of an argon metastable by collisions with an H_2 molecule or H atom are $k_{H_2} \approx 10^{-16}$ m^3/s and $k_H \approx 2 \times 10^{-16}$ m^3/s, respectively [124]. Therefore, with a hydrogen partial pressure of 30 mTorr ($n_{H_2} = 10^{21}$ m^{-3}), the mean lifetime of an argon metastable atom is < 10 μs.

The results of the experiments with argon-hydrogen[6] mixtures are shown in Fig. 5.12. In the left panel, we see that adding hydrogen to the argon discharge moderately decreased the plasma density inside the antenna, but the time-dependence remained largely unchanged. Out in the main chamber, however, there were more drastic effects (right panel), probably

[6] A gas species correction factor of 0.4 was applied to the hydrogen pressures measured by the thermocouple gauge, based on calibration of the thermocouple for H_2 using a capacitance manometer from the Caltech ice dusty plasma experiment [86].

because the argon pressure produced by the fast gas valve was lower at this location and thus the relative hydrogen concentration was higher. The size of the afterglow density peak was smaller relative to the density prior to the rise with $p_{H_2} = 20$ mTorr than it was with no hydrogen present, and with $p_{H_2} = 40$ mTorr the afterglow density rise disappeared altogether. These results suggest that pooling ionization may have been responsible for the observed behavior in the afterglow. Experiments were also carried out in which the chamber was filled uniformly with argon at 0–40 mTorr before additional argon gas was supplied to the discharge tube using the fast gas valve. The afterglow density increase persisted, confirming that only a hydrogen gas fill would impede the effect.

From Fig. 5.8, the observed rate of increase of the ion density in argon afterglows was $\partial n_i/\partial t \sim 10^{22}$ m^{-3}/s. Okada and Sugawara [125] measured the cross section for metastable-metastable ionization to be $\sigma_{mmi} = 1.35 \times 10^{-17}$ m^2. Assuming a typical relative velocity $v_r = 500$ m/s between the colliding metastable atoms ($T_g \approx 0.05$ eV), the rate coefficient[7] was $K_{mmi} \approx 7 \times 10^{-15}$ m^3/s. The pooling ionization rate per unit volume is $K_{mmi} n_m^2$, so in order to account for the measured $\partial n_i/\partial t$ in the afterglow, the metastable population density needed to be $n_m \approx 10^{18}$ m^{-3}. On the other hand, given that two metastables are destroyed in every pooling ionization reaction, an initial population density $n_m \gtrsim 2 \times 10^{18}$ m^{-3} was required in order to ultimately increase n_i by 10^{18} m^{-3} as in Fig. 5.8. These are plausible metastable densities, although larger than the downstream values of n_m predicted by the 1D discharge model from Sec. 4.4.2 for uniform gas pressures below 300 mTorr (see Fig. 4.24).

A possible problem for the pooling ionization hypothesis is that the expected rate of destruction of metastable atoms appears to be too high to explain the data, even in pure argon discharges. The dominant loss process for metastables in the afterglow was electron-impact transitions to the $4s$ resonant state followed by radiative decay to the ground state; the rate for the metastable-to-resonant transition was $\nu_{mr} = K_{mr} n_e$, where $K_{mr} = 2 \times 10^{-13}$ m^3/s (see Table 3.1). Therefore, with $n_e \approx 5 \times 10^{17}$ m^{-3} (a typical value during the afterglow density rise—see the right panel of Fig. 5.8), the metastable lifetime was only

[7] Elsewhere in the literature [126, 127], a rate coefficient $K_{mmi} \approx 6 \times 10^{-16}$ m^3/s for argon metastable-metastable ionization has often been adopted. However, this value was actually inferred from cross section measurements taken in other noble gases [128, 129] and thus it may not be accurate for argon.

$\nu_{mr}^{-1} \approx 10$ μs. However, the plasma density in the afterglow didn't peak until ~ 100 μs after RF turn-off, so some metastable atoms must have survived this long, if they were indeed responsible for the density increase (we have not identified any likely source of new metastables in the afterglow other than three-body recombination, which can be neglected in this discussion since recombination followed by pooling ionization did not lead to a net increase in the ion density). It is notable that all other instances of afterglow density rises due to pooling ionization that we know of [118, 119, 120, 121] occurred in plasmas with $n_e \leq 5 \times 10^{16}$ m^{-3}, so the metastable lifetime in the afterglow was 100 μs or longer.

Based on the results of experiments with argon-hydrogen mixtures shown in Fig. 5.12, it seems clear that atomic processes producing new ionization were the fundamental cause of the afterglow density rise in our RF discharge. However, the detailed sequence of processes involved, which may have been more complex than pooling ionization alone, remains to be conclusively determined. Preliminary numerical calculations were carried out in which pooling ionization terms were added to the 1D discharge model equations in Sec. 4.4.2: only very small afterglow density increases were observed in simulations of unmagnetized discharges with uniform gas pressure. This result is consistent with the data shown in Figs. 5.9 and 5.10, but calculations with nonuniform pressure and radial confinement will be required if the dramatic afterglow density peak observed in discharges with the bias field and fast gas valve used is to be reproduced. Direct measurements of the time-dependent metastable density (for example, using laser absorption) would be very valuable for confirming or refuting the proposed pooling ionization mechanism.

5.2.3 Bi-Maxwellian Electron Energy Distribution

Although the bulk electron temperature in the afterglow was 0.2–0.4 eV (see Fig. 5.8), some of our Langmuir probe measurements clearly revealed the presence of hotter electrons as well. An example is shown in the left panel of Fig. 5.13—the $\ln|I_e|$ curve cleanly separates into two linearly segments, indicative of an approximately bi-Maxwellian electron energy distribution (the data analysis procedure is explained in detail in Sec. D.6). One possible source of hot electrons in the afterglow is metastable-metastable ionization: each event produces a free electron with $E \sim 7.5$ eV (see Eq. 5.2), so a distinctive peak may be

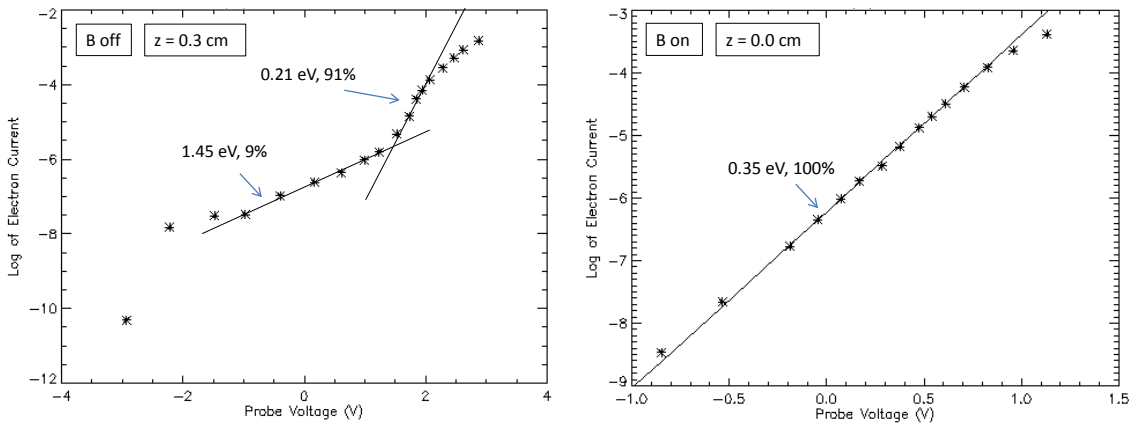

Figure 5.13: Electron temperature fits to $\ln|I_e|$ measured by the Langmuir probe near the output of the RF discharge tube. T_e is labeled for each Maxwellian component of the distribution function, along with the percentage of the electrons belonging to each population. Left: Probe measurement averaged from $t = 170$–180 μs for an unmagnetized discharge in which the RF power was turned off at $t = 100$ μs. Right: Probe measurement averaged from $t = 670$–680 μs for a discharge with the bias field coil and solenoid turned on, and the RF power turned off at $t = 500$ μs. The fast gas valve was used with $V_{gas,RF} = 550$ V in both cases.

visible in the measured distribution function if the process is occurring at a high rate [121]. However, the temperature of the "hot" component in our experiment was only 1–2 eV, so it was not definitively associated with energy pooling. Nevertheless, it appears that some process was reheating a portion of the electrons. In the absence of reheating, evaporating cooling was expected to reduce T_e to below 0.5 eV within the first 50 μs after RF power turn-off (see Figs. 4.22 and 4.26). Furthermore, the electron-electron collision frequency with $n_e \sim 10^{18}$ m^{-3} and $T_e \sim 1.5$ eV was $\nu_{ee} \sim 2 \times 10^7$ s^{-1} [4, p. 596], so the two electron populations would have quickly equilibrated unless new hot electrons were continuously being created.

Interestingly, bi-Maxwellian electron distributions were only observed in experiments with no magnetic field—in the magnetized discharges that exhibited a large afterglow density rise, the Langmuir probe I-V curves were always fit well by a single T_e distribution, as shown in the right panel of Fig. 5.13. In the $B = 0$ case, the fraction of hot electrons decreased in time and was lower further from the RF antenna—these trends are illustrated in Fig. 5.14. Further investigation into the conditions necessary for a bi-Maxwellian distribution to develop may yield insights into the dominant atomic processes in the afterglow and

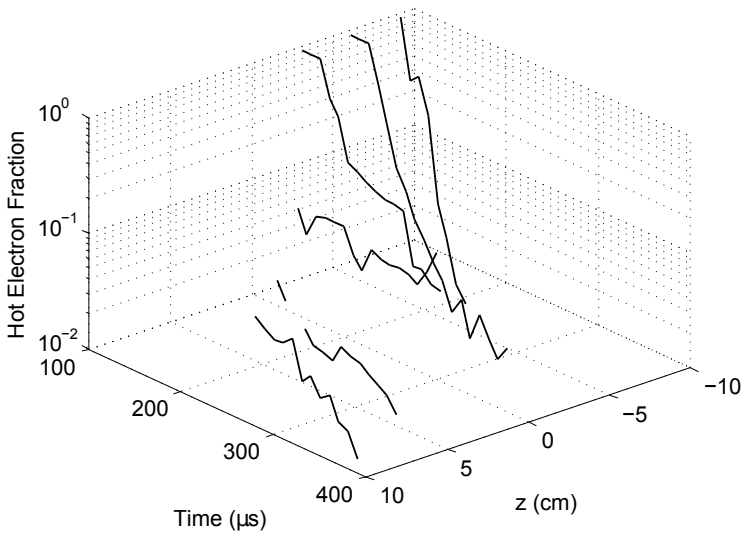

Figure 5.14: "Hot" (> 1 eV) electron fraction during the afterglow for unmagnetized discharges with the fast gas valve used. The RF amplifier was turned off at $t = 100$ μs.

could possibly provide useful information for understanding the afterglow density peak.

Chapter 6

Pre-Ionized MHD-Driven Jets

This chapter will describe the MHD-driven jets created with the aid of the RF pre-ionization system. Secs. 6.1, 6.2, and 6.3 cover the diagnostics used to study the jets, the effects of pre-ionization on the initial plasma breakdown, and the impact of the jet structure on the discharge circuit behavior, respectively. The reader who is mostly interested in results relevant to astrophysics or basic plasma physics may choose to skip to Sec. 6.4; note, however, that detailed knowledge of the diagnostic techniques described in Sec. 6.1 is invaluable for understanding the data.

Pre-ionized jet experiments were carried out primarily with argon gas, which produced the most interesting results. In principle, the gross jet behavior should have been similar for all gas species, as in the original Caltech MHD-Driven Jet Experiment (see [130], for example); however, the relative ease of breaking down argon in either DC or RF electric fields (see Fig. 1.10) allowed for a broader region of parameter space to be accessed than was possible with other gases.

As discussed in Sec. 1.7, the primary motivation for pre-ionization was to create hotter, faster MHD-driven jets and spheromaks with increased relevance to astrophysics and fusion plasmas. These goals were achieved, to some extent—Secs. 6.4.2 and 6.4.3 will show that the pre-ionized jets were indeed faster and hotter than those created previously. However, the density, temperature, and velocity differed by less than an order of magnitude from the corresponding properties of jets created without pre-ionization. The main impediment to further improvements will be discussed in Sec. 6.6.

Fast camera images of a typical argon jet formed without pre-ionization are shown in

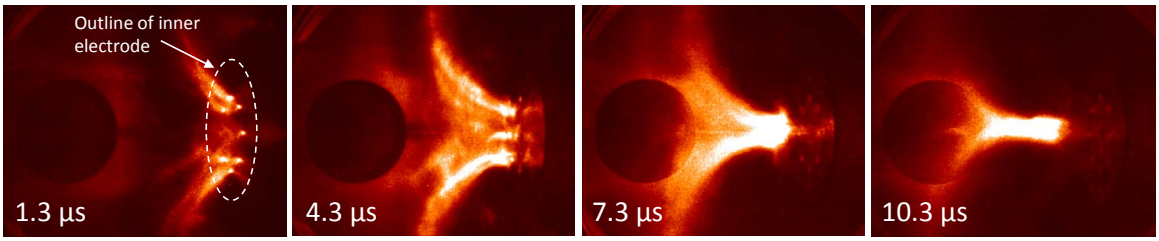

Figure 6.1: Imacon camera images of an argon jet formed without pre-ionization. The experiment parameters for this shot were $V_{main} = 5$ kV, $V_{bias} = 80$ V, $V_{gas,inner} = 700$ V, $V_{gas,outer} = 750$ V, and $V_{gas,RF} = 0$ V.

Fig. 6.1 (see also Fig. 1.5 for images of a typical hydrogen jet), while the evolution of a pre-ionized argon jet is shown in Fig. 6.2. The morphology of the pre-ionized jet is notably different, with a bright, narrow central column near the electrodes and a more diffuse flared structure at the front of the jet. Detailed investigations (see Secs. 6.4.3 and 6.5.2) revealed that the different location of neutral gas injection (through the RF discharge tube output at the center of the inner electrode rather than through the 8 holes located at $r = 4.8$ cm), rather than the lower initial gas pressure, was primarily responsible for the difference in jet structure between the pre-ionized and non-pre-ionized cases. This result has possible implications for astrophysical jets, suggesting that the intial mass distribution above the accretion disk may be critical for determining the ultimate jet properties.

Although the installation of the pre-ionization system altered the jet morphology, the fundamental driving mechanism was still the axial gradient in the toroidal magnetic field pressure (or equivalently, the hoop force exerted by the poloidal current), and many aspects of the jet evolution were similar to that described in Fig. 1.5. For example, the pre-ionized jets underwent a current-driven kink instability (see Sec. 1.2), as shown in the left panel of Fig. 6.3. The appearance of the kinking laboratory jet is strikingly similar to that of the AGN jet 3C31 shown in the right panel of the figure, and indeed, recent numerical simulations [131] have suggested that the wiggling structures observed in 3C31 and other AGN jets are manifestations of the kink instability. Systematic study of the kinking behavior in our pre-ionized laboratory jets and quantitative comparisons with astrophysical jets have not yet been carried out, however.

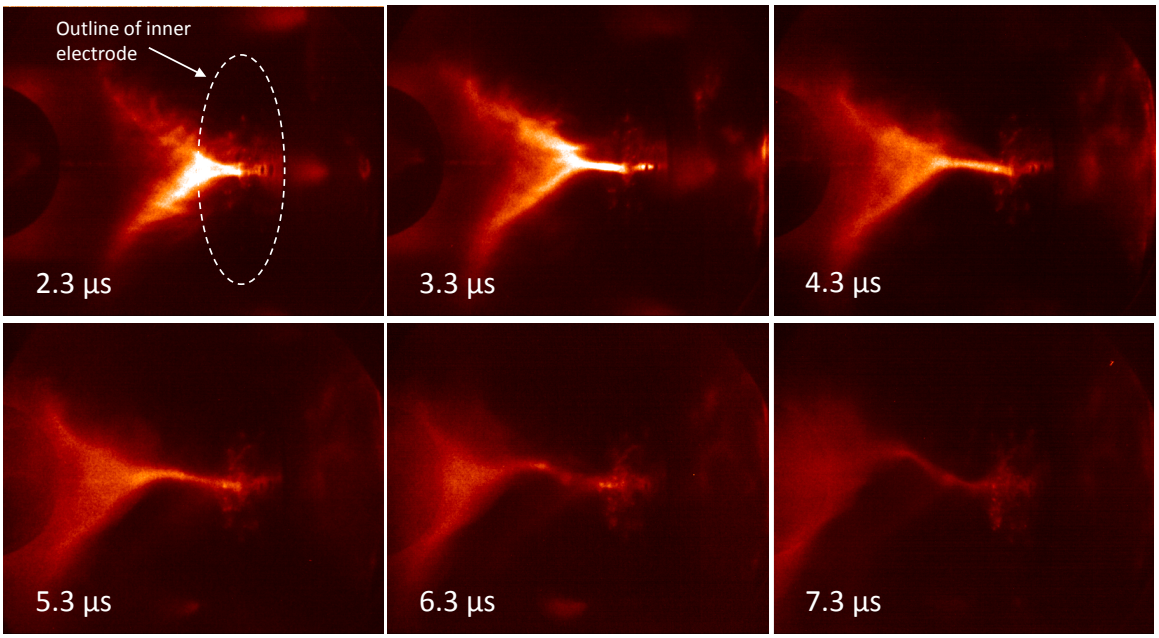

Figure 6.2: Imacon camera images of a pre-ionized argon jet formed with $V_{main} = 4$ kV, $V_{bias} = 80$ V, $V_{gas,RF} = 550$ V, $V_{gas,inner} = 460$ V, and $V_{gas,outer} = 709$ V.

6.1 Jet Diagnostics

6.1.1 Optically Coupled High Voltage Probe

The voltage between the anode and cathode of the pre-ionized jet experiment was measured with a novel floating wideband high voltage (HV) probe designed by Xiang Zhai and Paul M. Bellan [132]. The probe was electrically isolated from the VME data acquisition system (see Sec. 1.6.5) in order to avoid ground loops and to protect the VME from hazardous high voltages. Solar panels illuminated by the room lights charged up a capacitor to power the probe for ~ 1 ms—much longer than the ~ 50 μs time interval of interest for the V_{gun} measurement. The measured voltage was attenuated by a factor of ~ 3000 by a capacitive voltage divider and then transmitted to the VME as an amplitude modulated optical signal.

A photo of the HV probe installed on the chamber is shown in the left panel of Fig. 6.4. The probe was calibrated by applying a low voltage (< 5 V) waveform at the output of the voltage divider; this input signal was compared to the optical receiver output to determine the calibration factor, taking into account the known values of the voltage divider capacitances (see the right panel of Fig. 6.4). The probe calibration was verified by comparing the

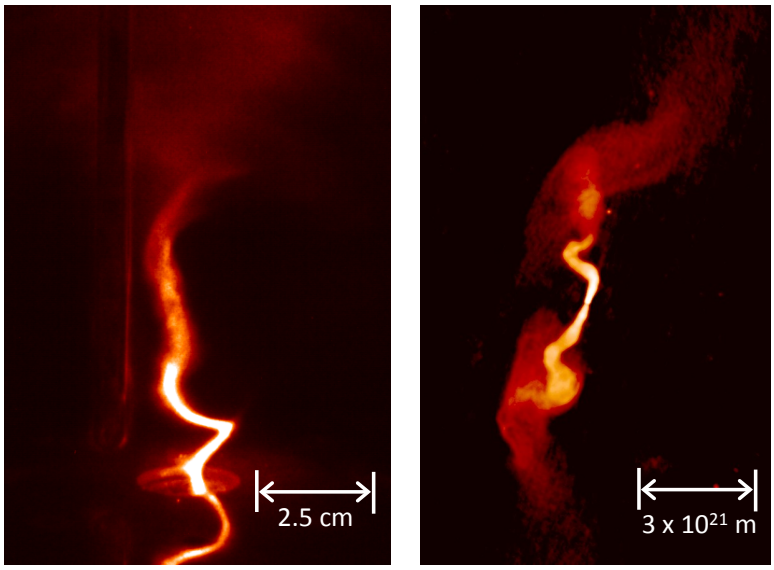

Figure 6.3: Left: An argon pre-ionized jet in the lab undergoing a kink instability. The mirror image of the kink structure at the very bottom of the image is a reflection off of the copper electrode. Right: Very Large Array (VLA) 20 cm (1.4 GHz) radio image of the 3C31 AGN jet. The length scale shown is a rough estimate. Image courtesy of NRAO/AUI.

probe's output during plasma shots with measurements made by a commercial Tektronix 6015A HV probe isolated from the VME by an optical link. The DC offset in the optical receiver output was determined for each shot by averaging over an interval of time prior to the triggering of the main bank.

The voltage divider and optical transmitter circuit were very well shielded from electrical noise (see reference [132] for a detailed description of the shielding geometry). However, while the probe operated with a noise level at or below the resolution of the VME (≤ 30 V) during standard discharges with no pre-ionization, the output signal included significant RF pickup when the 13.56 MHz RF amplifier was turned on. The pickup was traced to imperfect shielding of the optical receiver circuit—in order to remedy the problem, the entire receiver circuit including its 9 V battery and on-off switch were placed inside a hermetic metal box, and semi-rigid coaxial cable was used in place of standard RG-58 cable for connections between the receiver box and the VME and between the HV capacitor and the transmitter circuit.

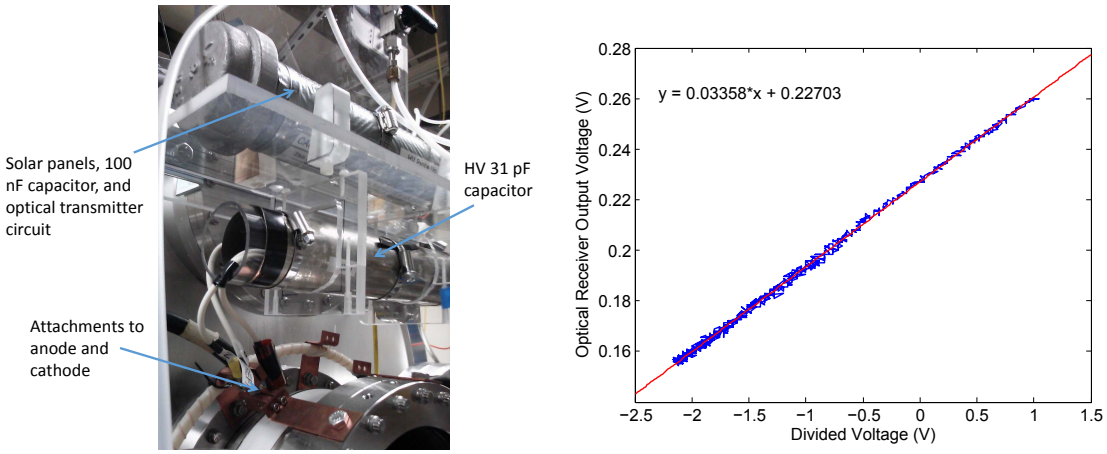

Figure 6.4: Left: Photo of the high voltage probe installed on the MHD-driven jet experiment. Right: High voltage probe calibration. A function generator was used to apply a low voltage sine wave signal across the 100 nF capacitor on the transmitter side, and the voltage output by the optical receiver was recorded. Multiplying the calibration factor derived from the regression shown by (31 pF) / (100 nF + 31 pF) gave an overall calibration factor $V_{out} = \left(1.04 \times 10^{-5}\right) \times V_{actual}$.

6.1.2 Rogowski Coil

The main bank current was measured with a Rogowski coil [8, p. 245] that encircled the re-entrant port. This diagnostic consisted of a coil wound on a length of flexible plastic tubing (essentially an air core transformer), which output a voltage equal to the rate of change of the magnetic flux through its windings. A passive integrator circuit was used to convert $V_{coil}(t)$ to a quantity proportional to the gun current $I(t)$. Details of the Rogowski coil design and calibration are provided in Appendix H.

6.1.3 High Speed Camera

Images of visible (and infrared) light emission by the plasma were taken using a DRS Hadland Imacon 200 high speed camera. This camera had seven individual intensified charge-coupled device (ICCD) modules, each of which could take two images in < 1 μs thanks to a fast charge transfer process (an eighth ICCD module inside the camera was not operational when the experiments described here were carried out), so a 14-frame movie of the jet evolution could be recorded. Each channel had 10-bit dynamic range and 1200×980 pixel spatial resolution. A beam splitter directed light entering the camera to each of the

ICCD detectors, leading to a factor of eight reduction in the incident intensity. Nevertheless, when photographing the extremely luminous jets, sufficiently bright images could always be obtained with a 20 ns exposure time. Although interframe times of < 100 ns were possible, significant ghosting (in which a dimmer version of the first image taken by a given detector appeared superimposed on the second image) and reverse ghosting (in which the first image did not finish reading out in time, and the second image appeared superimposed on the first as a result) were observed for interframe times shorter than 300 ns, so these were rarely used[1].

The ability to make a movie of a single shot was quite valuable; it saved time since the experiment could be fired no more frequently than once every 1–2 minutes, and it also allowed for the study of certain aspects of the jet behavior, such as the fast pinching described in Sec. 6.5.1 and the kink instability introduced in Sec. 1.2, that were not precisely reproducible from shot to shot. Quantitative analysis of the Imacon images was not convenient because the camera's gain and background signal level differed from channel to channel, and these changed each time the camera was turned on. Nevertheless, such analysis was possible if these spurious effects were carefully accounted for and if the camera gain was set low enough that the images were not saturated.

In contrast to the situation with the expanding RF plasma described in Sec. 4.2, for the jet experiment, electron density measurements using interferometry [39] and Stark broadening [130] have shown that the brightness of camera images generally traces the plasma density distribution. This is true even for hydrogen plasmas, in which the light emission is mostly from neutral atoms swept along with the jet or created by charge exchange. However, bright spots that do not correspond to density enhancements may appear due to local magnetic reconnection that heats the electrons [130], [133, p. 8], and magnetic probe measurements have shown that a significant fraction of the gun current flows outside the visible jet structure (see Sec. 6.5.2 and also [134, p. 83]). Therefore, caution must be exercised when interpreting the camera images.

[1]The trigger times for each of the 14 frames could be set independently, so if a very short interframe time was desired, the first seven frames could be triggered at the desired interval, with a longer time gap specified before the eighth frame in order to avoid reverse ghosting.

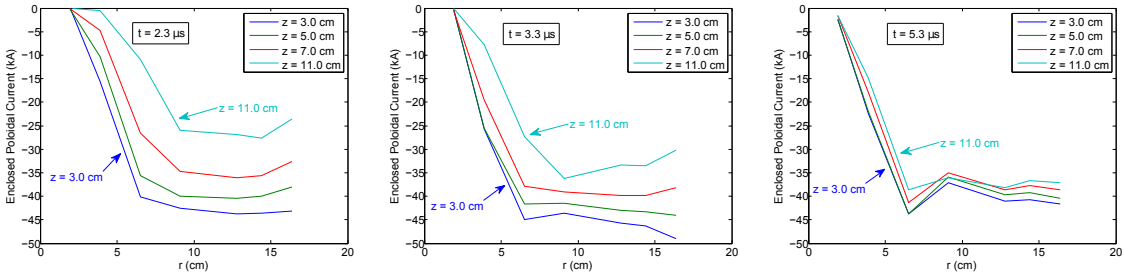

Figure 6.5: Measurements of the poloidal current profile $I(r)$ for hydrogen jets with $V_{main} = 4$ kV, $V_{bias} = 80$ V, $V_{gas,inner} = 600$ V, $V_{gas,outer} = 686$ V, and no pre-ionization. The toroidal magnetic field was measured, and the enclosed current was calculated from Ampere's law by assuming axisymmetry: $I(r) = 2\pi r B_{tor.}(r)\,/\mu_0$.

6.1.4 Magnetic Probe Array

The three-dimensional magnetic field in the plasma was measured with a 12-channel magnetic probe array [135] that was built by Shreekrishna Tripathi based on a design by Romero-Talamás, Bellan, and Hsu [136]. The probe array consisted of four clusters of three orthogonally mounted commercial chip inductors (Coilcraft Inc., model 1008CS-472XGBB). The local magnetic field in the direction perpendicular to each inductor was related to the induced voltage across it by Faraday's law, $V_{coil} = -d\Phi_B/dt$. Since the inductors were small compared to the length scale for changes in B, the field was approximately constant over the area A of the inductor, so $d\Phi_B/dt \approx (NA)\, dB_\perp/dt$, where N is the number of coil turns, and

$$B_\perp = B_0 - \frac{1}{NA}\int_0^t V_{coil}(t')\, dt'. \tag{6.1}$$

The coil voltages were measured directly by the VME, and the integration to determine B was carried out numerically.

The ~ 6 μH self-inductance of each coil [136] led to a voltage drop that subtracted from the V_{coil} induced by the external field, but this effect was negligible for variations in the magnetic field with characteristic frequency $\omega \lesssim 10^6$ rad./s, since the corresponding inductive impedance $|Z_L| = \omega L \lesssim 6\ \Omega$ was much less than the 50 Ω impedance of the VME. The ~ 12 Ω resistance of each coil [136] also created a voltage divider effect that reduced the output voltage measured by the VME, but this frequency-independent effect was taken into account when an effective value of NA was determined during calibration

with a known magnetic field. Calibration of a single probe channel was carried out by the author and Bao N. Ha using a Helmholtz coil driven by a function generator[2]—the calibration factors obtained at $f = 50$ kHz, 100 kHz, and 500 kHz were within 3% of the value $NA = 1.21 \times 10^{-4}$ m^2 measured by Romero-Talamás, Bellan, and Hsu [136] using a capacitor discharge through a Helmholtz coil. These authors reported that the NA value was the same for all the coils in their probe to within $< 5\%$, with the small discrepancy between coils arising because of differences in the lead geometries and because of the finite inductance tolerance of the commercial chip inductors. Therefore, the calibration factor $NA = 1.21 \times 10^{-4}$ m^2 was used for all 12 probe channels in this work.

The L-shaped probe was inserted into the vacuum chamber through a port located at the midplane—when it was aligned along the z-axis, pointing toward the jet experiment electrodes, the end of the quartz tube housing the probe clusters was located ~ 0.8 cm from the electrodes, and the probe clusters were located at $z = 3.0$ cm, 5.0 cm, 7.0 cm, and 11.0 cm. The probe shaft could be slid into and out of the chamber to access radii between $r = 0$ cm and $r = 16.4$ cm, and it could also be rotated, but this was usually unnecessary due to the axisymmetry of the jet experiment.

Magnetic probe measurement of the poloidal current distribution in hydrogen jets created without pre-ionization are shown in Fig. 6.5. These measurements are similar to those presented by Kumar [134, Figure 5.2]: the radius of the central current channel (i.e., the radius at which $I(r)$ stopped increasing) near the electrodes was ~ 6 cm, and $I(r)$ remained approximately constant between $r \approx 6$–16 cm, implying that the return current flowed mostly at $r > 16$ cm. The flaring of the jet was readily apparent at early times; by $t = 5.3$ μs, the flared jet front had propagated beyond $z = 11.0$ cm, and the current channel was fully collimated.

[2]The magnetic field at the center of a Helmholtz coil is $B = (4/5)^{3/2}\,\mu_0 nI/R$, where n is the number of turns in each half of the Helmholtz coil, I is the current through the coil, and R is the radius. For a sinusoidal input, the current is $I = V_{Helm.}/\omega L_{Helm.}$. Meanwhile, the voltage across a magnetic probe coil is $V_{probe} = -NA\omega B$. Combining these relationships, the calibration formula is $V_{probe} = -(NA)\left((4/5)^{3/2}\,\mu_0 n/L_{Helm.}R\right)V_{Helm.}$. For the Helmholtz coil used, $R = 4.5$ cm, $n = 5$, and $L_{Helm.} = 10.7$ μH, giving $NA = (0.107)\,V_{probe}/V_{Helm.}$ in S.I. units.

6.1.5 High Resolution Spectroscopy

UV and visible line emission from argon jets was measured using a JY Horiba 1000M spectrometer with a 1 meter focal length, 3600 grooves/mm diffraction grating, and an Andor DH520-25F-03 ICCD camera detector [137, Section 3.7]. Compared to the 0.5 meter monochromator used to study the RF plasma (see Sec. 3.1.2), this spectrometer had much higher spectral resolution (the dispersion varied from 3.6 pm/ICCD pixel at $\lambda = 500$ nm to 6.7 pm/pixel at $\lambda = 250$ nm—see [137, Figure 3.6]), so detailed line profiles and Doppler shifts could be resolved. The ICCD was capable of sub-microsecond exposure times but could only save a single image per shot.

The spectrometer was located in a separate lab from the pre-ionized MHD-driven jet experiment, on the other side of the building. Light from the plasma was transmitted to the entrance slit inside a ~ 1.3 mm core diameter optical fiber that ran down the hallway above the ceiling tiles (this fiber had been previously used in a high power laser-induced fluorescence system for another experiment). The trigger signals for the ICCD camera were transmitted by two additional fibers, and the computer that controlled the spectrometer and the camera was also operated remotely. The original spectrometer entrance optics designed by Gunsu S. Yun [137, Section 3.7] were retained; the end of the 1.3 mm fiber was attached inside a 0.5" OD plastic cylinder that could be easily mounted within the pre-existing system in place of the original 12-fiber bundle. Light of different wavelengths was dispersed across the ICCD in the horizontal direction, while the entrance slit was imaged in the vertical direction; since only one optical fiber was used for these experiments, the camera was operated in "full vertical binning" mode.

The transmission efficiency of the fiber decreased at UV wavelengths, with an ultimate cutoff (determined by tests with a continuum-emitting halogen lamp) at 280–285 nm. For most measurements a collimating lens was used to collect light from a localized region of the jet; the lens could only transmit wavelengths above ~ 320 nm. The fiber always viewed the plasma through the window on the chamber nearest to the jet experiment electrodes, with a line of sight that was nearly perpendicular to the jet.

6.1.5.1 Line Broadening

An electron collision with an excited atom or ion temporarily produces a local electric field that shifts its energy levels through the Stark effect. The cumulative effect of many such collisions is to produce "Stark broadening" of the line profile, along with additional wavelength shifts and profile distortions [137, Chapter 5]. The characteristic shape of a Stark broadened line is a Lorentzian profile [138, Section 10.6]:

$$\phi_L(\lambda) = \frac{1}{\pi} \frac{w_S/2}{(\lambda - \lambda_0)^2 + (w_S/2)^2}, \tag{6.2}$$

where λ_0 is the line center wavelength and w_S is the full-width at half-maximum (FHWM). For non-hydrogenic atoms and ions, the quadratic Stark effect applies[3], and w_S is directly proportional to the electron density:

$$w_S \approx w_m(T_e)\, n_e \tag{6.3}$$

where the temperature dependence of the Stark parameter w_m is usually relatively weak.

Emission lines can also be broadened by the Doppler effect due to the random thermal motions of the emitting species, which leads to a Gaussian line profile:

$$\phi_G(\lambda) = \sqrt{\frac{4 \ln 2}{\pi w_D^2}} \exp\left(\frac{-4 \ln 2\, (\lambda - \lambda_0)^2}{w_D^2}\right), \tag{6.4}$$

where the Doppler FWHM is

$$w_D = \lambda_0 \sqrt{\frac{8 \ln 2 k_B T_i}{m_i c^2}}. \tag{6.5}$$

Additional effective line broadening, known as instrumental broadening, is introduced by the optical system. The instrumental function is often approximately Gaussian, although it is not guaranteed to be. A final source of measurable line profile distortions in the Caltech experiments is Zeeman splitting, which is proportional to the magnetic field strength [139]. This effect was expected to be smaller than the others discussed here and will not

[3]Here the label "quadratic" refers to the fact that the term linear in the applied electric field vanishes when calculating the energy level shift using perturbation theory—it should not be confused with the dependence of the Stark width on density, which is in fact linear (see Eq. 6.3).

be considered further, but it could have possibly become important if the magnetic field strength was amplified to $B \gg 0.1$ T by the jet dynamics.

When multiple sources of broadening are present, the overall line profile is a convolution of the constituent profile functions. The convolution of two Lorentzians is another Lorentzian with FWHM $w_L = w_{L1} + w_{L2}$, and two Gaussians combine to yield a Gaussian with FWHM $w_G = \sqrt{w_{G1}^2 + w_{G2}^2}$. The convolution of a Gaussian profile and a Lorentzian profile is called a Voigt profile [140, p. 302]:

$$\phi_V(\lambda) = \int_{-\infty}^{\infty} \phi_G(\lambda')\, \phi_L(\lambda - \lambda')\, d\lambda' \propto \int_{-\infty}^{\infty} \frac{\exp\left(\frac{-4\ln 2(\lambda' - \lambda_0)^2}{w_G^2}\right)}{(\lambda - \lambda' - \lambda_0)^2 + \left(\frac{w_L}{2}\right)^2} d\lambda'. \tag{6.6}$$

By fitting this profile function to the measured shapes of spectral lines from MHD-driven jets, the Lorentzian and Gaussian FWHMs w_L and w_G were determined. The contribution to these FWHMs from instrument broadening was then subtracted off, leaving only the Stark and Doppler widths w_S and w_D, from which the electron density and ion temperature were calculated using Eqs. 6.3 and 6.4, respectively.

Voigt profiles were fit to the shapes of argon emission lines using IDL routines written by T. R. Metcalf [141] and D. M. Zarro [142]. The analysis focused on the Ar II lines at 372.931 nm and 434.806 nm; neither line had a particular large Stark broadening parameter w_m[4], but they were bright enough in our jets and sufficiently isolated from other lines to enable clean fitting to the line profiles (however, the 434.806 nm line exhibited asymmetric profile distortions when the plasma density was high that made the determination of n_e and T_i from the line shapes unreliable, so the 372.931 nm line data was ultimately used to derive the results presented in Sec. 6.5.1).

The instrument function was measured by observing emission lines from weakly ionized, low density spectral lamps, which were expected to have minimal Stark and Doppler broadening. The line shapes were nearly Gaussian, but Voigt profiles with a small Lorentzian component gave a superior fit away from the line center (in the line "wings"). With a 50 μm entrance slit width on the spectrometer, analysis of the Ar I lines at 394.90 nm and 416.42

[4]Averaging over measurements from a number of authors tabulated by Konjević et al. [143], we adopt the values $w_m = 2.0$ pm/10^{22} m^{-3} for the Ar II 372.931 nm line and $w_m = 2.7$ pm/10^{22} m^{-3} for the Ar II 434.806 nm line.

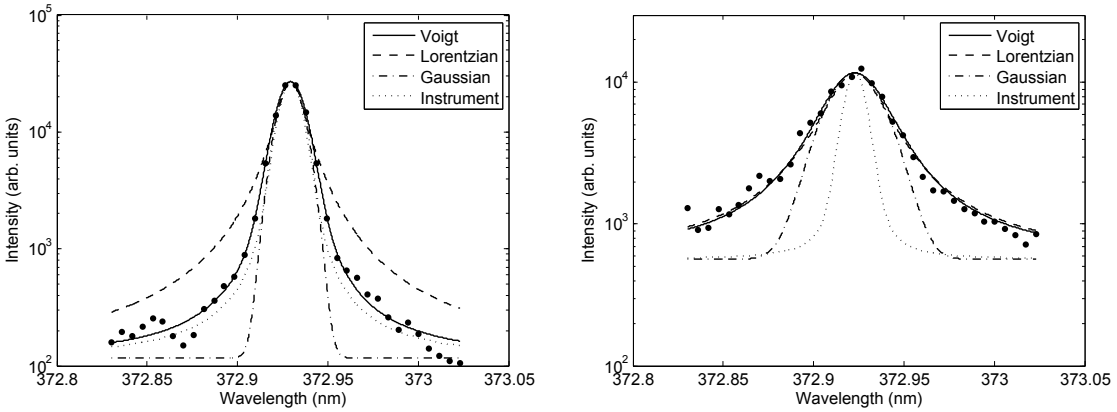

Figure 6.6: Examples of Voigt profile fits to the Ar II 372.931 nm line (data shown as dots). Lorentzian and Gaussian fits with the same amplitude, continuum level, and total FWHM (approximated from the Gaussian and Lorentzian components of the Voigt fit using $w_{total} \approx \sqrt{w_G^2 + w_L^2}$) are shown for comparison, and the Voigt profile fit to the instrument function is also shown. Both spectra were from pre-ionized jets ($V_{gas,RF} = 700$ V, $V_{gas,inner} = 0$ V, $V_{gas,outer} = 750$ V) at $z = 2.0$ cm. The left panel shows data taken at $t = 1.3$–2.3 μs, when the plasma density was low and the line shape was between Gaussian and Lorentzian (the Voigt profile fit gave $w_L = 4.4$ pm and $w_G = 15.3$ pm), while the right panel shows the approximately Lorentzian line shape ($w_L = 30.5$ pm, $w_G = 17.9$ pm) obtained with a high plasma density at $t = 4.3$–5.3 μs. The ICCD camera had a constant, non-uniform background level (typically 250-265 counts when the camera was cooled to $-10°$ C), which was subtracted off before making all profile fits.

nm gave the following Gaussian and Lorentzian instrumental FWHMs:

$$w_{IG} \approx 2.1 \text{ pixels} \quad ; \quad w_{IL} \approx 0.7 \text{ pixels.} \tag{6.7}$$

Examples of Voigt profile fits to the 372.931 nm emission line from pre-ionized jets are shown in Fig. 6.6, along with pure Lorentzian and pure Gaussian fits, which may be easily distinguished from one another because the Lorentzian function decays much more slowly away from the line center. Plotting the line profiles with a logarithmic y-axis was valuable for assessing the quality of the fit in the wings. At times when the electron density was low along the chosen line of sight, the measured line shape was between Gaussian and Lorentzian, as shown in the left panel of Fig. 6.6, while for the highest densities measured, the Stark broadening contribution dominated and the line shape was approximately Lorentzian (see the right panel of Fig. 6.6).

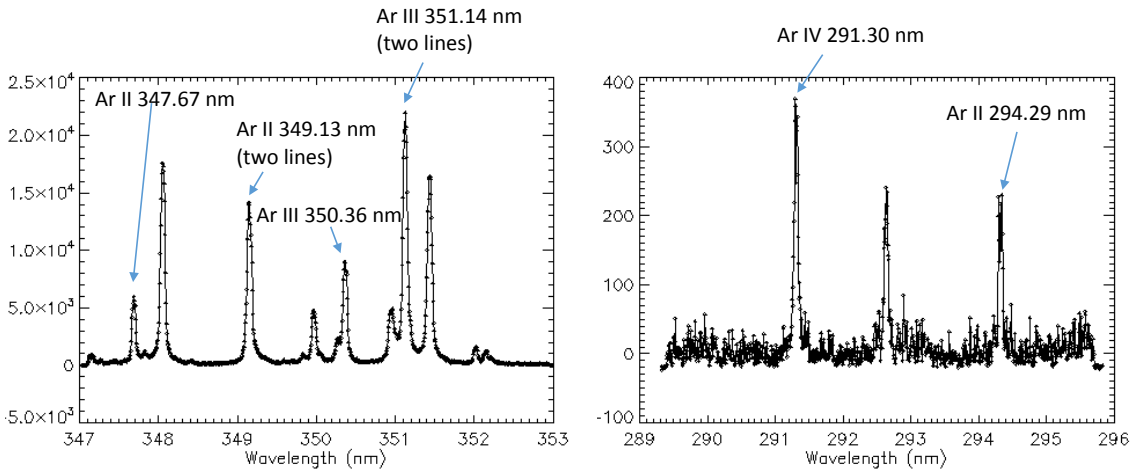

Figure 6.7: Sample argon jet spectra from shots with $V_{gas,RF} = 700$ V, $V_{gas,inner} = 0$ V, and $V_{gas,outer} = 750$ V. The emission lines used for line ratio calculations are labeled. The optical fiber was pointed directly at the base of the jet with no lens used, the ICCD was exposed from $t = 3.3$–4.3 μs, and the spectrometer entrance slit width was 300 μm.

6.1.5.2 Line Intensity Ratios

As discussed in Sec. 3.1.2, emission line intensity ratios contain information about the electron temperature and density and the ionization balance in a plasma, but the extraction of these parameters from the data is usually not straightforward. The MHD-driven jets had high enough density to be close in principle to the Local Thermodynamic Equilibrium (LTE) regime [74], and "partial LTE" (in which the populations of energy levels above some threshold level follow a Boltzmann distribution) [144, p. 129] has often been assumed in analysis of the Caltech experiments [130]. However, Fujimoto and colleagues [145, 105] showed that even energy levels that satisfy Griem's criterion for partial LTE will have populations well below the Saha-Boltzmann value if the plasma is in the ionizing phase, which may mean either that the ionization balance is changing in time or that collisional ionization is balanced by diffusive losses rather than by three-body recombination in a steady state situation (see Sec. 3.1.2 for more discussion). Perkins [133, Chapter 4] obtained compelling evidence that hydrogen plasmas in the Caltech Arched Flux Rope Experiment (which has similar plasma parameters to the MHD-driven jet experiment) were far from ionization equilibrium, so partial LTE is unlikely to apply in these experiments.

Although precise quantitative measurements of T_e and the ionization balance were not

possible, as in Sec. 3.4.2, line ratio measurements were useful for qualitatively tracking spatial and temporal variations in these parameters, and for making comparisons between different experiment configurations. The primary ratios utilized were [Ar III 351.14 nm] / [Ar II 349.13 nm], [Ar III 350.36 nm] / [Ar II 347.67 nm], and [Ar IV 291.30 nm] / [Ar II 294.29 nm]. These ratios were chosen because they were made up of two lines with similar wavelengths, which was advantageous for rough quantitative analysis because the wavelength-dependent response function of the spectrometer did not need to be known, and because the lines were sufficiently isolated from other argon lines from different ionization stages[5]. Sample spectra including these lines are shown in Fig. 6.7.

In calculating line intensity ratios, the quantity of interest is the area under each line profile (which is proportional to the total number of emitted photons and thus to the upper level population density for the associated atomic transition) rather than the height of the line peak. Therefore, curve fitting was necessary to calculate line ratios, just as in the Stark broadening analysis. Lorentzian fits were typically used, but the calculated line ratios were not very sensitive to the choice of profile function, as long as it was the same for both lines.

6.1.5.3 Effect of Re-Absorption

Emission line ratio measurements will yield misleading results if an appreciable number of photons of either wavelength are re-absorbed before leaving the plasma, since the measured intensity of each line will no longer be proportional to the upper level population density. The absorption cross section is highest at the line center wavelength and lower in the wings, meaning that re-absorption distorts the line profile and thus corrupts Stark and Doppler broadening measurements as well. In particular, the electron density or ion temperature may be overestimated if the measured intensity at the line center is attenuated by re-absorption because the apparent FWHM will actually correspond to the true line width at

[5]Note, however, that the Ar III 351.14 nm and Ar II 349.13 nm lines were actually each composed of two nearby lines, at 351.11 nm and 351.17 nm (both Ar III) and at 349.12 nm and 349.15 nm (both Ar II), respectively. When the spectrometer was operated with a relatively wide entrance slit (300 μm), the separate lines could not be resolved, and the line pairs appeared as single lines with a Gaussian profile due to the dominant instrumental broadening. On the other hand, when a narrow 50 μm entrance slit was used, the individual line profiles could be distinguished, but they overlapped on the spectrum, making reliable fitting to the line shapes difficult. Therefore, using the [Ar III 350.36 nm] / [Ar II 347.67 nm] ratio instead of the [Ar III 351.14 nm] / [Ar II 349.13 nm] ratio was preferred in this case.

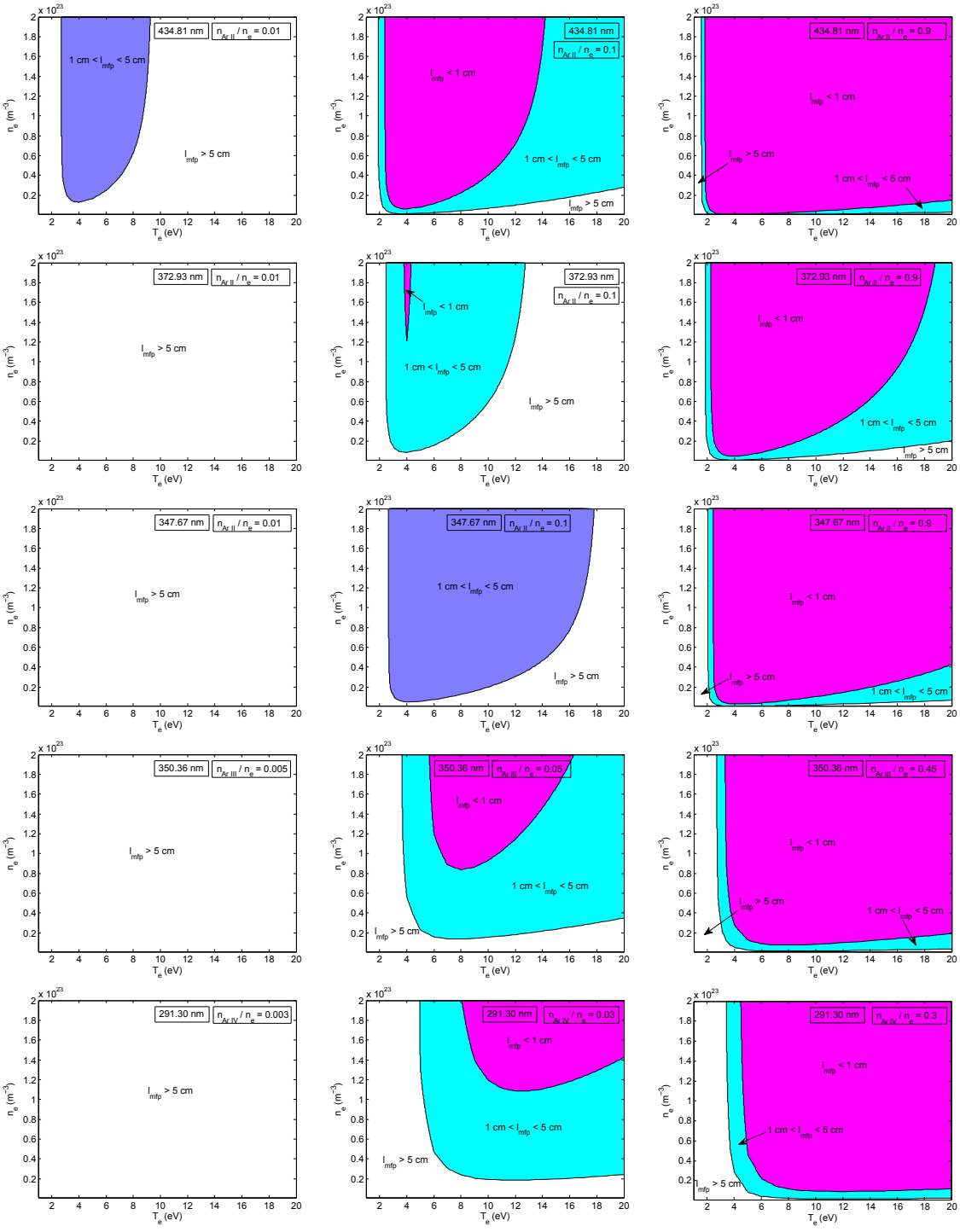

Figure 6.8: Absorption mean free paths for the Ar II 434.81 nm, Ar II 372.93 nm, Ar II 347.67 nm, Ar III 350.36 nm, and Ar IV 291.30 nm lines as a function of n_e and T_e, with various assumed values of the ratio of the relevant ion's population density to the electron density. The populations of excited states within a given ionization stage were assumed to follow a Boltzmann distribution, and $T_i = T_e$ was assumed.

an intensity below the half maximum.

The MHD-driven jets were transparent in camera images that were not saturated, so they were optically thin (meaning that the absorption mean free path was much longer than the plasma radius) in the continuum. However, it is still possible that there was non-negligible re-absorption at the wavelengths of the strongest emission lines. Indeed, given that re-absorption of line emission was important in the RF discharge, as discussed in Appendix E, it was reasonable to expect that it might play a significant role in the jet plasma as well.

Using $\phi(\nu) = \left(\lambda^2/c\right)\phi(\lambda)$ to convert from frequency to wavelength, Eq. E.4 for the absorption cross section becomes

$$\sigma_\lambda = \frac{\lambda^4}{8\pi c}\frac{g_\alpha}{g_\beta}A_{\alpha\beta}\left(1 - \frac{g_\beta n_\alpha}{g_\alpha n_\beta}\right)\phi(\lambda)\,. \tag{6.8}$$

As an approximation of the Voigt profile [137, Section 6.2], assume that the line profile is roughly Lorentzian, but with a total FHWM $w_{total} = \sqrt{w_S^2 + w_D^2}$. Then according to Eq. 6.2, the profile function at the line center is $\phi(\lambda_0) = 2/\pi\sqrt{w_S^2 + w_D^2}$, and the line center cross section is

$$\sigma_{\lambda_0} = \frac{\lambda_0^4}{4\pi^2 c}\frac{g_\alpha}{g_\beta}A_{\alpha\beta}\left(1 - \frac{g_\beta n_\alpha}{g_\alpha n_\beta}\right)\frac{1}{\sqrt{w_S^2 + w_D^2}}. \tag{6.9}$$

For lack of a better simple alternative, we will assume that the level populations follow a Boltzmann distribution, $n_\alpha/n_\beta = (g_\alpha/g_\beta)\exp\left(-\left(E_\alpha - E_\beta\right)/k_B T_e\right)$, as in the "partial LTE" model discussed in Sec. 6.1.5.2. However, since the jet plasma may be far from ionization equilibrium, l_{mfp} will be evaluated for several different possible ionization balances instead of using the Saha equation to calculate n_{ArII}, n_{ArIII}, and n_{ArIV} as a function of T_e. This is a reasonable approach because the relaxation time for the excited state populations in a time-varying plasma is much shorter than the timescale for the ionization balance to reach a steady state [74, p. 225].

Contour plots of the absorption mean free path $l_{mfp} = \left(n_\beta \sigma_{\lambda_0}\right)^{-1}$ as a function of n_e and T_e are shown in Fig. 6.8 for several lines of interest. Since the spectroscopy measurements presented in this chapter will focus on determining the properties of the bright narrow

section at the base of the pre-ionized jets, we take $l_{mfp} = 1$ cm as the cutoff below which re-absorption would start to have a deleterious effect on the analysis. It is clear that all of the lines studied were likely to be re-absorbed if the ionization stage from which they arose was dominant; on the other hand, lines associated with ions whose population densities were $\leq 1\%$ of the electron density had negligible re-absorption. Since the ionization balance was not well known, the actual effect on the data was uncertain, but re-absorption should be kept in mind as a possible confounding factor. A rough estimate from the measured line ratios shown in Figs. 6.12 and 6.15 suggests that Ar III or Ar IV was the dominant ion present.

6.2 Plasma Breakdown and Jet Formation

Without the pre-ionization system, plasma breakdown would not occur below certain threshold gas bank voltages, as expected from the Paschen criterion discussed in Sec. 1.7. Using the RF plasma source to inject a seed plasma prior to triggering the main capacitor bank removed this limitation. With the bank voltage and trigger timing[6] for the fast gas valve supplying gas to the RF discharge tube set to $V_{gas,RF} = 550$ V and $t_{gas,RF} = -6.15$ ms, respectively, breakdown could be achieved at a main bank voltage $V_{main} = 4$ kV with no gas input at all through the inner and outer electrode gas inlets. However, the plasma that formed in this configuration remained near the cathode and did not form a jet. Based on the scaling of gas pressure with gas bank voltage measured in Fig. 5.2, we may estimate that the total mass of gas in the chamber in this case was at least four times less than the minimum quantity needed to achieve breakdown in the absence of pre-ionization.

In order to create a well-defined jet, it was necessary to inject a large amount of gas through the outer electrode gas inlets (specifically, $V_{gas,outer} \geq 700$ V was required), in addition to injecting gas through the RF source tube and/or through the inner electrode gas inlets. This requirement for high $V_{gas,outer}$ was undesirable, as it limited the reduction in the total jet mass that could be achieved, but it was found to hold universally over a

[6] In this chapter, unless otherwise noted, all times are defined relative to the triggering of the main capacitor bank at $t = 0$ μs, unlike in Chapters 4 and 5, where gas valve trigger times were measured from the time of RF amplifier turn-on.

wide range of gas timings and voltages and RF plasma source configurations. The reasons for this behavior will be analyzed in Sec. 6.6.

Typically the experiment was operated with $V_{gas,outer} = 709$–750 V, and $V_{gas,inner}$ and $V_{gas,RF}$ were adjusted to vary the initial gas distribution and the total jet mass. $V_{main} = 4$ kV was usually used—the difference between the plasma parameters that could be attained with and without pre-ionization was smaller at higher main bank voltages ($V_{main} = 5$–6 kV). With $V_{main} = 4$ kV, $V_{gas,outer} = 709$ V, $V_{gas,RF} = 550$ V, and the RF amplifier turned off, gas breakdown would not occur with $V_{gas,inner} < 575$ V. On the other hand, when RF pre-ionization was employed, a jet could be created with any value of $V_{gas,inner}$ (including $V_{gas,inner} = 0$ V), and faster jets could be created as a result (see Fig. 6.11).

In addition to providing access to a new region of parameter space with a lower initial gas density, pre-ionization substantially reduced the delay and shot-to-shot variation in the breakdown time for experiments with intermediate levels of gas input. For example, in a set of experiments with $V_{main} = 4$ kV, $V_{gas,outer} = 709$ V and $V_{gas,inner} = 575$ V, argon gas breakdown occurred anywhere from 7.7–15.4 μs after the electrodes were energized when no pre-ionization was used, while with pre-ionization the range in breakdown times was 1.9–2.3 μs. Similar improvements were obtained in experiments with hydrogen or helium gas. Breakdown jitter can complicate the comparison of data from different shots if the camera and other diagnostics are triggered at the same time as the main capacitor bank. This issue has usually been surmounted in the Caltech experiments by triggering the diagnostics timing system off the leading edge of a light signal received from the plasma using the optical collimator setup described in Sec. 1.6.5. However, pre-ionization could make this added complexity unnecessary in many cases.

6.3 High Jet Impedance

The electrical impedance of the main capacitor bank and cables in the original MHD-driven jet experiment was generally much greater than the plasma impedance, so the bank acted approximately as a current source. Kumar, Moser, and Bellan [146, Figure 8] found that the temporal profile of the discharge current hardly changed when the main bank charging

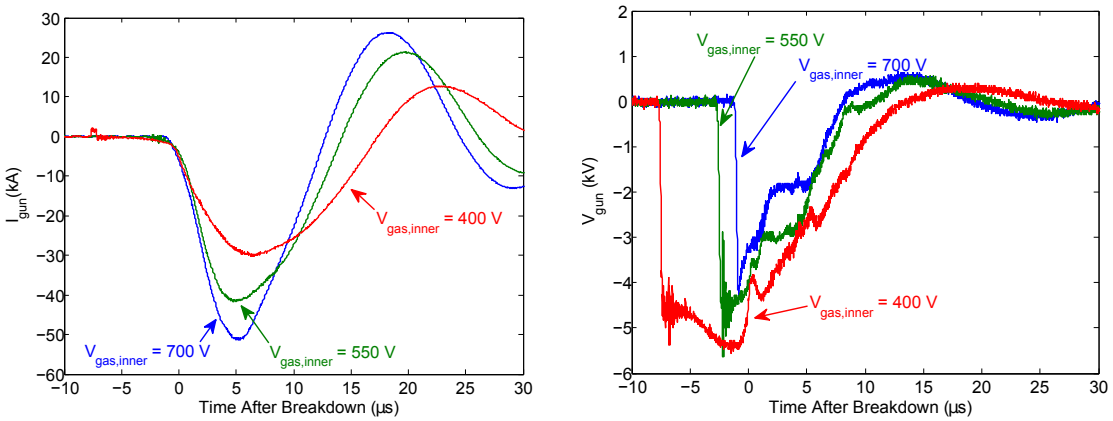

Figure 6.9: Gun current measured with the Rogowski coil (left) and cathode-anode voltage measured with the HV probe (right) for shots with $V_{gas,inner} = 700$ V, 550 V, and 400 V (the current waveforms were smoothed over 500 ns using a moving average filter). All three shots had $V_{gas,outer} = 709$ V, $V_{gas,RF} = 550$ V, and $V_{main} = 5$ kV. The breakdown time was defined as the time when the light intensity entering the optical collimator was sufficient to trigger the diagnostics timing system.

voltage, bias field strength, or gas species was varied. For the low-mass jets created with the aid of pre-ionization, on the other hand, changing the amount of gas input through the inner electrode had a dramatic effect on the gun current and voltage waveforms, implying that the jet impedance was comparable to the external circuit impedance. Fig. 6.9 shows that with lower $V_{gas,inner}$, the time for breakdown to occur (i.e., the delay between the time at which the electrodes were energized and the time when the gas broke down) was longer, the peak current was lower, and the period of the current oscillation was longer.

These trends may be understood by modeling the main bank discharge circuit as an underdamped series RLC circuit (see Fig. 1.7). The total resistance and inductance in the circuit are the sum of the plasma resistance and inductance and the resistance and inductance of the components external to the plasma, including the ignitron switch. If the initial voltage across the capacitor is V_0, then the circuit equation is

$$V_0 - \frac{1}{C}\int_0^t I(t')\,dt' = I(t)\,R(t) + \frac{dI}{dt}L(t) + I(t)\,\frac{dL}{dt}, \tag{6.10}$$

where the last term arises from Faraday's law in cases in which the inductance in the circuit is changing in time. This equation generally must be solved numerically, but to get a rough

sense of the behavior, neglect temporal variations in L due to the expansion of the plasma jet, in which case the solution is simply

$$I(t) = \frac{V_0}{L\omega^*} \exp\left(-\frac{t}{\tau}\right) \sin\left(\omega^* t\right) \tag{6.11}$$

$$\omega^* \equiv \sqrt{\frac{1}{LC} - \frac{R^2}{4L^2}} \quad ; \quad \tau \equiv \frac{2L}{R}. \tag{6.12}$$

As shown in Figs. 6.2 and 6.19, when $V_{gas,inner}$ was small, the jets became very narrow (visible radius $a_{vis.} < 1$ cm and current channel radius $a_{cur.} \sim 3$ cm). This made the jet inductance greater than that of high mass plasmas like the one shown in Fig. 6.1, which caused $L\omega^*$ to increase and the peak value of $I(t)$ to decrease. The effect on ω^* itself was ambiguous: $d\left(\omega^*\right)^2/dL = R^2/2L^3 - 1/L^2C$, so ω^* would decrease when L increased if $1/L^2C > R^2/2L^3 \rightarrow \tau > RC$. This condition was expected to hold for typical jet experiment circuit parameters [146, Table II], and indeed, Fig. 6.9 shows that the discharge period increased as $V_{gas,inner}$ was decreased. The plasma resistance was also expected to change[7] when $V_{gas,inner}$ was decreased, but the effect of variations in the inductance should have dominated since the plasma resistance made a negligible contribution to the overall series resistance of the discharge circuit [146, Table II].

Perkins [133, Figures 4.16 and 4.17] varied the amount of gas input in the Caltech Arched Flux Rope Experiment and observed changes in the discharge current and voltage waveforms similar to those shown in Fig. 6.9, demonstrating that the plasma made a non-negligible contribution to the total circuit impedance in this experiment as well. Because the current waveforms for low-, medium-, and high-mass plasmas overlapped during the first microsecond after breakdown, Perkins hesitated to attribute the differences between the waveforms at later times to variations in the plasma loop inductance due to the slower expansion velocity of the high-mass plasmas, instead pointing to changes in the magnetic topology as the loops began to merge as the likeliest explanation. Likewise, the current waveforms from the pre-ionized jet experiment shown in Fig. 6.9 only ceased to overlap at $t > 1$ μs. The jet velocity was moderately faster with low $V_{gas,inner}$ (see Fig. 6.11), but

[7] Jets created with low $V_{gas,inner}$ were both hotter (see Sec. 6.4) and narrower (compare Figs. 6.1 and 6.2) than those created with a higher amount of gas input, so the effect of varying $V_{gas,inner}$ on the plasma resistance $R = \eta L/\pi a^2$ was ambiguous ($\eta \propto T_e^{-3/2}$ [4, p. 596]).

the more important effect causing the inductance of these low mass jets to be higher was probably the pinch to a very narrow jet radius that occurred at $t \sim 2$–4 μs (see Sec. 6.5.1).

6.4 Jet Velocity, Mass, and Temperature

6.4.1 Jet Velocity Model

Since the jets in our experiment were driven by the toroidal magnetic field pressure gradient (see Fig. 1.5), the jet velocity was expected to be roughly determined by the magnetic energy density available:

$$\frac{1}{2}\rho v_{jet}^2 \sim \frac{B_\phi^2}{2\mu_0} \tag{6.13}$$

$$v_{jet} \sim \frac{B_\phi}{\sqrt{\mu_0 \rho}} \equiv v_{A\phi}. \tag{6.14}$$

This may be made more precise by modeling the jet as an axisymmetric, flared current channel with radially uniform axial current density, following Kumar and Bellan [39]. The jet radius is assumed to vary with distance from the electrodes[8] as $a(z) = a_0 e^{\kappa z}$, and the poloidal current passing through a circle of radius r centered on the z axis is $I(r,z) = I_0 \left(r/a\right)^2$. The toroidal magnetic field and poloidal current density for the general axisymmetric case are

$$\mathbf{B}_{tor.} = \frac{\mu_0 I}{2\pi r}\hat{\phi} = \frac{\mu_0 I}{2\pi}\nabla\phi \tag{6.15}$$

$$\mathbf{J}_{pol.} = \frac{1}{\mu_0}\nabla \times \mathbf{B}_{tor.} = \frac{1}{2\pi}\nabla I \times \nabla\phi \tag{6.16}$$

$$\mathbf{J}_{pol.} \times \mathbf{B}_{tor.} = -\frac{\mu_0 I}{\left(2\pi r\right)^2}\nabla I = -\frac{\mu_0}{\left(2\pi r\right)^2}\left(\hat{r}\frac{\partial}{\partial r}\left(\frac{I^2}{2}\right) + \hat{z}\frac{\partial}{\partial z}\left(\frac{I^2}{2}\right)\right). \tag{6.17}$$

Using $\nabla\phi = \hat{\phi}/r$ is convenient for this sort of calculation because $\nabla \times \nabla\phi = 0$.

Since the jet is long and narrow, radial equilibrium is achieved much faster than axial equilibrium, so we can balance forces in the radial direction first and then consider the implications for axial jet motion. Only the effect of the toroidal magnetic field will be considered. The poloidal field could be included in the model as well with a modest amount

[8] This assumed geometery is most accurate for modeling jets without pre-ionization such as those shown in Figs. 1.5 and 6.1, but it should be sufficient for deriving the scaling of jet velocity with gun current and plasma density for pre-ionized jets as well.

of additional effort by working with the poloidal flux function $\psi(r,z)$, as was done by Kumar and Bellan [39]; however, these authors ultimately showed that $\mathbf{B}_{pol.}$ had a negligible affect on the jet velocity for values of I and ψ relevant for the Caltech jet experiments, so the simplest possible model will be presented here.

In equilibrium, the r component of the MHD equation of motion (Eq. 1.10) is

$$\frac{\partial P}{\partial r} = (\mathbf{J}_{pol.} \times \mathbf{B}_{tor.}) \cdot \hat{r} = -\frac{\mu_0}{(2\pi r)^2} \frac{\partial}{\partial r}\left(\frac{I^2}{2}\right) = -\frac{\mu_0 I_0^2 r}{2\pi^2 a^4}. \tag{6.18}$$

Integrating and applying the boundary condition $P(r=a,z)=0$, we find

$$P(r,z) = \frac{\mu_0 I_0^2}{(2\pi a(z))^2}\left(1 - \left(\frac{r}{a(z)}\right)^2\right). \tag{6.19}$$

We will approximate the jet as a steady state flow, in which case the axial component of the MHD equation of motion is

$$\rho\left(\mathbf{U}\cdot\nabla\mathbf{U}\right)\cdot\hat{z} = \rho\left(U_z\frac{\partial U_z}{\partial z} + U_r\frac{\partial U_z}{\partial r}\right) = (\mathbf{J}_{pol.}\times\mathbf{B}_{tor.})\cdot\hat{z} - \frac{\partial P}{\partial z}. \tag{6.20}$$

Consider the situation along the jet axis ($r=0$). Here $\mathbf{B}_{tor.}=0$, so the jet motion must be driven entirely by the gradient in thermal pressure:

$$\rho(0,z)\frac{\partial}{\partial z}\left(\frac{(U_z(0,z))^2}{2}\right) = -\frac{\partial P(0,z)}{\partial z} = -\frac{\partial}{\partial z}\left(\frac{\mu_0 I_0^2}{(2\pi a(z))^2}\right) = -\frac{\mu_0 I_0^2}{(2\pi a_0)^2}\frac{\partial}{\partial z}\left(e^{-2\kappa z}\right). \tag{6.21}$$

Assuming that the jet is isothermal in the axial direction, so $\rho(0,z) \propto P(0,z) \propto 1/a(z)^2 \propto e^{-2\kappa z}$, this becomes

$$\rho_0 e^{-2\kappa z}\frac{\partial}{\partial z}\left(U_z^2\right) = \frac{\mu_0 I_0^2 \kappa}{\pi^2 a_0^2} e^{-2\kappa z}, \tag{6.22}$$

where $\rho_0 \equiv \rho(0,0)$. Integrating from $z=0$ to $z=L$ and using $U_z(0,0)\approx 0$, we find

$$U_z(0,L) \approx \sqrt{\frac{\mu_0 I_0^2 \kappa L}{\rho_0 \pi^2 a_0^2}} = \sqrt{\frac{B_{\phi a_0}^2}{\mu_0\rho_0} 4\kappa L}, \tag{6.23}$$

where $B_{\phi a_0} \equiv B_\phi(a_0,0) = \mu_0 I_0/2\pi a_0$. So indeed, the jet velocity scales as $B_\phi/\sqrt{\mu_0\rho}$ as predicted by the simple energy balance argument, but this quantity is not really the local

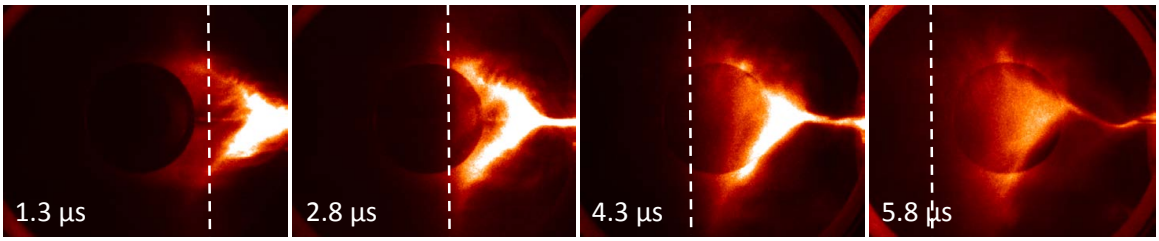

Figure 6.10: Example of a jet velocity measurement using Imacon camera images. The jet shown was created with $V_{main} = 4$ kV, $V_{gas,outer} = 709$ V, and $V_{gas,inner} = 460$ V. Since the jet front was not sharp, the identification of its location at each time, marked by the dashed lines, was somewhat subjective. Because the vacuum chamber walls were highly reflective, it was easiest to pinpoint the front location when the jet was passing in front of the window. The window was also useful for providing a sense of scale—with knowledge of its actual radius and of the distance from the camera to the jet and to the window, the distance in the plane of jet propagation corresponding to one horizontal pixel on the images could be calculated. We estimate that the uncertainty in the jet velocity measurement was about ±20%.

toroidal Alfvén velocity $v_{A\phi}$, since it is evaluated using ρ measured at the jet center but B_ϕ measured at the jet edge.

6.4.2 Jet Velocity Measurements

The velocities of the MHD-driven jets were measured from fast camera movies: the Imacon camera was aligned perpendicular to the direction of jet propagation, and the jet front location at each time was identified, as illustrated in Fig. 6.10. When the experiment was operated without pre-ionization, with roughly the same amount of argon gas input as was typically used on the old version of the jet experiment, a fully collimated jet formed only after the gun current had already peaked and begun to decrease (compare Figs. 6.1 and 6.9)[9]. However, even at times before the plasma had fully evolved into a jet, it was possible to define an expansion velocity by tracking the leading edge of the spider leg loops as they were driven to expand and merge by the MHD hoop force.

The left panel of Fig. 6.11 shows the jet velocity as a function of $V_{gas,inner}$, with $V_{gas,outer}$ and $V_{gas,RF}$ held fixed at 709 V and 550 V, respectively[10]. There was a modest trend

[9]The old jet experiment was able to follow the evolution of argon jets over a longer time interval because its main capacitor bank contained two 59 μF capacitors in parallel, compared to a single 59 μF capacitor in the experiment described here, and there was also a pulse forming network [43] available to further extend the current pulse duration when necessary.

[10]Values of $V_{gas,RF}$ below 550 V were also tested, but the jet velocity did not measurably increase compared

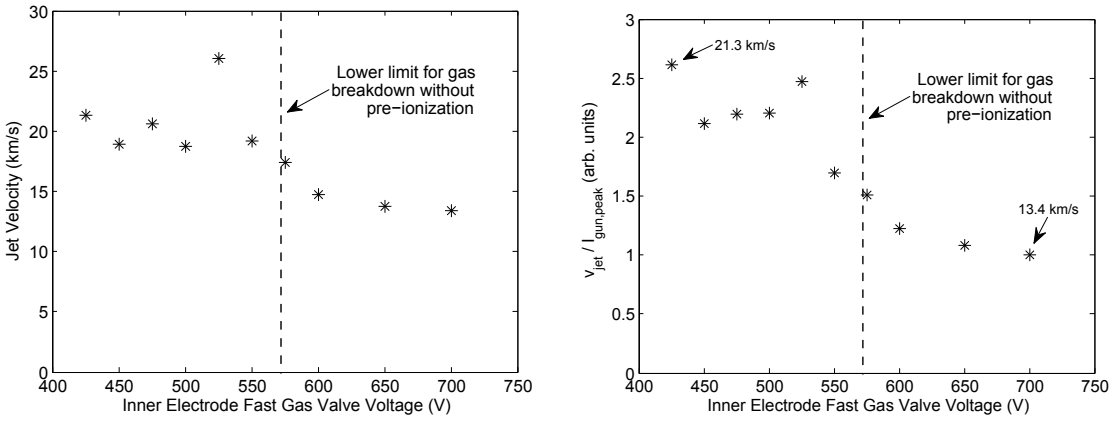

Figure 6.11: Left: Jet velocity as a function of $V_{gas,inner}$ measured from Imacon camera images with $V_{main} = 4$ kV, $V_{bias} = 80$ V, $V_{gas,outer} = 709$ V, and $V_{gas,RF} = 550$ V. Each data point was the average of two shots. Right: Velocities from the same shots normalized to the peak gun current for each shot.

toward faster jet velocities as $V_{gas,inner}$ was decreased. By enabling plasma breakdown with $V_{gas,inner} < 575$ V, the pre-ionization system allowed for the creation of faster jets than was previously possible with $V_{main} = 4$ kV.

In the right panel of Fig. 6.11, the jet velocities are plotted again, this time normalized to the peak discharge current for each shot, which was smaller for lower $V_{gas,inner}$ (see Fig. 6.9). Let N be the ion density per unit length in the jet, so $\rho_0 \propto N_0/\pi a_0^2$. Eq. 6.23 then yields

$$U_z(0, L) \propto \frac{I_0}{\sqrt{N_0}}\sqrt{\kappa L}. \tag{6.24}$$

The jets became more collimated as they lengthened, such that κL remained approximately constant. Therefore, $v_{jet}/I_{gun,peak}$ was proportional to $N_0^{-1/2}$. Neglecting small differences in the lengths of the pre-ionized jets, N_0 was proportional to the total jet mass, so comparing the normalized jet velocities at $V_{gas,inner} = 575$ V and $V_{gas,inner} = 425$ V, we may infer that pre-ionization allowed the jet mass to be decreased by a factor of $(2.6/1.5)^2 \approx 3$.

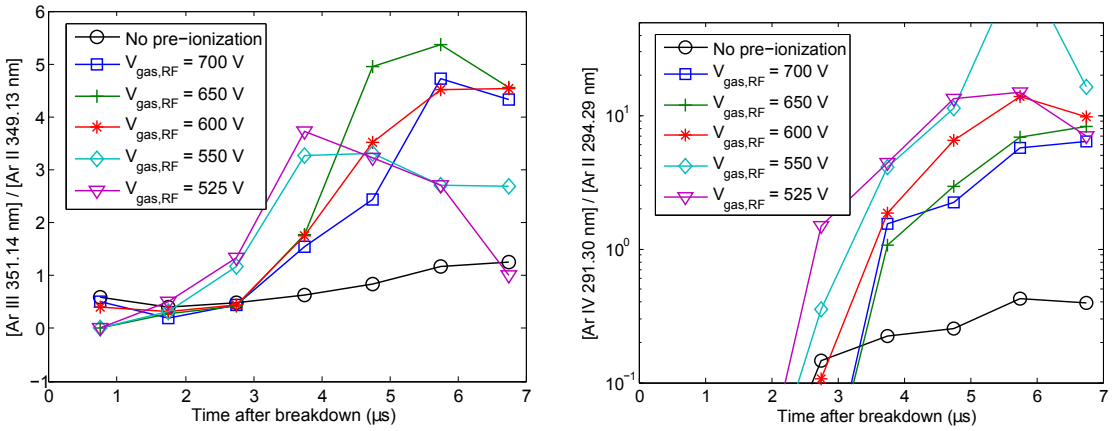

Figure 6.12: Global emission line ratios measured with the optical fiber viewing the jet directly, without a lens. The ICCD exposure time was 1 μs. Left: [Ar III 351.14 nm] / [Ar II 349.13 nm] intensity ratio, plotted with a linear y-axis scale. Right: [Ar IV 291.30 nm] / [Ar II 294.29 nm] intensity ratio, plotted with a logarithmic y-axis scale. $V_{gas,outer} = 750$ V was used for all shots. The shots labeled "No pre-ionization" had $V_{gas,inner} = 700$ V and $V_{gas,RF} = 0$ V, while the rest of the shots were pre-ionized (RF amplifier on) and had $V_{gas,inner} = 0$ V and variable $V_{gas,RF}$ (values labeled in the figure legend).

6.4.3 Jet Temperature and Ionization Balance

A coarse measure of the mean electron temperature and ionization balance in the jets was obtained by measuring global levels of Ar II, Ar III, and Ar IV emission as a function of time. The [Ar III 351.14 nm] / [Ar II 349.13 nm] and [Ar IV 291.30 nm] / [Ar II 294.29 nm] line intensity ratios are shown in Fig. 6.12 for pre-ionized jets with varying levels of gas input, as well as for jets formed without pre-ionization. The relative level of emission from the Ar III and Ar IV lines was significantly higher for the pre-ionized jets than it was for the non-pre-ionized jets, suggesting that the pre-ionized jets had a higher mean ionization state or higher electron temperature (probably both).

As discussed in Sec. 6.1.5.2, numerical values for T_e and the relative populations of the different ionization stages generally cannot be derived from measured line ratios without complex models. Table 6.1 shows the electron temperatures that would be implied by the data if LTE were a valid approximation—although the T_e values shown may not be

to the case with $V_{gas,RF} = 550$ V. As expected from the fast gas valve output measurements shown in Fig. 5.2, very little gas was released through the inner electrode gas inlets when $V_{gas,inner}$ was 400 V or less, and the jets created with these low inner gas voltages were indistinguishable from those formed with $V_{gas,inner} = 0$ V.

Ratio \ n_e	5×10^{21} m^{-3}	2×10^{22} m^{-3}	1×10^{23} m^{-3}
Pre-Ionized Jets			
Ar III / Ar II	2.4 eV	2.7 eV	3.1 eV
Ar IV / Ar II	2.6 eV	2.9 eV	3.2 eV
Jets with No Pre-Ionization			
Ar IV / Ar II	2.4 eV	2.6 eV	2.9 eV

Table 6.1: Electron temperatures calculated from measured emission line ratios by assuming LTE, for three different electron densities. LTE was not actually a valid approximation for the jets, so these values should be considered to be rough lower limits on T_e rather than accurate measurements—see the discussion in the text. The ratios considered were [Ar IV 291.30 nm] / [Ar II 294.29 nm] (typical values: ~ 5 for pre-ionized jets and ~ 0.3 for non-pre-ionized jets, from Fig. 6.12) and [Ar III 350.36 nm] / [Ar II 347.67 nm] (typical value: ~ 10 for pre-ionized jets, from Fig. 6.15). The NIST Saha-Boltzmann emission calculator [73] was used to construct this table.

accurate, the table is useful for demonstrating the extremely strong dependence of the equilibrium ionization balance on temperature. Because of this strong dependence, the order of magnitude increase in the [Ar IV] / [Ar II] emission ratio that was obtained with pre-ionization could have corresponded to T_e being hotter by only a few tenths of an eV. In fact, any LTE plasma in the relevant density range that has appreciable emission from both Ar II and Ar IV ions must have $T_e \sim 2.5$–3 eV. It must be stressed that we cannot actually conclude that the temperatures of the jets fell in this narrow range—T_e may have been much hotter given that the dynamical timescale of the experiment was shorter than the time required for the plasma to reach ionization equilibrium[11] (this will be discussed further in Sec. 6.5.1).

Increasing the amount of gas input through the RF source tube decreased the [Ar IV 291.30 nm] / [Ar II 294.29 nm] line ratio shown in the right panel of Fig. 6.12, suggesting that higher mass plasmas were cooler and had a lower mean ionization state, as expected. However, even for the highest gas voltage tested ($V_{gas,RF} = 700$ V), the line ratio was roughly 10 times higher than the corresponding ratio in the "No pre-ionization" case, which

[11] The relationship between the temperature and ionization balance in a steady state laboratory discharge can also be modified by losses of ions to the walls or electrodes [75]. As one example of how using the Saha equation can be misleading, consider the RF discharge equilibrium discussed in Ch. 3. A typical measured value of the [Ar II 434.8 nm] / [Ar I 696.5 nm] line ratio was ~ 0.3 (see Figs. 3.14, 3.15, and 3.16), which for $n_e \approx 5 \times 10^{19}$ m^{-3} gives $T_e \approx 0.9$ eV if LTE is assumed. However, detailed modeling of the collisional, radiative, and diffusive processes showed that T_e was actually 2–3 eV (see Table 3.2).

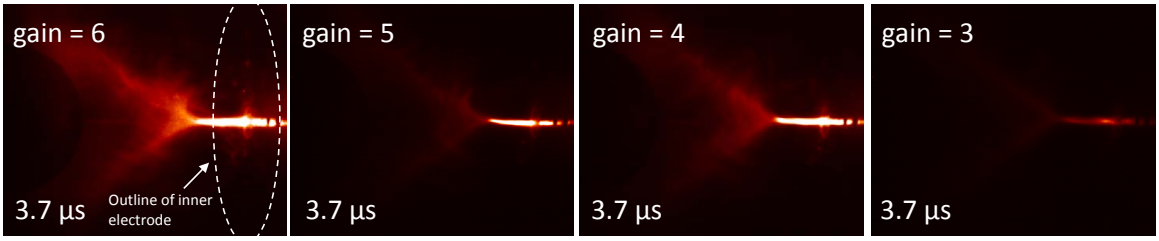

Figure 6.13: Imacon camera images of pre-ionized argon jets with successively decreasing ICCD gains, demonstrating that the narrow collimated structure near the base of the jet was many times brighter than the front of the jet. The experiment parameters were: V_{main} = 4 kV, V_{bias} = 80 V, $V_{gas,RF}$ = 550 V, $V_{gas,inner}$ = 460 V, and $V_{gas,outer}$ = 750 V.

had $V_{gas,RF} = 0$ V and $V_{gas,inner} = 700$ V. Although the gas bank voltages were the same in both cases, the initial gas pressure in front of the inner electrode may have been different because the gas delivery piping was not identical for the "inner" and "RF" gas valves[12], and the inner valve was triggered earlier relative to the gas travel distance to the electrodes than the RF gas valve was (see Table 1.2). Nevertheless, it appears likely that the pre-ionized jets were in a fundamentally different regime, independent of the amount of gas input. This conclusion is supported by images of the plasma structure, which showed that the pre-ionized jets created with $V_{gas,inner} = 0$ V always pinched down to a very narrow radius that was approximately independent of $V_{gas,RF}$ (see Fig. 6.21). This behavior will be discussed in the following sections.

6.5 Structure and Dynamics of Pre-Ionized Jets

6.5.1 Bright Pinch

The most striking characteristic of the pre-ionized jets was the extreme brightness of the narrow collimated portion of the jet near the electrodes. Fig. 6.13 shows that this segment of the jet was far brighter than the more diffuse front part of the jet, and it was also brighter than any feature visible in jets formed without pre-ionization. The bright emission suggested that the narrow jet column was very hot, very dense, or both. High time-resolution movies

[12]Here and throughout this thesis, the label "inner" denotes the fast gas valve feeding gas to the 8 holes on the inner electrode at $r = 4.8$ cm, "outer" denotes the fast gas valve feeding gas to the 8 holes on the outer electrode at $r = 17.8$ cm, and "RF" denotes the fast gas valve feeding in gas through the RF source tube at the center of the inner electrode.

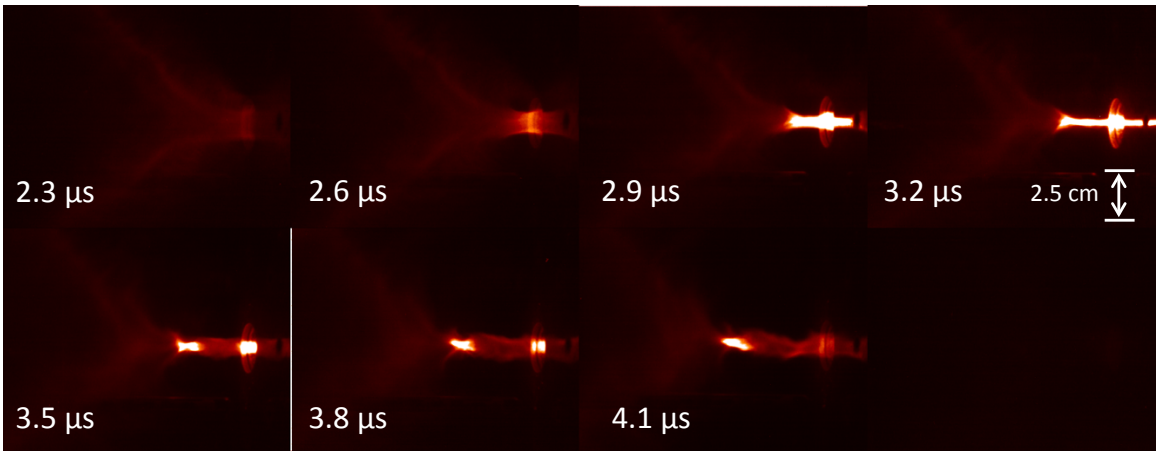

Figure 6.14: Imacon camera movie of the pinching behavior at the base of an argon pre-ionized jet formed with $V_{main} = 4$ kV, $V_{bias} = 80$ V, $V_{gas,RF} = 650$ V, $V_{gas,inner} = 0$ V, and $V_{gas,outer} = 750$ V.

(see Fig. 6.14) showed that the jet base pinched down to a remarkably narrow radius ($r \leq$ 0.3 cm) and then bounced back over a time interval of ~ 1 μs. The general behavior was similar to that of dense plasma focus [147] and Z-pinch [148] plasmas.

The [Ar III 351.14 nm] / [Ar II 349.13 nm] and [Ar IV 291.30 nm] / [Ar II 294.29 nm] line ratios shown in Fig. 6.12 rose suddenly at the time of the bright pinch ($t = 2.5$–4 μs), implying that the plasma was heated and became more ionized at this time. The increase in the line ratios occurred later for the more massive pre-ionized jets created with high $V_{gas,RF}$ than for jets created with low $V_{gas,RF}$, consistent with camera images showing that the overall evolution was slower and the pinch occurred later for the heavier jets. After the initial rapid rise, the [Ar IV] / [Ar II] line ratio continued to increase for several μs in all cases, and the [Ar III] / [Ar II] ratio also continued to rise from $t \approx 4$–6 μs for the heavier jets. For the low-mass jets with $V_{gas,RF} = 525$ V or 550 V, on the other hand, the [Ar III] / [Ar II] emission ratio decreased from $t \approx 4$–6 μs, at the same time that the [Ar IV] / [Ar II] ratio was rising, suggesting that the plasma was burning through the Ar III ionization stage (this observation rules out the possibility that the line ratios were increasing solely because T_e was rising, while the ionization balance remained approximately constant). Fig. 6.12 therefore confirms that the plasma was not in ionization equilibrium (see Sec. 6.1.5.2 for more discussion). The most significant heating of the electrons probably occurred during

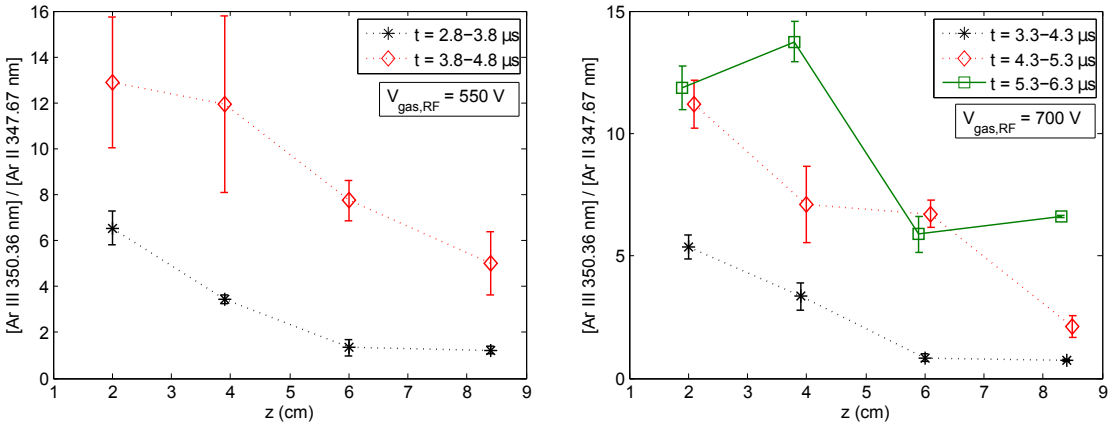

Figure 6.15: [Ar III 350.36 nm] / [Ar II 347.67 nm] line intensity ratio as a function of position around the time of the bright pinch for pre-ionized jets with $V_{gas,outer} = 750$ V, $V_{gas,inner} = 0$ V, and $V_{gas,RF} = 550$ V (left) or $V_{gas,RF} = 700$ V (right). A collimating lens was used to collected light from a narrow line of sight (diameter ~ 6 mm) aligned nearly perpendicular to the jet (the z value of each data point corresponds to the location at which the line of sight intersected the jet axis). Although all spectroscopy measurements were line of sight averages, these can be considered to be essentially local measurements with spatial resolution < 1 cm because the bright jet column was so narrow. The line ratios were averaged over 3 shots for each data point; the error bars show the standard deviation. The data points in the right panel have been offset slightly in time so that the error bars do not overlap.

the rapid pinch, although the Ohmic power input was also expected to increase in time as the main discharge current ramped up (see Fig. 6.9, for example). Fig. 6.12 shows that the mean ionization state of jets formed without pre-ionization also increased gradually throughout the shot.

Additional information about the temperature and ionization balance is contained in the spatially resolved [Ar III 350.36 nm] / [Ar II 347.67 nm] line ratio measurements shown in Fig. 6.15. These plots confirm that the relative level of Ar III emission increased rapidly at the time of the bright pinch. The mean ionization state was highest at the base of the jets and decreased moving away from the electrodes. The electrons were expected to be approximately isothermal in the axial direction due to the high field-aligned heat flux (see Eq. 4.20), but Table 6.1 shows that only a small gradient in T_e may have been necessary to produce a large variation in the ionization balance at different locations.

The time-dependent electron density of the jets at $z = 2.0$ cm, derived from the measured

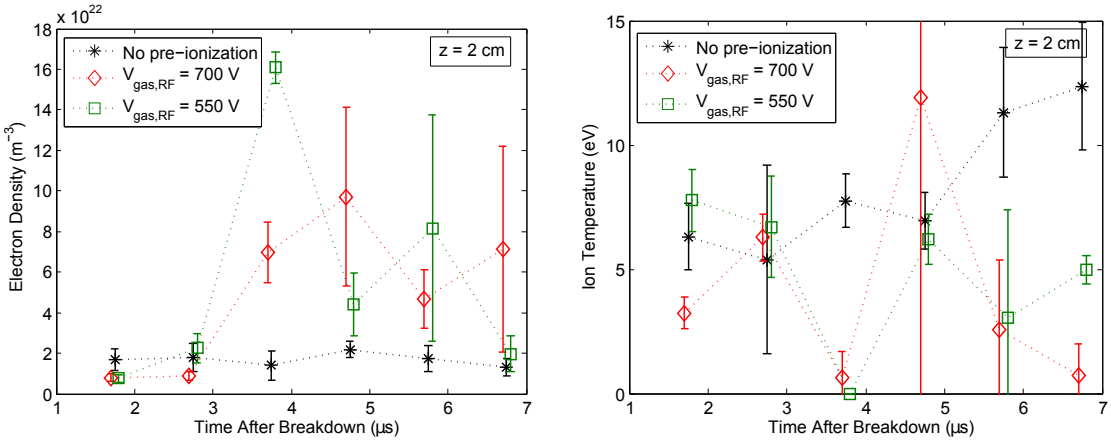

Figure 6.16: Electron density (left) and ion temperature (right) calculated from Voigt profile fits to the Ar II 372.931 nm line. A collimating lens was used to collected light from a narrow line of sight (diameter $\sim$ 6 mm) that intersected the jet axis at $z = 2.0$ cm in front of the electrodes. The spectrometer entrance slit width was 50 μm, and the ICCD exposure time was 1 μs. The n_e and T_i values were averaged over 3 shots for each data point; the error bars show the standard deviation. There were additional possible sources of systematic error that could have caused n_e and/or T_i to be overestimated—see the discussion in the text. The data points on the plots have been offset slightly in time so that the error bars do not overlap. $V_{gas,outer} = 750$ V was used for all shots. The shots labeled "No pre-ionization" had $V_{gas,inner} = 700$ V and $V_{gas,RF} = 0$ V, while the pre-ionized shots had $V_{gas,inner} = 0$ V and $V_{gas,RF} = 550$ V or 700 V, as noted in the plot legends.

Stark broadening of the Ar II 372.931 nm line, is shown in the left panel of Fig. 6.16. While n_e for non-pre-ionized jets[13] was approximately constant at 1–2 $\times$ 10^{22} m^{-3}, the density of the pre-ionized jets increased by a factor of 5–10 at the time of the bright pinch, reaching a peak value of $\sim 1.6 \times 10^{23}$ m^{-3} in the $V_{gas,RF} = 550$ V case. n_e subsequently appeared to oscillate between high and low values, possibly due to additional contractions and expansions of the jet radius; however, the errors bars for these points mostly overlapped, so the apparent pattern may not be significant. In these measurements the ICCD was exposed for 1 μs, which was the shortest achievable shutter time with the current triggering circuitry[14]—in the future the exposure window should be shortened in order to better resolve the time

[13]Higher electron densities exceeding 1×10^{23} m^{-3} have been measured for nitrogen jets formed without pre-ionization in the original Caltech MHD-Driven Jet Experiment [130, 139], which had twice the neutral gas input capability and twice the main bank capacitance of the new pre-ionized jet experiment.

[14]The trigger signals for the spectrometer were transmitted optically, as described in Sec. 6.1.5, and the circuit for converting the optical signal back to an electrical signal had a slow fall time that limited the minimum exposure time. The issue has not yet been investigated in detail, but the explanation may have been the slow turn-off of transistors operating in saturation, as discussed in Sec. A.2.2. In this case, the Baker clamp circuit shown in Fig. A.4 would be helpful.

dependence of the electron density.

There are two possible sources of error in the density measurement. At the times when the Ar II emission was brightest (at $t = 1.3$–3.3 μs for the pre-ionized jets and during the entire interval shown in Fig. 6.16 for the non-pre-ionized jets), the best-fit Voigt profile for the 372.931 nm line had a non-zero continuum level, but inspection of the full ~ 6 nm wide spectral window (like those shown in Fig. 6.7 for two other wavelength ranges) showed that there was in fact no measurable continuum emission. The apparent need for a continuum in the profile fit was almost certainly due to re-absorption that reduced the intensity at the line center (see Sec. 6.1.5.3). An example of a spectral line suffering from this problem is shown in the left panel of Fig. 6.6. Fixing the continuum level to be 0 in the profile fitting procedure had only a small effect on the calculated Stark and Doppler FWHMs, so it is likely that the error introduced by re-absorption was small, but it is possible that the densities for non-pre-ionized jets and those measured at $t < 3.3$ μs for pre-ionized jets were overestimated.

No false continuum was present in the Voigt profile fits for pre-ionized jets during and after the bright pinch, consistent with the evidence from Figs. 6.12 and 6.15 that the plasma had become more ionized by this time, and the Ar II concentration had been reduced enough that re-absorption was no longer important for the 372.931 nm line (see Fig. 6.8). However, the fitting procedure had difficulty accurately deconvolving the line profile during the high-density period ($t = 3$–7 μs): for some shots, the Gaussian FWHM implied by the fit was less than the Gaussian FWHM of the instrument function (T_i was set to 0 eV for these shots in the plot in the right panel of Fig. 6.16), implying that the fit overestimated the contribution from Stark broadening.

Nevertheless, the basic conclusion that the pre-ionized jets became very dense appears to be robust, as the lines were highly broadened and the dominant shape of the profiles was clearly Lorentzian, as shown in the right panel of Fig. 6.6. This result is not surprising based on the intense brightness of the jet column in the camera images, but there is notable irony given that the original stated goal of the pre-ionization project was to produce "lower density jets". However, it turned out that decreasing the plasma density was not possible due to the radial balance of MHD forces (to be discussed in the next section), nor was

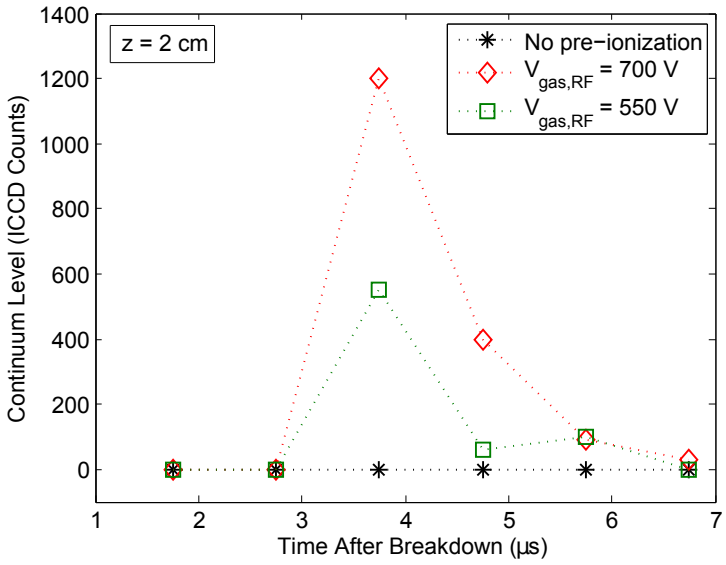

Figure 6.17: Continuum emission in the 370–376 nm wavelength range at $z = 2.0$ cm in front of the electrodes. $V_{gas,outer} = 750$ V was used for all shots. The shots labeled "No pre-ionization" had $V_{gas,inner} = 700$ V and $V_{gas,RF} = 0$ V, while the pre-ionized shots had $V_{gas,inner} = 0$ V and $V_{gas,RF} = 550$ V or 700 V, as noted in the plot legend.

it necessary in order to produce faster and hotter jets. The total mass of the jet (or equivalently the number of particles per unit length—see Eq. 6.24) was the parameter that actually mattered. It should be noted that a portion of the electron density increase in Fig. 6.16 was due to argon atoms becoming multiply ionized—n_i may have been lower than n_e by a factor of 2 or more.

Given the difficulty of extracting accurate ion temperatures from line profiles with dominant Stark broadening, it is questionable whether firm conclusions can be drawn from the T_i results shown in the right panel of Fig. 6.16. In general, the fits to the nearly Gaussian line shapes obtained when the electron density was $\leq 2 \times 10^{22}$ m^{-3} looked good (although there was a spurious continuum offset as discussed above), so the ion temperatures obtained for these cases may be reliable. The typical temperatures measured were $T_i \approx 5$–10 eV, which is notably hotter than the lower limit on the electron temperature of 2.5–3 eV calculated in Table 6.1, but T_i may have been overestimated due to re-absorption. There was no clear evidence that the ions in the pre-ionized jets were heated in the bright pinch; better Doppler profile measurements are needed for these cases, perhaps utilizing an Ar III or Ar

IV line that has minimal Stark broadening.

A surprising feature of the emission spectrum at the time of the dense pinch was a sudden increase in the continuum brightness, previously undetectable by our spectroscopy system, by a factor of 100 or more (see Fig. 6.17). The line profile shown in the right panel of Fig. 6.6 is one example of this effect; unlike the constant offset in the profile fits due to re-absorption discussed above, this was a true continuum, visible across all wavelengths in the full spectrum. The most obvious source of continuum radiation from the jet was thermal Bremsstrahlung; the emissivity in $\mathrm{W/m^3}$ is [138, p. 162]

$$\epsilon_{ff} = \left(1.5 \times 10^{-38}\right) T_{eV}^{1/2} n_e n_i Z^2, \tag{6.25}$$

where Ze is the typical ion charge. Assuming $n_e = 1 \times 10^{23}$ $\mathrm{m^{-3}}$, $n_i = 5 \times 10^{22}$ $\mathrm{m^{-3}}$, $Z = 2$, $T = 5$ eV, and $V = 10^{-5}$ $\mathrm{m^3}$ for the dense portion of the jet, we find a total radiated power $P_{ff} = 7 \times 10^3$ W. Based on measurements by Perkins [67, Figure 4.2] of visible radiated power exceeding 10^5 W from hydrogen plasmas with $n_e \approx 10^{21}$ $\mathrm{m^{-3}}$ in the Caltech Arched Flux Rope Experiment, we expect that the visible radiated power from line emission in the denser argon jet plasmas was $P_{vis.} \gtrsim 10^6$ W. Therefore, the thermal Bremsstrahlung might have been too small to be detectable by comparison. Non-thermal Bremsstrahlung arising from the sudden deceleration of the pinching plasma at the jet axis is an intriguing possibility, but further measurements and analysis are needed to determine whether it could reasonably produce sufficient optical power.

6.5.2 Radial Jet Structure

In addition to being extremely narrow, the pre-ionized jets had a nearly axially uniform visible radius $a_{vis.}$ over a distance $\Delta z \gg a_{vis.}$ (see Fig. 6.18). Since the magnetic field was expected to be approximately frozen into the plasma, the initially flared bias field lines shown in Fig. 2.2 must have been deformed by the jet flow. Bellan [149] explained how a flared current-carrying magnetic flux tube can become collimated, i.e., develop a uniform axial cross section, as the result of a sequence of MHD processes that is closely related to the jet acceleration model presented in Sec. 6.4.1. The $\mathbf{J} \times \mathbf{B}$ force accelerates

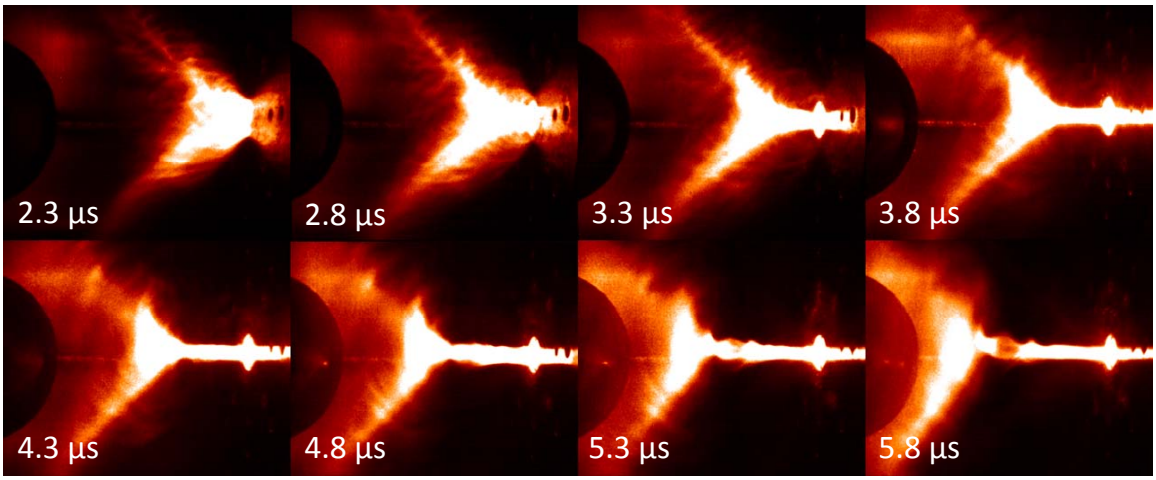

Figure 6.18: Imacon camera images of a pre-ionized argon jet formed with $V_{main} = 4$ kV, $V_{bias} = 80$ V, $V_{gas,RF} = 550$ V, $t_{gas,RF} = -6.75$ ms, $V_{gas,inner} = 0$ V, and $V_{gas,outer} = 709$ V. The camera gain was set higher for this image than for most others shown in this chapter, so much of the jet is saturated, obscuring some features but highlighting others.

plasma axially toward the region where the flux tube radius is large, and the local radial force balance condition leads to an axial pressure gradient that drives plasma in the same direction. Toroidal magnetic flux that is frozen into the plasma is convected along with the flow. If the flow stagnates for some reason, then this flux will pile up, increasing the radial MHD pinch force (see Fig. 1.1), which decreases the radius of the wide part of the flux tube until it is collimated. This MHD pumping process has been studied extensively in the Bellan plasma lab, where the ingestion of plasma by flared flux tubes has been tracked using spectroscopy [130] and color-coded imaging [40], and it may be responsible for the observed collimation of astrophysical jets as well.

A related and surprisingly subtle issue is what determines the final jet radius. Consider an isothermal axisymmetric cylinder of plasma in radial equilibrium, with current flowing only in the axial ($\hat{z}$) direction. Setting $\partial P/\partial r = -J_z B_\phi$ (see Eq. 1.10) and integrating from $r = 0$ to $r = a$, we can derive the Bennett relation [4, p. 317]:

$$I^2 = \frac{8\pi N k_B T}{\mu_0}, \tag{6.26}$$

where $N = \int_0^a (n_i + n_e)\, 2\pi r dr$ is the total number of particles per unit length. Eq. 6.26

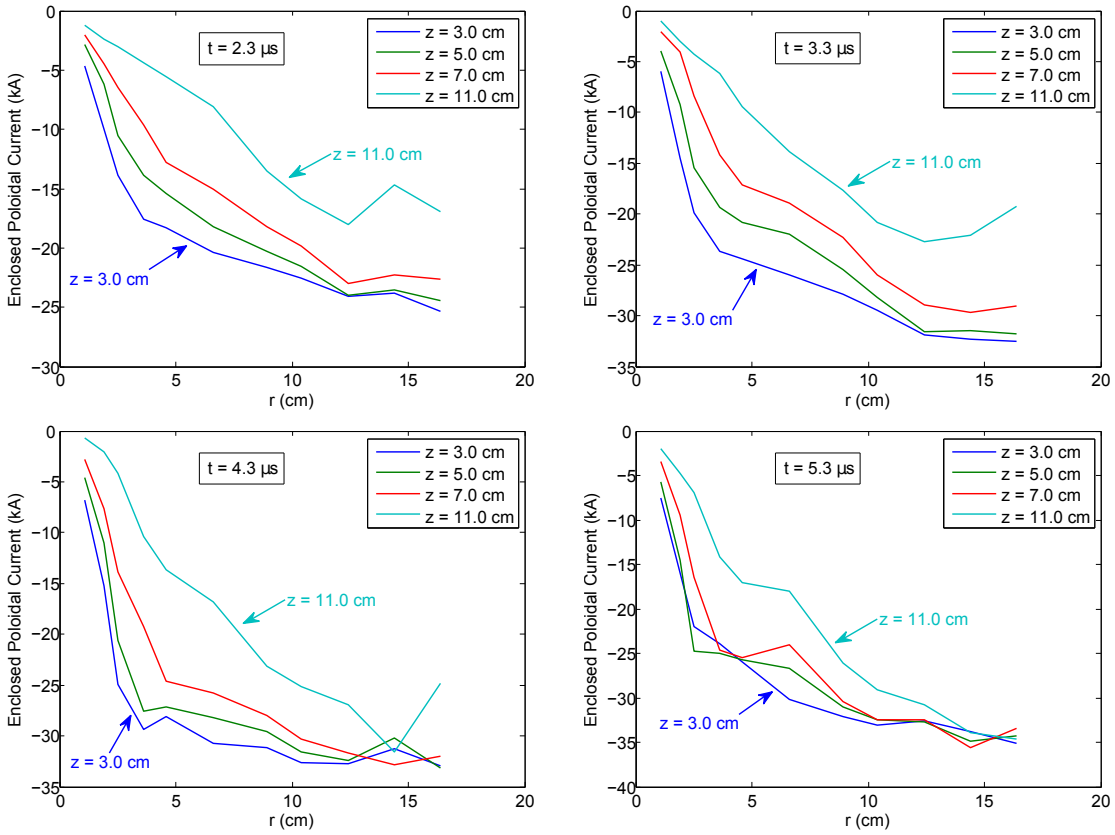

Figure 6.19: Poloidal current profile $I(r)$ for pre-ionized argon jets formed with V_{main} = 4 kV, V_{bias} = 80 V, $V_{gas,RF}$ = 550 V, $V_{gas,inner}$ = 460 V, and $V_{gas,outer}$ = 750 V. As in Fig. 6.5, axisymmetry was assumed in order to calculate $I(r)$ from the measured $B_{tor.}(r)$. This assumption may have started to break down by $t = 5.3$ μs, when many of the jets had already begun to kink.

specifies the axial current I needed to confine N particles per unit length at temperature T, but it places no restriction on the details of the current profile $J_z(r)$, nor on the radius of the plasma column. It is clear that a collimated jet that is in radial force balance will not expand or contract its radius, but the choice of that equilibrium radius must depend on the boundary conditions or on the past history of the jet evolution.

To better understand the radial structure of the pre-ionized jets, the magnetic probe array was used to measure the axial current distribution as a function of radius at four different axial locations. Results for jets with $V_{gas,RF}$ = 550 V, $V_{gas,inner}$ = 460 V, and $V_{gas,outer}$ = 750 V are shown in Fig. 6.19. The jets were highly flared at the probe cluster locations at early times (the current channel radius was larger further from the electrodes),

but at later times collimation was evident once the flared jet front had moved past the clusters at $z = 3.0$–7.0 cm. The current channel radius, defined as the radius inside which 70% of the total poloidal current was enclosed, was $a_{cur.} \sim 3$ cm near the electrodes. This was much larger than the final equilibrium visible jet radius, $a_{vis.} \approx 0.5$ cm (see Figs. 6.14 and 6.18). A similar but proportionally smaller discrepancy was observed for hydrogen jets formed without pre-ionization (see Fig. 6.5)—the visible radius of these jets was $a_{vis.} \approx 2$–3 cm, while the current channel radius near the electrodes was $a_{cur.} \sim 5$ cm. There must have been some plasma in the outer portion of these jets in order to carry the measured current, but its density was low enough that the visible brightness of the outer envelope was negligible compared to the brightness of the dense center of the jets.

If we assume that the current profile $J_z(r)$ in the pre-ionized argon jets was uniform (Fig. 6.19 suggests that it was actually somewhat centrally peaked) and that the electron density in the outer envelope of the jet was $n_e = 10^{21}$ m^{-3}, then the electron drift velocity necessary to carry the measured current ($I \sim 25$ kA) was

$$u_e = \frac{J_z}{n_e e} = \frac{I}{\pi a_{cur.}^2 n_e e} \approx 6 \times 10^4 \text{ m/s}. \tag{6.27}$$

This is a physically plausible fluid velocity (as discussed in Sec. I.1, kinetic instabilities would have been expected to develop for $u_e \gtrsim v_{Te} \sim 10^6$ m/s). Since the brightness of the fully ionized jets scaled approximately as $n_e n_i$ [28], it is likely that a region of the plasma with $n_e = 10^{21}$ m^{-3} would have indeed been invisible next to the central column, which had $n_e \gg 10^{22}$ m^{-3} (see the left panel of Fig. 6.16).

Now consider the radial force balance requirement in the outer part of the jet. A uniform axial current density leads to a parabolic pressure profile, $P(r) = P_0 \left(1 - (r/a)^2\right)$ (we are temporarily ignoring the dense central region of the jet in order to roughly analyze the outer region), so $\partial P/\partial r = -2P_0 r/a^2$. The radial pinch force is $(\mathbf{J} \times \mathbf{B})_r = -(J)(\mu_0 I(r)/2\pi r) = -\mu_0 J^2 r/2$. Therefore, in equilibrium we have

$$\frac{2P_0 r}{a^2} = \frac{\mu_0 J^2 r}{2} \tag{6.28}$$

$$P_0 = (n_e + n_i)\, kT = \frac{\mu_0 J^2 a^2}{4} = \frac{\mu_0 I^2}{4\pi^2 a^2}. \tag{6.29}$$

With $n_e + n_i = 1.5 \times 10^{21}$ m^{-3}, $I = 25$ kA, and $a = 3$ cm, Eq. 6.29 implies $T \approx 90$ eV. This is an unrealistically high temperature, so it appears that radial force balance could not have been satisfied with the calculated $\mathbf{J} \times \mathbf{B}$ force. The density would have needed to be an order of magnitude higher in order for Eq. 6.29 to give a plausible temperature, but then the plasma at 0.5 cm $< r <$ 3 cm surely would have been visible.

The solution to this dilemma is to conclude that the magnetic field in the outer region of the jet must have been force free—i.e., it had a helical structure such that $\mathbf{J} \parallel \mathbf{B}$. This interpretation was previously put forward by Kumar [134, p.83] to explain the aforementioned mismatch between the visible radius and current channel radius in non-pre-ionized hydrogen jets. It is well known that MHD plasmas with $\beta \equiv 2\mu_0 P/B^2 \ll 1$, including spheromaks and many astrophysical plasmas, naturally evolve toward a force-free state [4, p. 394]. However, it is not clear why a force-free field structure would have developed in the outer region of the jet, rather than the whole current channel pinching down to form a high density plasma column with $\beta_{tor.} \sim 1$. An important project for future research is to make detailed measurements of both $B_\phi(\mathbf{r})$ and $B_z(\mathbf{r})$ in order to confirm the existence of a force-free field geometry in both pre-ionized and non-pre-ionized jets.

We may repeat the radial force balance calculation for the dense central part of the jet. Estimating from Fig. 6.19 that the current within the visible jet ($a_{vis.} \approx 0.5$ cm) was $I = 4$ kA and setting $n_e + n_i = 5 \times 10^{22}$ m^{-3}, we find that Eq. 6.29 required $T = 2.5$ eV, which agrees well with the rough estimates in Table 6.1.

The analysis thus far has ignored the bias magnetic field, which exerted a radially outward force $F_B = -\partial/\partial r \left(B_z^2/2\mu_0\right)$ when it was compressed by the pinching of the jet. Because of this magnetic pressure force, which added to the thermal pressure force $-\partial P/\partial r$, applying a stronger bias field was expected to impede the pinching behavior. The measured current channel radius $a_{cur.}$ and the minimum visible jet radius $a_{vis.}$ during the pinch are shown as a function of V_{bias} in Fig. 6.20. Large values of V_{bias} led to a measurable increase in the minimum $a_{vis.}$, as expected, but the effect was too weak to be resolved at $V_{bias} \leq 120$ V, and no clear trend was visible in the current channel radii.

Increasing the initial neutral gas density (and consequently the initial plasma density, since the jets were nearly fully ionized) was likewise expected to cause the minimum radius

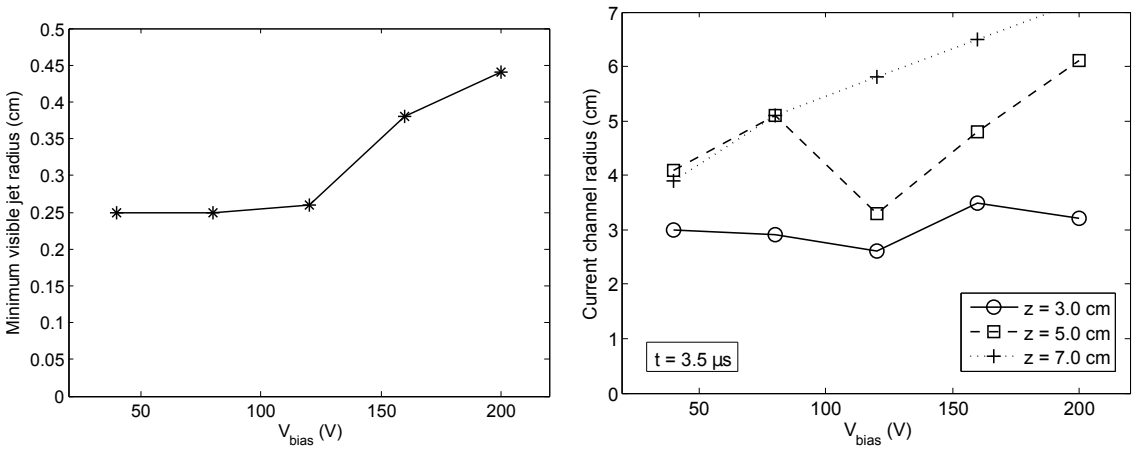

Figure 6.20: Left: Minimum visible jet radius $a_{vis.}$ during the bright pinch as a function of bias field strength. The radius was the defined as half of the visible plasma column width, measured by identifying the locations at which the brightness had fallen to 10% of the central peak value in unsaturated Imacon camera images. It was averaged over an axial length of ~ 0.5 cm near the electrodes. Right: Current channel radius $a_{cur.}$, defined as the location inside which 70% of the total poloidal current flowed, as a function of bias field strength at $t = 3.5$ μs, roughly the time at which the visible plasma column radius typically reached its minimum.

attained by the pinched jet to increase: for a given initial temperature, a plasma with high initial density would not need to be compressed as much in order for the thermal pressure to balance the magnetic pressure. However, Fig. 6.21 shows that neither $a_{vis.}$ nor $a_{cur.}$ became larger as $V_{gas,RF}$ was increased (in fact, the smallest visible pinch radius of all was obtained with $V_{gas,RF} = 700$ V). This surprising result implies that the extreme narrowness of the pre-ionized jets was probably not caused by the low level of neutral gas input enabled by pre-ionization. Instead, the jet morphology differed from that of non-pre-ionized jets such as the one shown in Fig. 6.1 because the gas from which the jet formed was injected at a different location—along the z axis rather than at $r = 4.8$ cm. The non-pre-ionized jets also started out of equilibrium and pinched down to a smaller radius, but the final equilibrium values of $a_{vis.}$ and $a_{cur.}$ were much larger than those for pre-ionized jets. One possible explanation for the difference is that the non-pre-ionized jets were composed of 8 individual "spider leg" loops (see Fig. 1.5) that had to merge along the z-axis in order for the jet radius to pinch down. In the limiting case of perfectly conducting, flux conserving plasma, this merging would not occur—once the flux tubes got close together, currents induced on

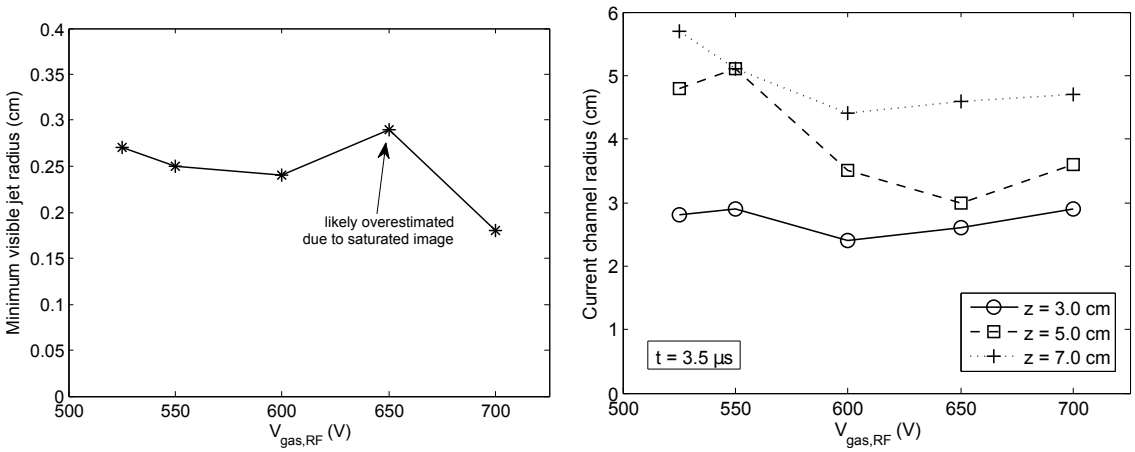

Figure 6.21: Left: Minimum visible jet radius $a_{vis.}$ during the bright pinch as a function of RF source fast gas valve voltage. Right: Current channel radius as a function of $V_{gas,RF}$ at $t = 3.5$ μs, roughly the time at which the visible plasma column radius typically reached its minimum.

their surfaces would cancel out the attractive force from the parallel poloidal currents. The actual spider legs had finite resistivity and thus could undergo magnetic reconnection and merge into a central jet column, but incomplete merging may have limited the pinching of the jet radius.

6.5.3 Departures from Ideal MHD

A final aspect of the pre-ionized argon jets that was interesting, although unfortunate for their relevance to astrophysics, was that their parameters placed them near the boundary of the MHD regime. Consider first the magnetic Reynolds number, $R_m \equiv \mu_0 LU/\eta$ (this is a generalized version of the Lundquist number defined in Eq. 1.29), which is infinite in ideal MHD. The length scale of the jets was $L \sim 20$ cm in the axial direction, their velocity was $U \sim 20$ km/s (see Fig. 6.11), and the resistivity with $T_e \sim 5$ eV and $Z \approx 2$ was $\eta = \left(1.03 \times 10^{-4}\right) Z \ln\Lambda / T_{eV}^{3/2} = 1.8 \times 10^{-4}$ Ω–m [4, p. 596], so we find $R_m \sim 28$, which is large enough for ideal MHD to be a good approximation. In the radial direction, on the other hand, the characteristic gradient length was only ~ 1 cm, so assuming the same parameters (Fig. 6.14 shows that 20 km/s was a reasonable estimate for the radial pinch velocity), the Reynolds number was $R_m \sim 1.4$. This means that the magnetic field was not

perfectly frozen into the plasma during the pinching process. One of the motivations for pre-ionization stated in Sec. 1.7 was to increase the Lundquist number by increasing v_A and T_e. Although these goals were individually achieved, the modest improvements were more than offset by the decrease in the jet radius and by the increase in the mean ion charge Z.

A similar calculation shows that another non-ideal MHD term in the generalized Ohm's law, called the Hall term [4, p. 55], also may have been important during the radial compression of the pre-ionized jets. This term is given by $-\mathbf{J} \times \mathbf{B}/n_e e$; its importance relative to the $\mathbf{U} \times \mathbf{B}$ term in Eq. 1.14 is measured by the ratio $(c/\omega_{pi})/L$, where c/ω_{pi} is called the ion skin depth. Using the visible jet radius $a_{vis.} \sim 0.5$ cm for L and assuming $n_i \sim 10^{22}$ m^{-3} and $Z \approx 2$, we find $(c/\omega_{pi})/a_{vis.} \sim 1.4$. The Hall term, which represents decoupling of the electron and ion fluid motions, is known to facilitate fast magnetic reconnection. In the original Caltech MHD-Driven Jet Experiment, Moser and Bellan [41] found that reconnection occurred and broke up the jet after an instability eroded its radius to below the ion skin depth. The images presented in this chapter show that the pre-ionized jets did not break up despite satisfying the same criterion, possibly because there was no force or inertia seeking to pull two segments of the jet in different directions.

Finally, using $B \sim 0.2$ T, $Z \approx 2$, and $T_i \sim 5$ eV, we see that the ion Larmor radius in the pre-ionized jets was also comparable to the visible jet radius: $r_{Li} = m_i v_{Ti}/ZeB \sim 0.5$ cm. The jets were therefore in a non-MHD, kinetic regime. Having r_{Li} comparable to the plasma radius has been found to suppress MHD instabilities in field reversed configurations (FRCs) [150], and it would be interesting to check whether the classic Kruskal-Shafranov kink instability criterion (see Sec. 1.2) is modified in the pre-ionized jets. The jet shown in Fig. 6.18 had ripples on its surface that may have been an $m = 0$ sausage instability, but it did not break up, suggesting that the instability saturated or was stabilized.

6.6 Reasons for Needing a Large Amount of Gas Input Through the Outer Electrode

As discussed in Sec. 6.2, the pre-ionized jet experiment was unable to create jets with masses more than a factor of 2–4 lower than those studied in the original Caltech MHD-Driven Jet

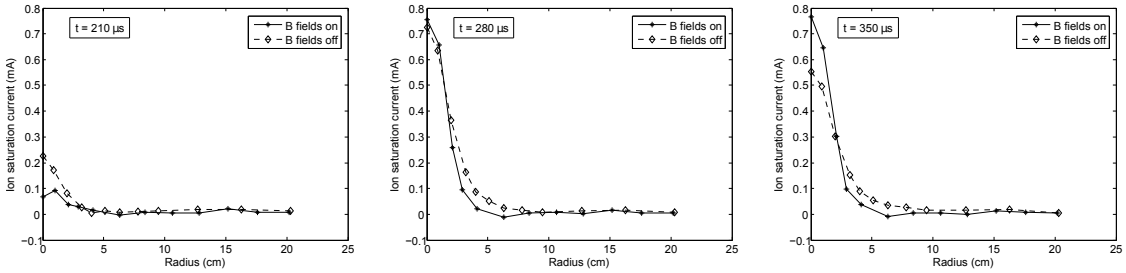

Figure 6.22: Langmuir probe ion saturation current as a function of radius measured at $z = 3.8$ cm at three different times during the RF plasma expansion (here the time of RF amplifier turn-on is defined as $t = 0$ μs). Gas was supplied through the rear end of the RF plasma source tube with the fast gas valve bank set to $V_{gas,RF} = 550$ V.

Experiment, because a jet would not form unless a substantial quantity of neutral gas was injected through the 8 gas inlets on the outer electrode. A portion of this gas was ionized and dragged along with the jet, limiting the maximum jet velocity that could be achieved (see Sec. 6.4.2). One probable reason for needing high $V_{gas,outer}$ was that pre-ionized RF plasma was injected only at the center of the inner electrode. If this plasma diffused out of the RF discharge tube along the magnetic field lines shown in Fig. 2.2, as suggested by the fast camera images in Figs. 4.1 and 4.2, then it could never reach the region near the outer electrode[15]. Therefore, the RF plasma alone could not enable the path for poloidal current flow needed to drive a jet, and breaking down additional neutral gas in the vicinity of the outer electrode was necessary.

In order to confirm that no RF plasma reached the region near the outer electrode, the straight Langmuir probe described in Sec. 3.1.1 was used to measure the ion saturation current as a function of radius at $z = 3.8$ cm. These measurements, shown in Fig. 6.22, verified that the RF plasma density was negligible beyond $r = 10$ cm (the inner radius of the outer electrode). The radius of the expanding plasma cone was only slightly greater with no confining magnetic field than with the bias and solenoid fields on, in agreement with the impression given by the camera images in Figs. 4.2 and 4.3.

The $I_{sat.}$ measurements in Fig. 6.22 were taken at $t > 200$ μs after RF amplifier turn-

[15]Furthermore, Fig. 4.11 showed that an appreciable downstream RF plasma density could only be achieved at locations where there was a pre-existing neutral gas cloud present, so even if the magnetic field geometry had been modified, no RF plasma could have reached the area near the outer electrode if gas was not injected through the outer electrode inlets.

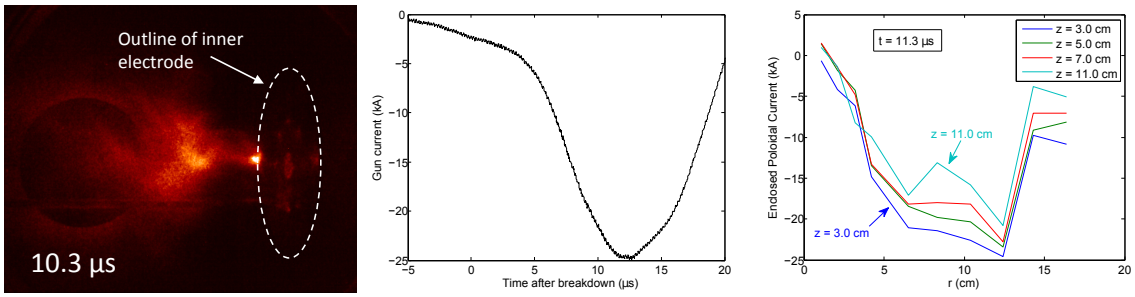

Figure 6.23: Left and center: Imacon camera image and Rogowski coil current measurement (smoothed over 500 ns using a moving average filter) for a pre-ionized argon shot with $V_{main} = 4$ kV, $V_{gas,RF} = 550$ V, $V_{gas,inner} = 460$ V, and $V_{gas,outer} = 650$ V. Right: Poloidal current distribution measured with the magnetic probe during a set of shots with these same parameters.

on, when a high density RF plasma had already expanded into the chamber. However, the beneficial effects of pre-ionization on the main plasma breakdown were realized even if the main bank was triggered only 10–150 μs after RF turn-on, when only a low density plasma created by fast electrons streaming out of the RF source was present in front of the electrodes (see Figs. 4.4, 4.5, and 4.6, and the discussion in Sec. 4.2). Most of the pre-ionized jets discussed in this chapter were created with the RF amplifier triggered 150 μs before the main bank. Increasing this time delay to 250–300 μs so that a plasma with $n \gtrsim 10^{18}$ m^{-3} was present in the chamber when the electrodes were energized did not enable any additional decrease in the amount of neutral gas input necessary for jet formation. Although our initial vision for the experiment was to form a jet primarily out of pre-ionized plasma, this did not turn out to be possible.

Although a well-defined pre-ionized jet would only form with $V_{gas,outer} > 700$ V, when lower values of $V_{gas,outer}$ were used breakdown could still be achieved, and the main bank was able to discharge through the plasma. Fig. 6.23 shows an example of the experiment behavior with $V_{gas,outer} = 650$ V, slightly below the threshold for good jet formation. The gun current ramped up slowly at first, indicating that the plasma impedance was high initially, and the plasma that was visible at later times in camera images did not propagate into the chamber as a jet. The magnetic data shows that the current channel radius was ~ 6 cm, roughly two times wider than was measured for pre-ionized jets with $V_{gas,outer} = 750$ V (see Fig. 6.19). Interestingly, $I(r)$ shown in Fig. 6.23 dipped suddenly

at r = 12–14 cm, indicating that most of the return current[16] flowed back to the outer electrode at this radial location. For successful jets, on the other hand, the return current flowed primarily at $r > 16$ cm (see Figs. 6.5 and 6.19), probably because the hoop force caused the outer segments of the spider legs to expand beyond their initial location at $r \approx 17.8$ cm.

It is not clear whether the location of the return current could be important for determining the basic jet propagation properties: the simple model of jet acceleration presented in Sec. 6.4.1 considered only the current flowing through the central jet column and neglected the return current, and recent numerical simulations of the Caltech experiment [28] were able to accurately replicate many aspects of the jet behavior despite predicting a return current radius that did not match the data. The magnitude of the poloidal current flowing through the plasma in the $V_{gas,outer} = 650$ V case was comparable to the total discharge current measured by the Rogowski coil, so the lack of jet formation could not be blamed on missing current that flowed to ground through an arc in the small gap between the electrodes or in the vicinity of the re-entrant port. It is possible that the slow initial ramp-up of the gun current (see the central panel of Fig. 6.23) was problematic—perhaps the $\mathbf{J} \times \mathbf{B}$ force during this period was sufficient to push the plasma away from the electrodes, so that when the current began to increase rapidly at $t \approx 6$ μs, the necessary initial conditions for jet formation no longer existed.

To overcome the problems discussed in this section and further explore the limits on low mass operation of the Caltech arc discharge experiments, a new setup has been devised to create a single pre-ionized arched flux rope using two RF plasma sources. By pre-ionizing plasma behind both of the experiment's electrodes instead of only behind the cathode as in the MHD-driven jet experiment, the need for a large amount of additional neutral gas injection will be obviated. The design of this experiment will be described in Appendix I.

[16]The direction of positive current flow was away from the outer electrode (anode) and toward the inner electrode (cathode), so the "return current" was actually a current in the $+z$ direction, while the current in the central jet column was in the $-z$ direction.

Chapter 7

Summary

This thesis has described the development of an electrically floating RF pre-ionization system for the Caltech MHD-Driven Jet Experiment. The main goals of this experiment were to simulate the launching and propagation of collimated jets from astrophysical accretion disks and to improve our understanding of the Woltjer-Taylor relaxation process that leads to spheromak formation. Pre-ionization expanded the accessible parameter regime in the experiment, enabling the creation of lower mass argon jets that were hotter and faster than those studied previously. Additionally, modifying the initial neutral gas distribution led to a notably different jet morphology, with an extremely narrow, collimated, high density structure at the base of the jet.

Independent of the pulsed arc discharge used to create MHD-driven jets, the RF plasma behavior was investigated in detail. The initial motivation for these experiments was to optimize the equilibrium RF discharge properties and the transport of the pre-ionized plasma into the jet experiment's chamber, but many interesting and unexpected phenomena were identified that were worthy of study in their own right. The RF discharge was designed to operate in a wave-heated helicon mode, but it was found that the primary energy coupling mechanism was actually inductive, and similar plasma densities were obtained with or without an applied axial magnetic field. The expansion of the RF plasma away from the antenna region involved the propagation of an ionization front mediated by ambipolar diffusion. The brightness of the expanding plasma did not scale with the ion density, so fast camera images were a poor indicator of the true dynamics. Peaks in both the total visible/infrared light emission and in the ion density were observed after the RF power

was turned off; the afterglow emission peak was used for an indirect measurement of the neutral gas density. The experimental results and modeling techniques developed in this thesis should be applicable to understanding the behavior of similar RF plasma discharges used in industrial materials processing. Additionally, the afterglows of inductively coupled plasmas are of significant interest in analytical chemistry.

Chapter 2 described the design of the RF pre-ionization system. The central component was a custom 13.56 MHz RF power amplifier that was powered by AA batteries, allowing it to be installed near the high voltage cathode of the jet experiment without risk of an arc to ground. Capacitors charged by the batteries stored enough energy to output 2–3 kW of RF power in pulsed (< 1 ms) operation. Variable impedance matching was accomplished with adjustable binary arrays of fixed value high voltage capacitors, and the net RF power delivered to the load was determined by directly measuring $I_L(t)$ and $V_L(t)$ and calculating $\langle I_L V_L \rangle$ numerically. Three different antenna designs were tested for coupling RF power to the plasma; a half-turn helical antenna [52] produced the highest plasma densities.

Chapter 3 introduced the diagnostics used to study the RF plasma and presented measurements of the scaling of the plasma density with RF power and magnetic field strength. A numerical steady state discharge model was developed that balanced the global rates of ionization and diffusive losses and calculated the population densities of neutral argon excited states in order to determine the equilibrium density and electron temperature of unmagnetized capacitively coupled and inductively coupled argon discharges. By comparing the model results with the measured plasma density values and scaling behaviors, it was shown that our RF discharge operated in a primary inductively coupled mode. Ion densities exceeding 5×10^{19} m^{-3} were achieved in the source tube.

Chapter 4 described the transport of the RF plasma from the antenna region where it was created into the main jet experiment chamber. Camera images were presented that appeared to show a complex multi-phase expansion sequence, but Langmuir probe measurements told a different story about the time-dependent plasma expansion—the bright region of emission visible at early times was shown to be primarily neutral gas glowing as it was bombarded by fast electrons accelerated by the antenna, and the dense plasma that later emerged from the source tube was nearly invisible in discharges with a magnetic field applied. Optical

emission spectroscopy was valuable for understanding the deceptive emission patterns; a key concept was the distinction between ionizing phase and recombining phase plasmas.

Building upon the global discharge model presented in Ch. 3, a 1D time-dependent discharge model was developed to explain the measured plasma transport. The ambipolar diffusion equation and the two-fluid electron energy equation were solved numerically, incorporating the treatment of collisional and radiative atomic processes from the global model. The model predictions for the time-dependent ion saturation current were compared with the Langmuir probe data: excellent quantitative agreement was obtained at $p_{Ar} = 30$–60 mTorr, while for $p_{Ar} \geq 120$ mTorr the model underestimated the downstream plasma density, suggesting that some process that was important at high pressures had been neglected in the calculation. In the regime where it was valid, the model provided detailed insights into the discharge properties including electron temperature, Ar I excited state populations, and the local energy budget as a function of position and time.

In Chapter 5, the interesting properties of the RF plasma afterglow were investigated in more detail. It was shown that the overall time-dependent visible and infrared emission depended on the neutral gas pressure in a predictable way, so it could be used to determine the unknown pressure in the source tube when gas was injected transiently using a fast gas valve. The pressure dependences of the emission intensity during the main discharge period and during the afterglow were explained using results from the numerical discharge model. In the second half of the chapter, the observed increase in the plasma density after RF power turn-off was analyzed. Ionization resulting from collisions between pairs of metastable atoms was identified as a possible cause of the density rise, but the expected rate of de-excitation of metastables by electron impacts was too high for this process to fully account for the data.

Finally, Chapter 6 described the MHD-driven jets created using RF pre-ionization. The jets were studied using high speed imaging, magnetic probes, high-resolution visible/UV spectroscopy, and discharge current and voltage diagnostics. Pre-ionization enabled plasma breakdown to occur with a lower amount of argon gas input than was previously possible, and the pre-ionized jets were faster as a result. However, the achievable decrease in the jet mass was limited by the need for a high initial gas density in front of the outer electrode

in order for a jet to form. Line intensity ratios showed that the pre-ionized jets were hotter and more highly ionized than their counterparts created without pre-ionization, and Stark broadening measurements revealed that the bright narrow jet column was very dense ($n_e \geq 10^{23}$ m^{-3} at the peak of the radial pinch). The current channel radius of ~ 3 cm was much larger than the visible jet radius (< 1 cm), implying that the jets consisted of a dense central plasma column surrounded by a low-density, current-carrying envelope within which the magnetic field must have been force-free. The unique narrow structure of the pre-ionized jets persisted even when the level of gas input through the RF discharge tube was increased, suggesting that the location of gas injection (along the z axis rather than at $r \approx 4.8$ cm as in the original experiment) was the most important factor leading to the observed dramatic pinching behavior.

Appendix A

Fast Ignitron Trigger Circuit Using Insulated Gate Bipolar Transistors

A.1 Background: Ignitrons, Krytrons, and IGBTs

The Caltech plasma experiments use ignitrons [151], plasma-based rectifiers containing mercury, to rapidly switch up to 100 kA of current at voltages from 3–8 kV. The ignitron used in the new MHD-driven jet experiment was a General Electric model GL-7703 size A ignitron [37]. In order to turn on this ignitron, a high voltage (1.5–3 kV), high current pulse must be applied to the ignitor, a semiconducting rod partially immersed in the pool of mercury that forms the ignitron cathode. For optimal triggering (for minimal jitter and prolonged ignitron lifetime), the current pulse amplitude should be 200-250 A [152],[153]. A trigger current rise time on the order of 1 μs was also desirable for fast turn-on of the ignitron at the initiation of a plasma discharge.

The Caltech experiments have traditionally used capacitor discharge circuits switched by krytrons to provide the ignitron trigger pulse. A krytron consists of a small tube of gas which is kept partially ionized by a "keep alive" electrode. When a high voltage pulse is applied to the trigger electrode, the gas quickly becomes fully ionized, and the krytron can conduct large currents between its anode and cathode.

Although krytrons have excellent switching behavior in a compact package, they are no longer commonly used, and new ones are difficult to acquire due to restrictions stemming from a history of military uses. Thus when the krytron in the jet experiment's main capacitor bank failed, we were compelled to switch to a more modern approach using insulated

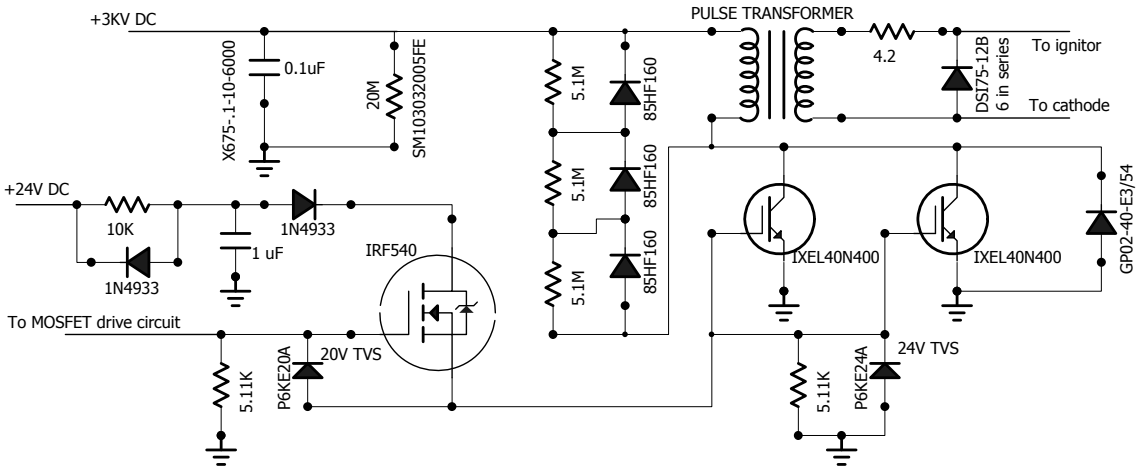

Figure A.1: Partial circuit diagram for the final ignitron trigger circuit implemented with two IXEL40N400 IGBTs in parallel. The circuit was powered by a single 24 V, 10 W DC power supply. Voltage regulator chips on the board (not shown) provided a 5 V DC supply for the MOSFET drive circuit (see Fig. A.2) and a 12 V DC supply for the input to the EMCO 3 kV proportional power supply. © 2013 IEEE.

gate bipolar transistors (IGBTs).

IGBTs are semiconductor-based devices which, as their name suggests, are a hybrid of a MOSFET (a power transistor with the input isolated from the other two terminals) and a bipolar junction transistor (BJT). Accordingly, the three terminals are labeled gate, collector, and emitter. IGBTs were invented in the 1970s and have become increasingly popular for high current, high voltage switching applications as their specifications have improved in recent years [154].

A.2 IGBT Circuit Implementation

A.2.1 Initial Circuit Design

The design of the new ignitron trigger circuit[1] was based on the old krytron board design (see Fig. A.13), with a 0.1 μF capacitor charged to 3 kV by an EMCO G30 proportional power supply and then discharged through a 1:2 pulse transformer (wound from Style 3239 #20 AWG 30 kVDC rated wire on a Ferroxcube U93/76/30-3C81+I93/28/30-3C81 U-

[1]Portions of this appendix were taken from reference [155]; this material is reused with permission under the IEEE copyright policy.

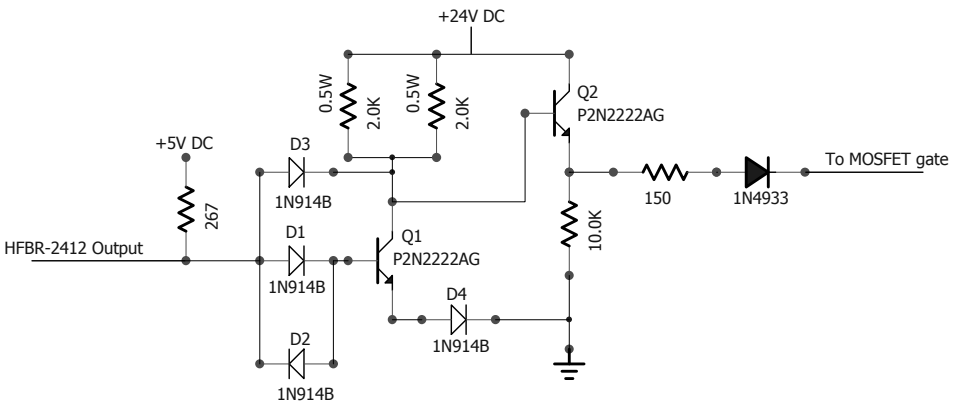

Figure A.2: Circuit used to trigger the MOSFET switch in the final design. © 2013 IEEE.

core+I-core ferrite pair, with 3 turns on the primary and 6 turns on the secondary). The secondary winding of the pulse transformer was connected between the ignitron's ignitor pin and cathode, with a 4.2 Ω resistor in series with the ignitor to limit the peak current into the ignitron. Although a step-up transformer was used, the voltage on the ignitor never exceeded 2 kV due to inductive voltage drops between the trigger board and the ignitor and because the ignitron would become a low impedance load once triggered (see Fig. A.9 and the discussion in Sec. A.2.6). The sequence to turn on the krytron in the old circuit was as follows (refer to Fig. A.13):

1. An optical pulse is received by the HFBR-2412 fiber optic receiver, causing the voltage on the open collector output to drop from its original value of 15 V to ∼0.5 V.

2. The PNP transistor $Q1$ turns on, causing the voltage on its collector to rise to nearly 15 V.

3. The gate of the MOSFET $Q2$ is charged up through a 10 Ω resistor, turning on the MOSFET. This allows the 1 μF capacitor $C1$ to discharge through the MOSFET and through the primary of a 1:40 step-up transformer.

4. Several hundred volts appears across the secondary of the step-up transformer, which is connected to the krytron's grid (trigger) electrode. The krytron begins to conduct, and the voltage on its cathode rises to nearly 3 kV.

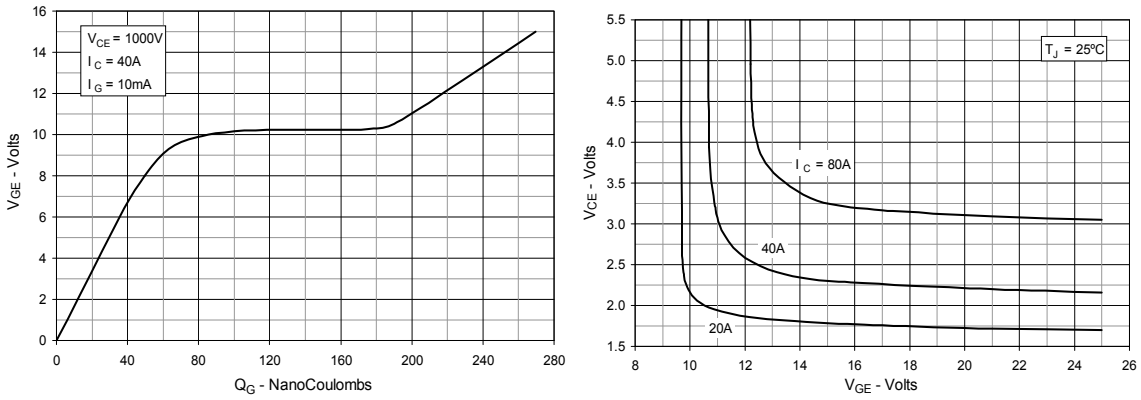

Figure A.3: Left: Gate-emitter voltage as a function of gate charge for the IXEL40N400 IGBT. The plateau in voltage as the gate charge rises and the device turns on is a ubiquitous feature for IGBTs. Right: Collector-emitter voltage as a function of gate-emitter voltage for the IXEL40N400. The horizontal part of each curve corresponds to the regime in which the IGBT is fully switched on. Notice that the gate-emitter voltage required to turn on the IGBT (which corresponds to the plateau voltage shown in the left panel) rises with increasing collector current. This sets a limit on the amount of current that the IGBT can conduct, even for short times, because there is a limit to the gate-emitter voltage that can be applied without ruining the IGBT (for the IXEL40N400, the rated maximum transient gate-emitter voltage is $V_{GEM} = 30$ V). Figures are from the device datasheet [156].

Tests of a nearly identical circuit with an IGBT replacing the krytron and a 1:1 5 kV hold-off transformer replacing the high voltage step-up transformer ran into several problems. Unlike a krytron, which will not turn off once triggered until current stops flowing between its anode and cathode, an IGBT requires a sustained voltage between its gate and emitter in order to remain on. This was difficult to achieve when triggering the IGBT through a transformer. The circuit was also difficult to diagnose in this configuration because the IGBT's emitter would rise to nearly 3 kV upon triggering, so an oscilliscope probe could not be connected directly between the gate and emitter to measure $V_{GE}(t)$. For these reasons, the circuit was reconfigured with the load (the pulse transformer and ignitron or, in bench-top tests of the circuit, a resistor) connected to the IGBT's collector, removing the need for a trigger transformer and ensuring that the gate and emitter remained near ground at all times. Circuit diagrams for the final design are shown in Figs. A.1 and A.2.

Initial tests were carried out with an inexpensive IXGH6N170A IGBT, rated for a maximum collector-emitter voltage (V_{CES}) of 1700 V and a peak current (I_{CM}) of 14 A for 1

ms. For these tests, the capacitor was only charged to ∼1400 V. A discharge current of ∼30 A through the IGBT was obtained, enough to trigger the ignitron and create a plasma on the Caltech Arched Flux Rope Experiment (where the tests were carried out), but the ignitron turn-on was noisy as a result of the lower-than-optimal current input to the ignitor, and after a small number of these tests the IGBT failed (most likely due to overheating and subsequent breakdown of the silicon [157]). For the final circuit design, a more powerful IGBT was chosen: the IXEL40N400 [156], rated at $V_{CES} = 4000$ V and $I_{CM} = 250$ A.

A.2.2 Drive Circuit Design

In order to turn on an IGBT, 10–20 V must be applied between the gate and emitter. This requires charging up the IGBT's input capacitance C_{ies}, which is typically a few nF. The effective capacitance varies as the IGBT is turned on (see Fig. A.3 in this manuscript and Fig. (3B) in [158]), so the total gate charge required for turn-on is typically quoted in addition to C_{ies} on IGBT datasheets and is used as a guideline for circuit design [159]. For fast switching of a high power IGBT like the IXEL40N400, a drive voltage close to 20 V is preferred. This presented a problem with the original krytron board drive circuit design because the HFBR-2412 optical receiver is only rated for a maximum of 18 V on its open collector output, so simply increasing the power supply voltage to ∼20 V was not an option. Instead, the drive circuit was redesigned (see Fig. A.2) with an NPN switching transistor and an emitter follower (implemented with a second NPN transistor) for current gain to achieve a faster MOSFET gate charging time. The power supply voltage was increased to 24 V, with only 5 V on the optical receiver output prior to triggering.

In the circuit shown in Fig. A.2, the 2N2222 transistor $Q1$ is on initially and is then switched off upon triggering. It was found that the time required for the transistor to turn off made a significant contribution to the total delay in the circuit. Further research revealed that bipolar transistors have difficulty turning off quickly when they have been operating in saturation (the state in which the transistor is fully switch on and the collector-emitter voltage drop is as small as possible), as in switching applications [160]. This situation is quantified by a transistor parameter called "storage time", which is around 225 ns for 2N2222 transistors. The key to achieving faster turn-off times is to keep the transistor

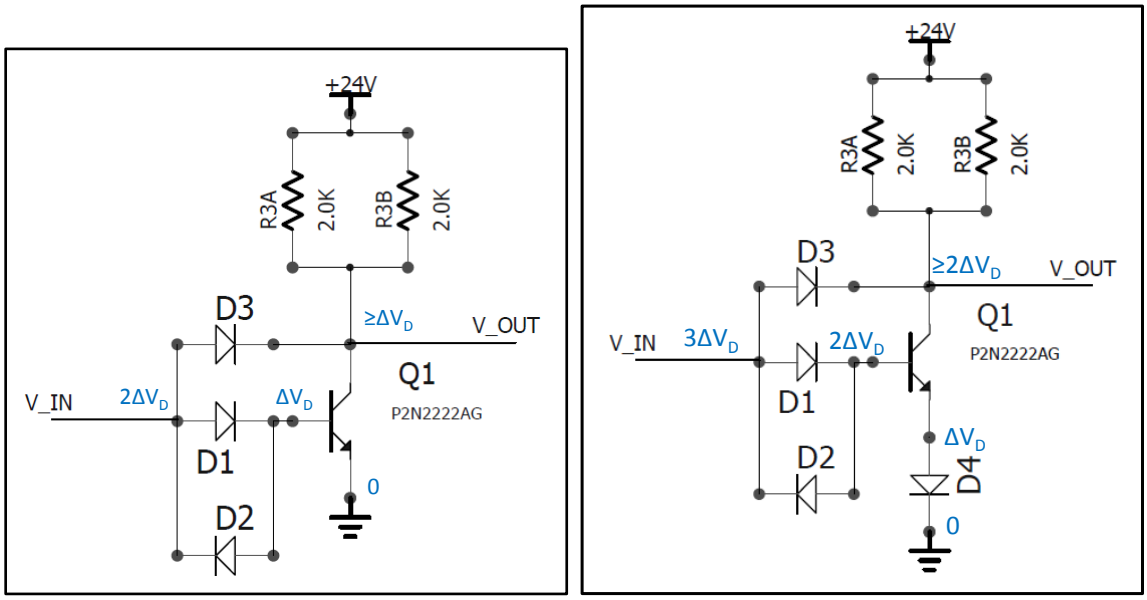

Figure A.4: A standard Baker clamp configuration (left) and the modified Baker clamp used here with an additional diode $D4$ at $Q1$'s emitter (right). The voltages in the circuit when $Q1$ is on (prior to the arrival of an optical trigger) are labeled on the figures (ΔV_D is the on-state voltage drop across a diode).

from going into saturation, a trick that can be accomplished using diodes in a configuration known as a Baker clamp [160].

A standard Baker clamp is composed of the diodes $D1$, $D2$, and $D3$ from Fig. A.2 (the relevant portion of the circuit is reproduced in Fig. A.4). The base-emitter junction of $Q1$ acts like a diode, so when $Q1$ is on, $D1$ ensures that the input voltage V_{in} is two diode voltage drops ($2\Delta V_D$) above the emitter voltage V_E (i.e., $V_{in} - V_E = 2\Delta V_D$). Meanwhile, $D3$ restricts the collector voltage V_C to be no more than one diode voltage drop below the input voltage, meaning that $V_C - V_E \geq \Delta V_D$. This condition prevents the transistor from going into saturation, and as a result the transistor can turn off extremely quickly. The diode $D2$ provides a current path for discharging the transistor's input capacitance during turn-off. $D4$ is not a part of a standard Baker clamp, but was necessary for this circuit because the input voltage provided at the optical receiver can only drop to ~0.5 V. With a standard Baker clamp (left panel of Fig. A.4), this input voltage is not low enough to make $D2$ start conducting and allow $Q1$ to turn off quickly. The addition of $D4$ (right panel of

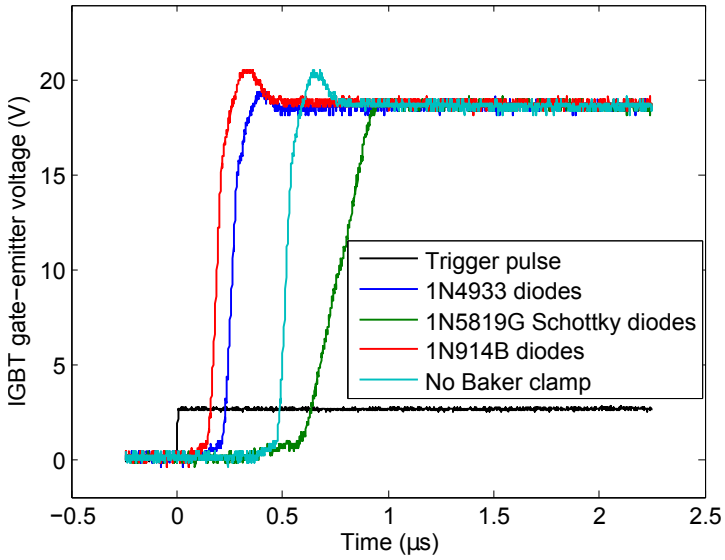

Figure A.5: Total delay between the optical trigger and the charging of the IGBT gate with the Baker clamp in place. Several different diodes were tested, with the 1N914B performing best.

Fig. A.4) raises the voltages on $Q1$'s pins by ΔV_D when the transistor is on, solving this problem. The change in switching time with the Baker clamp implemented using three different models of diode is shown in Fig. A.5. The inexpensive 1N914B high-speed diodes produced the best performance, so these were used in the final circuit design.

A.2.3 Importance of Circuit Layout

Because IGBT circuits involve high currents and rapid switching, $\frac{dI}{dt}$ can be quite high, and stray inductances in the circuit can wreak havoc on the expected behavior. Minimizing these inductances by paying careful attention to the circuit layout is critical for achieving fast switching times and avoiding other unwanted effects. In the initial tests of the new ignitron trigger circuit, the IGBT was connected with several inches of wire between its emitter and the ground side of the 0.1 μF high voltage capacitor. The results were less than favorable, as shown in Fig. A.6. Because of the inductance between the emitter and ground, a voltage appears on the emitter as the current ramps up, subtracting from V_{GE}. Due to the low gate-emitter voltage at early times, the IGBT turns on slowly. In the "short wire" example shown in the figure, $\frac{dI}{dt} \approx 60$ A/μs, and the dip in V_{GE} appears to be $\sim$2.5

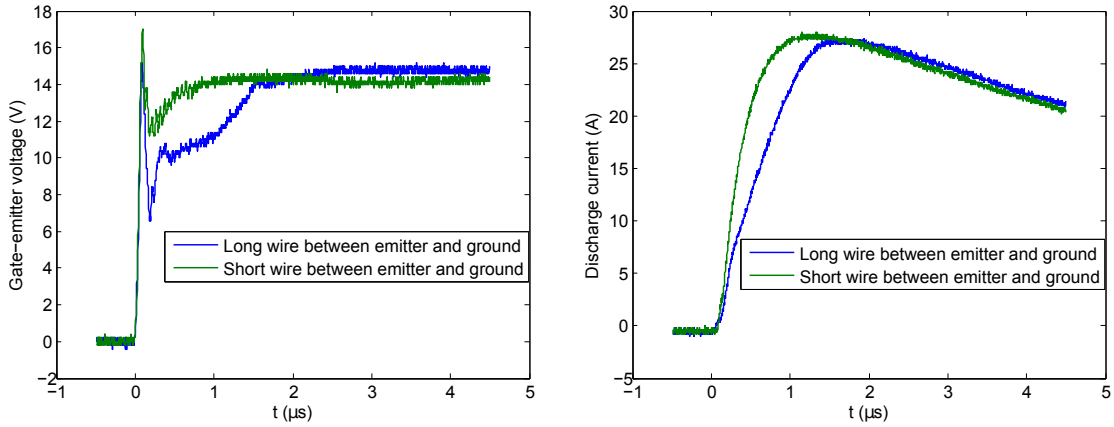

Figure A.6: Effect of having too much inductance between the IGBT emitter and high voltage capacitor ground. The capacitor was charged to 3 kV and discharged through a 100 Ω load. The $L\frac{dI}{dt}$ voltage drop between the emitter and ground causes V_{GE} to drop (left panel) as the discharge current ramps up; as a result, the IGBT turns on slowly (right panel). The effect is worse with a longer wire (higher inductance) between the emitter and ground.

V, implying that the inductance between the emitter and ground was ∼40 nH. This is a reasonable number given the rule of thumb that each inch of wire length adds about 20 nH of inductance [158]. However, we needed to do much better to rapidly switch > 400 A in the final circuit design. This was achieved by mounting the IGBT as close as possible to the capacitor $C2$'s ground (see Fig. A.8). An effort was also made to mount the MOSFET $Q3$ and the capacitor $C3$ close to the IGBT gate, as inductance in the gate drive circuit can also cause problems for ultra-fast turn-on of IGBTs [158].

A.2.4 Two IGBTs in parallel

Another crucial aspect of IGBT behavior for fast switching of large currents is that the V_{GE} required for turn-on increases with increasing collector current (see the right panel of Fig. A.3). When discharging the 0.1 μF capacitor at 3 kV through the IXEL40N400 IGBT and an 8 Ω load, the discharge current was seen to plateau before reaching its expected peak value ($I_{peak} = 3 \text{ kV}/(8\Omega + R_{ON,IGBT}) \approx 300$ A), as shown in Fig. A.7. This happened because the threshold V_{GE} had risen to a level approximately equal to the applied drive voltage. To increase the collector current further, the applied gate-emitter voltage would

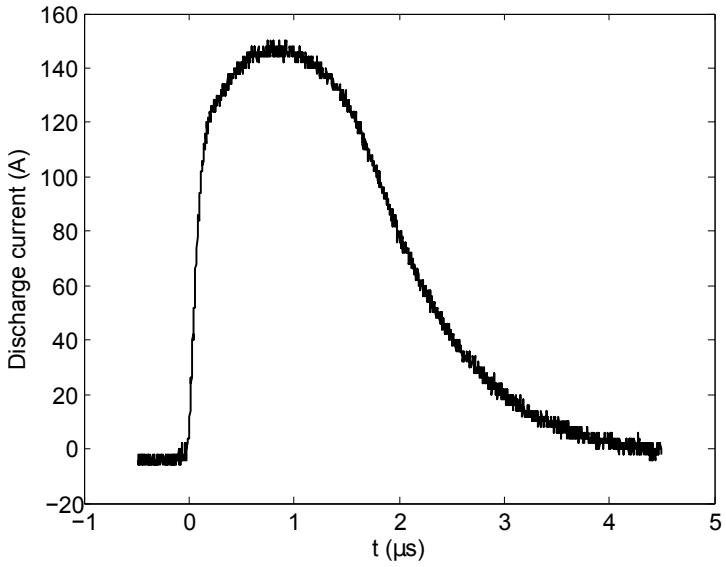

Figure A.7: Current through the IXEL40N400 IGBT with the 0.1 μF capacitor charged to 3 kV and an 8 Ω resistive load. The current rises extremely rapidly initially ($\frac{dI}{dt} \approx 800$ A/μs), but the rate of increase slows above $I_C = 120$ A as the threshold gate-emitter turn-on voltage (see the right panel of Fig. A.3) approaches the applied voltage.

have to be increased.

To match the performance of the krytron and deliver at least 200 A to the ignitron, the IGBT needed to conduct at least 400 A of current (due to the 1:2 pulse transformer). It was clear that this would not be possible with a single IXEL40N400 IGBT. Fortunately, the same negative feedback that limits the peak collector current also makes it possible to install multiple IGBTs in parallel without fear that the current will travel primarily through a single IGBT and damage it. Our final circuit design used two IXEL40N400s in parallel, as shown in Fig. A.1. The current output of the final ignitron trigger circuit is shown in Fig. A.9, and a photo of the finished circuit board is shown in Fig. A.8. The IGBT-based circuit produced a current pulse of comparable rise time and slightly higher amplitude than the krytron-based circuit. The IGBT circuit could output $\frac{dI}{dt} > 1.2$ kA/μs through an 8 Ω resistive load, but the load inductance limited the rate of current increase to be smaller than this when the circuit was connected to the ignitron. The sources of inductance in the load will be discussed in detail in Sec. A.2.6.

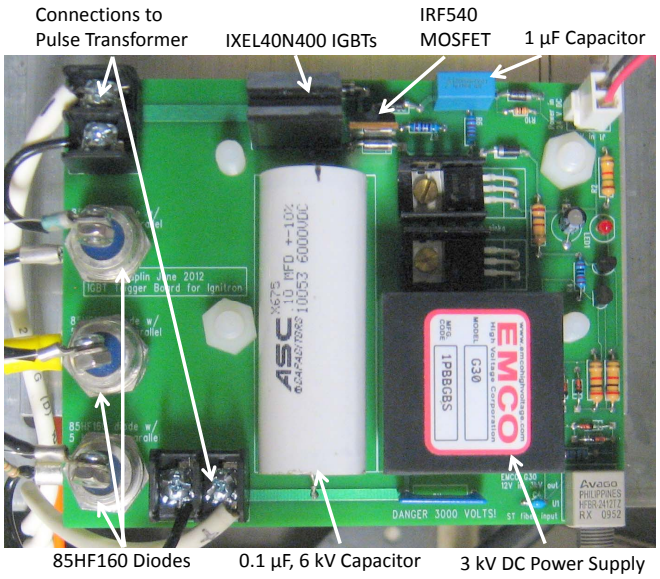

Figure A.8: Photo of the final ignitron trigger circuit using IGBTs (pulse transformer not shown). The board dimensions are 4 inches by 5 inches. Note the placement of the IGBTs as close as possible to the ground side of the 0.1 μF high voltage capacitor. © 2013 IEEE.

A.2.5 Protective Diodes

Diodes were installed at a number of locations in the circuit to protect the various components from damage. As shown in Fig. A.1, 85HF160 diodes were connected across the primary of the pulse transformer. These diodes are only rated for a maximum reverse voltage of 1.6 kV, but they needed to hold off 3 kV at the moment of IGBT turn-on, so three diodes were connected in series with a 5 MΩ resistor across each one to ensure an equal 1 kV voltage drop across each diode. When the voltage on the 0.1 μF capacitor fell below 0 during the LRC circuit discharge, current began to flow through the diodes, and the voltage on the collector of the IGBTs did not become negative. The diodes also protected the IGBTs from damage in the event that they were turned off at the gate while positive current was still flowing into the collector. In this case, the $L\frac{dI}{dt}$ voltage across the transformer primary could have caused the voltage on the collector to become so high that the collector-emitter breakdown voltage of the IGBT was exceeded; the diodes prevented this from happening. Six DSI75-12B diodes in series were also installed on the secondary side of the pulse transformer to prevent the ignitor-cathode voltage from becoming negative.

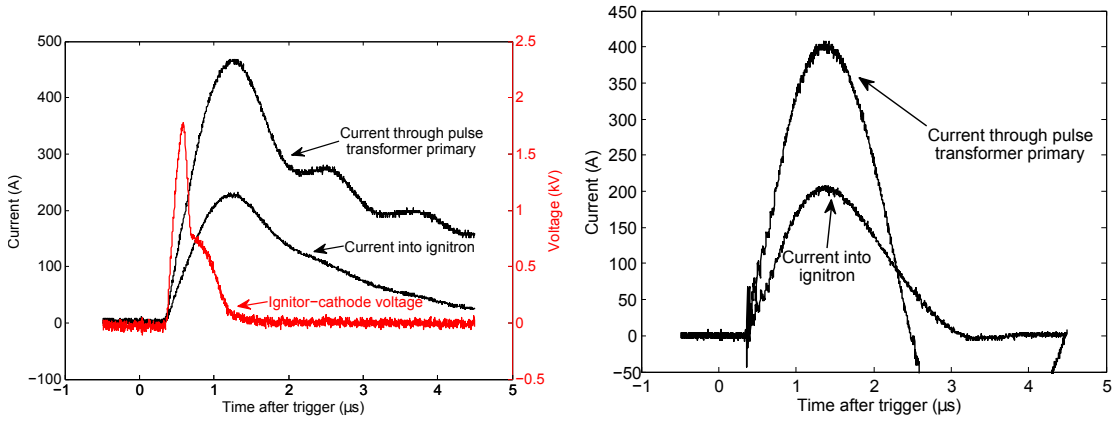

Figure A.9: Current delivered to the ignitron by the new IGBT-based circuit (left) and the old krytron-based circuit (right). The voltage at the ignitor is also shown for the new circuit. Initially, the ignitron acts approximately like a 22 Ω resistor, with $V_{ignitor} \approx 22 \times I_{ignitor}$. At $t \approx .58$ μs, the ignitor-to-cathode impedance begins to change, presumably due to mercury plasma breakdown in the ignitron, and from this point forward the voltage is no longer directly proportional to the current. Voltage was measured with a Tektronix 6015A high voltage probe and current was measured with an Ion Physics Model CM-1-L current monitor. The IGBT circuit had diodes across the primary of the pulse transformer, allowing positive current to continue flowing through the transformer even when the capacitor had fully discharged, while the krytron circuit did not.

As an additional protective measure, reverse diodes were also connected directly between the IGBT's collector and emitter, and between the gate and emitter, as shown in Fig. A.1. The diode between the gate and emitter was a transient-voltage-suppression (TVS) diode, which is designed to safely undergo reverse breakdown (with no damage to the diode) when the voltage across it exceeds 24 V. This diode was installed as a precaution to prevent the IGBT's gate-emitter breakdown voltage from being exceeded.

A.2.6 Load Inductance and Non-Ideal Pulse Transformer Coupling

As discussed in Sec. A.2.4, the IGBT-based circuit was able to achieve a greater rate of collector current increase with an 8 Ω resistive load than with the ignitron attached, implying that the inductance of the load in the final setup was limiting the current rise time. Comparisons of the voltage waveforms at various points in the circuit revealed that the connecting wires between the circuit board, pulse transformer, and ignitron made non-negligible con-

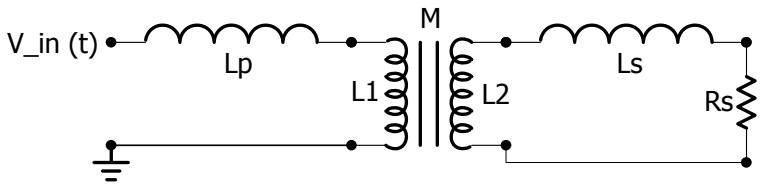

Figure A.10: Circuit analyzed in the transformer leakage inductance derivation.

tributions to the load inductance, but the main factor limiting the rise time was non-ideal behavior of the pulse transformer itself.

Since the primary and secondary windings in a real transformer cannot occupy exactly the same position in space, there will be some deviation from the ideal transformer condition in which identical magnetic flux links the primary and secondary. This stray flux leads to an effective inductance in series with the primary or secondary—this is known as the "leakage inductance" of the transformer.

To see how leakage inductance arises from non-ideal coupling between the windings [161], let L_1 be the primary inductance, L_2 be the secondary inductance, and M be the mutual inductance of the windings, and consider a circuit with some additional inductance L_p in series with the primary and inductance L_s and resistance R_s in series with the secondary (see Fig. A.10). If a voltage $V_{in}(t)$ is applied to the primary, the currents through the windings will be related by

$$L_1\dot{I}_1 + M\dot{I}_2 = V_{in}(t) - L_p\dot{I}_1 \tag{A.1}$$

$$M\dot{I}_1 + L_2\dot{I}_2 = -L_s\dot{I}_2 - R_sI_2. \tag{A.2}$$

Eliminating $\dot{I}_1$ to solve for $\dot{I}_2$ in terms of $V_{in}(t)$ and I_2:

$$\dot{I}_2 = \frac{-\left(L_1 + L_p\right)R_sI_2 - MV_{in}(t)}{\left(L_1 + L_p\right)\left(L_2 + L_s\right) - M^2}. \tag{A.3}$$

Define the transformer coupling coefficient $\kappa \equiv M/\sqrt{L_1L_2}$, so that $\kappa = 1$ for an ideal transformer and $\kappa < 1$ for a real transformer. Substituting in for M, and assuming $L_1, L_2 \gg L_p, L_s$ (since the transformer is wound on a ferrite which amplifies the flux through the

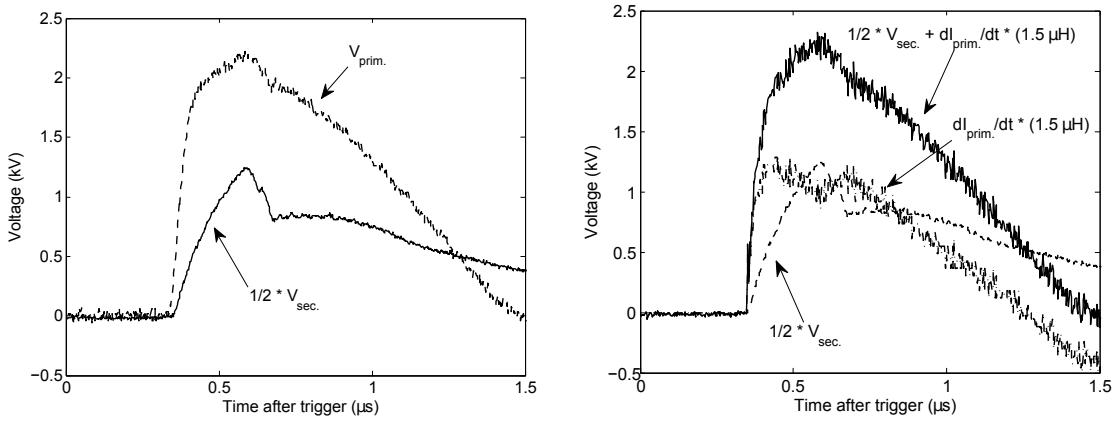

Figure A.11: Voltage across the pulse transformer primary and secondary windings during the first 1.5 μs of a pulse. If the transformer were ideal, the secondary voltage $V_{Sec.}$ would be exactly twice the primary voltage $V_{prim.}$. However, the actual secondary voltage is lower than this (left panel) due to imperfect coupling of flux between the primary and secondary. If a 1.5 μH leakage inductance is assumed to be present in series with the primary, the associated $L\frac{dI}{dt}$ voltage drop accounts for the discrepancy between the $V_{prim.}$ and $V_{Sec.}$ waveforms (right panel).

primary and secondary), the previous equation becomes

$$\dot{I}_2 = \frac{-L_1 R_s I_2 - \kappa\sqrt{L_1 L_2} V_{in}(t)}{L_1 L_2 \left(1-\kappa^2\right) + L_1 L_s + L_2 L_p}. \tag{A.4}$$

Consider the response of the circuit to a step function voltage input at $t = 0$. In this case solving the differential equation for the current through the secondary yields

$$I_2(t) = -V_{in}\frac{\kappa}{R_s}\sqrt{\frac{L_2}{L_1}}\left(1 - \exp\left(-\frac{t}{\tau_r}\right)\right) \tag{A.5}$$

$$\tau_r \equiv \frac{1}{R_s}\frac{L_2}{L_1}\left(L_1\left(1-\kappa^2\right) + \frac{L_1}{L_2}L_s + L_p\right). \tag{A.6}$$

This result shows that for the purpose of determining the rise time τ_r, setting $\kappa \neq 1$ is equivalent to adding an inductance $L_1\left(1-\kappa^2\right)$ in series with the primary, or $L_2\left(1-\kappa^2\right)$ in series with the secondary. Because of the dependence on κ^2 and the fact that $L_1, L_2 \gg L_p, L_s$, a small deviation from perfect coupling will have a large effect on the rise time.

For the pulse transformer utilized in this work, a B&K Precision Model 885 LCR/ESR Meter was used to measure $L_1 = 121.6\ \mu H$, $L_2 = 485.3\ \mu H$, and $M = 241.7\ \mu H$ (mutual

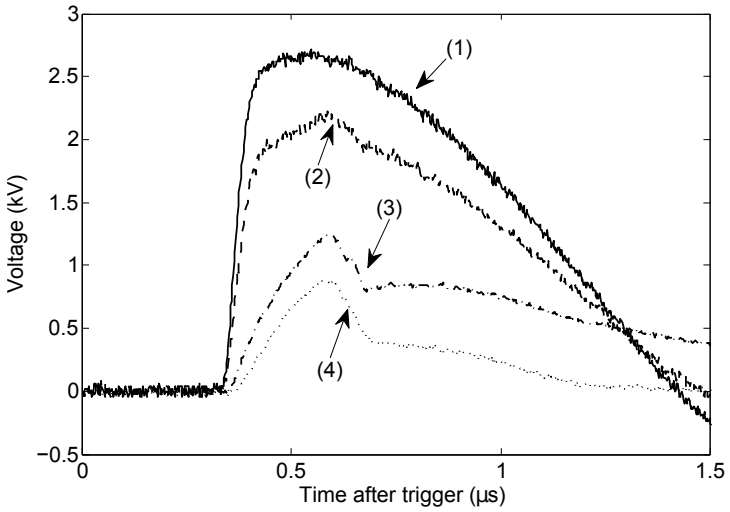

Figure A.12: Voltage waveforms during the first 1.5 μs of a pulse measured at four locations in the circuit: 1) Between the high voltage side of the 0.1 μF capacitor on the circuit board and the IGBT collectors. 2) Across the pulse transformer primary. 3) Across the pulse transformer secondary. 4) Between the ignitron ignitor and cathode. Waveforms (3) and (4) have been divided by 2 to remove the effect of the transformer voltage step-up and facilitate the identification of resistive and inductive voltage drops. The capacitor-to-collector voltage on the circuit board does not reach the full 3 kV charging voltage because of incomplete turn-on of the IGBTs at early times (i.e., the voltage drop across the IGBTs does not immediately fall to zero upon triggering, so at early times the collectors are several hundred volts above board ground).

inductance can be determined by measuring the inductance of the primary and secondary connected in series), so $\kappa = M/\sqrt{L_1 L_2} \approx 0.995$. For a more accurate measurement of κ, the voltage waveforms across the primary and secondary during a pulse from the ignitron trigger circuit were compared. These waveforms are shown in Fig. A.11. Although the transformer turns ratio was 1:2, the secondary voltage is not equal to twice the primary voltage since $\kappa < 1$. A good fit to the data is obtained with a leakage inductance value of 1.5 μH in series with the primary (nearly perfect agreement between the waveforms could be obtained if the measured winding resistances were also taken into account). Since the leakage inductance in series with the primary is $L_{leakage} = L_1\left(1-\kappa^2\right)$, this implies $\kappa = \sqrt{1 - L_{leakage}/L_1} \approx 0.994$.

The inductance contributed by the wiring between the circuit board, pulse transformer, and ignitron was also measured by identifying the $L\frac{dI}{dt}$ voltage drops in the circuit. Voltage

waveforms at four locations are shown in Fig. A.12. The voltage drop between the circuit board and the transformer primary is due to the inductance of the loops formed by the tracks on the board and the connecting wires (partially visible in Fig. A.8). A good fit to the data is obtained by assuming a value $L_p = 780$ nH. Similarly, the voltage drop between the transformer secondary and the ignitor is due to the inductance of the connecting wires and also the IR voltage drop across the 4.2 Ω resistor. Setting $L_s = 900$ nH gives an excellent fit to the data. Referring to Eq. A.6, the total effective inductance that contributes to the rise time is

$$L_{eff} \equiv L_1\left(1-\kappa^2\right) + \frac{L_1}{L_2}L_s + L_p = 1.50\ \mu\text{H} + \frac{1}{4}\times 0.90\ \mu\text{H} + 0.78\ \mu\text{H} = 2.51\ \mu\text{H}, \quad \text{(A.7)}$$

with the dominant contribution coming from the pulse transformer.

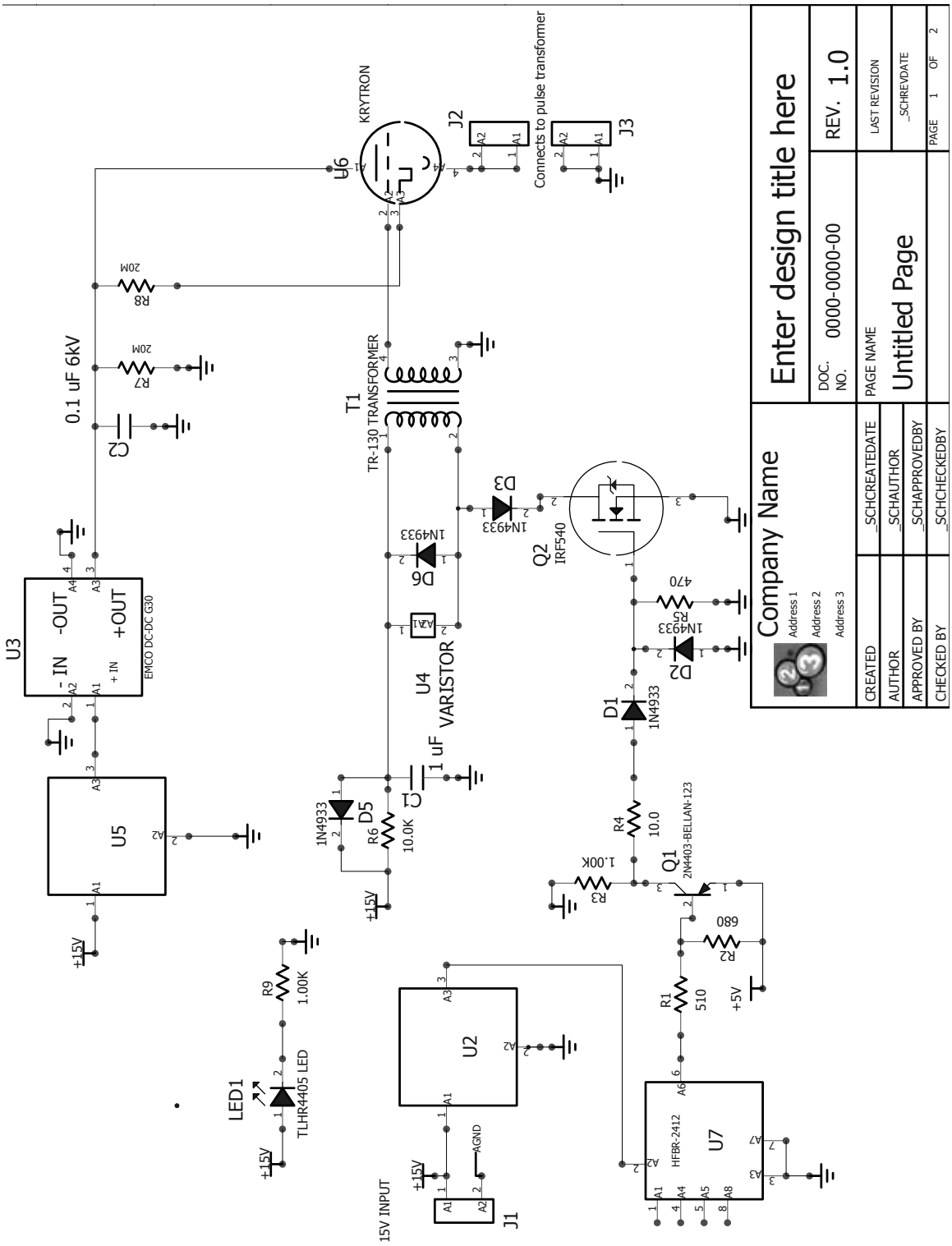

Figure A.13: Original ignitron trigger circuit with a krytron switch (designed by Paul Bellan).

Appendix B

RF Amplifier Circuit Diagram

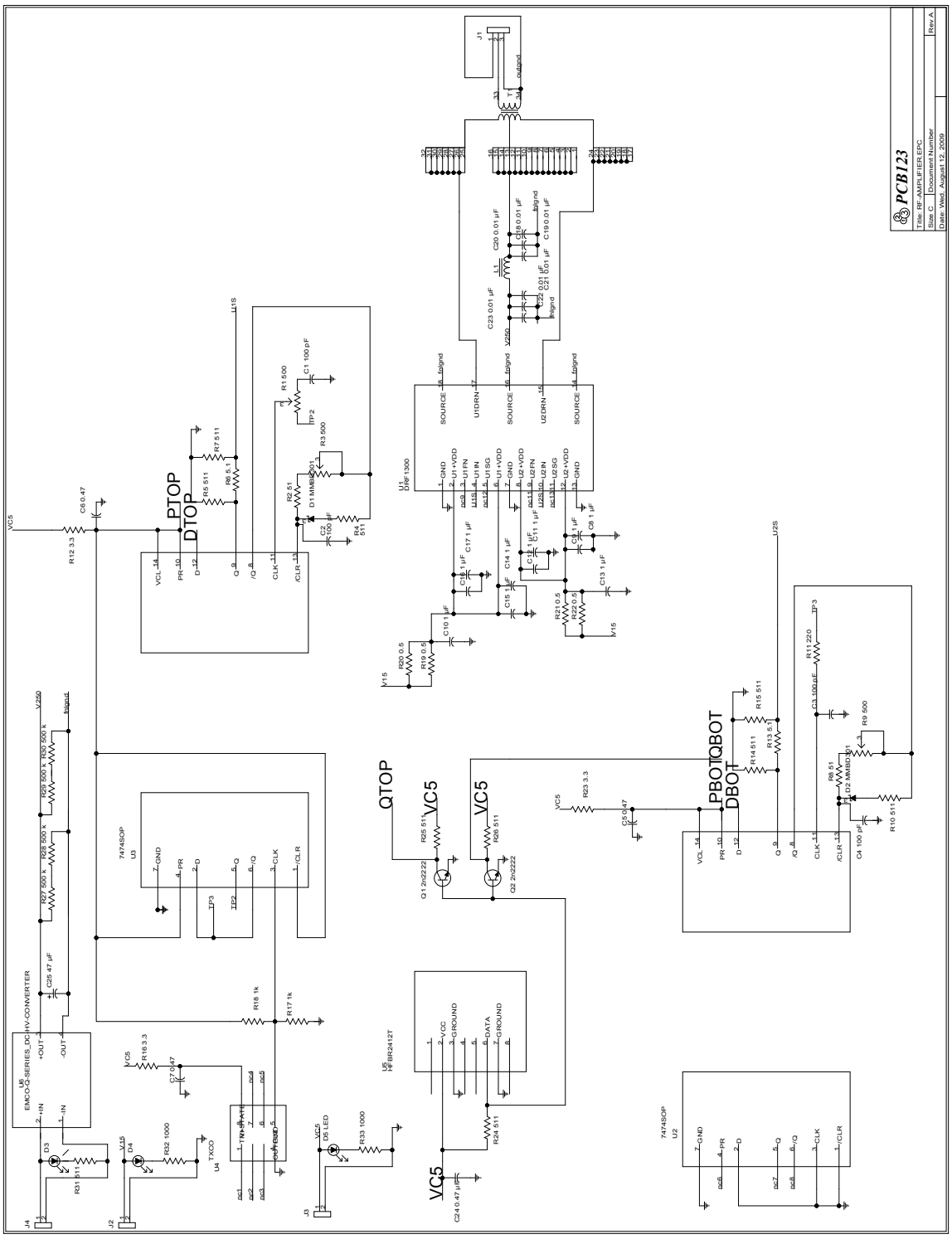

Figure B.1: Full circuit diagram for the pulsed 13.56 MHz RF amplifier, as originally designed by Paul M. Bellan. For normal operation with the amplifier gated by an optical trigger, the nodes labeled QTOP and DTOP were connected together, as were QBOT and DTOP. The Microsemi DRF1301 power MOSFET hybrid that was used in the final version of the amplifier has the same pin layout as the DRF1300 shown in this diagram. Note that the part numbers shown here do not match with those used in Fig. 2.8.

Appendix C

Power Output of an Ideal Class D RF Power Amplifier

In this appendix the power output of an ideal class D RF power amplifier with instantaneous switching and no internal resistance is derived. The results are of limited practical value since real class D amplifiers exhibit significant deviations from ideal behavior, but the analysis still yields several worthwhile insights into amplifier operation. The actual power output will approach the ideal result in cases in which the load impedance is much greater than the source output impedance.

A schematic of the RF amplifier output stage is shown in Fig. 2.6. The load, consisting of an inductor and resistor in series along with an impedance matching capacitor in series and another in parallel, is surrounded by a dashed box. For basic tests of amplifier operation with no plasma generation, this load can be replaced by a single resistor R_L. In this case, as discussed in Sec. 2.3.1, the amplifier output is a square wave voltage with amplitude $(n/m)\,V_{ps}$, and the current through the load over one RF cycle is

$$I_L(t) = \begin{cases} -\,(n/m)\,V_{ps}/R_L & ; \quad -\pi < \omega_i t < 0 \\ (n/m)\,V_{ps}/R_L & ; \quad 0 < \omega_i t < \pi \end{cases} , \tag{C.1}$$

where ω_i is the angular frequency of the RF signal. The power output averaged over one period is then

$$P_{avg} = \frac{1}{2\pi}\int_0^{2\pi} V_{ps}(t)\,I(t)\;\mathrm{d}\,(\omega_i t) = \left(\frac{n}{m}\right)^2 \frac{V_{ps}^2}{R_L}. \tag{C.2}$$

The measured output power into several resistive loads for our RF amplifier is shown in

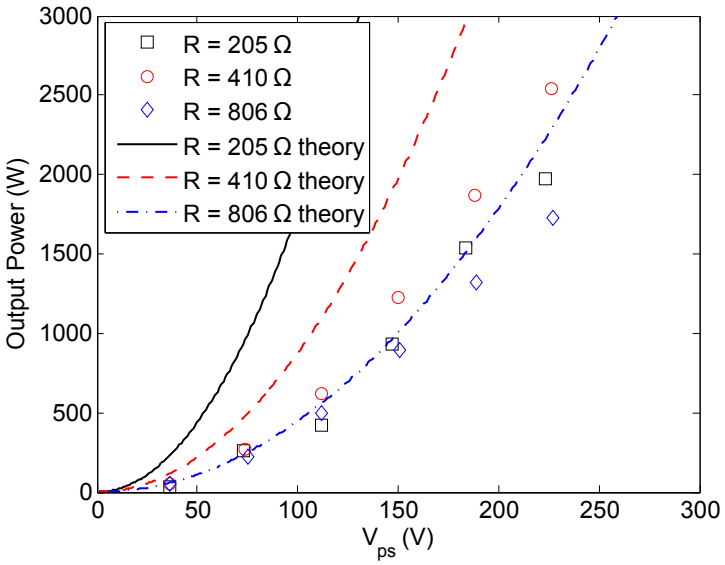

Figure C.1: Measured RF amplifier output power into resistive loads with $n/m = 6/1$. The $P \propto V_{ps}^2$ scaling holds for all loads, but only when the effective load impedance was $R_{eff} \gg R_{source}$ did the output power approach the theoretical value for an ideal class D RF amplifier with zero output impedance. Among the three loads tested, the power delivered was maximized with $R_{eff} = (m/n)^2 R_L = (410\ \Omega)/36 \approx 11\ \Omega$; thus the maximum power transfer theorem (Sec. 2.4) suggests that the source output impedance was near this value. Note that these measurements were taken with an early version of the RF amplifier circuit that contained a Microsemi DRF1300 power MOSFET hybrid rather than a DRF1301; the MOSFETs in the DRF1301 have a higher on-state resistance, and thus the source impedance was likely higher in the final version of the amplifier.

Fig. C.1. Since the amplifier was not ideal and had a finite output impedance, the power delivered to the load was less than the theoretical value given by Eq. C.2, but it approached the ideal result for large R_L.

Now consider the load shown in Fig. 2.6, with an inductor, resistor, and two variable capacitors. We will initially neglect the parallel capacitor C_p, since it doesn't affect the power delivered to the resistor in the ideal case. The series LCR circuit that remains can be tuned so that the current through the resistor is approximately sinusoidal, even though the RF amplifier output voltage is a square wave. Such resonant circuits are commonly used in commercial switching-mode RF amplifiers to produce a sinusoidal output.

If the voltage across the transformer secondary is $V(t)$, then the current through the

load (with $C_p = 0$ assumed) is given by

$$V(t) = RI(t) + L\frac{dI}{dt} + \frac{1}{C_s}\int I(t)\,\mathrm{d}t. \tag{C.3}$$

Take the Fourier transform to turn this integro-differential equation into an algebriac equation:

$$\hat{V}(\omega) = R\hat{I}(\omega) + L\left(i\omega\hat{I}(\omega)\right) + \frac{1}{C_s}\left(\frac{1}{i\omega}\hat{I}(\omega)\right) \tag{C.4}$$

$$\hat{I}(\omega) = \hat{V}(\omega)\left(\frac{1}{i\left(\omega L - \frac{1}{\omega C_s}\right) + R}\right). \tag{C.5}$$

Then $I(t)$ is the inverse Fourier transform:

$$I(t) = \frac{1}{\sqrt{2\pi}}\int_{-\infty}^{\infty}\hat{V}(\omega)\left(\frac{1}{i\left(\omega L - \frac{1}{\omega C_s}\right) + R}\right)e^{i\omega t}\,\mathrm{d}\omega. \tag{C.6}$$

As above, let ω_i be the angular frequency of the RF output. To minimize clutter in the equations, define $V_0 \equiv (n/m)\,V_{ps}$, so

$$V(t) = \begin{cases} -V_o \;\; ; \;\; -\pi < \omega_i t < 0 \\ V_o \;\; ; \;\; 0 < \omega_i t < \pi \end{cases} \tag{C.7}$$

$$\hat{V}(\omega) = \frac{1}{\sqrt{2\pi}}\int_{-\infty}^{\infty}V(t)\,e^{-i\omega t}\,\mathrm{d}t. \tag{C.8}$$

To evaluate this integral, expand $V(t)$ in a Fourier series:

$$V(t) = \sum_{m=-\infty}^{\infty}V_m e^{im\omega_i t} \tag{C.9}$$

$$\int_{-\pi}^{\pi}V(t)\,e^{-in\omega_i t}\,\mathrm{d}(\omega_i t) = \int_{-\pi}^{\pi}\sum_{m=-\infty}^{\infty}V_m e^{im\omega_i t}e^{-in\omega_i t}\,\mathrm{d}(\omega_i t) \tag{C.10}$$

Plugging in for $V(t)$ from Eq. C.7, this becomes

$$\frac{V_o}{in}\left(2 - e^{in\pi} - e^{-in\pi}\right) = 2\pi V_n \tag{C.11}$$

$$V_n = \begin{cases} \frac{2V_o}{in\pi} & ; \quad n \text{ odd} \\ 0 & ; \quad n \text{ even} \end{cases} \tag{C.12}$$

$$V(t) = \sum_{n \text{ odd}} \frac{2V_o}{in\pi} e^{in\omega_i t}. \tag{C.13}$$

Now it is straightforward to evaluate $\hat{V}(\omega)$:

$$\hat{V}(\omega) = \frac{1}{\sqrt{2\pi}} \int_{-\infty}^{\infty} \sum_{n \text{ odd}} \frac{2V_o}{in\pi} e^{in\omega_i t} e^{-i\omega t}\, \mathrm{d}t \tag{C.14}$$

$$= \sum_{n \text{ odd}} \frac{2V_o}{in} \sqrt{\frac{2}{\pi}}\, \delta(n\omega_i - \omega)\,. \tag{C.15}$$

Plugging back in for $I(t)$:

$$I(t) = \frac{1}{\sqrt{2\pi}} \int_{-\infty}^{\infty} \sum_{n \text{ odd}} \frac{2V_o}{in} \sqrt{\frac{2}{\pi}}\, \delta(n\omega_i - \omega) \left(\frac{e^{i\omega t}}{i\left(\omega L - \frac{1}{\omega C_s}\right) + R} \right) \mathrm{d}\omega \tag{C.16}$$

$$= \frac{2V_o \omega_i C_s}{\pi} \sum_{n \text{ odd}} \frac{e^{in\omega_i t}}{1 - n^2\omega_i^2 LC_s + in\omega_i RC_s} \tag{C.17}$$

$$= \frac{4V_o \omega_i C_s}{\pi} \sum_{n=1,3,\ldots} \frac{\left(1 - n^2\omega_i^2 LC_s\right)\cos\left(n\omega_i t\right) + \left(n\omega_i RC_s\right)\sin\left(n\omega_i t\right)}{\left(1 - n^2\omega_i^2 LC_s\right)^2 + n^2\omega_i^2 R^2 C_s^2}. \tag{C.18}$$

Now assume the circuit is tuned to the LC resonance; i.e., C_s is chosen to make $\omega_i^2 = 1/\left(LC_s\right)$. Also assume that $\omega_i RC_s \ll 1$.[1] The first two terms in the above sum then become

$$I(t) = \frac{4V_o \omega_i C_s}{\pi} \left(\frac{\sin\left(\omega_i t\right)}{\omega_i RC_s} + \frac{-8\cos\left(3\omega_i t\right) + \left(3\omega_i RC_s\right)\sin\left(3\omega_i t\right)}{64 + 9\omega_i^2 R^2 C_s^2} + \ldots \right) \tag{C.19}$$

$$\approx \frac{4V_o \omega_i C_s}{\pi} \left(\frac{\sin\left(\omega_i t\right)}{\omega_i RC_s} - \frac{1}{8}\cos\left(3\omega_i t\right) \right) \approx \frac{4V_o}{\pi R}\sin\left(\omega_i t\right). \tag{C.20}$$

Thus when L and C_s are tuned to the resonance, the output current is approximately sinusoidal, even though the output voltage is a square wave, because all frequency components

[1] For our RF plasma source, $R \approx 2\ \Omega$ (see Sec. 2.4), $\omega_i = 2\pi \times 13.56$ MHz, and $L = 242$ nH (for the half-turn helical antenna), so tuning to the LC resonance requires $C_s = 569$ pF, in which case $\omega_i RC_s \approx 0.1$, so $\omega_i RC_s \ll 1$ is satisfied.

of $V(t)$ except the fundamental at $\omega = \omega_i$ are filtered out.

The average power dissipated in the resistor (the net power output by the RF amplifier) is then

$$P_{avg} = \frac{1}{2\pi}\int_0^{2\pi} I^2 R \,\mathrm{d}\left(\omega_i t\right) \approx \left(\frac{8}{\pi^2}\right)\frac{V_o^2}{R} = \left(\frac{8}{\pi^2}\right)\left(\frac{n}{m}\right)^2 \frac{V_{ps}^2}{R}. \tag{C.21}$$

This is larger by a factor of 2 than the formula in the DRF1300 application note by G. Choi [61], but it agrees with the results derived in [60] and [162]. For a given V_{ps}, the power output with the resonant series LCR load is smaller by a factor $\left(8/\pi^2\right)$ than the power output with a purely resistive load.

For an ideal class D RF amplifier, we can reintroduce C_p into the circuit without changing the output power; the output voltage across the transformer is still given by Eq. C.7, so the current through R is still given by Eq. C.6. The current through C_p may be calculated from

$$V(t) = \frac{1}{C_p}\int I_p(t)\,\mathrm{d}t. \tag{C.22}$$

$$\hat{I}_p(\omega) = i\omega C_p \hat{V}(\omega)\,. \tag{C.23}$$

Using Eq. C.15 for $\hat{V}(\omega)$:

$$I_p(t) = \frac{iC_p}{\sqrt{2\pi}}\int_{-\infty}^{\infty}\omega \sum_{n\ \mathrm{odd}} \frac{2V_o}{in}\sqrt{\frac{2}{\pi}}\delta\left(n\omega_i - \omega\right)e^{i\omega t}\,\mathrm{d}t \tag{C.24}$$

$$= \frac{4V_o C_p \omega_i}{\pi}\sum_{n=1,3,\ldots}\cos\left(n\omega_i t\right). \tag{C.25}$$

This is a series of positive δ-function current spikes at $t = 0$, $\frac{2\pi}{\omega_i}$, ... and negative δ-function current spikes at $t = \frac{\pi}{\omega_i}$, $\frac{3\pi}{\omega_i}$, ... It is clear intuitively that this is what is required to make the voltage across C_p a square wave under these idealized conditions.

Although any real RF amplifier will have dissipation in all circuit elements that will prohibit such infinite currents from flowing, the preceding analysis gives a qualitative sense of the nature of the currents that flow in the antenna and matching network capacitors, and shows how the current in the load may be made approximately sinusoidal. Having a sinusoidal current through the antenna rather than a square wave or some more complicated

waveform was potentially important for efficienctly exciting helicon waves in the plasma.

The type of RF amplifier analyzed here is called a "transformer-coupled voltage-switching (TCVS)" class D RF amplifier. Another limit exists, known as a "transformer-coupled current-switching (TCCS)" class D RF amplifier [60]. In this setup, a high-inductance RF choke is placed between the 47 μF capacitor and the center tap of the transformer in Fig. 2.6, so that the current into the center tap is approximately constant in time. The output current of the RF amplifier is then approximately a square wave. If a capacitor and inductor tuned to the resonant frequency of the RF output are placed in parallel with the load resistor R, rather than in series as in Fig. 2.6, then a similar analysis to that presented above [60] shows that the amplifier output voltage will be approximately sinusoidal, and the output power will be $P_{avg} = \left(\pi^2/8\right)(n/m)^2\left(V_{ps}^2/R\right)$.

Appendix D

Langmuir Probe Analysis

This appendix describes the procedure used to determine the density and electron temperature of the RF plasma from Langmuir probe I-V curves. Considerations for probe measurements in the presence of magnetic fields, RF, and multiple electron populations will also be discussed.

D.1 Introduction

As summarized in Sec. 3.1.1, a typical I-V curve for a plasma with Maxwellian electrons consists of three sections: the ion saturation region, in which $V_{probe} \ll V_{plasma}$ so electrons are repelled from the probe and only ions are collected, an intermediate region in which the electron current collected rises exponentially as V_{probe} approaches V_{plasma}, and an electron saturation region in which $V_{probe} > V_{plasma}$ so ions are repelled. The plasma potential V_{plasma} usually differs from the laboratory "ground" potential because $v_{Te} \gg v_{Ti}$, so in an unmagnetized plasma with $V_{plasma} = 0$ the flux of electrons to the chamber walls is much higher than the ion flux. This net negative current leaving the plasma causes V_{plasma} to increase, retarding the escaping electrons and accelerating the ions, and ultimately an equilibrium develops in which both species diffuse out of the plasma at the same velocity. In a magnetically confined plasma, on the other hand, ions may be able to diffuse out of the plasma more easily than electrons, in which case the plasma potential will be negative. Since the bulk plasma is quasineutral, most of the potential drop from V_{plasma} to ground occurs over a narrow edge region of thickness $\sim \lambda_D$ known as the sheath.

A sheath also develops around any electrode or object (such as a Langmuir probe)

inserted into the plasma. A simple 1D theory of Langmuir probe behavior [4, Section 2.9] shows that when the probe is biased negatively with respect to V_{plasma}, ions enter the sheath with velocity $u_i \approx c_s \equiv \sqrt{k_B T_e / m_i}$. The ion current collected is then $I_i = n_s e A c_s$, where n_s is the sheath edge density and A is the probe surface area. For typical laboratory discharges with $T_e \gg T_i$, the ion acoustic speed c_s is much greater than the ion thermal velocity, meaning that the ions must have been accelerated through a potential difference in an extended "pre-sheath" before reaching the sheath. Conservation of energy for collisionless ions implies that the sheath edge potential is

$$e\left(V_{plasma} - V_s\right) = \frac{1}{2} m_i c_s^2 = \frac{1}{2} k_B T_e \tag{D.1}$$

$$V_s = V_{plasma} - \frac{1}{2}\frac{k_B T_e}{e}. \tag{D.2}$$

The electron density in the pre-sheath and sheath is given by the zeroth moment of the velocity distribution function (see Sec. 1.1.2):

$$n_e(\mathbf{x}) = \int f_e(\mathbf{x}, \mathbf{v})\, d^3 v = \int \frac{n_0}{v_{Te}\sqrt{\pi}} \exp\left(-\frac{v^2}{v_{Te}^2} + \frac{e\left(V(\mathbf{x}) - V_{plasma}\right)}{k_B T_e}\right) d^3 v, \tag{D.3}$$

where the standard Maxwellian distribution function has been modified to account for variations in electrostatic potential [4, Section 2.9]. Integrating yields

$$n_e(\mathbf{x}) = n_0 \exp\left(\frac{e\left(V(\mathbf{x}) - V_{plasma}\right)}{k_B T_e}\right), \tag{D.4}$$

which is known as the Boltzmann relation. Since the pre-sheath is much larger than a Debye length, the plasma must remain quasineutral in this region ($n_i = n_e$), so the ion density at the edge of the sheath is

$$n_s = n_0 \exp\left(\frac{e\left(V_s - V_{plasma}\right)}{k_B T_e}\right) = n_0 \exp\left(-\frac{1}{2}\right) \approx 0.6 n_0. \tag{D.5}$$

Therefore, the bulk plasma density is related to the ion saturation current by

$$n_0 \approx \frac{I_{sat.}}{0.6 e A c_s}. \tag{D.6}$$

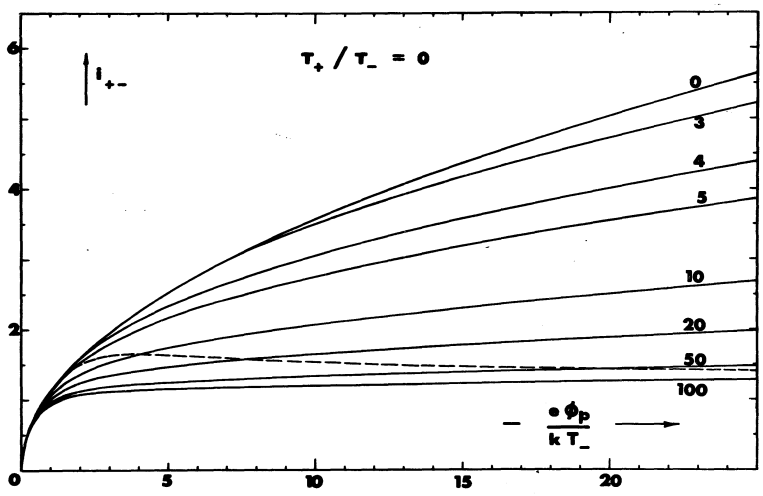

FIGURE 40 ION CURRENT i_{+-} VS PROBE POTENTIAL FOR VARIOUS RATIOS OF PROBE RADIUS TO ELECTRON DEBYE LENGTH. ION-ATTRACTING CYLINDRICAL PROBE; $T_+/T_- = 0$. DOTTED CURVE SHOWS TRAPPED-ORBIT BOUNDARY.

Figure D.1: Numerically calculated dimensionless ion current to a negatively biased cylindrical probe, reproduced from reference [163, Fig. 40]. The figure gives the ion current for a zero ion temperature plasma as a function of $e\left(V_{plasma} - V_{probe}\right)/kT_e$; different curves correspond to different ratios of the probe radius to the Debye length. The relationship between i_{+-} and the physical ion current I_i is given by Eq. D.9.

Sweeping the probe bias through the voltage range over which non-negligible electron current is collected allows T_e to be determined. If we approximate the probe as a 1D plane (this is reasonable for a cylindrical or spherical probe if $r_{probe} \gg \lambda_{De}$), then the electron current density incident on its surface is

$$J_e(x_{probe}) = \int_0^\infty -ev f_e(x_{probe}, v)\, dv = \frac{-n_0 e v_{Te}}{2\sqrt{\pi}} \exp\left(\frac{e\left(V_{probe} - V_{plasma}\right)}{k_B T_e}\right), \tag{D.7}$$

where the integral is from 0 to ∞ because only electrons moving toward the probe contribute. Therefore,

$$|I_e| = \frac{n_0 e A v_{Te}}{2\sqrt{\pi}} \exp\left(\frac{e\left(V_{probe} - V_{plasma}\right)}{k_B T_e}\right), \tag{D.8}$$

so a plot of $\ln|I_e|$ vs. V_{probe} will be linear, with slope equal to $e/k_B T_e$.

D.2 Numerical Calculations by Laframboise and Collisional Effects

In reality the ion saturation current is not entirely independent of the probe voltage, and the probe geometry is also important. Laframboise [163] carried out numerical ion orbit calculations that improved upon the density estimate given by Eq. D.6, providing the dimensionless parameter i_{+-} in the equation

$$n_0 = \frac{I_i\sqrt{2\pi}}{eAc_s i_{+-}}. \tag{D.9}$$

Fig. D.1 shows i_{+-} as a function of probe potential and the ratio r_{probe}/λ_{De}. Comparing Eqs. D.6 and D.9, we see that the approximate formula agrees with the numerical results when $i_{+-} \approx 1.5$.

The Laframboise calculations assume that the plasma is unmagnetized and collisions are of negligible importance in the sheath and pre-sheath (however, the bulk plasma must be sufficiently collisional to make both the electron and ion velocity distributions Maxwellian). The theory is only valid when the ion-neutral collision mean free path satisfies $\lambda_{in} \gg r_{probe}, \lambda_{De}$ [164]. Using $\sigma_{in} \approx 5 \times 10^{-19}$ m^2 for argon [5, Figure 3.15], the mean free path is $\lambda_{in} = (n_g\sigma_{in})^{-1} = (0.06 \text{ m})/p_{\text{mTorr}}$. The probe radius used in our experiments was $r_{probe} \approx 2.5 \times 10^{-4}$ m, and $\lambda_{De} \lesssim 5 \times 10^{-5}$ m for our RF plasma (see Sec. D.4), so the condition $\lambda_{in} \gg r_{probe}$ was the more difficult one to satisfy. When this condition is violated, a Langmuir probe depletes the plasma density in its vicinity. A rough calculation [164, Section 4.1] shows that in the limit $\lambda_{in} \ll r_{probe}$, the ion current collected is reduced by approximately a factor λ_{in}/r_{probe}, so the probe measurement underestimates the plasma density by this same factor.

Overzet and Hopkins [165, 166] experimentally confirmed this scaling of the error with λ_{in} by comparing density measurements made using a Langmuir probe with those from a microwave interferometer. Using a cylindrical probe with radius $r_{probe} = 1.25\times10^{-4}$ m, they found that the Langmuir probe agreed with the interferometer for $p_{Ar} \lesssim 125$ mTorr, but the probe underestimated the true density by a factor of 2 at $p_{Ar} = 250$ mTorr and by a factor

of 4 at $p_{Ar} = 500$ mTorr. Given that the radius of our Langmuir probe was approximately twice that used by Overzet and Hopkins, we expected our density measurements to be accurate for $p_{Ar} \lesssim 60$ mTorr. At higher pressures, collisional effects reduced the measured $I_{sat.}$, so the magnitude of n_i could not be reliably determined; however, the probe could still be used to identify relative variations in n_i as a function of position and time.

D.3 Data Analysis Procedure

In order to analyze our Langmuir probe data (see Fig. 3.2 for an example), a linear fit was made to the measured I-V characteristic in the ion saturation current region (where $V_{probe} \ll V_{plasma}$), and this fit was extrapolated to determine the ion current at higher probe voltages for which electron current was collected as well[1]. The electron current was then isolated by calculating $I_e = I_{probe} - I_i$, and T_e was determined from the slope of a plot of $\ln|I_e|$ vs. V_{probe}. Once the electron temperature was known, n_0 was estimated from Eq. D.6. This initial density estimate was used to estimate $\lambda_{De} = \sqrt{\epsilon_0 k_B T_e / n_0 e^2}$, and the calculated n_0 was refined using Eq. D.9 and Fig. D.1.

Since the electron current collected by a Langmuir probe stops rising exponentially with V_{probe} when $V_{probe} = V_{plasma}$, the location at which the plot of $\ln|I_e|$ vs. V_{probe} stopped being linear gave an indication of the plasma potential. We also measured a related quantity called the "floating potential", which is the voltage that an insulated or electrically floating object in a plasma will charge to. Just as the chamber wall potential is usually lower than the plasma potential, the floating potential V_f is negative with respect to V_{plasma} in an unmagnetized plasma. A floating object draws no net current, so setting $I_i = I_e$ using Eqs.

[1]This linear extrapolation approach is commonly used in the literature [167], while other authors [168, 169] have assumed $I_{sat.} \sim \sqrt{V_{plasma} - V_{probe}}$, which may be a better approximation than $I_{sat.} \sim (V_{plasma} - V_{probe})$ for probe voltages near the plasma potential (see Fig. D.1). However, the differences are of little consequence for approximate determinations of T_e and n_e, since the electron current is much larger than the ion current for V_{probe} near V_{plasma}. If the most precise possible measurement were desired, then the results of Laframboise's numerical calculations could be used to account for the precise functional form of $I_i(V_{probe})$.

D.6 and D.8, we have

$$\exp\left(-\frac{1}{2}\right) n_0 e A c_s = \frac{n_0 e A v_{Te}}{2\sqrt{\pi}} \exp\left(\frac{e\left(V_f - V_{plasma}\right)}{k_B T_e}\right) \tag{D.10}$$

$$V_{plasma} - V_f = \frac{k_B T_e}{e}\left(\ln\sqrt{\frac{m_i}{2\pi m_e}} + \frac{1}{2}\right). \tag{D.11}$$

Expressing T_e in eV, we have for hydrogen, $V_{plasma} - V_f = 3.3T_{eV}$, for helium, $V_{plasma} - V_f = 4.0T_{eV}$, and for argon, $V_{plasma} - V_f = 5.2T_{eV}$.

D.4 Langmuir Probe Measurements in the Presence of Magnetic Fields

A fully satisfactory theory of Langmuir probe behavior in a magnetized plasma does not exist. However, probes are still commonly used in plasmas with magnetic fields, and it is found in practice that the results do not differ too greatly from the predictions of the unmagnetized theory. In particular, for highly negative probe voltages, when few electrons are being drained from the plasma, the plot of $\ln|I_e|$ vs. V_{probe} should still be linear even in the presence of a magnetic field, allowing the electron temperature to be calculated for the case of an isotropic Maxwellian distribution (if $T_{e\|}$ and $T_{e\perp}$ differ, then the probe will measure $T_{e\|}$, since most of the electrons that strike the probe are traveling along $\mathbf{B}$). In a weak magnetic field such that $r_{Li} \gg r_{probe}, \lambda_{De}$, the ion current should be minimally altered by the field, but the field can still affect the electron motion and cause the sheath to become asymmetric [164].

The cylindrical probes used in this thesis had radius $r_{probe} \approx 2.5 \times 10^{-4}$ m, and the magnetic field strength was typically $B \lesssim 0.1$ T, which for argon ions with $T_i = 600$ K (0.05 eV) implies $r_{Li} = m_i v_{Ti}/eB \gtrsim 2 \times 10^{-3}$ m. The RF plasmas had $n_e \sim 10^{17}$–10^{20} m^{-3} and $T_e \sim 0.3$ – 5 eV, so $\lambda_{De} = \sqrt{\epsilon_0 k T_e/\left(n_e e^2\right)} \sim 4 \times 10^{-7}$ – 5×10^{-5} m. Therefore, the condition $r_{Li} \gg r_{probe}, \lambda_{De}$ was satisfied for our measurements.

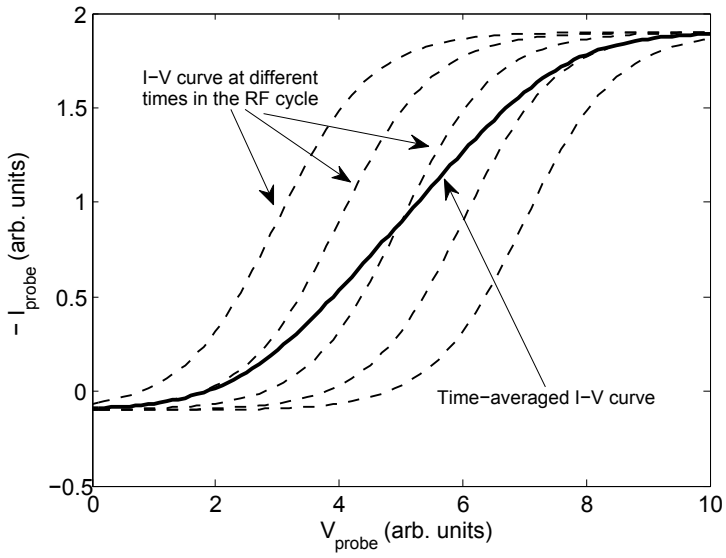

Figure D.2: Distortion of the Langmuir probe I-V curve measured in the presence of RF fluctuations in the plasma potential. As the plasma potential varies over the course of each RF cycle, the I-V curve shifts horizontally, as indicated by the dashed curves, since $V_{probe} - V_{plasma}$ is varying. The measured probe current at each probe voltage V_{probe} is the time average over the currents collected at different phases of the RF cycle, meaning that the measured I-V curve, shown in bold, is the average of the dashed curves. Because the I-V curve is non-linear, the slope of the measured curve is smaller than the true slope, causing the electron temperature to be overestimated.

D.5 Langmuir Probe Measurements in the Presence of RF

When RF power is capacitively coupled to a plasma, the plasma potential oscillates at the RF frequency [5, p. 201]. This effect corrupts the Langmuir probe electron temperature measurement, because the measured probe current is a time average over several RF cycles, and the non-linearity of the I-V curve means that the slope of the time-averaged curve will be different from the true instantaneous slope. Since there is always some capacitive coupling between the plasma and the RF antenna, even in a source that is primarily inductively coupled or wave heated, it is generally difficult to accurately measure T_e is an RF plasma while the RF power is on.

The mechanism for the distortion is illustrated in Fig. D.2. The measured I-V curve, shown in bold, is the average of the dashed curves, which represent the instantaneous I-V curves at different phases of the RF cycle. This time-averaged I-V curve has a shallower

slope than the true I-V curve. Since the electron temperature is determined from the rate of exponential growth of $|I_e|$ (see Eq. D.8), this decrease in the apparent slope of the I-V curve leads to an overestimate of the electron temperature.

It is possible to modify the probe circuit in various ways to enable accurate T_e measurements in the presence of RF. These modifications are known as "RF compensation" of the probe. Commonly, an inductor is built into the probe in series with the probe tip; the high impedance of the inductor at RF frequencies causes the probe tip to oscillate with the plasma potential so that $V_{probe} - V_{plasma}$ remains constant and there is no variation in I_{probe} at the RF frequency [5, p. 202-203]. However, in practice more complex circuitry usually must be used to avoid other problems—for details see [170].

In the experiments described in this thesis, we did not attempt to implement RF compensation for our probes; instead we waited until after the RF power had been turned off to measure T_e. On the other hand, we were able to estimate the plasma density while the RF power was on using measurements of the ion saturation current; since the I-V curve is approximately linear in the ion saturation current regime ($V_{probe} \ll V_{plasma}$), $I_{sat.}$ measurements are not distorted by the time-averaging of the RF plasma potential fluctuations. This technique was used extensively in Chapters 3, 4, and 5.

D.6 Multiple Electron Temperatures

It is straightforward to extend the Langmuir probe analysis to a situation in which there are two or more distinct Maxwellian electron populations. Assume that a fraction f_1 of the electrons have temperature T_{e1} and a fraction f_2 have temperature T_{e2}, where $T_{e2} > T_{e1}$ and $f_1 + f_2 = 1$. The distribution function is

$$f_e(\mathbf{x}, v) = \frac{f_1 n_0}{v_{Te1}\sqrt{\pi}} \exp\left(-\frac{v^2}{v_{Te1}^2} + \frac{e\left(V(\mathbf{x}) - V_{plasma}\right)}{k_B T_{e1}}\right) + \frac{f_2 n_0}{v_{Te2}\sqrt{\pi}} \exp\left(-\frac{v^2}{v_{Te2}^2} + \frac{e\left(V(\mathbf{x}) - V_{plasma}\right)}{k_B T_{e2}}\right), \quad \text{(D.12)}$$

so in analogy to Eq. D.4, the electron density is

$$n_e(\mathbf{x}) = n_0 \left(f_1 \exp\left(\frac{e\left(V(\mathbf{x}) - V_{plasma}\right)}{k_B T_{e1}} \right) + f_2 \exp\left(\frac{e\left(V(\mathbf{x}) - V_{plasma}\right))}{k_B T_{e2}} \right) \right). \tag{D.13}$$

Using Eq. D.7, the electron current to the probe is

$$I_e = -\frac{n_0 e A}{2\sqrt{\pi}} \left(f_1 v_{Te1} \exp\left(\frac{e\left(V_{probe} - V_{plasma}\right)}{k_B T_{e1}} \right) + f_2 v_{Te2} \exp\left(\frac{e\left(V_{probe} - V_{plasma}\right)}{k_B T_{e2}} \right) \right). \tag{D.14}$$

It is clear that there is no longer a linear relationship between $\ln|I_e|$ and V_{probe}. However, since $T_{e2} > T_{e1}$ and the contribution to the current from each electron population depends exponentially on the probe voltage, at large negative probe voltages (i.e., $e\left(V_{plasma} - V_{probe}\right)/k_B T_{e1} \gg 1$) the contribution from population 2 will dominate and the electron current will be simply

$$I_e \approx I_{e2} = -\frac{f_2 n_0 e A v_{Te2}}{2\sqrt{\pi}} \exp\left(\frac{e\left(V_{probe} - V_{plasma}\right)}{k_B T_{e2}} \right) \tag{D.15}$$

$$\ln|I_e| \approx \ln\left(\frac{f_2 n_0 e A v_{Te2}}{2\sqrt{\pi}} \right) + \frac{e\left(V_{probe} - V_{plasma}\right)}{k_B T_{e2}}. \tag{D.16}$$

So T_{e2} is readily determined from the far left portion of a plot of $\ln|I_e|$ vs. V_{probe}. This linear portion of the curve can be extrapolated over the full range of probe voltages, allowing I_{e2} to be subtracted from I_e to isolate I_{e1}. The slope of a plot of $\ln|I_{e1}|$ vs. V_{probe} can then be used to determine T_{e1}. Frequently in experiments, the density of the high temperature electron population is much lower than that of the low temperature population ($f_2 \ll f_1$); in this case, I_{e1} will dominate over I_{e2} at probe voltages near the plasma potential, and the overall plot of $\ln|I_e|$ vs. V_{probe} will roughly separate into two linear segments of different slopes. An example is shown in Fig. D.3.

As in the single electron temperature case, there will be an inflection point in the plot of $\ln|I_e|$ vs. V_{probe} at the plasma potential. Once V_{plasma} is known, we can compare the magnitudes of I_{e1} and I_{e2} when the probe potential is equal to the plasma potential to

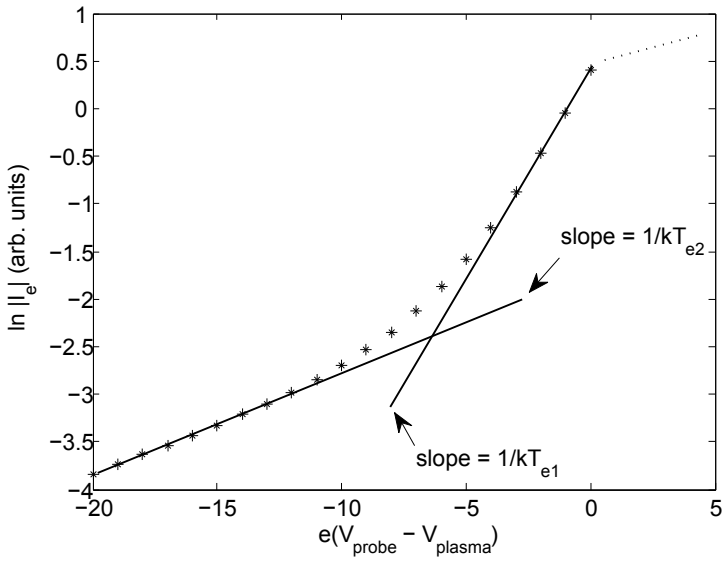

Figure D.3: Theoretical plot of $\ln|I_e|$ vs. V_{probe} for a case with $T_{e1} = 2$ eV, $T_{e2} = 10$ eV, $f_1 = .95$, $f_2 = .05$. The curve approximately separates into two linear segments, with the slope of each giving the temperature of one of the Maxwellian electron populations.

determine f_2/f_1 (see Eq. D.14):

$$\frac{I_{e2}(V_{probe} = V_{plasma})}{I_{e1}(V_{probe} = V_{plasma})} = \frac{f_2 v_{Te2}}{f_1 v_{Te1}}. \tag{D.17}$$

The presence of multiple electron populations also affects the ion flux to the probe. A unique ion acoustic speed is no longer defined; instead the ion inflow velocity at the sheath edge is [171]

$$u_{i0} \approx \sqrt{\frac{k_B T_{e1}}{m_i \left(f_1 + f_2 T_{e1}/T_{e2}\right)}}. \tag{D.18}$$

As before, the ion saturation current is $I_{sat.} = n_s e A u_{i0}$. We may find the sheath edge density n_s using the same procedure as in Sec. D.1. The sheath edge potential is

$$e\left(V_{plasma} - V_s\right) = \frac{1}{2} m_i u_{i0}^2 = \frac{k_B T_{e1}}{2\left(f_1 + f_2 T_{e1}/T_{e2}\right)} \tag{D.19}$$

$$V_s = V_{plasma} - \frac{k_B T_{e1}}{2e\left(f_1 + f_2 T_{e1}/T_{e2}\right)}. \tag{D.20}$$

From Eq. D.13 and quasineutrality

$$n_s = n_0 \left(f_1 \exp\left(\frac{e\left(V_s - V_{plasma}\right)}{k_B T_{e1}} \right) + f_2 \exp\left(\frac{e\left(V_s - V_{plasma}\right))}{k_B T_{e2}} \right) \right) \tag{D.21}$$

$$= n_0 \left(f_1 \exp\left(\frac{-T_{e2}}{2\left(f_1 T_{e2} + f_2 T_{e1}\right)} \right) + f_2 \exp\left(\frac{-T_{e1}}{2\left(f_1 T_{e2} + f_2 T_{e1}\right)} \right) \right). \tag{D.22}$$

Therefore, the bulk plasma density is

$$n_0 = \frac{I_{sat.}}{\left(n_s/n_0\right) e A u_{i0}}, \tag{D.23}$$

where u_{i0} and (n_s/n_0) are given by Eqs. D.18 and D.22, respectively.

Finally, there is of course no guarantee that the distribution function will be Maxwellian at all; in non-Maxwellian cases the Langmuir probe characteristic contains information about the form of $f_e(v)$ that can in principle be extracted, but the procedure is difficult to carry out in practice unless the I-V curve can be measured with great precision [164].

Appendix E

Re-Absorption of Line Emission

This appendix describes the procedure for calculating the effective spontaneous emission rates for argon used in the steady-state global and 1D time-dependent models of the RF discharge (in Secs. 3.3 and 4.4.2, respectively). The rate $A_{\alpha\beta}$ for a spontaneous transition from energy level α to level β is a constant that depends only on the internal properties of the atom. However, if the lower level population density n_β is high enough, an appreciable number of photons may be re-absorbed before escaping the plasma. When this occurs, the upper level α is re-populated, so the effective volume-averaged transition rate $A_{\alpha\beta,eff.}$ is reduced.

From [138, Chapter 1], the absorption cross section is

$$\sigma_\nu = \frac{h\nu}{4\pi}\phi(\nu)\left(B_{\beta\alpha} - \frac{n_\alpha}{n_\beta}B_{\alpha\beta}\right). \tag{E.1}$$

Here $\phi(\nu)$ is the normalized line profile function and $B_{\beta\alpha}$ and $B_{\alpha\beta}$ are the Einstein coefficients for absorption and stimulated emission, respectively. The formulas relating these coefficients (called "Einstein relations") may take several different forms depending on what measure one uses for light intensity [172]. Here we will follow the convention used by Rybicki and Lightman [138] and define the Einstein coefficients in terms of the "specific intensity" of the radiation, which has units of energy/time/area/solid angle/frequency interval. The

Einstein relations are then written as

$$A_{\alpha\beta} = \frac{2h\nu^3}{c^2} B_{\alpha\beta} \tag{E.2}$$

$$g_\beta B_{\beta\alpha} = g_\alpha B_{\alpha\beta}, \tag{E.3}$$

where $g_\alpha = 2J_\alpha + 1$ is the statistical weight of the level α. Using these relationships, the absorption cross section becomes

$$\sigma_\nu = \frac{c^2}{8\pi\nu^2} \frac{g_\alpha}{g_\beta} A_{\alpha\beta} \left(1 - \frac{g_\beta n_\alpha}{g_\alpha n_\beta}\right) \phi(\nu)\,. \tag{E.4}$$

Assuming that the absorbing atoms have a Maxwellian velocity distribution with temperature T_g, the Doppler-broadened line profile function [138, Section 10.6] is

$$\phi(\nu) = \frac{1}{\Delta\nu_D\sqrt{\pi}} \exp\left(-\frac{(\nu-\nu_0)^2}{(\Delta\nu_D)^2}\right) \quad ; \quad \Delta\nu_D \equiv \frac{\nu_0}{c}\sqrt{\frac{2k_B T_g}{m_i}}. \tag{E.5}$$

At the line center frequency ν_0, the profile function is simply $1/\Delta\nu_D\sqrt{\pi}$, so plugging into Eq. E.4 we have

$$\sigma_{\nu_0} = \frac{c^3}{8\sqrt{2}\pi^{3/2}\nu_0^3} \frac{g_\alpha}{g_\beta} A_{\alpha\beta} \left(1 - \frac{g_\beta n_\alpha}{g_\alpha n_\beta}\right) \sqrt{\frac{m_i}{k_B T_g}}, \tag{E.6}$$

or in terms of wavelength:

$$\sigma_{\lambda_0} = \frac{\lambda_0^3}{8\sqrt{2}\pi^{3/2}} \frac{g_\alpha}{g_\beta} A_{\alpha\beta} \left(1 - \frac{g_\beta n_\alpha}{g_\alpha n_\beta}\right) \sqrt{\frac{m_i}{k_B T_g}}, \tag{E.7}$$

which agrees with the Eq. 2.10 in [173] when the $g_\beta n_\alpha / g_\alpha n_\beta$ term (which accounts for stimulated emission) is neglected.

For the global discharge model in Sec. 3.3, we assume that all photons emitted within one mean free path l_{mfp} of the edge of the plasma escape, while all photons emitted further from the boundary are re-absorbed. The effective transition rates are therefore reduced by a factor

$$A_{\alpha\beta,eff.} = A_{\alpha\beta} \left(\frac{\pi R^2 L - \pi\left(R - l_{mfp}\right)^2 \left(L - 2l_{mfp}\right)}{\pi R^2 L}\right), \tag{E.8}$$

where $l_{mfp} = \left(n_\beta \sigma_{\lambda_0}\right)^{-1}$. If $l_{mfp} \ll R, L$, then keeping only the lowest order terms in l_{mfp}

yields

$$A_{\alpha\beta,eff.} = 2A_{\alpha\beta} l_{mfp} \left(\frac{1}{R} + \frac{1}{L}\right) = \frac{16\sqrt{2}\pi^{3/2}}{n_\beta \lambda_0^3} \frac{g_\beta}{g_\alpha} \left(1 - \frac{g_\beta n_\alpha}{g_\alpha n_\beta}\right)^{-1} \sqrt{\frac{k_B T_g}{m_i}} \left(\frac{1}{R} + \frac{1}{L}\right), \quad \text{(E.9)}$$

which is independent of the intrinsic transition rate $A_{\alpha\beta}$. The condition $l_{mfp} \ll R$ was satisfied for resonant transitions (i.e., transitions to the ground state) in our experiment because $n_\beta = n_g$ was high, and furthermore these transitions had $n_\beta \gg n_\alpha$ so the stimulated emission term was negligible. In this case, the effective transition rate in S.I. units simplifies to

$$A_{\alpha\beta,eff.} = \left(1.8 \times 10^3\right) \frac{\sqrt{T_g}}{n_\beta \lambda_0^3} \frac{g_\beta}{g_\alpha} \left(\frac{1}{R} + \frac{1}{L}\right). \quad \text{(E.10)}$$

This formula was used to calculate $A_{rg,eff.}$ in the discharge models. In the global model, $T_g = 600$ K was assumed, while in the 1D time-dependent model we assumed $T_g = T_i$, and the ion temperature was a free parameter in the model. In the 1D model, only radial losses of photons were considered (this corresponds to setting $L \to \infty$). The two neutral argon resonant lines are nearby in wavelength (at 104.8 nm and 106.7 nm) and both have $g_\alpha = 3$, so they both have approximately the same $A_{\alpha\beta,eff.}$; this value was used for $A_{rg,eff.}$ in the models (for example, at 10 mTorr and 600 K, assuming $n_g \approx n_{total}$, we find $A_{rg,eff.} = 3.8 \times 10^6$ s^{-1}).

For $4p \to 4s$ transitions, on the other hand, l_{mfp} was comparable to the tube radius, and the lower level population density n_β was not necessarily much greater than the upper level population density n_α, so the more accurate formulas in Eqs. E.7 and E.8 had to be used[1]. To calculate the values of $A_{pm,eff.}$ and $A_{pr,eff.}$ for transitions from the $4p$ manifold to the $4s$ metastable and $4s$ resonant manifolds, the values of $A_{\alpha\beta,eff.}$ were first calculated for each of the individual $4p \to 4s$ emission lines with $A_{\alpha\beta} > 2 \times 10^6$ s^{-1} (this includes a total of ten $4p \to 4s_m$ transitions and eleven $4p \to 4s_r$ transitions—these are listed in Table E.1). These effective transition rates were then summed, weighted by the upper level statistical weights, to determine the overall effective rates for transitions between the energy

[1]Note that if $l_{mfp} > R$, then Eq. E.8 is not valid—in this case there is no re-absorption in our model, and $A_{\alpha\beta,eff.} = A_{\alpha\beta}$.

λ_0 (nm)	$A_{\alpha\beta}$ (s^{-1})	g_α	g_β
696.54	6.4×10^6	3	5
706.72	3.8×10^6	5	5
763.51	2.45×10^7	5	5
772.38	5.2×10^6	3	5
772.42	1.17×10^7	3	1
794.82	1.86×10^7	3	1
801.48	9.3×10^6	5	5
811.53	3.31×10^7	7	5
866.79	2.4×10^6	3	1
912.30	1.89×10^7	3	5
738.40	8.5×10^6	5	3
750.39	4.45×10^7	1	3
751.47	4.02×10^7	1	3
800.62	4.9×10^6	5	3
810.37	2.5×10^7	3	3
826.45	1.53×10^7	3	3
840.82	2.23×10^7	5	3
842.46	2.15×10^7	5	3
852.14	1.39×10^7	3	3
922.45	5.0×10^6	5	3
965.78	5.4×10^6	3	3

Table E.1: Ar I emission lines included in the calculation of the effective $4p \rightarrow 4s$ spontaneous transition rates. The first 10 lines listed contribute to $A_{pm,eff.}$, while the final 11 lines contribute to $A_{pr,eff.}$. g_α is the upper level statistical weight and g_β is the lower level statistical weight for each transition. All atomic data is from NIST [73].

level groups considered in the model:

$$A_{pm,eff.} = \frac{\sum g_\alpha A_{\alpha\beta,eff.}}{\sum g_\alpha} = \frac{\sum g_\alpha A_{\alpha\beta,eff.}}{36} \tag{E.11}$$

(and similarly for $A_{pr,eff.}$).

Appendix F

Analytical Solution of the 1D Ambipolar Diffusion Equation

This appendix describes the method used to analytically solve the one-dimensional ambipolar diffusion equation with a source term proportional to the plasma density (Eq. 4.14):

$$\frac{\partial n}{\partial t} - D_a \frac{\partial^2 n}{\partial z^2} = \nu_{i-l} n. \tag{F.1}$$

We will seek a solution valid over the interval $0 < z < L$, and adopt the boundary conditions $n(z = 0, t) = n_0$, $n(z = L, t) = 0$ and the initial condition $n(z > 0, t = 0) = 0$. For clarity in the derivation, the subscripts on D_a and ν_{i-l} will be suppressed in this section (i.e., they will be written simply as D and ν). The source term in Eq. F.1 can be eliminated by making the substitution $n(z, t) \equiv e^{\nu t} p(z, t)$. We find

$$\nu e^{\nu t} p + e^{\nu t} \frac{\partial p}{\partial t} - D e^{\nu t} \frac{\partial^2 p}{\partial z^2} = \nu e^{\nu t} p \tag{F.2}$$

$$\frac{\partial p}{\partial t} - D \frac{\partial^2 p}{\partial z^2} = 0. \tag{F.3}$$

The price to pay for this simplification is that the $z = 0$ boundary condition becomes time-dependent:

$$p(z = 0, t) = n_0 e^{-\nu t}. \tag{F.4}$$

The following procedure for handling this time-dependent boundary condition is a specific example of a general method described in reference [174]. We would like to find the simplest function $w(z, t)$ that satisfies the inhomogenous boundary conditions, and then decompose

$p(z,t)$ into a sum of this function and another function $u(z,t)$ that satisfies the homogeneous boundary conditions $u(0,t) = u(L,t) = 0$. We will ultimately be able to solve for $u(z,t)$ using the method of eigenfunction expansions.

Define

$$p(z,t) \equiv w(z,t) + u(z,t) \tag{F.5}$$

$$w(z,t) = p(0,t) + \frac{z}{L}\left(p(L,t) - p(0,t)\right) = n_0 e^{-\nu t}\left(1 - \frac{z}{L}\right), \tag{F.6}$$

where $w(z,t)$ has been constructed to satisfy the time-dependent boundary conditions as desired. Eq. F.3 gives

$$\frac{\partial w}{\partial t} + \frac{\partial u}{\partial t} = D\left(\frac{\partial^2 w}{\partial z^2} + \frac{\partial^2 u}{\partial z^2}\right) = D\frac{\partial^2 u}{\partial z^2} \tag{F.7}$$

$$\frac{\partial u}{\partial t} - D\frac{\partial^2 u}{\partial z^2} = -\frac{\partial w}{\partial t} \equiv S(z,t)\,. \tag{F.8}$$

This is another diffusion equation with a time-dependent source term; however, the situation has improved relative to Eq. F.1 because the new source term is not proportional to u.

We can expand $u(z,t)$ and $S(z,t)$ in Fourier sine series[1] with time-dependent coefficients:

$$S(z,t) \equiv n_0 \nu e^{-\nu t}\left(1 - \frac{z}{L}\right) = \sum_{m=1}^{\infty} \hat{S}_m(t) \sin\left(\frac{m\pi z}{L}\right) \tag{F.9}$$

$$u(z,t) = \sum_{m=1}^{\infty} \hat{u}_m(t) \sin\left(\frac{m\pi z}{L}\right) \tag{F.10}$$

$$\frac{\partial u}{\partial t} = \sum_{m=1}^{\infty} \frac{d\hat{u}_m}{dt} \sin\left(\frac{m\pi z}{L}\right) \tag{F.11}$$

$$\frac{\partial^2 u}{\partial z^2} = -\sum_{m=1}^{\infty} \hat{u}_m(t) \left(\frac{m\pi}{L}\right)^2 \sin\left(\frac{m\pi z}{L}\right). \tag{F.12}$$

[1]The expansion of $S(z,t)$ in a Fourier sine series is allowed even though $S(0,t) = n_0\nu e^{-\nu t}$, while $\sin\left(m\pi\left(0\right)/L\right) = 0$. The series will still converge to $S(z,t)$ everywhere in the interval $0 < z < L$. One may imagine extending $S(z,t)$ into the region $-L < z < 0$ as an odd function (so $S(-z,t) = -S(z,t)$), in which case the spatial dependence of $S(z,t)$ would be a sawtooth shape, making a sine series expansion appropriate. An even extension of $S(z,t)$ would have led to the use of a Fourier cosine series, but that would have been less convenient in this case.

Substituting into Eq. F.8, we have

$$0 = \sum_{m=1}^{\infty} \left(\frac{d\hat{u}_m}{dt} + D\left(\frac{m\pi}{L}\right)^2 \hat{u}_m(t) - \hat{S}_m(t) \right) \sin\left(\frac{m\pi z}{L}\right). \tag{F.13}$$

Because the $\sin\left(\frac{m\pi z}{L}\right)$ are linearly indepedent, each term must separately be equal to zero, which implies

$$\frac{d\hat{u}_m}{dt} + D\left(\frac{m\pi}{L}\right)^2 \hat{u}_m(t) = \hat{S}_m(t). \tag{F.14}$$

This first order ordinary differential equation may be solved using an integrating factor:

$$\frac{d}{dt}\left(\exp\left(D\left(\frac{m\pi}{L}\right)^2 t \right) \hat{u}_m(t) \right) = \exp\left(D\left(\frac{m\pi}{L}\right)^2 t \right) \hat{S}_m(t) \tag{F.15}$$

$$\hat{u}_m(t) = \exp\left(-D\left(\frac{m\pi}{L}\right)^2 t \right) \left(\int_0^t \exp\left(D\left(\frac{m\pi}{L}\right)^2 t' \right) \hat{S}_m(t')\, dt' + c_m \right). \tag{F.16}$$

To proceed further, we must explicitly calculate the Fourier coefficients $\hat{S}_m(t)$. Multiplying both sides of Eq. F.9 by $\sin(q\pi z/L)$ and integrating from $z = 0$ to $z = L$, we find

$$\int_0^L n_0 \nu e^{-\nu t} \left(1 - \frac{z}{L}\right) \sin\left(\frac{q\pi z}{L}\right) dz = \int_0^L \sum_{m=1}^{\infty} \hat{S}_m(t) \sin\left(\frac{m\pi z}{L}\right) \sin\left(\frac{q\pi z}{L}\right) dz \tag{F.17}$$

$$n_0 \nu e^{-\nu t} \left(\frac{L}{q\pi}\right) = \hat{S}_m\left(\frac{L}{2}\right) \delta_{mq} \tag{F.18}$$

$$\hat{S}_q = \left(\frac{2}{q\pi}\right) n_0 \nu e^{-\nu t}. \tag{F.19}$$

Substituting into Eq. F.16 and carrying out the integration yields

$$\hat{u}_m(t) = \frac{2 n_0 \nu e^{-\nu t}}{(m\pi)\left(D\left(\frac{m\pi}{L}\right)^2 - \nu \right)} + c_m e^{-D\left(\frac{m\pi}{L}\right)^2 t}. \tag{F.20}$$

The constant c_m is determined from the initial condition for the problem; since $p(z,0) = n(z,0) = 0$, we require

$$u(z,0) = -w(z,0) = -n_0\left(1 - \frac{z}{L}\right) = \sum_{m=1}^{\infty} \left(\frac{2 n_0 \nu}{(m\pi)\left(D\left(\frac{m\pi}{L}\right)^2 - \nu \right)} + c_m \right) \sin\left(\frac{m\pi z}{L}\right). \tag{F.21}$$

Using the Fourier sine series expansion of $(1 - z/L)$ once again, we find

$$c_m = \frac{-2n_0}{m\pi - \frac{\nu L^2}{Dm\pi}}. \tag{F.22}$$

Thus we finally obtain

$$u(z,t) = 2n_0 \sum_{m=1}^{\infty} \left(\frac{\nu e^{-\nu t}}{(m\pi)\left(D\left(\frac{m\pi}{L}\right)^2 - \nu\right)} - \frac{e^{-D\left(\frac{m\pi}{L}\right)^2 t}}{\left(m\pi - \frac{\nu L^2}{Dm\pi}\right)} \right) \sin\left(\frac{m\pi z}{L}\right) \tag{F.23}$$

$$p(z,t) = n_0 e^{-\nu t}\left(1 - \frac{z}{L}\right) + 2n_0 \sum_{m=1}^{\infty} \left(\frac{\nu e^{-\nu t}}{(m\pi)\left(D\left(\frac{m\pi}{L}\right)^2 - \nu\right)} - \frac{e^{-D\left(\frac{m\pi}{L}\right)^2 t}}{\left(m\pi - \frac{\nu L^2}{Dm\pi}\right)} \right) \sin\left(\frac{m\pi z}{L}\right) \tag{F.24}$$

$$n(z,t) = n_0\left(1 - \frac{z}{L}\right) + 2n_0 \sum_{m=1}^{\infty} \left(\frac{\nu}{(m\pi)\left(D\left(\frac{m\pi}{L}\right)^2 - \nu\right)} - \frac{e^{\left(\nu - D\left(\frac{m\pi}{L}\right)^2\right)t}}{\left(m\pi - \frac{\nu L^2}{Dm\pi}\right)} \right) \sin\left(\frac{m\pi z}{L}\right). \tag{F.25}$$

Plots of this solution for positive and negative values of ν are shown in Sec. 4.4.1. Its accuracy has been confirmed by solving Eq. F.1 numerically and demonstrating that the results agree with the analytical solution.

Appendix G

Numerical Algorithm for the 1D Time-Dependent Discharge Model

This appendix describes the numerical procedures used to implement the 1D time-dependent discharge model described in Sec. 4.4.2 by solving Eqs. 4.39–4.43. The calculations were carried out in IDL. The equations were discretized with a spatial grid spacing h_z and time step h_t. Throughout this section, a superscript i will label the spatial grid point, and j will label the time step. The spatial derivatives in Eqs. 4.39 and 4.40 were approximated using a second-order finite difference formula [175]:

$$\frac{\partial^2 \bar{P}_e^{i,j}}{\partial \bar{z}^2} \rightarrow \frac{\bar{P}_e^{i+1,j} - 2\bar{P}_e^{i,j} + \bar{P}_e^{i-1,j}}{h_z^2}, \tag{G.1}$$

and the time derivatives were approximated by a simple first-order difference formula:

$$\frac{\partial \bar{P}_e^{i,j}}{\partial \tau} \rightarrow \frac{\bar{P}_e^{i,j} - \bar{P}_e^{i,j-1}}{h_t}. \tag{G.2}$$

A straightforward way to solve the model equations would be to evaluate all terms on the right-hand side of each equation at time $j-1$, in which case the equations readily give the values of the pressure and population densities at time j. For example, Eq. 4.39

becomes

$$\bar{n}_e^{i,j} = \bar{n}_e^{i,j-1} + h_t \left[A \left(\frac{\bar{P}_e^{i+1,j-1} - 2\bar{P}_e^{i,j-1} + \bar{P}_e^{i-1,j-1}}{h_z^2} \right) + \bar{n}_e^{i,j-1} \left(\sum_\alpha \bar{K}_{\alpha i}^{i,j-1} \bar{n}_\alpha^{i,j-1} - B^{i,j-1} - \bar{\nu}_r^{i,j-1} \right) \right]. \quad \text{(G.3)}$$

Using this "explicit" time advance procedure, it is easy to start with the initial conditions for the problem and step the equations forward to find $\bar{n}_e$, $\bar{P}_e$, $\bar{n}_m$, $\bar{n}_r$, and $\bar{n}_p$ at all later times. Unfortunately, the algorithm is unstable: spurious oscillatory modes that inevitably exist due to rounding errors will grow in time and dominate the solution unless h_t is chosen to be smaller than a threshold value that scales with h_z^2 [175, Sec. 7.1]. The problem, in essence, is that functions of the form $\psi_\lambda \sim \sin(\lambda \pi i / (N_z - 1))$ (where N_z is the number of spatial grid points and λ can take on values from 1 to $N_z - 2$) are eigenfunctions of the discretized second derivative operator (Eq. G.1).

Generally for diffusion-like equations (i.e., equations with a second-order spatial derivative and first-order time derivative), the time step necessary to avoid numerical instability when using an explicit time advance algorithm is much smaller than the time step that would otherwise be necessary for an accurate solution, even when a simple first-order approximation for the time derivative is employed (using higher order Runge-Kutta methods does not improve the situation). Therefore, explicit algorithms are inefficient and often impractical for these types of problems. The performance was particularly bad for the energy equation in our model (Eq. 4.40), which has a nonlinear second derivative term.

In order to achieve a stable numerical solution in a reasonable amount of computational time, it was necessary to compute the second derivative terms implicitly by evaluating them at time j rather than at time $j-1$. This approach ensures stability against the oscillatory modes described above, no matter what time step h_t is used [175, Sec. 7.2]. The other terms in the equations that did not involve spatial derivatives could safely be treated explicitly.

Using the implicit approach, Eq. G.3 is modified to read

$$\bar{n}_e^{i,j} = \frac{h_t A}{h_z^2}\left(\bar{P}_e^{i+1,j} - 2\bar{P}_e^{i,j} + \bar{P}_e^{i-1,j}\right) + W^{i,j-1}, \tag{G.4}$$

where the terms in the equation that are evaluated at time $j-1$ have been grouped together as $W^{i,j-1}$:

$$W^{i,j-1} \equiv \bar{n}_e^{i,j-1}\left[1 + h_t\left(\sum_\alpha \bar{K}_{\alpha i}^{i,j-1}\bar{n}_\alpha^{i,j-1} - B^{i,j-1} - \bar{\nu}_r^{i,j-1}\right)\right]. \tag{G.5}$$

Similarly, the energy equation (Eq. 4.40) is discretized as

$$P_e^{i,j} = \frac{h_t C}{h_z^2}\left[\left(\frac{\bar{P}_e^{i+1,j}}{\bar{n}_e^{i+1,j}}\right)^{7/2} - 2\left(\frac{\bar{P}_e^{i,j}}{\bar{n}_e^{i,j}}\right)^{7/2} + \left(\frac{\bar{P}_e^{i-1,j}}{\bar{n}_e^{i-1,j}}\right)^{7/2}\right] + V^{i,j-1}, \tag{G.6}$$

where

$$\begin{aligned} V^{i,j-1} &\equiv h_t \bar{p}_{RF}^{i,j-1} + \bar{P}_e^{i,j-1}\left(1 - h_t E^{i,j-1}\right) \\ &+ h_t \bar{n}_e^{i,j-1}\left(\bar{\nu}_{Er}^{i,j-1} - D^{i,j-1} - \sum_\alpha \bar{K}_{E\alpha i}^{i,j-1}\bar{n}_\alpha^{i,j-1} - \sum_{\alpha\beta} \bar{K}_{E\alpha\beta}^{i,j-1}\bar{n}_\alpha^{i,j-1} - \bar{K}_{El.}^{i,j-1}\bar{n}_g^{i,j-1}\right). \end{aligned} \tag{G.7}$$

The unknown electron densities at time j may be eliminated from the system of equations by substituting Eq. G.4 into Eq. G.6:

$$\begin{aligned} P_e^{i,j} = \frac{h_t C}{h_z^2}\Bigg[&\left(\frac{\bar{P}_e^{i+1,j}}{\frac{h_t A}{h_z^2}\left(\bar{P}_e^{i+2,j} - 2\bar{P}_e^{i+1,j} + \bar{P}_e^{i,j}\right) + W^{i+1,j-1}}\right)^{7/2} \\ &- 2\left(\frac{\bar{P}_e^{i,j}}{\frac{h_t A}{h_z^2}\left(\bar{P}_e^{i+1,j} - 2\bar{P}_e^{i,j} + \bar{P}_e^{i-1,j}\right) + W^{i,j-1}}\right)^{7/2} \\ &+ \left(\frac{\bar{P}_e^{i-1,j}}{\frac{h_t A}{h_z^2}\left(\bar{P}_e^{i,j} - 2\bar{P}_e^{i-1,j} + \bar{P}_e^{i-2,j}\right) + W^{i-1,j-1}}\right)^{7/2}\Bigg] + V^{i,j-1}. \end{aligned} \tag{G.8}$$

This equation is valid for $2 \le i \le N_z - 3$. At the points adjacent to the boundaries ($i = 1$

and $i = N_z - 2$), either $\bar{P}_e^{i-2,j}$ or $\bar{P}_e^{i+2,j}$ is outside the simulation domain, and the boundary value $\bar{n}_e^{0,j}$ or $\bar{n}_e^{N_z-1,j}$ should be used in the denominator of the appropriate term in Eq. G.8 instead of plugging in from Eq. G.4. The pressures at the boundaries are determined by the boundary condition $\partial T_e/\partial \bar{z} = 0$. Taylor expansions of $T_e(h_z)$ and $T_e(2h_z)$ about $z = 0$ can be combined to derive the following asymmetric finite difference formula for the derivative:

$$\frac{\partial T_e^{0,j}}{\partial \bar{z}} \rightarrow \frac{4T_e^{1,j} - 3T_e^{0,j} - T_e^{2,j}}{2h_z}. \tag{G.9}$$

Setting this expression equal to 0 yields

$$T_e^{0,j} = \frac{4T_e^{1,j} - T_e^{2,j}}{3}. \tag{G.10}$$

The dimensionless pressure at $\bar{z} = 0$ can then be evaluated as

$$\bar{P}_e^{0,j} = \frac{\bar{n}_e^{0,j} T_e^{0,j}}{T_{e0}} = \frac{\bar{n}_e^{0,j}}{T_{e0}} \left(\frac{4T_e^{1,j} - T_e^{2,j}}{3} \right) = \frac{\bar{n}_e^{0,j}}{3} \left(\frac{4\bar{P}_e^{1,j}}{\bar{n}_e^{1,j}} - \frac{\bar{P}_e^{2,j}}{\bar{n}_e^{2,j}} \right) \tag{G.11}$$

$$= \frac{\bar{n}_e^{0,j}}{3} \left(\frac{4\bar{P}_e^{1,j}}{\frac{h_t A}{h_z^2} \left(\bar{P}_e^{2,j} - 2\bar{P}_e^{1,j} + \bar{P}_e^{0,j} \right) + W^{1,j-1}} - \frac{\bar{P}_e^{2,j}}{\frac{h_t A}{h_z^2} \left(\bar{P}_e^{3,j} - 2\bar{P}_e^{2,j} + \bar{P}_e^{1,j} \right) + W^{2,j-1}} \right). \tag{G.12}$$

The corresponding formula at $\bar{z} = L/z_0$ is

$$\bar{P}_e^{N_z-1,j} = \frac{\bar{n}_e^{N_z-1,j}}{3} \left(\frac{4\bar{P}_e^{N_z-2,j}}{\frac{h_t A}{h_z^2} \left(\bar{P}_e^{N_z-1,j} - 2\bar{P}_e^{N_z-2,j} + \bar{P}_e^{N_z-3,j} \right) + W^{N_z-2,j-1}} - \frac{\bar{P}_e^{N_z-3,j}}{\frac{h_t A}{h_z^2} \left(\bar{P}_e^{N_z-2,j} - 2\bar{P}_e^{N_z-3,j} + \bar{P}_e^{N_z-4,j} \right) + W^{N_z-3,j-1}} \right). \tag{G.13}$$

Eqs. G.8, G.12, and G.13 make up a system of N_z nonlinear algebraic equations, which were solved at each time step using IDL's built-in NEWTON routine. The solution for $\bar{P}_e^{i,j}$ was then plugged into Eq. G.4 to determine $\bar{n}_e^{i,j}$. The physical electron temperature $T_e^{i,j} = T_{e0} \bar{P}_e^{i,j} / \bar{n}_e^{i,j}$ was also calculated, since it was needed to evaluate the dimensionless parameters in Eqs. 4.35 – 4.38 prior to the next time step.

Since Eqs. 4.41, 4.42, and 4.43 for the excited state population densities contain no spatial derivatives, they could be advanced in time explicitly. The discretized formulas are

$$\bar{n}_m^{i,j} = h_t \left(\bar{n}_e^{i,j-1} \sum_\alpha \bar{K}_{\alpha m}^{i,j-1} \bar{n}_\alpha^{i,j-1} + \bar{A}_{pm}^{i,j-1} \bar{n}_p^{i,j-1} \right) + \bar{n}_m^{i,j-1} \left[1 - h_t \left(\bar{n}_e^{i,j-1} \sum_\beta \bar{K}_{m\beta}^{i,j-1} + \bar{D}_{eff.}^{i,j-1} \right) \right] \quad \text{(G.14)}$$

$$\bar{n}_r^{i,j} = h_t \left(\bar{n}_e^{i,j-1} \sum_\alpha \bar{K}_{\alpha r}^{i,j-1} \bar{n}_\alpha^{i,j-1} + \bar{A}_{pr}^{i,j-1} \bar{n}_p^{i,j-1} \right) + \bar{n}_r^{i,j-1} \left[1 - h_t \left(\bar{n}_e^{i,j-1} \sum_\beta \bar{K}_{r\beta}^{i,j-1} + \bar{A}_{rg}^{i,j-1} + \bar{D}_{eff.}^{i,j-1} \right) \right] \quad \text{(G.15)}$$

$$\bar{n}_p^{i,j} = h_t \bar{n}_e^{i,j-1} \left(\sum_\alpha \bar{K}_{\alpha p}^{i,j-1} \bar{n}_\alpha^{i,j-1} + \bar{\nu}_r^{i,j-1} \right) + \bar{n}_p^{i,j-1} \left[1 - h_t \left(\bar{n}_e^{i,j-1} \sum_\beta \bar{K}_{p\beta}^{i,j-1} + \bar{A}_{pm}^{i,j-1} + \bar{A}_{pr}^{i,j-1} + \bar{D}_{eff.}^{i,j-1} \right) \right]. \quad \text{(G.16)}$$

In order to maintain stability while advancing these equations forward in time, it was necessary for h_t to be small enough that each rate term in the equations was much smaller than the population density $\bar{n}_\alpha^{i,j-1}$ at the previous timestep. Because of the relatively high collisional transition rates between the excited states (see Table 3.1), this turned out to require a much smaller value of h_t than was needed for solving the diffusion and energy equations. Rather than decrease the overall time step size for the simulation, each time step was broken into 10 sub-time steps of size $h_t/10$ for the purpose of evaluating Eqs. G.14, G.15, and G.16, while $\bar{P}_e$ and $\bar{n}_e$ were only updated at intervals separated by h_t. This saved significant computation time since the solution of the nonlinear system comprising Eqs. G.8, G.12, and G.13 was the most computationally intensive part of the calculation.

$\bar{P}_e(\bar{z}, \tau)$ changed very fast early in the simulation, so small time steps were required for numerical stability, while h_t could be made larger after the discharge reached a nearly

steady state. The values of the time step used were typically $H_t = 5$–10 ns for the first 5 μs of the simulation, $H_t = 40$ ns for the next 20 μs, and $H_t = 100$ ns thereafter (a capital H is used here to denote the time step in physical units, as distinct from the dimensionless time step $h_t = H_t \nu_{in}$). With 101 spatial grid points ($H_z = 1$ cm in physical units), a 250 μs simulation could run in 3–4 minutes on the office PC, while simulations with 201 spatial grid points took about 4 times longer (the results with these two grid resolutions were nearly identical, indicating that $H_z = 1$ cm was sufficiently small for the calculations of interest).

A final subtlety was the specification of the RF power input density on the discrete spatial grid. The length L_{RF} of the region of power input did not necessarily span an integral number of grid points. For grid points located well inside this region, the physical and dimensionless power input densities (see Eq. 4.38) are simply

$$p_{RF}^{i,j} = \frac{P_{RF}^{j}}{\pi R^2 L_{RF}} \quad ; \quad \bar{p}_{RF}^{i,j} = \frac{2}{3} \frac{P_{RF}^{j}}{\pi R^2 L_{RF} \nu_{in} n_0 k_B T_{e0}}. \tag{G.17}$$

We may think of each grid point as being at the center of a volume of length H_z. In order to ensure that $P_{RF}^{j} = \int_0^L p_{RF}^{j}(z)\, \pi R^2 dz \rightarrow \sum_i p_{RF}^{i,j} \pi R^2 H_z$, the values of $p_{RF}^{i,j}$ at the grid points at the edges of the power deposition region must be reduced from the value given by Eq. G.17 by a factor equal to the fraction of the volume associated with these edge grid points that falls within the region. For example, with $H_z = 1$ cm and $L_{RF} = 10.5$ cm, if the power deposition region is at the center of the simulation domain, then the central 9 grid points will have $p_{RF}^{i,j}$ given by Eq. G.17, while p_{RF} at the two grid points adjacent to these on either end of the power deposition region should be lower by a factor $(L_{RF} - 9H_z) \,/\, (2H_z) = 0.75$.

Appendix H

Rogowski Coil for the MHD-Driven Jet Experiment

A Rogowski coil [8, p. 245] was constructed to measure the main gun current for the new MHD-driven jet experiment. The coil and passive integrator circuit designs were closely based on the Rogowski coil designed by Paul M. Bellan for the old MHD-driven jet experiment [137, Figure 3.2].

H.1 Theory of Operation

A Rogowski coil consists of a wire wound in a helical pattern on a flexible tube. The return winding is passed through the center of the tube so that both leads exit from the same end, canceling out the net toroidal turn that would otherwise exist when the tube is wrapped around the conductor of interest to make a current measurement. This feature, along with the lack of an iron core, is the main difference between Rogowski coils and other types of current transformers; since the two ends of the tube need not be connected to form a closed torus, a Rogowski coil can be wrapped around a pre-existing portion of a circuit without disturbing it.

When the Rogowski coil is wrapped around a current-carrying conductor, a change in the magnetic flux through the wire loops will induce a voltage $V_{coil} = -\frac{d}{dt}\Phi_B = -\frac{d}{dt}\sum_{i=1}^{n}\Phi_{Bi}$ across the coil, where Φ_{Bi} is the flux through an individual turn. The time integral of the voltage thus gives the flux, $\sum_{i=1}^{n}\Phi_{Bi} = -\int_0^t V_{coil}(t')\,dt'$. If the minor radius of the coil is small compared to the distance from the coil to the conductor, then the magnetic field will

Figure H.1: Photos of the Rogowski coil before it was enclosed in heat shrink.

not vary much inside a given turn and it can be assumed that $B\cos\theta = \Phi_{Bi}/A$ for each loop, where Φ_{Bi} is the flux through the loop, A is its cross-sectional area, and θ is the angle between the field and the loop normal. Meanwhile, the integral form of Ampere's law gives $\oint \mathbf{B}\cdot d\mathbf{l} = \oint B\cos\theta dl = \oint (\Phi_{Bi}/A)\, dl = \mu_0 I_{enclosed}$. If the turns on the Rogowski coil are closely and evenly spaced, then the line integral can be approximated by adding up the flux through all of the turns: $\oint (\Phi_{B1}/A)\, dl \approx \frac{l}{n}\sum_{i=1}^{n} (\Phi_{Bi}/A)$, where l is the length of the Rogowski coil (i.e., the toroidal circumference if the tube has been bent into a torus). Thus the current passing through the Rogowski coil is

$$I_{enclosed} = -\frac{l}{\mu_0 nA}\int_0^t V_{coil}(t')\, dt'. \tag{H.1}$$

Integration of the coil voltage may be accomplished with a passive or active integrator circuit, or carried out numerically.

H.2 Coil Design

Since the plasma gun for the MHD-driven jet experiment had rapidly changing high voltages, capacitive coupling of noise into the coil was a major concern. In order to achieve nearly perfect shielding, the coil was wound using narrow semi-rigid coaxial cable (UT-34) rather than ordinary wire. The outer conductor of the semi-rigid cable was grounded at both ends

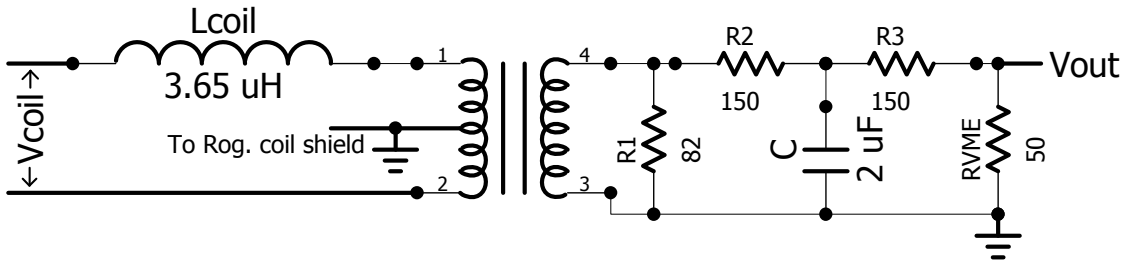

Figure H.2: Passive integrator circuit for the Rogowski coil.

and served as an electrostatic shield, while the inner conductor served as the measurement coil. In this configuration, the time-varying gun current would tend to induce opposing currents in the shield conductor that would attenuate the magnetic field inside the Rogowski coil; in order to avoid this effect, a small gap was left in the shield at one point along the coil. Triaxial cable (Belden 9222 50 Ω Triax) was used to convey the measured signal to the integration box, with the outer conductor serving as a shield and the inner and middle conductors carrying the signal. The Rogowski coil was also isolated from the data acquisition system by a 1:1 transformer (see Fig. H.2 for a full circuit diagram).

The coil was wound by hand on a piece of 3/8" diameter plastic tubing (Parker Parflex). In order to achieve even turn spacing, 3/8" wide masking tape was first wound on the tube in a helical pattern, with $\sim 1/8$" gaps between the turns, and the semi-rigid cable was then wound on the tube using the masking tape as a guide (see the photos in Fig. H.1). Finally, the entire coil was enclosed in heat shrink to hold the windings in place and isolate the coil shielding from the vacuum chamber. The finished coil had 79 turns and $l = 36.75$".

Preventing the coil from making electrical contact with the chamber was important, because if such contact had been made there would have been two paths from the coil shielding to ground, one through the vacuum chamber and one through the data acquisition system. Rapidly varying magnetic flux from the plasma gun would have induced a voltage around the "ground loop" present in this configuration, adding a spurious signal to the Rogowski coil ouput. Such a phenomenon was encountered during initial efforts to calibrate the coil, as the cable connector (described below), whose casing was connected to the Rogowski coil shield, was inadvertently touching the chamber and creating a ground loop.

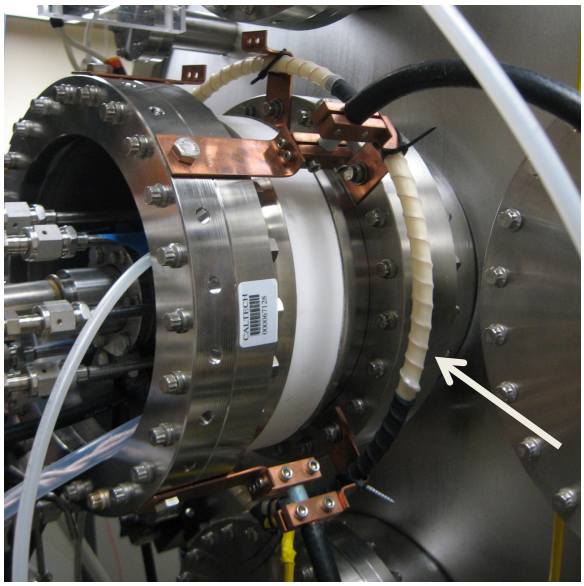

Figure H.3: Photo of Rogowski coil installed on the chamber.

The integrated output of the Rogowski coil was larger than expected in this case and varied unpredictably depending on the precise positioning in space of the cables leading to the VME digitizer.

The inner conductors of the semi-rigid cable at each end of the coil were connected to the inner and middle conductors of a short length of triaxial cable, and the shield of the semi-rigid cable was connected to the triax shield. A Neutrik NJ3FC6 1/4" phone cable jack and NP3XL 1/4" phone plug were used for the connection between the short length of triax and a longer triax cable leading to the circuit box and the VME digitizer. The shield conductor of this longer triax cable was connected to the aluminum chassis surrounding the transformer and integrator circuit, which was in turn connected to the ground of the VME digitizer.

A passive RC integrator circuit, shown in Fig. H.2, was used to automatically calculate $\int_0^t V_{coil}(t')\,dt'$ during each current measurement. The isolating transformer was wound with 26 turns on a Ferroxcube EC70-3C90 ferrite. In order to closely approximate the ideal of having the primary and secondary windings occupy identical locations in space, the transformer was wound from a single length of RG174A/U coaxial cable, with the outer conductor serving as the primary and the inner conductor serving as the secondary (see

Sec. A.2.6 for a discussion of magnetic flux coupling in transformers). A center tap was implemented on the primary by cutting a small hole in the outer cable insulation at a point halfway along the winding and soldering a wire between this point and the chassis.

Assuming the transformer behavior is ideal, the voltages and currents in the circuit shown in Fig. H.2 are related by the following equations:

$$V_{coil} = L_{coil}\frac{dI_{coil}}{dt} + I_1 R_1 \tag{H.2}$$

$$I_1 R_1 = I_2 R_2 + \frac{1}{C}\int_0^t I_C\left(t'\right) dt' \tag{H.3}$$

$$I_{coil} = I_1 + I_2 \tag{H.4}$$

$$I_2 = I_C + I_3 \tag{H.5}$$

$$\int_0^t I_C\left(t'\right) dt' = I_3\left(R_3 + R_{VME}\right) \tag{H.6}$$

$$V_{out} = I_3 R_{VME}. \tag{H.7}$$

Combining these equations to eliminate the currents and using the fact that $RC \gg \frac{L_{coil}}{R}$ for all of the resistors in the circuit (L_{coil} was measured to be 3.65 μH), we ultimately find

$$V_{coil} = V_{out}\left(\frac{R_2 + R_3 + R_{VME}}{R_{VME}}\right) + \frac{dV_{out}}{dt} C R_2 \left(\frac{R_3 + R_{VME}}{R_{VME}}\right) \tag{H.8}$$

$$+ \frac{d^2 V_{out}}{dt^2} L_{coil} C \left(\frac{\left(R_1 + R_2\right)\left(R_3 + R_{VME}\right)}{R_1 R_{VME}}\right). \tag{H.9}$$

Ideal integrator behavior corresponds to the $\frac{dV_{out}}{dt}$ term on the right hand side dominating; this will occur when

$$\left(\frac{R_2 + R_3 + R_{VME}}{C R_2\left(R_3 + R_{VME}\right)}\right) \ll \omega \ll \left(\frac{R_1 R_2}{L_{coil}\left(R_1 + R_2\right)}\right), \tag{H.10}$$

or plugging in the component values from Fig. H.2

$$\left(9 \times 10^2 \text{ Hz}\right) \ll f \ll \left(2 \times 10^6 \text{ Hz}\right). \tag{H.11}$$

When the bandwidth condition is satisfied, the voltage measured by the VME is related to

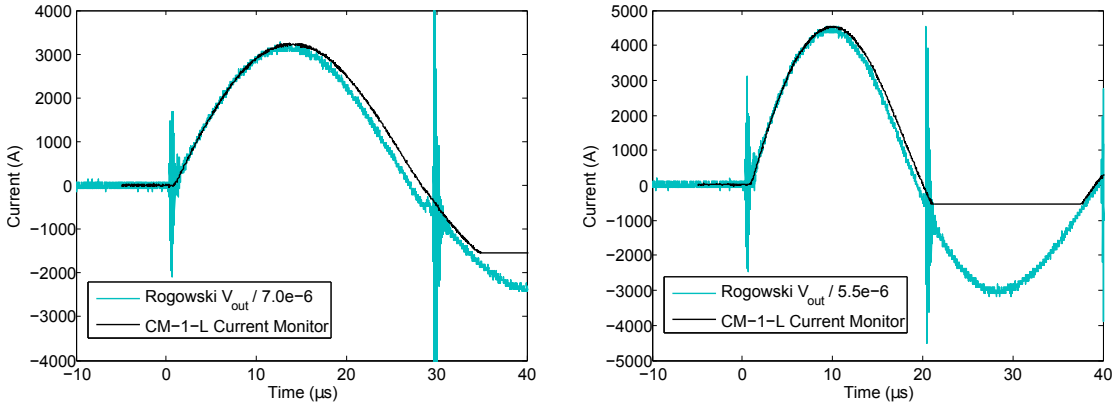

Figure H.4: Initial calibration with the Rogowski coil surrounding the re-entrant port. The main bank was charged to 510 V and discharged through a cable shorting the electrodes, which was passed through the Rogowski coil and an Ion Physics CM-1-L current monitor, and the output waveforms were compared to determine the calibration factor. However, the shorting cable passed too close to the Rogowski coil windings, and this caused the apparent calibration factor to vary depending on the shorting cable geometry. The data shown is from shots 75 (left panel) and 78 (right panel), which had different shorting cable lengths and positioning. The deviation of the Rogowski coil output from the reference waveform at late times is due to non-ideal behavior of the RC integrator—this effect is smaller for the higher frequency discharge shown on the right, as expected. The current monitor waveforms are clipped by the oscilloscope at late times.

the Rogowski coil voltage by

$$\int_0^t V_{coil}(t')\,dt' = V_{out} R_2 C \left(\frac{R_3 + R_{VME}}{R_{VME}}\right). \tag{H.12}$$

Thus substituting into Eq. H.1, the current enclosed by the Rogowski coil is related to the output voltage by

$$I_{enclosed} = -\frac{l}{\mu_0 n A} R_2 C \left(\frac{R_3 + R_{VME}}{R_{VME}}\right) V_{out}. \tag{H.13}$$

Plugging in the dimensions of the Rogowski coil and the component values used gives a predicted calibration factor

$$V_{out}\ (\text{mV}) = (6.32) \times I_{enclosed}\ (\text{kA}). \tag{H.14}$$

The 82 Ω resistor R_1 in parallel with the transformer secondary is included in the circuit for impedance matching and does not affect the integration. At the frequency of

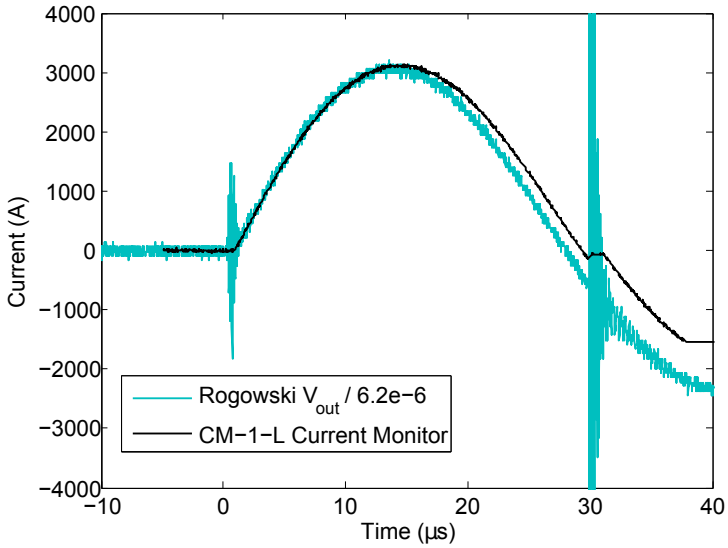

Figure H.5: Final calibration of the Rogowski coil (data shown is from shot 80). The main bank was charged to 510 V and discharged through a cable shorting the electrodes, which was passed through the center of the Rogowski coil and through an Ion Physics CM-1-L current monitor.

the gun current ($\sim$ 40 kHz), the 2 μF capacitor is low impedance ($\sim$ 2 Ω), so the input impedance of the integrator circuit is 82 Ω $\|$ 150 Ω $\approx$ 53 Ω, which approximately matches the 50 Ω characteristic impedance of the long triaxial cable between the Rogowski coil and the integrator and thus prevents signal reflections in the cable.

H.3 Calibration

The Rogowski coil was installed encircling the re-entrant port (see Fig. H.3 for a photo); the coil was mounted with at least 2 cm air gap separating it from the components of the plasma gun that would charge up to high voltage during a discharge, so high voltage insulation was not needed.

An initial calibration was carried out with the coil in place on the chamber: the electrodes were shorted by connecting a cable between the high voltage portion of the re-entrant port and the chamber ground, and the cable was passed through the Rogowski coil and a commercial current monitor. The main capacitor bank was charged to 500–1000 V and discharged through this cable, and the current monitor output was compared to the output

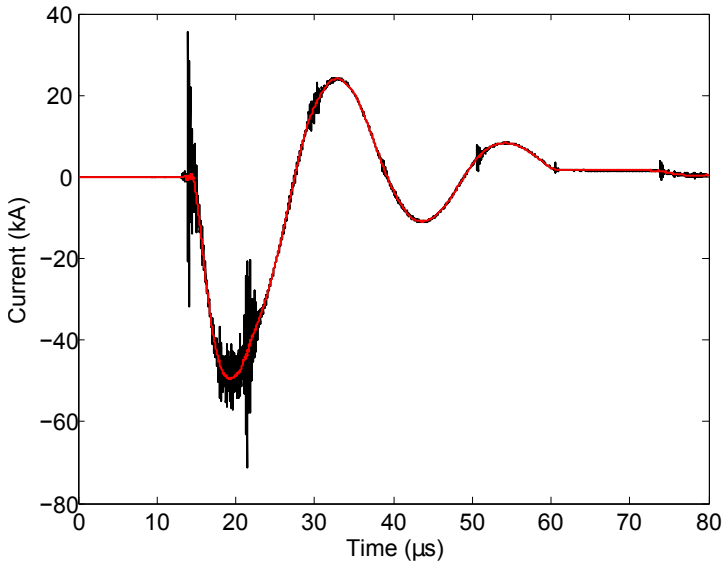

Figure H.6: Gun current measured by the Rogowski coil for pre-ionized jet experiment shot # 287. The raw data is shown in black, and a smoothed current trace (500 ns boxcar average) is overlaid in red. This was a hydrogen shot with $V_{main} = -5.03$ kV and the RF plasma source turned off.

from the Rogowski coil integrator. The Rogowski coil signal faithfully reproduced the shape of the reference waveform (see Fig. H.4), but the calibration factor varied depending on the positioning of the shorting cable. Because the re-entrant port took up most of the space inside the Rogowski coil in this configuration (see Fig. H.3), the cable necessarily had to pass near the edge of the Rogowski coil. As discussed in Sec. H.1, a necessary condition for ideal Rogowski coil operation is that the distance from the current-carrying conductor to the coil is much larger than the coil's minor radius. This condition was violated in this case, so the magnetic field was not uniform within a given turn on the coil, finite spacing between the turns may have become an issue, and the coil could not accurately calculate $\oint \mathbf{B} \cdot d\mathbf{l}$.

To obtain a more accurate calibration, the coil was removed from the chamber, and the procedure was repeated with the current-carrying cable passing through the coil near the center of the torus. The final calibration data, shown in Fig. H.5, yielded a calibration factor:

$$V_{out}\ (\text{mV}) = (6.2) \times I_{enclosed}\ (\text{kA}) \tag{H.15}$$

in excellent agreement with the theoretical prediction from Eq. H.14.

The Rogowski coil is inherently linear when the bandwidth condition is satisfied, so the calibration should be valid for much higher currents that would saturate the Ion Physics current monitors. A typical current waveform during a discharge of the experiment is shown in Fig. H.6.

Appendix I

Pre-Ionized Arched Flux Rope Experiment

I.1 Motivation and Overview

This appendix describes the design of a new experiment that will use RF pre-ionization to enable the creation of lighter, hotter plasma loops in the Caltech Arched Flux Rope Experiment[1] (also known as the Caltech Solar Coronal Loop Experiment) [177, 40]. The current-carrying plasma arches created in this experiment (see Fig. I.1) are relevant to solar coronal loops, prominences, and coronal mass ejections (CMEs). Like the original version of the MHD-Driven Jet Experiment, the Arched Flux Rope Experiment is an arc discharge that uses DC high-voltage to ionize a neutral gas cloud, so the Paschen criterion (see Fig. 1.10) sets a lower limit on the initial gas pressure and consequently on the plasma mass. RF pre-ionization will remove this limitation. Based on the results with pre-ionized MHD-driven jets described in Ch. 6, the pre-ionized flux ropes are expected to expand faster and have higher temperature than flux ropes created without pre-ionization, so they will be closer to the ideal MHD regime with $S \equiv \mu_0 v_A L/\eta \to \infty$.

The original goal of the pre-ionization project was to create MHD-driven jets with densities several orders of magnitude lower than was possible using Paschen breakdown alone. This proved to be impossible for two reasons: a jet would not form unless a large quantity of neutral gas was injected through the eight outer electrode gas inlets because no pre-ionized plasma could reach the region near the outer electrode (see Sec. 6.6 and Fig.

[1] A "flux rope" is defined as a tubular magnetic structure with helical field lines [176, p. 38].

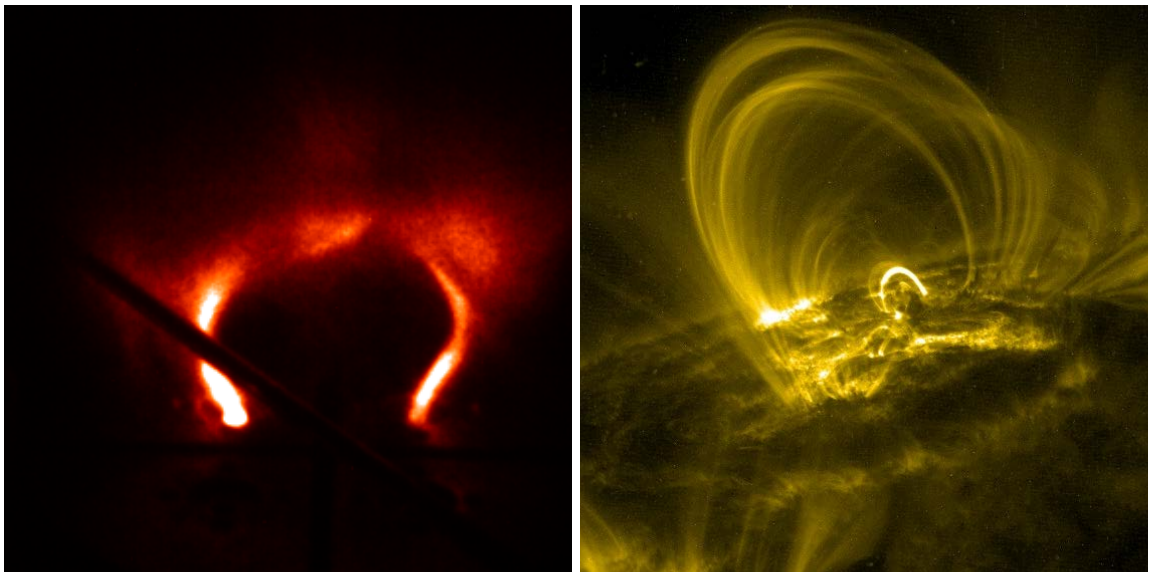

Figure I.1: Left: A laboratory plasma loop created in an earlier version of the Caltech Arched Flux Rope Experiment (argon plasma, $V_{main} = 5.0$ kV, $V_{bias} = 200$ V, $V_{gas} = 550$ V, image taken at $t = 3.0$ μs). The dark shaft running diagonally across the image is a magnetic probe array. Right: Extreme Ultraviolet (17.1 nm) image of solar coronal loops taken by the Transition Region and Coronal Explorer (TRACE) satellite (image from http://trace.lmsal.com/POD/TRACEpodarchive24.html). TRACE was a mission of the Stanford-Lockheed Institute for Space Research and was part of the NASA Small Explorer program.

6.22), and the MHD pinch force caused the jet column to become extremely narrow and dense (see Sec. 6.5). The pre-ionized flux rope experiment is designed to overcome the first of these issues: whereas in the pre-ionized jet experiment RF plasma emerged only from the central hole in the inner electrode, in the pre-ionized flux rope experiment plasma will be created behind both arch footpoints (see Fig. I.2), so that when it expands into the chamber it fills the entire volume where the initial loop structure will form. With the restrictions on the neutral gas pressure imposed by Paschen's law and the experiment's geometry removed, it will be possible to systematically study the limitations on the plasma density set by MHD (and possibly non-MHD) physics.

One phenomenon that may occur when the gas input is decreased is kinetic instabilities due to the high electron drift velocity necessary to carry the discharge current. Stringer [42, Figure 2] showed that in a collisionless plasma with $T_i \approx T_e$, electrostatic waves grow spontaneously if $(u_e - u_i) \gtrsim v_{Te}$. The drift velocity in a flux rope is $(u_e - u_i) \approx u_e \approx$

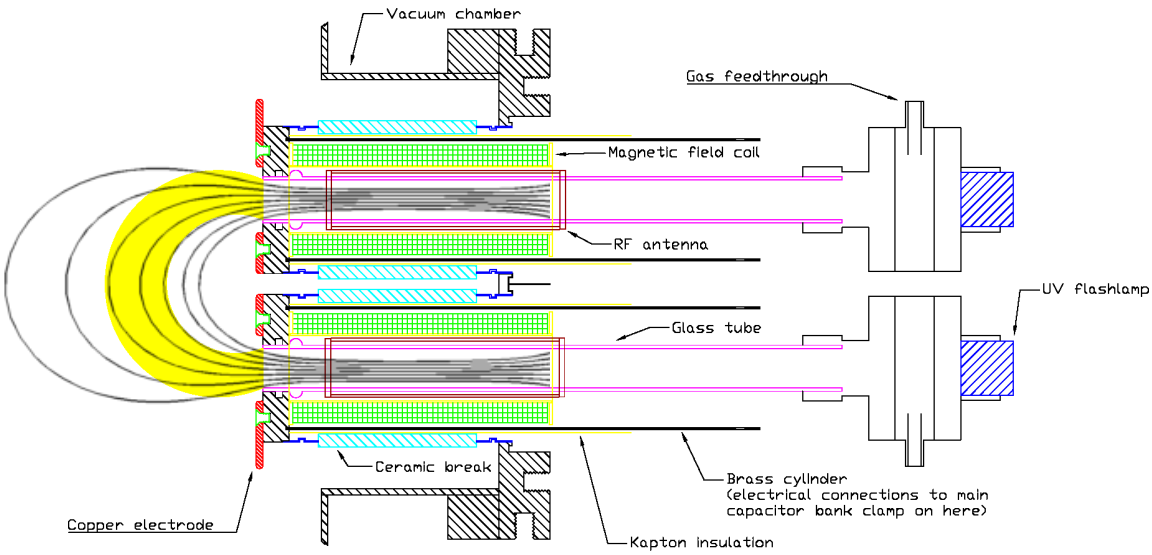

Figure I.2: Two-dimensional cross section of the plasma gun for the new pre-ionized flux rope experiment. The cable attachment assemblies, supports for the glass tubes, and polycarbonate pieces that clamp the bias coils in place have been omitted for clarity. RF plasma is created within each of the glass tubes and expands into the chamber along the magnetic field lines shown, which were calculated using an IDL program written by Bao N. Ha. The initial flux rope structure created when the main capacitor bank is triggered is sketched in yellow.

$I/n_e e\pi a^2 \approx I/N_e e$, where a is the minor radius and N_e is the electron number density per unit length. Typical values in the original Caltech experiments [135] were $n_e \sim 10^{21}$ m^{-3} and $a = 1$ cm, so $N_e = 3 \times 10^{17}$ m^{-1}. The main bank current was $I_{gun} \sim 50$ kA, but magnetic probe measurements [135] showed that only $\sim 10\%$ of this current flowed through the visible loop structure, so $I \sim 5$ kA, and thus $u_e \sim 10^5$ m/s $\ll v_{Te}$. If N_e were decreased by a factor of 10 in the pre-ionized flux rope experiment, then the electron velocity required to carry 5 kA of current would be $u_e \sim 10^6$ m/s, which is comparable to the thermal velocity ($v_{Te} \approx 10^6$ m/s for $T_e = 3$ eV), so unstable wave modes might exist. The fast-growing instability could destroy the flux rope, or the waves might be damped by collisions. Varying the plasma density in the vicinity of the threshold for instability should lead to very interesting insights.

The design of the new experiment is shown in Fig. I.2. Fast gas valves (see Sec. 1.6.4) are used to inject neutral gas into the two glass tubes, where it is ionized by RF power supplied by two electrically floating RF amplifiers like the one described in Ch. 2. The RF

plasma expands into the region in front of the copper electrodes, where the main capacitor bank (see Sec. 1.6.2) drives a current through it to create an arched magnetic flux rope. The amount of gas present in front of the electrodes can be varied by adjusting the trigger timing $t_{gas,RF}$ and capacitor bank voltage $V_{gas,RF}$ for the fast gas valves that supply gas to the two RF discharge tubes; unlike in the pre-ionized MHD-driven jet experiment, there is no additional source of neutral gas. With a high level of gas input, the plasma behavior is expected to be similar to that obtained in earlier versions of the Caltech Arched Flux Rope Experiment, which had neutral gas injected at the loop footpoints instead of pre-ionized plasma. With reduced $V_{gas,RF}$ or $t_{gas,RF}$, the new experiment should be able to operate in a previously inaccessible regime.

I.2 Design Details and Status of Construction

Whenever possible, design elements from the previous versions of the Caltech Arched Flux Rope experiment (see [177, Figure 19]) were retained in the new apparatus. The main modification was the replacement of the gas lines that ran down the center of the bias field coils with glass tubes in which pre-ionized plasma could be created. The magnetic material (cold rolled steel) that was mounted inside the coils in the former designs in order to increase the bias field strength also had to be removed to make room for the RF discharge tubes and antennas.

The major custom and off-the-shelf parts for the new experiment have all already been purchased, but the final assembly of the plasma gun, which will be mounted on the vacuum chamber end dome that currently houses the pre-ionized MHD-driven jet experiment, has not yet been carried out at the time of writing. Many of the necessary components will be reused from the pre-ionized jet experiment or from other Bellan lab experiments that have been decommissioned. A list of the parts required for the new experiment is provided in Table I.1.

The RF antennas that surround the glass discharge tubes will be constructed from strips of 0.01" thick copper sheet purchased from Basic Copper. Half-turn helical antennas similar to the one shown in Fig. 2.3 will be used initially, and alternate antenna geometries may

be tried if necessary. Since the RF plasma density will decay relatively quickly moving downstream of the antenna (see Fig. 4.10, for example), each antenna should be made long enough that its front edge reaches to within $\sim$ 2–3 cm of the plane of the electrodes, while the rear end of the antenna should extend out beyond the back end of the bias coil bobbin so that there is room to attach a coaxial cable.

As in the pre-ionized jet experiment (see Sec. 2.2), the "ground" reference for each floating RF amplifier, capacitive matching network, and bias/gas capacitor bank will be electrically connected to the associated electrode through a 15 Ω high pulse energy non-inductive resistor, so that these components follow changes in the electrode voltage. Kapton insulation will be used when necessary to avoid arcing hazards when two parts that will charge to different high voltages must be located nearby one another.

Part	Detailed Specifications	Source or Vendor
	Main Discharge Circuit	
Main capacitor bank	See Sec. 1.6.2	Reused from jet experiment
High voltage cables	Belden YK-198	Reused from jet experiment
Cable attachments	Clamps onto brass cylinder	Reused from DL experiment
	Plasma Gun	
Main welded assembly	Customized 10" CF flange with ceramic breaks, SS end caps and brass tubes attached	DV Manufacturing
Two ceramic breaks	40 kV rated, ID = 2.5"	MDC part # 9631010
Two non-inductive high pulse energy resistors	15 Ω, 15 kJ, HVR Advanced Power Components	One reused from jet experiment, one purchased
Two copper electrodes	Half circles, $R = 8.9$ cm	Reused from SL experiment
	Gas Delivery	
Floating capacitor banks	See Sec. 1.6.4	Reused from jet experiment
Fast gas valves	See Sec. 1.6.4	Reused from jet experiment
Two double-sided flanges with NPT holes	MDC part # 420002	One reused from jet experiment, one purchased
	Bias Magnetic Field	
Two bias field coils	4x52 turns, $L = 12.4$ cm, $R = 2.15$ cm	Using spares from other Caltech experiments
Six 3.3 mF capacitors	EVOX RIFA PEH200ZX4330MB2	Five reused from jet experiment, one purchased
Bank power supplies	Ultravolt 1/2C24-P125, 500 V, 125 W	One reused from jet experiment, one purchased
	RF Plasma Sources	
Two 3 kW RF amplifiers	See Sec. 2.3	Reused from jet experiment
Matching capacitors	See Sec. 2.4	Reused from jet experiment
Two UV flashlamps	Excelitas part numbers FX-1165, FYD-1150, PS-1120	One reused from jet experiment, one purchased
Two flashlamp mounts	Customized 2 3/4" CF flange	One reused, one from CCE Instrument Shop
Two quartz tubes	$L = 34.3$ cm, $OD = 2.22$ cm, $ID = 1.90$ cm, with maria	Caltech glass shop (Rick Gerhart)
Two quick-disconnects	7/8" tube, 2 3/4" CF flange	MDC part # 412009

Table I.1: List of main parts needed for the new pre-ionized flux rope experiment. The "double loop" (DL) and "single loop" (SL) experiments were previous versions of the Caltech Arched Flux Rope Experiment (see [177, Chapters 4 and 5]). Some additional minor parts were purchased that are not listed here.

Bibliography

[1] B. N. Ha, M. R. Stoneking, and J. P. Marler. Using numerical simulations to extract parameters of toroidal electron plasmas from experimental data. *Phys. Plasmas*, 16:032110, 2009.

[2] R. G. Greaves. Creation and uses of positron plasmas. *Phys. Plasmas*, 5:1439, 1994.

[3] M. J. Edwards et al. Progress toward ignition on the National Ignition Facility. *Phys. Plasmas*, 20:070501, 2013.

[4] P. M. Bellan. *Fundamentals of Plasma Physics*. Cambridge University Press, New York, 2006.

[5] M. A. Lieberman and A. J. Lichtenberg. *Principles of Plasma Discharges and Materials Processing*. Wiley-Interscience, Hoboken, N.J., 2nd edition, 2005.

[6] J. Wesson. *Tokamaks*. Oxford University Press, Oxford, UK, 2nd edition, 1997.

[7] R. Aymar, P. Barabaschi, and Y Shimomura. The ITER design. *Plasma Phys. Control. Fusion*, 44:519–565, 2002.

[8] P. M. Bellan. *Spheromaks: A Practical Application of Magnetohydrodynamic Dynamos and Plasma Self-Organization*. Imperial College Press, London, 2000.

[9] J. P. Freidberg. *Plasma Physics and Fusion Energy*. Cambridge University Press, New York, 2007.

[10] S. C. Hsu and P. M. Bellan. Experimental identification of the kink instability as a poloidal flux amplification mechanism for coaxial gun spheromak formation. *Phys. Rev. Lett.*, 90(21):215002, 2003.

[11] K. I. Thomassen, E. B. Hooper, and D. D. Ryutov. The spheromak path to fusion. *J. Fusion Energy*, 17(3):193–199, 1998.

[12] L. Woltjer. A theorem on force-free magnetic fields. *P. Natl. Acad. Sci.*, 44:489, 1958.

[13] J. B. Taylor. Relaxation of a toroidal plasma and generation of reverse magnetic fields. *Phys. Rev. Lett*, 33:1139, 1974.

[14] J. B. Taylor. Relaxation and magnetic reconnection in plasmas. *Rev. Mod. Phys.*, 58(3):741–763, 1986.

[15] C. G. R. Geddes, T. W. Kornack, and M. R. Brown. Scaling studies of spheromak formation and equilibrium. *Phys. Plasmas*, 5(4):1027–1034, 1998.

[16] S. C. Hsu and P. M. Bellan. Study of magnetic helicity injection via plasma imaging using a high-speed digital camera. *IEEE Trans. Plasma Sci.*, 30(1):10–11, Feb. 2002.

[17] S. C. Hsu and P. M. Bellan. On the jets, kinks, and spheromaks formed by a planar magnetized coaxial gun. *Phys. Plasmas*, 12:032103, 2005.

[18] P. M. Bellan, M. Livio, Y. Kato, S. V. Lebedev, T. P. Ray, A. Ferrari, P. Hartigan, A. Frank, J. M. Foster, and P. Nicolai. Astrophysical jets: Observations, numerical simulations, and laboratory experiments. *Phys. Plasmas*, 16:041005, 2009.

[19] N. Vlahakis and A. Königl. Magnetic driving of relativistic outflows in active galactic nuclei. I. Interpretation of parsec-scale accelerations. *ApJ*, 605:656–661, 2004.

[20] P. Hartigan and J. Morse. Collimation, proper motions, and physical conditions in the HH 30 jet from Hubble Space Telescope slitless spectroscopy. *ApJ*, 660:426–440, 2007.

[21] Michael D. Smith. *Astrophysical Jets and Beams*. Cambridge University Press, Cambridge, 2012.

[22] A. Königl and A. R. Choudhuri. Force-free equilibria of magnetized jets. *ApJ*, 289:173–187, 1985.

[23] R. D. Blandford and D. G. Payne. Hydromagnetic flows from accretion discs and the production of radio jets. *MNRAS*, 199:883–903, 1982.

[24] K. Asada, M. Inoue, Y. Uchida, S. Kameno, K. Fujisawa, S. Iguchi, and M. Mutoh. A helical magnetic field in the jet of 3C 273. *Publ. Astron. Soc. Japan*, 54:L39–L43, 2002.

[25] R. T. Zavala and G. B. Taylor. Faraday rotation measure gradients from a helical magnetic field in 3C 273. *ApJ*, 626:L73–L76, 2005.

[26] S. A. Balbus and J. F. Hawley. A powerful local shear instability in weakly magnetized disks. I. Linear analysis. *ApJ*, 376:214–222, 1991.

[27] D. Lynden-Bell. Magnetic jets from swirling discs. *MNRAS*, 369:1167–1188, 2006.

[28] X. Zhai, H. Li, and P. M. Bellan. Three-dimensional MHD simulations of the Caltech plasma jet experiment: First results. *ApJ*, 791:40, 2014.

[29] M. Nakamura, H. Li, and S. Li. Structure of magnetic tower jets in stratified atmospheres. *ApJ*, 652:1059–1067, 2006.

[30] J. A. Biretta, W. Junor, and M. Livio. Evidence for initial jet formation by an accretion disk in the radio galaxy M87. *New Astronomy Review*, 46:239–245, 2002.

[31] T. P. Ray, R. Mundt, J. E. Dyson, S. A. E. G. Falle, and A. C. Raga. Hubble Space Telescope observations of jets from young stars. *ApJ*, 468:L103–L106, 1996.

[32] R. Mundt, T. P. Ray, and A. C. Raga. Collimation of stellar jets — constraints from the observed spatial structure. II. Observational results. *Astron. Astrophys.*, 252:740–761, 1991.

[33] P. M. Bellan. Consideration of the relationship between Kepler and cyclotron dynamics leading to prediction of a nonmagnetohydrodynamic gravity-driven Hamiltonian dynamo. *Phys. Plasmas*, 14:122901, 2007.

[34] P. Hartigan, A. Frank, P. Varniére, and E. G. Blackman. Magnetic fields in stellar jets. *ApJ*, 661:910–918, 2007.

[35] T. P. Ray, T. W.B. Muxlow, D. J. Axon, A. Brown, D. Corcoran, J. Dyson, and R. Mundt. Large-scale magnetic fields in the outflow from the young stellar object T Tauri S. *Nature*, 385:415–417, 1997.

[36] P. P. Kronberg, R. V. E. Lovelace, G. Lapenta, and S. A. Colgate. Measurement of the electric current in a kpc-scale jet. *ApJ Letters*, 741:L15, 2011.

[37] General Electric: Microwave Devices Products Section, Schenectady, N. Y. *Product Information: GL-7703 Ignitron.*

[38] P. M. Bellan. Thermal instability of electrolytic capacitor bank used for gas puff valve. *Rev. Sci. Instrum.*, 73:2900–2905, 2002.

[39] D. Kumar and P. M. Bellan. Nonequilibrium Alfvénic plasma jets associated with spheromak formation. *Phys. Rev. Lett.*, 103:105003, 2009.

[40] E. V. Stenson and P. M. Bellan. Magnetically driven flows in arched plasma structures. *Phys. Rev. Lett.*, 109:075001, 2012.

[41] A. L. Moser and P. M. Bellan. Magnetic reconnection from a multiscale instability cascade. *Nature*, 482:379–381, 2012.

[42] T. E. Stringer. Electrostatic instabilities in current-carrying and counterstreaming plasmas. *J. Nucl. Energy, Part C Plasma Phys.*, 6:267–279, 1964.

[43] A. L. Moser. *Dynamics of magnetically driven plasma jets: An instability of an instability, gas cloud impacts, shocks, and other deformations.* PhD thesis, California Institute of Technology, 2012.

[44] A. V. Phelps and Z. Lj. Petrović. Cold-cathode discharges and breakdown in argon: Surface and gas phase production of secondary electrons. *Plasma Sources Sci. Technol.*, 8:R21–R44, 1999.

[45] F. Paschen. Ueber die zum funkenübergang in luft, wasserstoff und kohlensäure bei verschiedenen drucken erforderliche potentialdifferenz (On the potential difference required for spark initiation in air, hydrogen, and carbon dioxide at different pressures). *Annalen der Physik*, 273(5):69–75, 1889.

[46] K. Kajiwara, Y. Ikeda, M. Seki, S. Moriyama, T. Oikawa, T. Fujii, and JT-60 Team. Electron cyclotron heating assisted startup in JT-60U. *Nucl. Fusion*, 45:694–705, 2005.

[47] Y. S. Bae and A. C. England. Study on pre-ionization using second-harmonic electron cyclotron waves for the KSTAR first plasma. *Journal of the Korean Physical Society*, 51(4):1313–1319, 2007.

[48] G. L. Jackson, T. A. Casper, T. C. Luce, D. A. Humphreys, J. R. Ferron, A. W. Hyatt, E. A. Lazarus, R. A. Moyer, T. W. Petrie, D. L. Rudakov, and W. P. West. ITER startup studies in the DIII-D tokamak. *Nucl. Fusion*, 48:125002, 2008.

[49] A. C. Hossack, T. Firman, T. R. Jarboe, J. R. Prager, B. S. Victor, J. S. Wrobel, and T. Ziemba. Reduction of plasma density in the Helicity Injected Torus with Steady Inductance experiment by using a helicon pre-ionization source. *Rev. Sci. Instrum.*, 84:103506, 2013.

[50] P. K. Chattopadhyay, R. Pal, N. R. Ray, and P. K. Gupta. Breakdown and preionization experiments in the SINP tokamak. *Nucl. Fusion*, 36(9):1205–1209, 1996.

[51] R. W. Boswell. Very efficient plasma generation by whistler waves near the lower hybrid frequency. *Plasma Physics and Controlled Fusion*, 26(10):1147–1162, 1984.

[52] T. Shoji, Y. Sakawa, S. Nakazawa, K. Kadota, and T. Sato. Plasma production by helicon waves. *Plasma Sources Sci. Technol.*, 2:5–10, 1993.

[53] P. Zhu and R. W. Boswell. Ar II laser generated by Landau damping of whistler waves at the lower hybrid frequency. *Phys. Rev. Lett.*, 63(26):2805, 1992.

[54] A. R. Ellingboe and R. W. Boswell. Capacitive, inductive and helicon-wave modes of operation of a helicon plasma source. *Phys. Plasmas*, 3(7):2797, 1996.

[55] F. F. Chen and R. W. Boswell. Helicons—the past decade. *IEEE Trans. Plasma Sci.*, 25(6):1245, 1997.

[56] F. F. Chen. Plasma ionization by helicon waves. *Plasma Physics and Controlled Fusion*, 33(4):339–364, 1991.

[57] R. T. S. Chen, R. A. Breun, S. Gross, N. Hershkowitz, M.-K. J. Hsieh, and J. Jacobs. Experimental studies of multimode helicon waves. *Plasma Sources Sci. Technol.*, 4:337–344, 1995.

[58] Y. Sakawa, N. Koshikawa, and T. Shoji. Characteristics of the high density plasma production by m = 0 helicon wave. *Appl. Phys. Lett.*, 69(12):1695–1697, 1996.

[59] S. Yun, S. Cho, G. Tynan, and H. Chang. Density enhancement near lower hybrid resonance layer in m = 0 helicon wave plasmas. *Phys. Plasmas*, 8(1):358–363, 2001.

[60] M. Albulet. *RF Power Amplifiers*. Nobel Publishing Associates, United States, 2001.

[61] G. Choi. *13.56 MHz, Class D Push-Pull, 2KW RF Generator with Microsemi DRF1300 Power MOSFET Hybrid*. Microsemi, September 2011. Application Note 1812.

[62] Microsemi. *DRF1301 MOSFET Push-Pull Hybrid*, C edition, 2011.

[63] S. J. Orfanidis. Electromagnetic waves and antennas. `www.ece.rutgers.edu/~orfanidi/ewa`, 1996–2013.

[64] J. P. Rayner, A. D. Cheetham, and G. N. French. Radio frequency matching for helicon plasma sources. *J. Vac. Sci. Technol. A*, 14(4):2048–2055, 1996.

[65] Y. Mouzouris and J. E. Scharer. Wave propagation and absorption simulations for helicon sources. *Phys. Plasmas*, 5(12):4253, 1998.

[66] D. J. Griffiths. *Introduction to Electrodynamics*. Prentice Hall, Upper Saddle River, New Jersey, 3rd edition, 1999.

[67] R. J. Perkins and P. M. Bellan. Elimination of radiofrequency noise by identifying and diverting large RF ground currents. *AIP Conference Proceedings*, 1406:531–534, 1991.

[68] I. Langmuir. The interaction of electron and positive ion space charges in cathode sheaths. *Phys. Rev.*, 33:954, 1929.

[69] L. Tonks and I. Langmuir. A general theory of the plasma of an arc. *Phys. Rev.*, 34:876, 1929.

[70] S. Chen and T. Sekiguchi. Instantaneous directdisplay system of plasma parameters by means of triple probe. *J. Appl. Phys.*, 36(8):2363, 1965.

[71] R. L. Stenzel and J. M. Urrutia. Oscillating plasma bubbles. II. Pulsed experiments. *Phys. Plasmas*, 19:082106, 2012.

[72] H. V. Willett. Spectroscopic analysis of a plasma for an astrophysical jet experiment. Caltech Summer Undergraduate Research Fellowship (SURF) Technical Paper, 2011.

[73] A. Kramida, Y. Ralchenko, J. Reader, and NIST ASD Team. NIST Atomic Spectra Database (ver. 5.1), [Online]. Available: `http://physics.nist.gov/asd` [2014, January 6]. National Institute of Standards and Technology, Gaithersburg, MD., 2013.

[74] R. W. P. McWhirter. Spectral intensities. In R. H. Huddlestone and S. L. Leonard, editors, *Plasma Diagnostic Techniques*, volume 21 of *Pure and Applied Physics*. Academic Press, New York, 1965.

[75] T. Fujimoto. Kinetics of ionization-recombination of a plasma and population density of excited ions. I. Equilibrium plasma. *J. Phys. Soc. Japan*, 47(1):265, 1979.

[76] F. F. Chen and D. D. Blackwell. Upper limit to Landau damping in helicon discharges. *Phys. Rev. Lett.*, 82(13):2677, 1999.

[77] K. P. Shamrai and V. B. Taranov. Volume and surface RF power absorption in a helicon plasma source. *Plasma Sources Sci. Technol.*, 5:474–491, 1996.

[78] E. E. Scime, A. M. Keesee, and R. W. Boswell. Mini-conference on helicon plasma sources. *Phys. Plasmas*, 15:058301, 2008.

[79] F. F. Chen, I. D. Sudit, and M. Light. Downstream physics of the helicon discharge. *Plasma Sources Sci. Technol.*, 5:173–180, 1996.

[80] A. J. Perry, D. Vender, and R. W. Boswell. The application of a helicon source to plasma processing. *J. Vac. Sci. Technol. B*, 9(2):310–317, 1991.

[81] C. M. Franck, O. Grulke, A. Stark, T. Klinger, E. E. Scime, and G. Bonhomme. Measurement of spatial structures of different discharge modes in a helicon source. *Plasma Sources Sci. Technol.*, 14:226–235, 2005.

[82] I. G. Mikellides and I. Katz. Numerical simulations of Hall-effect plasma accelerators on a magnetic-field-aligned-mesh. *Phys. Rev. E*, 86:046703, 2012.

[83] S. Ashida, C. Lee, and M. A. Lieberman. Spatially averaged (global) model of time modulated high density argon plasmas. *J. Vac. Sci. Technol. A*, 13(5):2498–2507, 1995.

[84] M.-H. Lee and C.-W. Chung. Effect of multistep ionizations on the electron temperature in an argon inductively coupled plasma. *Appl. Phys. Lett*, 87:131502, 2005.

[85] M. Park, H.-Y. Chang, S.-J. You, J.-H. Kim, and Y.-H. Shin. Anomalous evolution of Ar metastable density with electron density in high density Ar discharge. *Phys. Plasmas*, 18:103510, 2011.

[86] K. B. Chai and P. M. Bellan. Spontaneous formation of nonspherical water ice grains in a plasma environment. *Geophys. Res. Lett.*, 40(23):6258–6263, 2013.

[87] F. F. Chen. Experiments on helicon plasma sources. *J. Vac. Sci. Technol. A*, 10:1389–1401, 1992.

[88] C. M. Franck, O. Grulke, and T. Klinger. Mode transitions in helicon discharges. *Phys. Plasmas*, 10(1):323–325, 2003.

[89] C. D. Conway, A. J. Perry, and R. W. Boswell. Evolution of ion and electron energy distribution functions in pulsed helicon plasma discharges. *Plasma Sources Sci. Technol.*, 7:337–347, 1998.

[90] V. Kaeppelin, M. Carrère, and J.-M. Layet. Langmuir probe study in the post-discharge of a pulsed helicon discharge. *Plasma Sources Sci. Technol.*, 11:53–56, 2002.

[91] M. D. Carter, F. W. Baity Jr., R. H. Goulding, E. F. Jaeger, F. R. Chang-Diaz, and J. P. Squire. Light ion helicon plasma sources. In T. K. Mau and J. deGrassie, editors, *Radio Frequency Power in Plasmas: 14th Topical Conf.*, pages 465–472, 2001.

[92] R. W. Boswell and F. F. Chen. Helicons—the early years. *IEEE Trans. Plasma Sci.*, 25(6):1229, 1997.

[93] R. W. Boswell and D. Vender. An experimental study of breakdown in a pulsed helicon plasma. *Plasma Sources Sci. Techno.*, 4:534–540, 1995.

[94] K. Toki, S. Shinohara, T. Tanikawa, and K. P. Shamrai. Small helicon plasma source for electric propulsion. *Thin Solid Films*, 506–507:597–600, 2006.

[95] P. Kerdtongmee, D. Srinoum, and M. Nisoa. Development of a compact permanent magnet helicon plasma source for ion beam bioengineering. *Rev. Sci. Instrum*, 82:103503, 2011.

[96] D. Kuwahara, A. Mishio, T. Nakagawa, and S. Shinohara. Development of a small-diameter, inductively coupled magnetized plasma device. *Rev. Sci. Instrum.*, 84:103502, 2013.

[97] S. Shinohara, T. Hada, T. Motomura, K. Tanaka, T. Tanikawa, K. Toki, Y. Tanaka, and K. P. Shamrai. Development of high-density helicon plasma sources and their applications. *Phys. Plasmas*, 16:057104, 2009.

[98] O. V. Batishchev. Minihelicon plasma thruster. *IEEE Trans. Plasma Sci.*, 37(8):1563–1571, 2009.

[99] E. S. Weibel. Anomalous skin effect in a plasma. *Phys. Fluids*, 10(4):741, April 1967.

[100] C. Charles and R. Boswell. Current-free double-layer formation in a high-density helicon discharge. *Appl. Phys. Lett.*, 82(9):1356, 2003.

[101] J. Denavit. Collisionless plasma expansion into a vacuum. *Phys. Fluids*, 22(7):1384–1392, 1979.

[102] U. Samir, K. H. Wright, Jr., and N. H. Stone. The expansion of plasma into a vacuum: Basic phenomena and processes and applications to space plasma physics. *Rev. Geophys. Space Phys.*, 21(7):1631–1646, 1983.

[103] C. Chan, N. Hershkowitz, A. Ferreira, T. Intrator, B. Nelson, and K. Lonngren. Experimental observations of self-similar plasma expansion. *Phys. Fluids*, 27(1):266–268, 1984.

[104] T. Fujimoto. Kinetics of ionization-recombination of a plasma and population density of excited ions. IV. Recombining plasma—low-temperature case. *J. Phys. Soc. Japan*, 49(4):1569, 1980.

[105] A. Hirabayashi, Y. Nambu, M. Hasuo, and T. Fujimoto. Emission spectroscopy of a pulsed helium-discharge plasma: Transition from the ionizing phase to the recombining phase. *Phys. Rev. A*, 37(1):77–82, 1988.

[106] A. Bogaerts. The afterglow mystery of pulsed glow discharges and the role of dissociative electron-ion recombination. *J. Anal. At. Spectrom.*, 22:502–512, 2007.

[107] G. P. Jackson and F. L. King. Bulk plasma properties in the pulsed glow discharge. *Spectrochimica Acta Part B*, 58:1417–1433, 2003.

[108] S. I Braginskii. Transport processes in a plasma. In *Reviews of Plasma Physics*, volume 1. Consultants Bureau, New York, 1965.

[109] Y. Celik, T. V. Tsankov, M. Aramaki, S. Yoshimura, D. Luggenhölscher, and U. Czarnetzki. Recombination and enhanced metastable repopulation in the argon afterglow. *Phys. Rev. E*, 85:056401, 2012.

[110] M.-H. Lee and C.-W. Chung. Self-consistent global model with multi-step ionizations in inductively coupled plasmas. *Phys. Plasmas*, 12:073501, 2005.

[111] C. Kenty. The recombination of argon ions and electrons. *Phys. Rev.*, 32:624–635, 1928.

[112] N. Kang, F. Gaboriau, S. Oh, and A. Ricard. Modeling and experimental study of pulse modulated ICP discharge: Production of Ar highly excited states. *Plasma Sources Sci. Technol.*, 20:035002, 2011.

[113] X. Yan, Y. Lin, R. Huang, W. Hang, and W. W. Harrison. A spectroscopic investigation of the afterglow and recombination process in a microsecond pulsed glow discharge. *J. Anal. At. Spectrom.*, 25:534–543, 2010.

[114] Ph. Belenguer, M. Ganciu, Ph. Guillot, and Th. Nelis. Pulsed glow discharges for analytical applications. *Spectrochimica Acta Part B*, 64:623–641, 2009.

[115] T. Watari, T. Hatori, R. Kumazawa, S. Hidekuma, T. Aoki, T. Kawamoto, M. Inutake, S. Hiroe, A. Nishizawa, K. Adati, T. Sato, T. Watanabe, H. Obayashi, and K. Takayama. Radiofrequency plugging of a high density plasma. *Phys. Fluids*, 21:2076–2081, 1978.

[116] W. J. Fader, R. A. Jong, J. H. Stufflebeam, and E. A. Sziklas. RF plugging of a plasma by the ponderomotive effect on electrons. *Phys. Rev. Lett.*, 46(15):999, 1981.

[117] G. Dimonte, B. M. Lamb, and G. J. Morales. Effects of nonadiabaticity on applications of the ponderomotive force near gyroresonance. *Plasma Phys.*, 25(7):713–722, 1983.

[118] M. A. Biondi. Diffusion, de-excitation, and ionization cross sections for metastable atoms. I. *Phys. Rev.*, 88(3):660–665, 1952.

[119] K. E. Greenberg and G. A. Hebner. Electron and metastable densities in parallel-plate radio-frequency discharges. *J. Appl. Phys.*, 73(12):8126–8133, 1993.

[120] Y. Ohtsu, K. Shimizu, and H. Fujita. Growth mechanism of electron density in radio frequency afterglow plasmas. *Electrical Engineering in Japan*, 135(2):26–32, 2001.

[121] L. J. Overzet and J. Kleber. Effect of metastable atom reactions on the electron energy probability functions in afterglows. *Plasma Sources Sci. Technol.*, 7:512–523, 1998.

[122] G. Gamez, A. Bogaerts, and G. M. Hieftje. Temporal and spatially resolved laser-scattering plasma diagnostics for the characterization of a ms-pulsed glow discharge. *J. Anal. At. Spectrom.*, 21:350–359, 2006.

[123] A. Bogaerts. Hydrogen addition to an argon glow discharge: A numerical simulation. *J. Anal. At. Spectrom.*, 17:768–779, 2002.

[124] A. Bogaerts and R. Gijbels. Effects of adding hydrogen to an argon glow discharge: Overview of relevant processes and some qualitative explanations. *J. Anal. At. Spectrom.*, 15:441–449, 2000.

[125] T. Okada and M. Sugawara. Determination of ionization cross section for argon metastable-metastable collision by means of afterglow technique. *Jpn. J. Appl. Phys.*, 35:4535–4540, 1996.

[126] N. Baguer, A. Bogaerts, Z. Donko, R. Gijbels, and N. Sadeghi. Study of the Ar metastable atom population in a hollow cathode discharge by means of a hybrid model and spectrometric measurements. *J. Appl. Phys.*, 97:123305, 2005.

[127] S. Rauf and M. J. Kushner. Argon metastable densities in radio frequency Ar, Ar/O_2, and Ar/CF_4 electrical discharges. *J. Appl. Phys.*, 82(6):2805–2813, 1997.

[128] C. M. Ferreira, J. Loureiro, and A. Ricard. Populations in the metastable and the resonance levels of argon and stepwise ionization effects in low-pressure argon positive column. *J. Appl. Phys.*, 57(1):82–90, 1985.

[129] A. V. Phelps and J. P. Molnar. Lifetimes of metastable states of noble gases. *Phys. Rev.*, 89(6):1202, 1953.

[130] G. S. Yun and P. M. Bellan. Plasma tubes becoming collimated as a result of magnetohydrodynamic pumping. *Phys. Plasmas*, 17:062108, 2010.

[131] M. Nakamura, H. Li, and S. Li. Stability properties of magnetic tower jets. *ApJ*, 656:721–732, 2007.

[132] X. Zhai and P. M. Bellan. An earth-isolated optically coupled wideband high voltage probe powered by ambient light. *Rev. Sci. Instrum.*, 83:104703, 2012.

[133] R. J. Perkins. *Experimental and Analytical Studies of Merging Plasma Loops on the Caltech Solar Loop Experiment*. PhD thesis, California Institute of Technology, 2011.

[134] D. Kumar. *Experimental Investigations of Magnetohydrodynamic Plasma Jets*. PhD thesis, California Institute of Technology, 2009.

[135] E. Stenson. *Fields, Forces, and Flows: What Laboratory Experiments Reveal About The Dynamics of Arched Plasma Structures*. PhD thesis, California Institute of Technology, 2012.

[136] C. A. Romero-Talamás, P. M. Bellan, and S. C. Hsu. Multielement magnetic probe using commercial chip inductors. *Rev. Sci. Instrum.*, 75:2664, 2004.

[137] G. S. Yun. *Dynamics of Plasma Structures Interacting with External and Self-Generated Magnetic Fields*. PhD thesis, California Institute of Technology, 2008.

[138] G. B. Rybicki and A. P. Lightman. *Radiative Processes in Astrophysics*. Wiley-VCH, Germany, 2nd edition, 2004.

[139] T. Shikama and P. M. Bellan. Development of a polarization resolved spectrscopic diagnostic for measurements of the vector magnetic field in the Caltech coaxial magnetized plasma jet experiment. *Rev. Sci. Instrum.*, 84:023507, 2013.

[140] W. L. Wiese. Line broadening. In R. H. Huddlestone and S. L. Leonard, editors, *Plasma Diagnostic Techniques*, volume 21 of *Pure and Applied Physics*. Academic Press, New York, 1965.

[141] T. R. Metcalf. voigtfit (IDL function). `http://hesperia.gsfc.nasa.gov/ssw/gen/idl/fitting/voigtfit.pro`, 1994.

[142] D. M. Zarro. pvoigt (IDL program). `http://hesperia.gsfc.nasa.gov/ssw/gen/idl/fitting/pvoigt.pro`, 1993.

[143] N. Konjević, A. Lesage, J. R. Fuhr, and W. L. Wiese. Experimental Stark widths and shifts for spectral lines of neutral and ionized atoms (a critical review of selected data for the period 1989 through 2000). *J. Phys. Chem. Ref. Data*, 31(3):819–927, 2002.

[144] H. R. Griem. *Plasma Spectroscopy.* McGraw Hill, 1964.

[145] T. Fujimoto. Kinetics of ionization-recombination of a plasma and population density of excited ions. II. Ionizing plasma. *J. Phys. Soc. Japan*, 47(1):273, 1979.

[146] D. Kumar, A. L. Moser, and P. M. Bellan. Energy efficiency analysis of the discharge circuit of the Caltech spheromak experiment. *IEEE Trans. Plasma Sci.*, 2(1):47–52, Jan. 2010.

[147] L. Soto. New trends and future perspectives on plasma focus research. *Plasma Phys. Control. Fusion*, 47:A361–A381, 2005.

[148] M. G. Haines. A review of the dense Z-pinch. *Plasma Phys. Control. Fusion*, 53:093001, 2011.

[149] P. M. Bellan. Why current-carrying magnetic flux tubes gobble up plasma and become thin as a result. *Phys. Plasmas*, 10(5):1999–2008, 2003.

[150] J. T. Slough, A. L. Hoffman, R. D. Milroy, R. Maqueda, and L. C. Steinhauer. Transport, energy balance, and stability of a large field-reversed configuration. *Phys. Plasmas*, 2(6):2286–2291, 1995.

[151] T. G. Wilson. The evolution of power electronics. *IEEE Transactions on Power Electronics*, 15(3):439–446, May 2000.

[152] M. Stanway and R. Seddon. *Ignitron Firing Time and Jitter.* EEV Internal Memorandum, June 1986.

[153] National Electronics. *NL7703 Ignitron*, B edition, June 2009.

[154] J. Dodge. IGBT tutorial: Part 1 — selection. *EE Times*, March 2007. `http://www.eetimes.com/design/power-management-design/4012153/IGBT-tutorial--Part-1--Selection`.

[155] V. H. Chaplin and P. M. Bellan. Fast ignitron trigger circuit using insulated gate bipolar transistors. *IEEE Trans. Plasma Sci.*, 41(4):975–979, 2013.

[156] IXYS Corporation. *Very High Voltage IGBT IXEL40N400*, Dec. 2009.

[157] R. S. Chokhawala, J. Catt, and L. Kiraly. A discussion on IGBT short-circuit behavior and fault protection schemes. *IEEE Transactions on Industry Applications*, 31(2):256–263, March/April 1995.

[158] A. D. Pathak. *Application Note AN0002: MOSFET/IGBT Drivers, Theory and Applications*. IXYS Corporation, Santa Clara, CA, 2001.

[159] J. Dodge. IGBT tutorial: Part 2 — static, dynamic characteristics. *EE Times*, March 2007. `http://www.eetimes.com/design/power-management-design/4012154/IGBT-Tutorial-Part-2--Static-dynamic-characteristics`.

[160] ON Semiconductor. *Rectifier Applications Handbook (HB214/D)*, 2 edition, 2001.

[161] P. M. Bellan. Transformer design. Unpublished note.

[162] M. K. Kazimierczuk. Class D voltage-switching MOSFET power amplifier. *IEE Proc. B*, 138(6):285–296, November 1991.

[163] J. G. Laframboise. Theory of spherical and cylindrical Langmuir probes in a collisionless, Maxwellian plasma at rest. Technical Report 100, Institute for Aerospace Studies, University of Toronto, 1966.

[164] F. F. Chen. Electric probes. In R. H. Huddlestone and S. L. Leonard, editors, *Plasma Diagnostic Techniques*, volume 21 of *Pure and Applied Physics*. Academic Press, New York, 1965.

[165] L. J. Overzet and M. B. Hopkins. Comparison of electron-density measurements made using a Langmuir probe and microwave interferometer in the Gaseous Electronics Conference reference reactor. *J. Appl. Phys.*, 74(7):4323–4330, 1993.

[166] M. B. Hopkins. Langmuir probe measurements in the Gaseous Electronics Conference RF reference cell. *J. Res. Natl. Inst. Stand. Technol.*, 100(4):415–425, 1995.

[167] C. Cui and R. W. Boswell. Role of excitation frequency in a low pressure, inductively coupled radio frequency, magnetized plasma. *Appl. Phys. Lett.*, 63(17):2330, 1993.

[168] T. E. Sheridan, M. J. Goeckner, and J. Goree. Observation of two-temperature electrons in a sputtering magnetron plasma. *J. Vac. Sci. Technol. A*, 9(3), 1991.

[169] E. Eser, R. E. Ogilvie, and K. A. Taylor. Measurements of plasma discharge characteristics for sputtering applications. *J. Vac. Sci. Technol.*, 15:199, 1978.

[170] F. F. Chen. Lecture notes on Langmuir probe diagnostics. In *Mini-Course on Plasma Diagnostics, IEEE-ICOPS Meeting, Jeju, Korea*, 2003. `http://www.seas.ucla.edu/~ffchen/Publs/Chen210R.pdf`.

[171] R. W. Boswell, A. J. Lichtenberg, and D. Vender. Bohm velocity with a two-temperature distribution of negative particles. *IEEE Trans. Plasma Sci.*, 20(2):62, 1992.

[172] R. C. Hilborn. Einstein coefficients, cross sections, f values, dipole moments, and all that. *Am. J. Phys.*, 50:982, 1982.

[173] T. Holstein. Imprisonment of resonance radiation in gases. *Phys. Rev.*, 72(12):1212–1233, 1947.

[174] A. Peirce. Introductory lecture notes on partial differential equations, lecture 20: Heat conduction with time dependent boundary conditions using eigenfunction expansions. `http://www.math.ubc.ca/~peirce/M257_316_2012_Lecture_20.pdf`, March 2014.

[175] S. E. Koonin. *Computational Physics*. The Benjamin/Cummings Publishing Company, Inc., Menlo Park, California, 1986.

[176] National Research Council. *Plasma Physics of the Local Cosmos*. The National Academies Press, Washington, D.C., 2004.

[177] J. F. Hansen. *Laboratory Simulations of Solar Prominences*. PhD thesis, California Institute of Technology, 2001.